Quantum Transport and Scale Invariance in Expanding Fermi Gases

by

Ethan Robert Elliott

Department of Physics
Duke University

Date:_____
Approved:

_____
John Thomas, Supervisor

_____
Steffen Bass

_____
Alfred Goshaw

_____
Jian Guo Liu

_____
Ying Wu

Dissertation submitted in partial fulfillment of the
requirements for the degree of Doctor of Philosophy
in the Department of Physics
in the Graduate School of
Duke University

2014

<u>ABSTRACT</u>

(Physics)

Quantum Transport and Scale Invariance in Expanding Fermi Gases

by

Ethan Robert Elliott

Department of Physics
Duke University

Date:_____
Approved:

_____
John Thomas, Supervisor

_____
Steffen Bass

_____
Alfred Goshaw

_____
Jian Guo Liu

_____
Ying Wu

An abstract of a dissertation submitted in partial fulfillment of
the requirements for the degree of Doctor of Philosophy
in the Department of Physics
in the Graduate School of
Duke University

2014

To Stefanie

Abstract

This dissertation describes the first experimental measurement of the energy and interaction dependence of the shear viscosity η and bulk viscosity ζ in the hydrodynamic expansion of a two-component Fermi gas near a broad collisional (Feshbach) resonance. This thesis also presents the first experimental test of scale invariance in the expansion of a strongly interacting Fermi gas: after release from an anisotropic optical trap, we observe that a resonantly interacting gas obeys scale-invariant hydrodynamics, where the mean square cloud size $\langle \mathbf{r}^2 \rangle = \langle x^2 \rangle + \langle y^2 \rangle + \langle z^2 \rangle$ expands ballistically (like a non-interacting gas) and the energy-averaged bulk viscosity is consistent with zero, $0.00(0.04)\,\hbar\,n$, with n the density, as predicted for a scale-invariant hydrodynamic system. In contrast, the aspect ratios of the cloud exhibit anisotropic "elliptic" flow with an energy-dependent shear viscosity. Tuning away from resonance, we observe conformal symmetry breaking, where $\langle \mathbf{r}^2 \rangle$ deviates from ballistic flow. Using conformal field theory methods, a universal minimum has been predicted for the ratio of shear viscosity to entropy density, defining a perfect fluid. We find that η has both a quadratic and a linear dependence on the interaction strength $1/(k_{FI}a)$, where a is the s-wave scattering length and k_{FI} is the Fermi wave vector for an ideal gas at the trap center. At low energy, the minimum is less than the resonant value and is significantly shifted toward the BEC side of resonance, to $1/(k_{FI}a) = 0.2$, suggesting that bosonic degrees of freedom may lower the shear viscosity and

potentially allow a more perfect fluid.

Acknowledgements

The most egregious simplification that I shall make in this dissertation is the finite length of this section. No one completes any scientific work without an expansive support system, including grants, mentors, impactful grade school teachers, coworkers, friends and family. The complete list gets intractable quickly. A PhD takes years, and I hope that friends who are omitted understand that I have been grateful for all of their distractions or encouragement. In reflecting on what made me originally want to become a scientist, or remembering the late nights or weekends I have spent working alone in the lab listening to audiobooks, there is also an extensive list of fictional characters that I will skip in thanking.

I first thank my advisor, John Thomas. Most graduate students enter a field of specialization with little true understanding of what the important contemporary questions of that discipline are. At best, they end up with an advisor that does. In first meeting John, I was shocked at the stories he would casually tell about his youth that sounded a lot like the adventures of some sort of comic book boy genius. Currently an adult genius, John has an innate ability to understand what is scientifically cool, and seems to have always been able to ask the right questions at the right time. I am truly grateful for all of the conversations we have had over the years and the guidance he has provided in terms of physics and life in general. He is truly an exceptional teacher. I have also always been impressed by his ability to command a room when presenting a scientific talk. My final defense

presentation was helped greatly by his example.

Prior to beginning graduate school, I owe a great deal to Frank Narducci for the training in experimental physics he provided. In addition to running a government lab with regular employees, the dedication that Frank has to teaching students is extraordinary. I was very fortunate to be taught by him when I was. During the same time period, I also encountered my first professional co-worker in atomic physics, Chris Lehman, who left me with the unreasonable expectation that all future lab partners would have the same taste in ridiculous television or movies that I did.

I am also grateful to the postdocs I worked with directly, Jessie Petrika, Hiabin Wu, and James Joseph. Equipment suggested and provided by Ilya Arakelyan also led to the discovery and correction of a particulary insidious flaw in our experimental apparatus. In the final years of my dissertation work, the contribution from James has been immense. From designing and implementing a new computer control system for the experimental apparatus to endless hours of data processing, James's efforts allowed me to concentrate my own time on operating the experiment and collecting data.

While writing this thesis, I became distracted by my own attempts at an additional experiment to measure the shear viscosity of a Fermi gas as a function of interaction strength and constant entropy. I am very thankful to graduate student husband and wife team Arunkumar Jagannathan and Nithya Arunkumar for taking time away from their own work in order to finish collecting this data so that I could return to my thesis and stand a chance of graduating. A heartfelt thank you to all other graduate students in John's group as well.

Contents

List of Tables

List of Figures

Chapter 1

Introduction

This dissertation describes the first experimental measurement of dissipative hydrodynamics in the expansion of an ultra-cold Fermi gas of atoms as a function of interaction strength. Following release from an optical trap, the expansion of the gas into free space creates a low frequency flow where the consequences of dissipative forces can be directly observed. The experiments are conducted in the vicinity of a collisional (Feshbach) resonance, where the s-wave scattering length a_s for interactions between spin-up and spin-down fermions can be tuned from zero, where the gas is non-interacting, to a resonant regime where $a_s \to \infty$ and the cloud is the most strongly interacting, non-relativistic quantum system known [1]. A central connection between these two regimes is scale invariance, or the lack of an intrinsic length scale, and a thermal equilibrium pressure P related to the energy density $\mathcal{E}$ by $P = (2/3)\mathcal{E}$ [2,3]. For a scale invariant system, where every thermodynamic quantity is expressible in terms of density and temperature, this relationship provides an equation of state [2,3]. In addition to conservation laws and the equations of motion, an equation of state is a prerequisite for the complete description of any hydrodynamic flow. While $P = (2/3)\mathcal{E}$ has been experimentally verified for a trapped, equilibrated gas [4], it has only been assumed in the hydrodynamic expansion process. By comparison to the expansion of the

non-interacting gas, we present the first demonstration that $P = (2/3)\mathcal{E}$ and scale invariance is maintained in the expansion of the resonantly interacting Fermi gas.

1.1 Low Viscosity Quantum Fluids

Near a collisional resonance produced by a bias magnetic field, the behavior of a dilute, ultra-cold gas of spin-up and spin-down fermions is well described by low viscosity hydrodynamics [5,6]. First produced in 2002, these systems are now widely studied for their ability to model in table top experiments the physics of high temperature superconductivity, neutron stars, and nuclear matter [7–11]. The later example refers to the quark gluon plasma (QGP), thought to exist microseconds after the big bang, and first produced experimentally at the Brookhaven National Laboratory's Relativistic Heavy Ion Collider [12,13]. Although the strongly interacting QGP is 19 orders of magnitude hotter and 25 orders of magnitude denser than an ultra-cold Fermi gas, both behave as extremely low viscosity fluids [11].

The viscosity of a fluid is a measure of its internal friction, characterizing how much momentum is irreversibly transferred from points where the velocity of the fluid is large, to where it is small [14]. Viscosity is characterized by two different viscosity coefficients; the *shear viscosity coefficient* η and the *bulk viscosity coefficient* ζ. Shear viscosity is proportional to the dissipative force that resists the parallel sliding of nearby fluid elements in the presence of a velocity gradient, while the bulk viscosity is proportional to the dissipative force arising form the direct collisions of fluid elements normal to their boundaries during uniform expansion or contraction. A situation which illustrates the effect shear viscosity in two dimensions [15] is given in Fig. 1.1. Here, two solid plane surfaces are
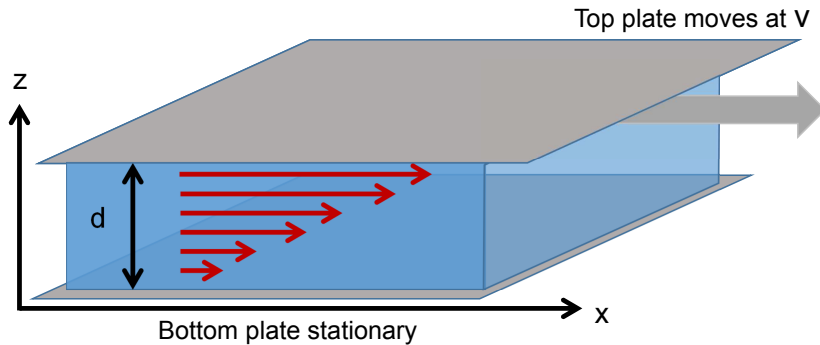
Figure 1.1: Viscous drag in a fluid between two parallel plates.

arranged with a viscous fluid between them, and the bottom plane is kept stationary. If the top plane moves at velocity v, then the shear viscosity will transfer momentum within the fluid from the direction of the top plate to the bottom plate, so that a force F is required to maintain the velocity of the top plate. This force, equal and opposite to the force related to shear viscosity, is proportional to the area of the plates A and the velocity gradient in the fluid v/d, where d is the distance between the plates so that

$$\frac{F}{A} = \eta \frac{v}{d}. \tag{1.1}$$

The viscosity of a fluid is determined by the way the particles which make up that fluid interact. If the fluid between the two plates in Fig. 1.1 is taken to be comprised of elastically colliding particles, then η is directly proportional to the mean free path [16]. If the mean free path is large, a single particle can travel a greater portion of the distance d and transfer more of the momentum from the top plane to portions of the fluid nearer the bottom plane, consistent with a larger viscosity. It is for this reason that the resonantly interacting Fermi

gas and the QGP, with their strong interactions and vanishing collisional mean free paths, exhibit extremely low shear viscosities.[1]

Dimensionally, Eq. 1.1 indicates that η has units of momentum over area. A natural momentum scale is $\hbar/L$ where $\hbar$ is Plank's constant and L is the interparticle spacing. The corresponding area is then L^2. Each viscosity coefficient then has units $\hbar/L^3 = \hbar n$, where n is the density. Hence,

$$\eta = \hbar n \, \alpha_S \tag{1.2}$$

$$\zeta = \hbar n \, \alpha_B, \tag{1.3}$$

where α_S and α_B are dimensionless shear and bulk viscosity coefficients, respectively. Noting the presence of $\hbar$, *quantum viscosity* is an appropriate label for the viscosity of a fluid where α_S is order unity or less. To provide a sense of scale, $\alpha_S \approx 300$ for water, while the air we breath has an $\alpha_S \approx 6000$, due to its low density. A resonantly interacting Fermi gas is 10^6 times *less* dense then air. However, we shall see that α_S for this system is indeed less than one.

---

[1] For a dilute Fermi gas, where the shear viscosity is proportional to the mean free path, it is found that the collisional cross section increases at lower temperatures, so that the shear viscosity decreases with decreasing temperature [5]. The viscosity of a fluid such as honey or oil arises from completely different physical mechanisms. Within these fluids, it is the gridlock of large organic molecules as they try to move past each other which produces the kind of flow we intuitively recognize as viscous. For larger temperatures, the molecules within these fluids have greater amounts of random thermal motion, which assists them in unjamming after a collision. This results in a decreasing viscosity for an increasing temperature. A practical example is the problem of early engine oils which lost viscosity when heated. The solution is not simply a higher viscosity oil, as the oil must be able to initially flow over the engine components when the engine is first started and cold. Instead, long poly(lauryl methacrylate) molecules are added [17]. These molecules coil into spheres at low temperatures, negligibly contributing to the viscosity of the oil. These spheres unwind into long chains as the temperature rises, increasingly hindering the flow of oil molecules, and creating a "visco-static" fluid defined by a viscosity more independent of temperature.

1.2 Perfect Fluidity

If the flow of a strongly interacting Fermi gas is well described by low viscosity hydrodynamics, an appropriate question becomes exactly how low. Below a certain temperature, a strongly interacting Fermi gas transitions into a *superfluid*, where the shear viscosity vanishes. Above the superfluid transition, we define the *normal fluid* state, where the shear viscosity should be small but finite, reaching a minimum just before the transition point. Derived using holographic duality methods [11], there exists a conjectured universal minimum for the ratio of the shear viscosity η to the entropy density s in the normal fluid phase [18]. The conjecture states that for a broad class of strongly interacting quantum fields,

$$\frac{\eta}{s} \geq \frac{\hbar}{4\pi k_B} \ . \tag{1.4}$$

A fluid that reaches this minimum is defined to be a *perfect fluid.*

The divergent interaction strength in a resonant Fermi gas makes it a compelling system to investigate perfect fluidity, further motivating the measurement of its viscosity. Recent measurements of the shear viscosity for the resonantly interacting Fermi gas find $\alpha \simeq 0.4$ for the normal fluid phase and η/s just 4.5 times the lower bound [5], comparable to that of the QGP. However, in the present work, we describe the results of a grealty improved measurement technique for the low energy shear viscosity in a resonantly interacting Fermi gas. Additionally, we shall present initial evidence for a *lower* viscosity occurring where the interaction strength is repulsive and large, but *finite.*

There are however, more questions in the study of transport coefficients in Fermi gas beyond the minimum values they can achieve. In addition to this perfect

fluid conjecture, the dependences of viscosity on initial energy and interaction strength provide important benchmarks for nonperturbative many-body theories.

1.3   Elliptic Flow

A hallmark of low viscosity hydrodynamics is *ellipical flow*, a flow pattern that results if the system in question starts with an elliptical density and pressure distribution. In our experimental setup, a strongly interacting Fermi gas of ^{6}Li atoms is prepared in an anisotropic optical trap created by a strongly focused CO_2 laser beam. When the gas is initially confined, the equilibrium density is determined by the balance between the outward pressure force and the inward restoring force of the confining potential. The anisotropic trap shape therefore creates both an anisotropic initial cloud shape and an anisotropic initial pressure; the smallest direction of the atomic cloud corresponding to the largest gradient in the confining potential and the largest gradient in the pressure. When the optical potential is extinguished to initiate expansion, the imbalanced pressure drives the gas outward. The largest pressure gradient results in the largest acceleration, so what was initially the smallest direction will become the largest dimension of the cloud during the expansion process. Qualitatively, the cloud shape changes from a vertical cigar to a horizontal ellipse.

Elliptic flow, along with the rest of our data, is tracked experimentally using absorbtion imaging, in which a spatially uniform laser pulse is transmitted through the cloud towards the CCD (charge coupled device) array of a camera. The cloud is destroyed as it partially absorbs the light, but the shadow cast by its density distribution is recorded in a camera image. By creating new atomic
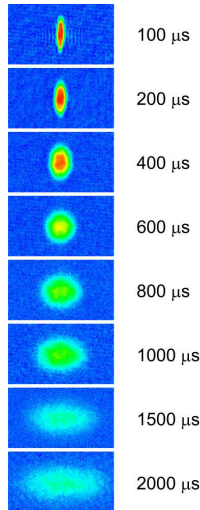
Figure 1.2: Elliptic flow in the expansion of a strongly interacting Fermi gas [7].

clouds with the same initial conditions and imaging as a function of time after release from the optical trap, we create a slide show of expansion, as shown in Fig. 1.2.

We quantitatively describe elliptic flow in terms of an aspect ratio, defined as the ratio of the cloud width in the initially small direction to the width in the initially larger direction, so that its initial value is less than one. When the cloud aspect ratio surpasses a value of one, elliptic flow and hydrodynamics are confirmed. In this way, the creation of the first strongly interacting Fermi gas was demonstrated using the data in Fig. 1.2 [7].

Elliptic flow and the associated evolution of the aspect ratio are also sensitive to shear viscosity. If shear viscosity is present, momentum will be transferred *out of* the more quickly expanding direction and *into* the more slowly expanding direction. This slows the time dependent growth of the aspect ratio by both lowering its numerator and increasing its denominator, making it a powerful means
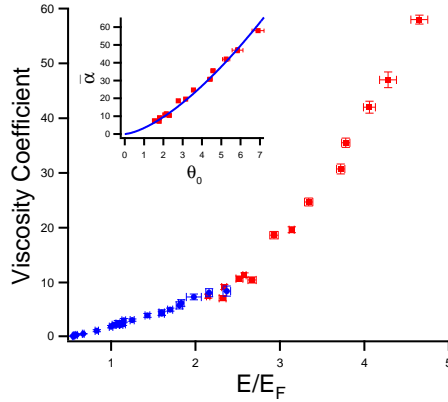
Figure 1.3: First measurement of shear viscosity as a function of energy in a unitary Fermi gas. Values in red are obtained from observing the evolution of the atomic cloud aspect ratio following release from an optical trap. Values in blue are obtained from measurements of collective mode damping. Collective oscillations are susceptible to breakdowns of hydrodynamics which cause the blue data to join the red data with a different curvature. Inset shows the data as a function of reduced temperature [5].

of measuring the shear viscosity. This method was used by our group to perform the first measurement of the shear viscosity in a resonant Fermi gas [5]. However, elliptic flow has not been used to measure viscosity in the low energy regime, where the superfluid transition and the minimum values of the shear viscosity occur. This was due to the small number of atoms present at low temperatures that prevented accurate characterization of the density profile, in addition to a trap shape that created an elliptic flow pattern in which the smaller viscosities were difficult to distinguish.

Instead, the low energy viscosity was obtained from previous measurements of collective mode damping [5, 19]. Shown in Fig. 1.3 (in blue) and compared to viscosity data found using elliptic flow (in red), the collective mode data joins the high temperature expansion data, but with a different curvature. This is a

result of the thermalization rate at higher energies decreasing to a point where it is comparable to the finite collective mode oscillation frequency, causing a breakdown of hydrodynamics. In contrast, the associated frequency in an expansion experiment is the inverse of the expansion time, causing the system to become *more* hydrodynamic as the cloud expands. In the current work, we report the first measurement of shear viscosity in the low energy regime of the resonant gas using expansion, made possible with an optical trap shape that creates an elliptic flow pattern that is particulary sensitive to shear viscosity. This trap shape further allows accurate study of the shear viscosity as a function of scattering length.

1.4 Scale Invariance

When the s-wave scattering length diverges in the resonant regime, an ultra-cold Fermi gas loses its only intrinsic length scale, becoming a *scale invariant* system. For physical systems (some hypothetical mathematical distinctions exist), this is synonymous with a *conformally symmetric* regime. Lacking an intrinsic length scale, all properties of the resonant gas are determined by only the density n and the temperature T [2,3]. As a consequence, the equation of state for the resonant gas in local thermal equilibrium is the beautifully simple relation $P = (2/3)\mathcal{E}$, where P is the pressure and $\mathcal{E}$ is the (internal) energy density. This has been verified to high precision in the trapped, equilibrated gas [4], but has only been *assumed* to hold during expansion, where an equation of state is necessary to write the complete hydrodynamic equations that include viscous flow. Therefore, a demonstration that $P = (2/3)\mathcal{E}$ during expansion would not only examine if local thermal equilibrium and scale invariance is maintained in the expansion

process, but also check the validity of invoking $P = (2/3)\mathcal{E}$ in all hydrodynamic measurements.

Scale invariance also directly restricts the viscous transport coefficients themselves. By requiring scale invariance in the equations of hydrodynamics, it can also be shown theoretically that the bulk viscosity of the resonant gas is exactly zero at all temperatures [20]. Previously, we have roughly estimated the size of the bulk viscosity in the resonant gas using a consistency argument from only a single measurement at a high temperature [6]. The present work shall present direct measurements of bulk viscosity at a range of energies, in addition to investigating the possibility of a non-zero bulk viscosity when scale invariance is broken and the scattering length is finite.

Tunable interactions allow us to create a separate scale invariant system, where the scattering length is zero and the gas is non-interacting. Despite the largest possible difference in interaction strength from the resonant gas, scale invariance requires that the properties of both systems are determined only by the density and temperature. In fact, for the ideal non-interacting gas, the equation of state in the familiar $PV = Nk_BT$, where equipartition gives the total kinetic energy $E_{kin} = \mathcal{E}V = (3/2)Nk_BT$, so that the equation of state is equivalently

$$P = \frac{2}{3}\mathcal{E}, \tag{1.5}$$

exactly the same as the resonant gas.

When the aspect ratio of a non-interacting gas expanding from an anisotropic potential is examined, it does not exhibit elliptical flow. There is no acceleration in the expansion of the initial smaller direction, and each atom expands from

the trap while maintaining its initial velocity. This behavior is therefore labeled as *ballistic expansion*. Ballistic expansion of the cloud is easily described using simple arguments. If a non-interacting gas is confined in a potential U that is extinguished at time $t = 0$ to initiate expansion, then the ith gas particle with initial position $\mathbf{r}_{i0}$ will have a time dependent position given by $\mathbf{r}_i = \mathbf{r}_{i0} + \mathbf{v}_{i0}\, t$. If we look at a mean square width of the cloud in the x direction, where the average is taken over the density distribution, we have

$$\langle x^2 \rangle = \langle x^2 \rangle_0 + \langle v_x^2 \rangle_0\, t^2. \tag{1.6}$$

If the z-direction is assumed to be initially larger than the x-direction and the x-z aspect ratio $\sqrt{\langle x^2 \rangle / \langle z^2 \rangle}$ is examined, we have

$$\sqrt{\frac{\langle x^2 \rangle}{\langle z^2 \rangle}} = \sqrt{\frac{\langle x^2 \rangle_0 + \langle v_x^2 \rangle_0\, t^2}{\langle z^2 \rangle_0 + \langle v_z^2 \rangle_0\, t^2}}. \tag{1.7}$$

Because the average initial speed is the same in all directions, at large times the aspect ratio in ballistic flow asymptotes to unity, in contrast to elliptic flow which must by definition surpass an aspect ratio of one.

If we instead consider the mean square cloud *radius* $\langle \mathbf{r}^2 \rangle = \langle \mathbf{x}^2 \rangle + \langle \mathbf{y}^2 \rangle + \langle \mathbf{z}^2 \rangle$ of the entire cloud during ballistic expansion, we find that

$$\langle \mathbf{r}^2 \rangle = \langle \mathbf{r}^2 \rangle_0 + \langle \mathbf{v}^2 \rangle_0\, t^2 \tag{1.8}$$

$$\frac{d^2}{dt^2} \frac{m}{2} \langle \mathbf{r}^2 \rangle = \langle \mathbf{r} \cdot \nabla U \rangle_0, \tag{1.9}$$

where the virial theorem for a trapped cloud yields $m\langle \mathbf{v}^2 \rangle_0 = \langle \mathbf{r} \cdot \nabla U \rangle_0$ [21]. A primary result of this dissertation is that as a consequence of scale invariance,

11

Eq. 1.9 surprisingly holds for the mean square cloud radius of the *resonant* gas. This is despite of the presence of strong interactions, and an energy dependent shear viscosity. It will be demonstrated that any deviation from the right hand side of Eq. 1.9 in a hydrodynamic system is directly relatable to a finite change in the equation of state or the emergence of bulk viscosity, both of which constitute a loss of scale invariance, or *conformal symmetry breaking.* In addition to the bulk viscosity, by defining a conformal *symmetry breaking pressure,*

$$\Delta P = P - \frac{2}{3}\mathcal{E}, \tag{1.10}$$

we may investigate how the equation of state changes as a function of interaction strength by observing the expansion of $\langle \mathbf{r}^2 \rangle$ at different scattering lengths. Further, we may study $\langle \mathbf{r}^2 \rangle$ and the size of ΔP in the expansion of the resonant gas to examine the degree to which local thermal equilibrium is maintained.

1.5   New Optical Trap Geometry

The original measurements reported in this dissertation are made possible by a new geometry for our optical trap and the addition of second camera to our imaging system, shown in Fig. 1.4. Using a pair of cylindrical telescopes, we have created an optical trap that is elliptic in *two* planes. This creates an atomic cloud that is in the shape of tri-axial ellipsoid, with a $1.0 : 2.7 : 33$ (x:y:z) initial aspect ratio. Previous measurements of expansion relied on the elliptical flow in a cylindrically symmetric trap, where the initial aspect ratio was roughly 1/30 [5]. We shall demonstrate that the elliptical flow pattern starting from a 1/2.7 aspect ratio allows for a more sensitive measurement of the shear viscosity at any inter-
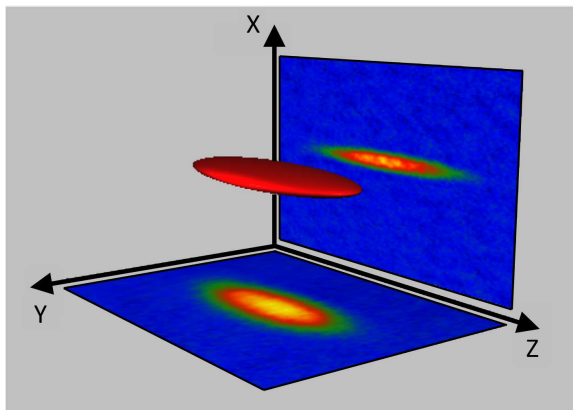
Figure 1.4: Two CCD cameras are used to image the density profile of the expanding cloud, providing widths of all three dimensions. The cloud is released from an asymmetric optical trap with a $1.0 : 2.7 : 33$ (x:y:z) aspect ratio, where the y-z plane is imaged by camera-1 and the x-z plane is imaged by camera 2.

action strength. As the propagation of the high power CO_2 laser that creates this optical trap is along the z-axis, observation of the x-y plane is accomplished by comparing an image of the y-z plane to a simultaneously acquired image of the x-z plane taken with a second camera.

Simultaneous imaging of the cloud from two directions and measurement of all three mean square sizes additionally grants us the ability to study the expansion of $\langle \mathbf{r}^2 \rangle$ for the first time. This allows the first demonstration of scale invariance in the expansion of the resonant gas by comparison to a measurement of $\langle \mathbf{r}^2 \rangle$ taken in the non-interacting gas. This also presents a means to study the bulk viscosity and ΔP as a function of interaction strength as noted above. Further, we shall demonstrate that a measurement of $\langle \mathbf{r}^2 \rangle$ provides a new method of characterizing the confining potential of the trapped atoms, reducing systematic errors in all of our measurements.

1.6   Primary Results

With some background established by the preceding pages, the primary results
of this dissertation are briefly summarized below. The next chapters will begin
in depth derivations of hydrodynamic equations and descriptions of experimental
techniques, and this section is intended to give the casual reader some context as
to what should be anticipated.

1.6.1   Unitary Shear Viscosity at Low Energy

We observe an elliptic flow pattern in the expanding x-y aspect ratio $\sqrt{\langle x^2 \rangle / \langle y^2 \rangle}$
of the unitary gas that is highly sensitive to the shear viscosity η, allowing the
measurement of small shear viscosities at low energies previously unaccessible
in expansion experiments [5, 6]. We find that the shear viscosity grows from -
$0.02(4)\hbar n$ in the superfluid regime, to $3.39(32)\hbar n$ at a total energy per particle
$E = 1.70(4)E_F$, where E_F is the Fermi energy of an ideal gas at the trap center
and n is the density. From these measurements alone, we are able to fit a curve
that very well extrapolates to the high energy $E \simeq 4.5\, E_F$ region where previous
expansion data was taken [5].

1.6.2   Demonstration of Scale Invariance

We demonstrate that the mean square cloud radius $\langle \mathbf{r}^2 \rangle = \langle x^2 \rangle + \langle y^2 \rangle + \langle z^2 \rangle$ of
the resonantly interacting gas expands ballistically, identical to a non-interacting
gas. This is in contrast to the aspect ratio, which expands hydrodynamically
with an energy dependent shear viscosity. Such behavior is a consequence of scale
invariance, and provides evidence that the equation of state $P = 2/3\,\mathcal{E}$ and local

thermal equilibrium are maintained throughout the expansion. Quantitatively examining the expansion of $\langle \mathbf{r}^2 \rangle$, we also find that the energy-averaged unitary bulk viscosity is consistent with zero, $0.00(0.04)\hbar\,n$, as predicted for scale-invariant hydrodynamics [20].

1.6.3 Observation of Conformal Symmetry Breaking

We tune the interaction strength away from resonance, where we observe conformal symmetry breaking as $\langle \mathbf{r}^2 \rangle$ deviates from ballistic flow. Our analysis finds that the primary contribution to this behavior is a change in the equation of state $\Delta P = P - 2/3\,\mathcal{E}$, rather then the emergence of a finite bulk viscosity.

1.6.4 Shear Viscosity as a Function of Interaction Strength

We study the shear viscosity as a function of energy and interaction strength $1/(k_{FI}a)$, where a_s is the s-wave scattering length and k_{FI} is the Fermi wave vector for an ideal gas at the trap center. At low energy, the minimum is less than the resonant value and is significantly shifted toward the BEC side of resonance, to $1/(k_{FI}a) = 0.2$. This suggests that a Bose-Fermi mixture permits a lower shear viscosity and higher collision rate than the resonantly interacting Fermi gas. This result also indicates that a Fermi gas at $1/(k_{FI}a) = 0.2$ could behave as a more perfect fluid than the resonant gas.

1.7 Dissertation Organization

The language of an introduction tends to favor bold claims rather than useful explanations. The later, the author hopes, will be found in the following chapters.

Firstly, Chapter 2 provides a description of how tunable interactions are possible in an ultra-cold atomic gas through the application of a bias magnetic field. While a chapter can be found discussing this same topic in six previous dissertations from this very group, the material is important enough to the following chapters in this dissertation that it will be presented a seventh time. The twist for this retelling will be the belief that much of the behavior of the scattering length in an ultra-cold gas near a Feshbach resonance can be understood from the canonical Quantum Mechanics problem of a finite square well with a bound state near its threshold when considered in the zero energy limit. This section will define and describe the jargon behind the BEC-BCS crossover, the unitary regime, and exactly why a divergent scattering length makes the system independent of the macroscopic potential between the atoms.

As this dissertation was performed over a period of time that saw not only a rebuild of the experimental apparatus to match the design of [22, 23] but also a complete dismantle and reassembling necessitated by a change of laboratory space, Chapter 3 will cover the upgrades to the experimental apparatus as well as descriptions of experimental methods. Where techniques appear that are not specific to this experiment but needed in the grand scheme of producing and imaging an ultra-cold Fermi gas, these well-established methods will be briefly summarized.

Chapter 4 describes the equations of hydrodynamics which are used to derive a scaling solution for the mean square cloud size $\langle x_i^2 \rangle$, where i indicates the ith direction, and an *exact* solution for the mean square cloud radius (given by $\langle \mathbf{r}^2 \rangle$), both as a functions of time after release from an optical trap. We compare this equation of motion for $\langle \mathbf{r}^2 \rangle$ in a hydrodynamic system to that of the scale invariant

resonant and non-interacting gas, finding that they differ only by the conformal symmetry breaking pressure $\Delta P = P - \frac{2}{3}\mathcal{E}$, a bulk viscosity term, and the effect of the finite magnetic curvature resulting from the applied field that tunes the interatomic interactions.

A means of finding $\Delta P = P - \frac{2}{3}\mathcal{E}$ and the viscosity coefficients as a function of a finite scattering length is given Chapter 5. Assuming the high temperature limit, ΔP is determined with a fugacity expansion and written in terms of a second virial coefficient b_2, which is then related to experimentally accessible quantities. Based on a recent theoretical prediction, a form of the bulk viscosity for a Fermi gas is given in terms of the scattering length, energy, and a dimensionless constant [24]. Also assuming a high temperature limit, the bulk viscosity is determined in terms of the parameters necessary to compare to our measurements. A general shear viscosity term that is made up of a temporally constant part and one that varies with the scattering length and temperature is also presented.

A detailed characterization of the trapping potentials created by the optical trap and bias magnetic field is given in Chapter 6. The form of each potential is treated as effectively harmonic, so that any deviations from perfectly harmonic are contained within an energy dependent oscillation frequency. The use and limitations of parametric excitations of the optical potential as a technique to find these frequencies is discussed, with an emphasis on how extremely sensitive the analysis of $\langle \mathbf{r}^2 \rangle$ is to the measured axial frequency. Because of this, a new method of determining the confining frequencies from measurements of $\langle \mathbf{r}^2 \rangle$ in the non-interacting gas and resonant superfluid regimes is presented.

With the context established by the previous chapters, Chapter 7 gives a comprehensive description of data analysis procedures and results. Serving as a

reference for both the bulk viscosity at resonance and the shear viscosity in the case of a finite scattering length, the new measurements of the shear viscosity in the resonant gas are presented first. These results are followed by an examination of the effects that break the scale invariant expansion of $\langle \mathbf{r}^2 \rangle$, where it is found that ΔP, not the bulk viscosity is the primary cause. This chapter concludes with a presentation of the measurements of the shear viscosity off resonance, which is found to have a minimum for a large and positive scattering length.

Chapter 2

Magnetically Tunable Interactions

An ultra-cold atomic Fermi gas is a powerful paradigm for scale-invariant quantum fluids with the unique trait of interactions that are precisely tunable between scale-invariant strongly interacting and non-interacting systems. While the investigation of the strongly interacting gas rightfully attracts more interest, the ability to directly compare to the noninteracting regime can provide a crucial reference point for the behavior of the strongly interacting case. This tunability is accomplished through the existence of a *Feshbach Resonance*, which only takes a change in the strength of an applied bias magnetic field to produce arbitrarily strong or weak interactions, with either an attractive or repulsive nature. How this is possible is the subject of this chapter.

Both interaction strength and scale invariance in an ultra-cold gas can be quantified through a single parameter, a_s, the *s-wave scattering length*. Since a_s provides a length scale for interatomic interactions, tuning the interactions can be equivalently treated as tuning a_s. For the s-wave scattering of two atoms with

relative momentum $\hbar k$, the collisional cross section is given by

$$\sigma_c = \frac{4\pi a_s^2}{1 + (ka_s)^2},$$ (2.1)

where a_s is related to the range and depth of the interatomic potential. For low energy and $k\, a_s \ll 1$, $\sigma_c \approx 4\pi a_s^2$, the scattering length appears as the radius that determines the cross section, although a_s can have a positive or negative value. For the system to be scale invariant, by definition it can not have a length scale, and a_S must not have a finite value. The scale-invariant, strongly interacting case occurs when a_s diverges, so that $1/a_s = 0$ and the cross section is given by $4\pi/k^2$. In this *universal regime*, σ_c is a function of only the relative momentum between colliding atoms, or equivalently their de Broglie wavelength. The scale-invariant, non-interacting gas corresponds to the case of $a_s = \sigma_c = 0$.

The atomic species composing the ultra-cold Fermi gas studied in this dissertation is the fermionic isotope of lithium, ^{6}Li. Much can be said about properties specific to this atom, and the daily operation of our experimental apparatus requires that spectroscopic details of its ground and excited states be known in detail. Great references have been compiled on this topic [25, 26], and it is not the purpose of this chapter to be ranked among them. Instead, this chapter aims to describe generally (using only first semester quantum mechanics) the manner in which interatomic potentials between spin-up and spin-down atoms can give rise to a magnetic field dependent a_S through a Feshbach resonance. Once the discussion of this topic concludes, this chapter ends with summary of the *BEC-BCS crossover*, a broad term for the different characteristics a Fermi system can assume as a function of scattering length.

2.1 Consequences of Low Energy Scattering

We begin by noting that a collision between two particles can be equivalently treated as a single particle of reduced mass μ_m and linear momentum given by $\langle \mathbf{p} \rangle = \hbar \mathbf{k}$, scattering off of a central potential $V(r)$. We also note two important properties of the ultra-cold Fermi gas based only on its name. First, it is ultra-cold, meaning a low energy limit will be assumed in any related scattering calculation. This corresponds to a low momentum limit, so that both linear and angular momentum will be treated as vanishingly small. Argued more qualitatively, the range of the interatomic potential between colliding ^{6}Li atoms[1] is roughly $r_0 \approx 20\,\text{Bohr} \approx 1$ nm, and the temperature of the gas is on the order of 1μK, corresponding to a thermal de Broglie wavelength of approximately $\lambda_T = 700$ nm. The wavelength is significantly larger than the range of the potential, so that if we quantize the angular momentum l of the gas via the relation $l\hbar = r_0 p = r_0 (h/\lambda_T)$, then l is given by:

$$l = \frac{2\pi r}{\lambda_T} \approx 0.001, \tag{2.2}$$

so that we need only consider s-wave ($l = 0$) collisions. We then proceed with the assumption that $l = 0$.

Secondly, an ultra-cold Fermi gas should be composed of fermions, which must have a total wave function that is antisymmetric. However, the spatial part of an s-wave collision is *symmetric*, so that an ultra-cold Fermi gas is entirely collisionless *unless two separate spin states are trapped*, to permit an anti-symmetric

---

[1]The number given here corresponds to the triplet molecular potential, the use of which will be justified in a later section.

wavefunction. For this reason, we trap the two lowest energy hyperfine ground states of ^{6}Li, labeled as $|1\rangle$ and $|2\rangle$, which can be equivalently labeled as simply spin-up and spin-down. Luckily, due to atomic fermions possessing internal structure, manipulation of a spin state is as simple as the application of a radio frequency pulse.

2.2 The s-wave Cross Section

The general form of a wave function undergoing a scattering event is written in spherical coordinates, where the z-axis is chosen parallel to the momentum $\mathbf{p} = \hbar\mathbf{k}$ of the incoming particle which will undergo a scattering event at the origin. The incoming particle itself is represented as an incoming plane wave given by e^{ikz}. The result of the scattering event will be observed in the far field, far past the range of an interatomic potential, so that the outgoing, scattered wave can be approximated as a spherical wave. Though the potential goes to zero as $r \to \infty$, the *effect* of the potential on the scattered wave is contained in the amplitude of this spherical wave, labeled as *the scattering amplitude*, which is a function of the incoming momentum, and in general, the coordinate angles θ and ϕ, written as $f(\theta, \phi, k)$. As $V(r)$ is spherically symmetric in our case, the scattering amplitude must also be spherically symmetric, so that $f(\theta, \phi, k) = f(\theta, k)$.

The form of the collision cross section σ_c is related to $f(\theta, k)$ through the conservation of probability. When the ratio of the rate of probability leaving the scattered area in the differential solid angle $d\Omega$ compared to rate of probability incident in the plane perpendicular to the incoming plane wave is taken, it is

found that:

$$\frac{d\sigma_c}{d\Omega} = |f(\theta, k)|^2, \tag{2.3}$$

so that the calculation of the cross section only requires an integration of $|f(\theta, k)|^2$ over the solid angle.

To find a form of the scattering amplitude, we choose the basis for $|f(\theta, k)|^2$ to be Lengendre polynomials, $P_l(\cos \theta)$, given by:

$$P_l(\cos \theta) = \left(\frac{4\pi}{2l+1}\right)^{1/2} Y_l^0, \tag{2.4}$$

where Y_l^0 is the $m = 0$ spherical harmonic. When $f(\theta, k)$ is expanded in terms of this basis, the coefficients for each Lengendre polynomial will contain the k dependence, and be written as $a_l(k)(2l+1)$. Here, $a_l(k)$ is

$$a_l(k) = \frac{e^{2i\delta_l} - 1}{2ik} = \frac{e^{i\delta_l} \sin \delta_l}{k}, \tag{2.5}$$

where δ_l is *lth partial wave shift*, the k dependent phase difference between the outgoing spherical wave which scattered from the potential compared to the case of an unscattered outgoing spherical wave which saw no potential. This form of $a_l(k)$ is found from the radial Schrödinger equation for angular momentum l, and its advantage here is that we may drop all $l \neq 0$ terms in the expansion of $f(\theta, k)$. Thus, while $f(\theta, k)$ in general is

$$f(\theta, k) = \sum_{l=0}^{\infty} (2l+1) \, a_l(k) P_l(\cos \theta), \tag{2.6}$$

we need only consider the $l = 0$ term so that

$$f(k) = \frac{e^{i\delta}\sin\delta}{k}, \tag{2.7}$$

and δ will be understood to mean $\delta = \delta_0(k)$. When the modulus square of $f(k)$ is integrated over the solid angle $d\Omega = \sin\theta \, d\theta \, d\phi$, we arrive finally at an expression for the s-wave collisional cross section given by

$$\sigma_c = \frac{4\pi}{k^2}\sin^2\delta. \tag{2.8}$$

2.3   The Scattering Length a_s

If the s-wave cross section is an area quantifying the distance over which particles scatter, then an associated one-dimensional length scale, labeled as the s-wave scattering length, must contain the same information. Consider the s-wave phase shift in the low energy limit, found from the radial Schrödinger equation with a general potential,

$$\frac{d^2u}{dr^2} + \frac{2\mu_m}{\hbar^2}[E - V(r)]u = 0. \tag{2.9}$$

where the full radial wave function $R(r)$ is related to u via $R(r) = u(r)/r = u/r$. Again, the consequences of a scattering event will be observed in the far field, far past the range of an interatomic potential. In this limit, the potential term is neglected in the Schrödinger equation,

$$\frac{d^2u}{dr^2} + \frac{2\mu_m}{\hbar^2}Eu = 0, \tag{2.10}$$

24

resulting in a solution of the form

$$u(r) = A\sin(kr + \delta). \tag{2.11}$$

So long as $V(r)$ is short range, this solution *form* is entirely independent of the potential, but the variables within it are not. Emphasizing that this is an elastic collision, k will not be altered during the collision, and will be the same as the case of zero cross section. Thus, the effect of the collision will be contained in the phase shift δ and small change in the normalization, $|A|^2$. Working in the low energy limit of vanishing k, the above form of $u(r)$ is given to first order in k by

$$u(r) = A\left(1 + \frac{k}{\tan\delta}r\right)\sin\delta. \tag{2.12}$$

From this linearized version of a simple solution to the radial Schrödinger equation in the limit of low energy and a short range potential, we may ask for what value of r does this line cross the r axis. It is this value of r, given by

$$0 = A\left(1 + \frac{k}{\tan\delta}r\right)\sin\delta. \tag{2.13}$$

which defines the s-wave scattering length as:

$$a_s \equiv -\frac{\tan\delta}{k}. \tag{2.14}$$

Looking back at form of the cross section, trig identities give,

$$\sigma_c = \frac{4\pi}{k^2}\sin^2\delta = \frac{4\pi}{k^2}\frac{\tan^2\delta}{1 + \tan^2\delta} = \frac{4\pi a_s^2}{1 + (ka_s)^2}, \tag{2.15}$$

so that the scattering length is contained within it.

Eq.2.15 indicates that the cross section is maximized for a given k when $\sin\delta$ is equal to one. This case is referred to as the *unitary* limit. It for this reason that the term *unitary gas* is an interchangeable label with a resonantly interacting gas. The cross section then further increases if $\sin\delta$ remains one while k^2 and the temperature both decrease.

For the unitary limit to be reached, the phase shift must be equal to $\delta = [(1/2) \pm n]\pi$ for $n = 0$ and all integer values. This will also cause the $\tan\delta$ term, and hence the scattering length, to diverge to an infinite value. In order for this to occur, we look at how simple forms of short range scattering potentials $V(r)$ can affect δ to produce strong interactions. Whether or not the scattering length is positive or negative will be determined by how the scattered wave function curves at the boundary of the potential in order to maintain its continuity.

A solution to the canonical problem of two identical scattering particles with a short range interaction requires knowledge of the particle mass, relative energy, and, in the case of a square-well potential, the height and depth of the potential. We have already stated a reduced mass, μ_m, and specified that we are operating in the low energy, low k limit. We label the range of the potential R, and its depth, if finite, as given by $V = \hbar^2 k_0^2/2\mu_m$. The effect of a repulsive potential on the scattering length is rather mundane compared to what an attractive potential can do, but we begin with the repulsive case so that the association of *repulsive* interactions and a *positive* scattering length is established.

2.4   Scattering From Repulsive Potentials

The simplest example of a scattering potential that produces a finite phase shift (and an associated scattering length) compared to the free particle solution is a barrier of infinite height and range R. Considering only the spherically symmetric case where $l = 0$, this canonical potential is labeled as "the hard sphere of radius R." This impenetrable barrier causes the first node of the wavefunction at be $r = R$, rather than $r = 0$. A phase shift $\delta = -R\,k$ is then produced, so that the scattering length is

$$a_s = \lim_{k \to 0} \frac{-\tan\left(-R\,k\right)}{k} = R. \tag{2.16}$$

A plot of $u(r)$ is given in Figure 2.1 along with an unscattered $u_f(r) = A\sin(kr)$ for comparison. Additionally, the linearization of $A\sin(kr+\delta)$ as $A\sin\delta\left(1 + \frac{k}{\tan\delta}\,r\right)$ is given as the dotted line, the r-intercept of which gives the scattering length. It is then visually obvious that the scattering length must be R. In the far field, the wave function appears shifted *out* relative to the un-scattered case. This is due to the infinite barrier creating a region of *excluded volume* that the scattered wave function does not enter. In this case, it seems that the spatial extent of the interaction, and hence the scattering length, is exactly the same as the range of the potential creating this interaction. This is not true in general, as we shall see in the case of an attractive well. It is true, however, that an infinite barrier can only produce a finite, positive value of the scattering length. The value of R can not be made arbitrarily large, for if the range of the potential starts to be on the order of $1/k$, the assumption of low energy breaks down. Because a repulsive potential can only produce a positive scattering length, we therefore

(a) Far-Field   (b) Within Range of the Potential
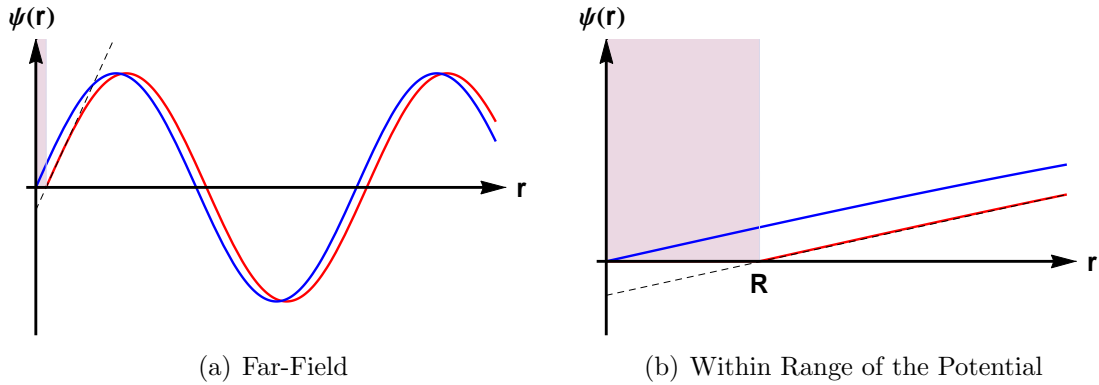
Figure 2.1: Scattering off of an infinite potential of range R, where the radial wave function is given by $R(r) = u(r)/r$. In red, the scattered wavefunction $A \sin(kr + \delta)$, where $\delta = -Rk$ which is shifted out from the unscattered wave function, $A \sin(kr + \delta)$, in blue. The dotted line gives $A \sin \delta \, (1 + \frac{k}{\tan \delta} r)$, so that its r-intercept (also R) is the scattering length. The interaction is repulsive, and the scattering length is positive.

label a *positive* scattering length as being a *repulsive* interaction. We shall see that the scattering length arising in a finite, attractive well, is a far more interesting function of the potential range and depth.

2.5   Scattering From a Finite Attractive Well

We take the potential of a finite, attractive well to be given by

$$
V(r) = \begin{cases} -\hbar^2 k_0^2/2\mu_m & \text{for } 0 \leq r < R \\ 0 & \text{for } r > R \end{cases}
$$

so that by inserting this form into the radial Schrödinger equation for $l = 0$, the radial wave function $R(r) = u(r)/r$ takes the form:

$$u(r) = \begin{cases} A\sin(\kappa\, r) & \text{for } 0 \le r < R \\ B\sin(kr + \delta) & \text{for } r > R \end{cases}$$

where $\kappa^2 \equiv k_0^2 + k^2$. For the $0 \le r < R$ region, the sine solution is chosen so that $u(0) = 0$ and $R(r)$ is normalizable. By demanding that $u(r)$ and $u'(r)$ are continuous at $r = R$, we find that

$$\frac{A\sin(\kappa\, R)}{\kappa\, A\cos(\kappa\, R)} = \frac{B\sin(k\, R + \delta)}{k\, B\cos(k\, R + \delta)}, \tag{2.17}$$

and the phase shift δ is given by

$$\delta = \tan^{-1}\left(\frac{k}{\kappa}\tan(\kappa R)\right) - k\, R. \tag{2.18}$$

This is far more interesting result than the repulsive case, for here $\tan\delta$ (and hence the scattering length), can be positive, negative, or divergent. For the divergent case, δ must be equal to $\pi/2$ which in the low k limit will happen when R and $\kappa \approx k_0$ have the following relation:

$$R = \frac{\pi}{\kappa}\left(n + \frac{1}{2}\right) \tag{2.19}$$

for $n = 0$ and all integer values. This is the same relationship that exists between R and k_0 for a finite attractive well which can support n bound states with an additional bound state forming at its threshold. This additional bound state at the top of the potential well is sometimes called a *virtual state*, as it not yet a true

29

bound state, but would be if either R or k_0 increased by an infinitesimal amount. Because the same values of R or k_0 create a virtual state at the top of the well and a divergent scattering length, we are encouraged to look for a connection between these two circumstances.

For a bound state of a particle to exist in a finite attractive well, at least a quarter wavelength of its wave function (1/4 of $2\pi/\kappa$) must fit in the well width, R. A virtual state will be created if this condition is exactly satisfied, and if R and κ are to able to increase, this state will become bound and a new virtual state will exist whenever an additional half wavelength can fit within R. Whenever this happens, the highest peak or lowest trough of the wave function will occur at exactly R, a consequence of $u(0) = 0$. Because the wave function must be continuous across this boundary of the potential, the slope of this peak or trough will be matched by the slope of the phase-shifted free particle state outside the well. Shown in Fig. 2.2, it is where the line tangent to this slope passes the r-axis that gives the scattering length, and for a maximum or minimum of the wave function occurring at $r = R$, this line is parallel to the r-axis and the scattering length is infinite. If a virtual state is about to form, the line tangent to the free particle state at $r = R$ will intersect the r-axis to the left of the origin, and the scattering length will be negative. If the virtual state has just become a true bound state, then the free particle wave function will curve towards the r-axis for increasing r, and the scattering length will be positive. Additionally, a case where the line tangent to the slope of the wave function at $r = 0$ intersects the origin is also possible, producing a scattering length of 0 and no apparent phase shift. An attractive well can therefore produce scattering lengths of arbitrary sign and amplitude. Alternatively phrased, an attractive well can produce attractive

and repulsive interactions, while a repulsive potential can only produce repulsive interactions.

It may appear that in order to tune the scattering length, we are required to tune either the value of R or k_0. This is not the case. For the above example of the finite attractive well, it has been shown that the same values of R or k_0 which produce virtual states at the threshold of the potential also produce a divergent scattering length. In the low energy limit of vanishing k, the potential threshold energy is the same as the *total* relative energy of the incoming particles. From this example alone, it is not clear whether R and k_0 are causing the divergence of the scattering length, or if it is the virtual state with the same energy as the incoming particles that produces this effect, *where R and k_0 are necessary only to produce this virtual state.* If it was somehow possible to produce a state with the same energy as the incoming particles not by changing the shape of a single potential, but by introducing a separate, overlapping potential, would the scattering length also diverge?

The collision between two atoms can involve more than a single interatomic potential to describe. An atom has internal structure, and two atoms of the same species can be in different internal states because of this. The different electronic spin states of two atoms have different potential energy curves as a function of internuclear distance between the two atoms. Different spin states may also respond differently to an applied magnetic field. In the next section, it will be shown that the relative energy spacing of two separate attractive potentials associated with two different electronic spin states can be moved by a magnetic field so that the bound state of one has the same energy as the incoming particles in another. In doing so, the scattering length will behave as if it seeing an emergent

(a) Virtual State formed, $a_s = \infty$.

(b) Virtual state almost formed, $a_s < 0$.

(c) Bound state formed, $a_s > 0$.

(d) Between bound states, $a_s = 0$.
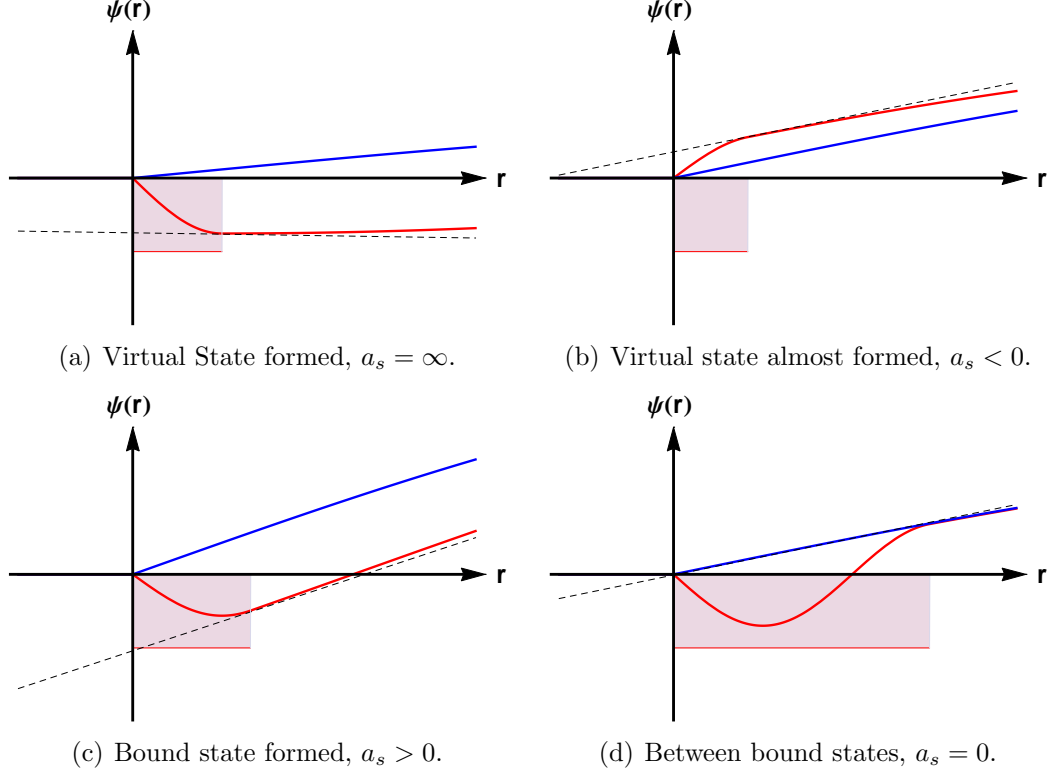
Figure 2.2: Different scattering lengths produced by various shapes and sizes of an attractive potential in the limit of low energy scattering $k \to 0$. The boundaries of the repulsive potential are given by the shaded region of width R and depth $\hbar^2 k_0^2 / 2\mu_m$. The red curve gives the the scattered wave function defined as $u(r) = A \sin(\kappa r)$ for $0 \leq r < R$ and $u(r) = B \sin(kr + \delta)$ for $r > R$, where $\delta = \tan^{-1}\left(\frac{k}{\kappa} \tan(\kappa R)\right) - k R$ and $\kappa^2 \equiv k_0^2 + k^2$. The blue curve is the unscattered wave function $u(r) = B \sin(kr)$. The dashed line is $A \sin \delta \left(1 + \frac{k}{\tan \delta} r\right)$, the line tangent to the scattered wave function at point $r = R$. The intersection of the dashed line with the r-axis defines the s-wave scattering line a_s. The curvature of the scattered wave function at the point $r = R$ and (hence the scattering length) can be related to how much of a change in the depth or width of the finite well is required to form a virtual state at its threshold.

bound state at the threshold of a single potential.

2.6   Collisional (Feshbach) Resonances

The existence of two distinct attractive potential wells is allowed in an atomic gas through the presence of electronic spin states. As these are attractive potentials between two atoms, it is appropriate to call them *molecular potentials.* For our experiment, the electronic spin state of ^{6}Li is effectively determined by the spin of the lone valence electron. When two of these atoms collide, their respective electronic spins, $\mathbf{s}_1$ and $\mathbf{s}_2$, will add to make a total electronic spin $\mathbf{S}_{tot} = \mathbf{s}_1 + \mathbf{s}_2$, which will have a value of either 0 or 1. The $S_{tot} = 1$ case is a triplet state, a symmetric electronic spin state with angular momentum projections given by $m_s = -1, 0$ and 1. The $S_{tot} = 0$ case, on the other hand, is a singlet state, an antisymmetric electronic spin state with the single angular momentum projection $m = 0$. Because electrons are fermions, their overall electronic wave function must be antisymmetric, so the triplet state must accompany a spatially antisymmetric two electron state, while the singlet requires a spatially symmetric two electron state. The spatially symmetric state allowed by the singlet concentrates the electrons towards the middle of the two atoms, attracting the nuclei inward, creating a potential well much deeper than the spatially antisymmetric state associated with the triplet state.

The different symmetries of these two electronic spin states also causes their associated collisional potentials to respond differently when the collision occurs in a static magnetic field. Because the triplet spins are parallel, the application of a magnetic field moves the energy of a triplet state more than the anti-parallel spins

of the singlet state, which tend to resist the field more equally and oppositely. In the low energy limit of vanishing kinetic energy, the threshold potential energy is equivalent to the *total* energy of the free atoms when fully separated before and after a collision. When no magnetic field is present, these values are equivalent for the singlet and triplet. However, a finite magnetic field will move the triplet potential curve downward in energy relative to the singlet, giving the deeper singlet well a higher threshold energy when compared to triplet state. Thus, while both attractive wells exist when a magnetic is on, it is energetically required that the atoms enter and exit a scattering process along the triplet threshold. The different abstract possibilities which may exist before and after a scattering event are refereed to as scattering *channels*, so that in this case, the singlet potential is an energetically forbidden, *closed channel*. The triplet potential, therefore, is the *open channel* in an elastic collision between ultra-cold alkali atoms.

Despite this, the triplet potential is not entirely unable to interact with the singlet potential. In addition to electronic spin, an atom also has a small nuclear spin coupled to its electronic spin through the hyperfine interaction, the associated energy of which is given by $V_{hf} = a_{hf}(\mathbf{s} + \mathbf{i})$, where $\mathbf{i}$ is the nuclear spin and a_{hf} is the hyperfine coupling. If the total hyperfine interaction between two colliding atoms is considered,

$$
\begin{aligned}
V_{hf\,tot} &= V_{hf\,1} + V_{hf\,2} = a_{hf}(\mathbf{s}_1 \cdot \mathbf{i}_1 + \mathbf{s}_2 \cdot \mathbf{i}_2) & (2.20)\\
&= \frac{a_{hf}}{2}[(\mathbf{s}_1 + \mathbf{s}_2)(\mathbf{i}_1 + \mathbf{i}_2) + (\mathbf{s}_1 - \mathbf{s}_2)(\mathbf{i}_1 - \mathbf{i}_2)], & (2.21)
\end{aligned}
$$

the net interaction potential is not diagonal in $\mathbf{S}_{tot} = \mathbf{s}_1 + \mathbf{s}_2$, the basis used to construct the singlet and triplet states. It is this coupling that allows a nearby bound

state of the deeper singlet well to affect the scattered atoms we are considering, though they must enter and exit along the triplet channel.

From the case of the single finite well, we know that since the threshold of the triplet channel corresponds to the incoming energy of the scattering state, different locations of the singlet bound state relative the triplet threshold will result in a different scattering length. If the thresholds of the singlet and triplet move relative to each other, then the location of this singlet bound state in energy space also moves relative to the triplet. Thus, a magnetic field is able to adjust the scattering length of ultra-cold alkali atoms. Fig. 2.3 shows different locations of the singlet bound state relative to the triplet threshold and the qualitative size and sign of the scattering length that this will produce. The black line indicates a bound state of the singlet. For low energy scattering, the total energy of the scattered particles matches the triplet threshold, which is extrapolated to where the triplet potential takes on an infinite value as a light blue line. Depending on the location of the triplet threshold relative to the singlet bound state, the scattering length changes as indicated. A comparison to the formation of a virtual state at the threshold of a single attractive well is included to give a simple model of similar behavior.

When the triplet threshold is equal to the energy of the bound singlet state, this resonant condition is labeled as a *Feshbach resonance*, a collisional resonance that is created by the overlap of a closed channel bound state on a separate open channel. Feshbach resonances are not unique to ultra-cold gasses, and were originally developed to explain resonant conditions in the cross sections of nuclear scattering events as a function of energy [27]. Feshbach resonances in ultra-cold gasses are also able to be created through additional optical fields, so the Feshbach
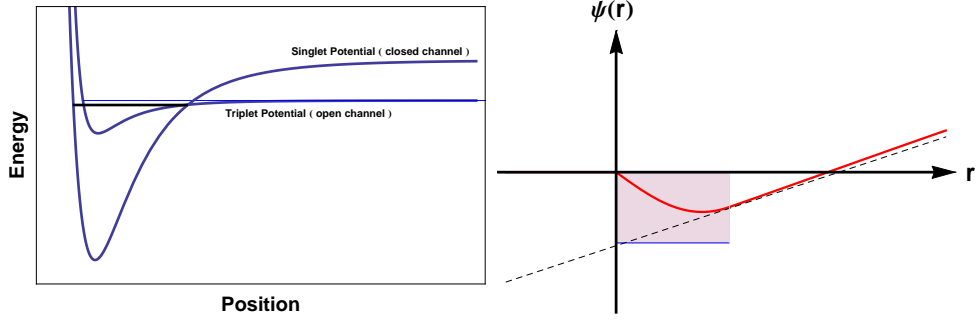
(a) Bound state of the closed channel just below the energy of the free scattering state, $a_s > 0$.

(b) Bound state has formed in the attractive well, its energy is just below the free scattering state, $a_s > 0$.
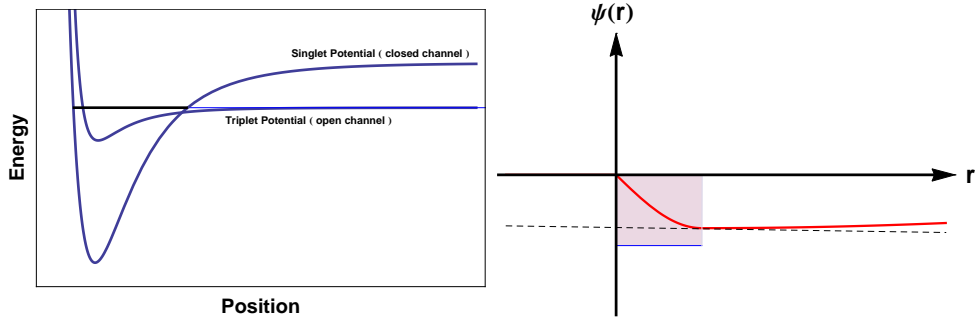
(c) Bound state of the closed channel equals (is resonant with) the energy of the free scattering state, $a_s = \infty$.

(d) Virtual state has just formed at the threshold of the attractive well. Its energy equals the energy of the free scattering state, $a_s = \infty$.
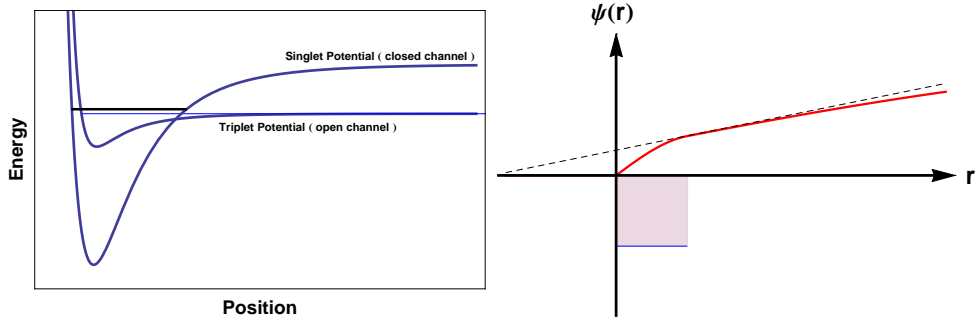
(e) Bound state of the closed channel with energy just above the energy of the scattering state, $a_s < 0$.

(f) A virtual state could form in the attractive well if it were slightly deeper or wider. Its energy can be imagined to be above the well, and above the energy of the free scattering state, $a_s < 0$.

Figure 2.3: Qualitative changes in the scattering length produced by a Feshbach resonance compared to the scattering length as determined by the position of bound state relative to the threshold of an attractive potential well.

resonance employed for this current work can be appropriately distinguished as a tunable *magnetic Feshbach resonance.*

In the vicinity of this resonance, the scattering length as a function of magnetic field B can be approximated as [28]:

$$a_s = a_b \left(1 - \frac{\Delta}{B - B_0} \right), \qquad (2.22)$$

where B_0 is the resonant field, Δ is the width of the resonance, and a_b is the background scattering length, unmodified by an external field. Currently[2], the best measurements of these quantities [30] give values of $B_0 = 832.18(8)$ G, $\Delta = -262.3(3)$ G, and $a_b = -1582(1) \, a_0$. These values are used to produce a plot of Eq. 2.22 shown in Fig. 2.4. Comparison to Fig. 2.3 indicates the because the scattering length is positive for magnetic fields below resonance and negative for fields above, the triplet state must indeed begin above the singlet bound state, being brought lower relative to the singlet for increasing values of B. The width of the resonance is quite wide, so that a magnetic field that is stable to a tenth of a Gauss allows a scattering length which is accurately reproducible. Note also that the scattering length is not symmetric in magnitude about the resonance point, due to the background scattering length.

2.7   The BEC-BCS Crossover

A system of fermions can behave very differently depending on the sign and strength of the interactions between them. Above resonance, where the scatter-

---

[2]The work reported in this dissertation assumed that a divergent scattering length occurs at a value of $B_0 = 834.15$ G, based on the previous measurements reported in [29]. This does not have any appreciable effect, as argued in Chapter 7.
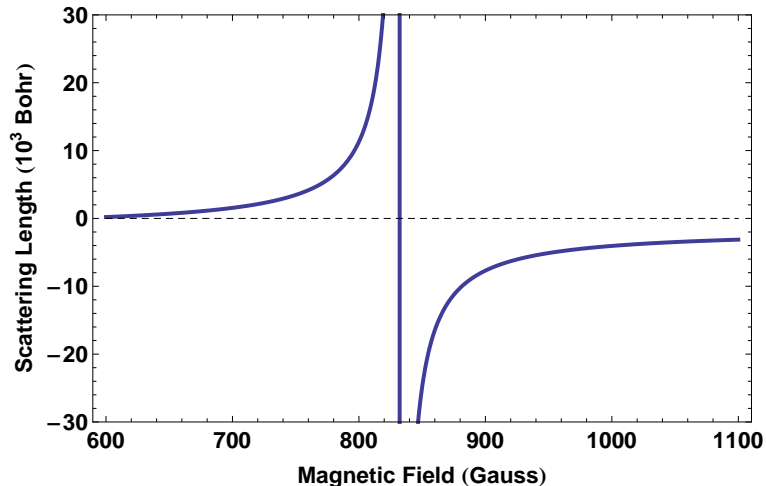
Figure 2.4: The s-wave scattering length of ^{6}Li near a broad Feshbach resonance as a function of applied magnetic field as reported by [30]. The existence of a large negative background scattering length causes the asymmetry around the resonance point at 832.18, leading to a negative scattering length which varies more quickly as a function of magnetic field below resonance compared to the variation of the positive scattering length above resonance.

ing length is finite, negative, and attractive, Cooper pairing can exist between the atoms if the temperature is cold enough. When this happens, the behavior of the system resembles the pairing of electrons in a superconducting metal. As Bardeen, Cooper, and Schrieffer authored the first theory that explained superconductivity through the pairing of fermions [31] (the electrons within the superconductor), this range of interactions in a Fermi gas is labeled as the *BCS region*. Below resonance, where the scattering length is finite and positive, the associated repulsive interactions allow the adiabatic formation of ^{6}Li$_2$ molecules. As these molecules are composites of two fermions, they are bosonic in nature and are permitted to form a Bose-Einstein condensate when cooled below a critical temperature. For this reason, the range of interactions below resonance is termed the *BEC-region*. Looking at these behaviors of a Fermi gas comprehensively, the entire range of

interactions possible near a Feshbach resonance is referred to as the *BEC-BCS crossover*.

2.7.1 Molecules From Repulsive Interactions and the Binding Energy

Intuitively, the formation of molecules requires a molecular bond. In turn, a molecular bond is usually associated with some sort of attraction between two atoms. Why then, do *repulsive* interactions on the BEC side form molecules? Recall that there are two very different sources for repulsive interactions: they can arise from both a repulsive *or* an attractive well. Because a repulsive potential in a scattering event can only produce an excluded volume and a positive scattering length, it is reasonable to identify a positive scattering length as a repulsive interaction. However, it was shown above that a bound state just below the threshold of an attractive well can also produce an excluded volume and a positive scattering length in collision, which we are consistent in labeling a repulsive interaction. Repulsive interactions arising from a repulsive potential will not produce molecules, but the repulsive interactions from an attractive molecular potential can, if the bound state just below the potential threshold can somehow be populated. For the elastic collisions between two atoms in a static magnetic field that we have been considering, this is not possible; the atoms will leave the well as easily as enter it. However, if *three*-body collisions occur, then the potential energy of two of the atoms can be carried away by the kinetic energy of a third, so that the remaining will be trapped in the singlet bound state, forming a molecule. The rate at which molecules are formed through this process is thus dependent on the probability of a three-body collision, so within our dilute atomic gas it is assumed

that the time scale of observed expansion is less than required for any change in the molecular population. It is also possible to adiabatically adjust the value of the magnetic field so that the triplet threshold sweeps from above the bound state to below it, which will also lead to the formation of a molecular population [32].

The molecular bound state also has an associated *binding energy*, given by E_b. On a vertical energy axis, this is simply the distance from the bound state to the well threshold. Since the scattering length should be the only length scale necessary to quantify all of s-wave scattering, near resonance it is possible to write the binding energy in terms a_s, rather than simply the depth of the well.

To derive E_b in terms of the scattering length, we shall consider the wave function of two atoms in the upper most bound state of a finite well. We shall assume that the bound state is close to the threshold of a deep well, $V \gg E_b$, so that the scattering length is large (much greater than the range of the potential) and positive, $a_s \gg R$. Along with E_b, we define an associated wave number, k_b, so that $k_b = \sqrt{2\,\mu_m\,|\,E_b\,|}/\hbar^2 = \sqrt{m\,|\,E_b\,|}/\hbar^2$, where $\mu_m = m/2$, the reduced mass of two identical atoms of mass m. Thus, for a total well depth of $V_0 = k_0^2\,\hbar^2/m$ the bound state radial wave function is given by

$$u(r) = \begin{cases} A\sin[\sqrt{(k_0^2 - k_b^2)}\,r] & \text{for } 0 \leq r < R \\ B\,e^{-k_b\,r} & \text{for } r > R \end{cases}$$

so that continuity of $u(r)$ and $u'(r)$ across $r = R$ gives

$$\frac{1}{\sqrt{k_0^2 - k_b^2}}\tan[\sqrt{(k_0^2 - k_b^2)}\,R] = -\frac{1}{k_b}. \tag{2.23}$$

40

Noting that $k_0^2 \gg k_b^2$, this expression becomes

$$\cot(k_0 R) = -\frac{k_b}{k_0} \,. \tag{2.24}$$

To relate Eq. 2.24 to the scattering length, we again consider the free scattering state, given by Eq. 2.18, also in the limit of $k_0 \gg k$ and $a_s \gg R$.

$$\tan\delta \;=\; \frac{k}{\kappa}\tan(\kappa R) - \tan(k\,R) \tag{2.25}$$

$$\frac{\tan\delta}{k} \;=\; \frac{1}{k_0}\tan(k_0 R) \tag{2.26}$$

$$\frac{1}{a_s} \;=\; -k_0\cot(k_0 R) \tag{2.27}$$

Comparing this expression to Eq. 2.24 gives $1/a_s = k_b$, leading to a relation for the binding energy in terms of the scattering length:

$$E_b = \frac{\hbar^2 k_b^2}{m} = \frac{\hbar^2}{m\,a_s^2} \,. \tag{2.28}$$

Note also that the relation $1/a_s = k_b$ indicates that the scattering length is the decay length of the bound state wave function in the energetically forbidden region outside the well. As the bound state gets closer to threshold, the binding energy decreases, and the allowed region of the wave function outside the potential well, as well as the scattering length, both increase.

2.7.2 The Zero Crossing and the Narrow Feshbach Resonance

Eq. 2.22 serves as an accurate means of determining the scattering length around resonance, but it is incomplete in its description for magnetic field values far below 834 G. While this resonance has a width $\Delta = -262.3(3)$ G, there also exists a much narrower Feshbach resonance at roughly 544 G [33]. The width of this Feshbach resonance is on the order of 0.1 G, so that the entire spectrum of interaction strengths fits within this small range of magnetic fields. Our apparatus is not currently equipped to reliably reproduce magnetic field values under a tenth of a Gauss, so this *narrow Feshbach resonance* (as opposed to the *broad Feshbach resonance* at 834) is not used to vary the scattering length in the present work.

Additionally, Eq. 2.22 approximates that far to the left of the Feshbach resonance, the scattering length crosses zero at around 570 G, and is slightly negative below that value. This is true qualitatively, but not quite quantitatively. There is a zero crossing far below resonance, but it occurs at a value of 528 G. Experimentally, this is the magnetic field value we use to produce a non-interacting gas that will exhibit ballistic flow when released form our optical trap.

As an experimental consideration, we use an evaporative process to cool the gas, where evaporation requires collisions. We expect the highest collision rate to occur at resonance, resulting in the most efficient evaporation and the coldest temperatures. This motivates us to evaporatively cool at 834 G, and then shift interactions of the cooled gas to whatever magnetic field near resonance is required. However, a shift in magnetic field all the way from 834 to 528 will not only create molecules, but also cross the narrow Feshbach resonance, the combined effect of

which produces a substantial loss of atoms from the trap by three-body collisions. In order to avoid this, experiments performed in the non-interacting regime at 528 G are first evaporatively cooled at 300 G. At his field the scattering length is negative and finite, but also far enough from resonance that it is much larger than indicated by Eq.2.22. It takes far longer to cool the gas at this field, but the gain in atom number substantially outweighs this inconvenience. There are other drawbacks to this method as well as potential alternatives with their own set of issues, and these will be included in the summary of our apparatus and procedures covered in the next chapter.

Chapter 3

Experimental Methods

This chapter summarizes the general experimental methods and the apparatus required for creating and imaging an ultra cold cloud of atomic fermions, providing detailed descriptions of the new techniques specific to the current work. All of the information we have about the gas is obtained from absorption images, which come at the cost of destroying the cloud itself. We therefore require a highly reliable apparatus that can repeatability create the same initial conditions for every imaged cloud. In many ways, our approach to reliability has been one of simplicity, so that the layout of experimental system should not be seen as overly complicated once its purpose is understood. Very broadly, the experiment is the sum of a vacuum chamber featuring a lithium source and Zeeman slower, a magnet system surrounding this chamber, two lasers and the associated optics, and a CCD camera system. This general apparatus, the physics behind it, and methods of its operation has been discussed extensively in previous dissertations from this group, and the reader is refereed to these for a more thorough treatments of these well established techniques [22, 23, 34, 35]. They are briefly summarized here to provide the proper context for descriptions of the novel additions to the apparatus including a low profile magnet system, an optical trap shape that is elliptical along both its axial and transverse directions, and the addition of a second camera that

allows the simultaneous imaging of the cloud from two directions.

3.1 Basic Optical Cooling and Trapping

The overwhelming majority of the space occupied by our experimental apparatus is dedicated to the optics for two separate laser systems. Before describing the set up of these optical systems, an elementary appreciation of their purpose is necessary. Each of these laser systems uses a very different physical mechanism to cool and trap atoms. Our dye laser system produces red light near the 670.979 nm transition in ^{6}Li that slows and spatially confines the atoms through the selective absorbtion and emission of photons. In contrast, our high power CO_2 laser outputs a wavelength of 10.6 μm, far away from resonance, and that confines atoms in a small region of high intensity around its focal point through an electric dipole polarizability interaction. In this way, the cooling and trapping mechanism of the first exploits the particle nature of light, while the second relies on the wave nature. The essential physics behind these two methods is briefly summarized below.

3.1.1 Velocity Dependent Radiation Pressure and the Optical Molasses

Because a photon carries momentum $p = h\nu/c = h/\lambda$, it is able to transfer this momentum to a stationary atom during a resonant absorption process. As a result of momentum conservation, the momentum acquired by the atom is always along the direction the photon was traveling before the absorption. When the atom spontaneously emits this photon, the emission will occur in a random direction,

and the atom will receive another momentum kick opposite to this direction of emission. If a laser provides a source of many resonant co-propagating photons, repeated absorption and emissions will result in a net momentum transfer along the direction of the laser beam, as the random momentum transfers arising from spontaneous emissions will average out to produce no net effect.

While the interaction of a photon with a stationary atom is easy to imagine, a stationary atom is a rarity in nature. The finite velocity of an atom towards a laser source will shift the resonance frequency of the atom in accordance with the Doppler effect, given as

$$ f = \left(1 + \frac{v_a}{c}\right) f_0 \,, \tag{3.1} $$

where f is the frequency observed by the atom, f_0 is the laser frequency, c is the speed of light, and v_a is the velocity of the atom. Depending on the sign of v_a, an atom moving counter to the propagation of a laser beam will see a higher frequency, and an atom co-propagating along a laser beam path will see a lower frequency.

Consider an atom moving in one dimension, where the Doppler shift allows a laser that is detuned below an atomic resonance (red-detuned) to resist atomic motion, when the laser field counter-propagates with respect to the velocity of the atom. In moving towards this laser, the atom will see a frequency upshifted towards its resonant frequency, and lose forward momentum through the absorbtion and emission of incoming photons. As the atom slows, it will see less of a frequency shift, and the rate of photon absorption events and corresponding momentum transfers will drop. If a second laser of the same frequency is over lapped

with the first, but propagating in the opposite direction, this laser will not transfer momentum to the atom moving away from it, as this atom will see a frequency that is further de-tuned from its resonant value. However, this second laser would slow other atoms of a different velocity class if they were to move towards it, in which case these atoms would be unaffected by the first laser. Therefore, no matter the initial velocity class of an atom, two red-detuned counter propagating laser fields will reduce the atom momentum in one dimension.

This case is easily generalized to the three dimensions by simply adding two more counter-propagating red-detuned laser beam pairs, for a total of six beams in three counter propagating pairs along three orthogonal directions. In this setup, the beams will resemble the axis of the cartesian coordinate system forming a common intersection at the origin. This scheme was originally termed to be an *optical molasses*, a reference to the velocity dependent force the light provides being similar to that of body suspended in a viscous molasses.

3.1.2 Spatially Dependent Radiation Pressure and Zeeman Tuning

While the optical molasses produces a velocity dependent force that *cools* atoms, a spatial dependent force is required to actually *trap* them. Without this additional force, atoms slowed in an optical molasses can simply (slowly) move out of the laser beams. A spatially dependent force can supplied by combining a red detuned optical field of the correct polarization with a spatially varying magnetic field gradient. For an atom with an F=0 ground state and an F=1 excited state, the Zeeman shift provided by a field gradient that starts at zero would shift the energies of the $m_F \pm 1$ excited state sublevels in opposite directions in energy

space, and this energy spacing would increase the further the atom moved out from the point of zero gradient. When combined with a red detuned laser beam, this produces a spatially dependent detuning analogous to the velocity dependent detuning produced by the Doppler shift. The only additional consideration is polarization of the laser light. For a photon to be absorbed and induce a transition from the ground state where $m_F = 0$ to either of the $m_F \pm 1$ excited states, it must be circularly polarized and of the correct handedness, given by either σ_+ or σ_-. Consider a one dimensional case. If an atom were to find itself in a region of a positive magnetic field gradient that increased in a direction opposite to the propagation of a σ_- red detuned laser beam, the $m_F = -1$ state would be shifted down in energy and closer to resonance with the laser light, pushing the atom toward areas of decreasing field gradient. Likewise, an atom in a region of negative magnetic field gradient counter to a σ_+ red-detuned laser beam would be forced towards the direction of increasing field gradient. When this effect is generalized to three dimensions, it can supplement the velocity dependent forces of the optical molasses to both trap and cool atoms. In one dimension, this effect allows massive deceleration of atoms over a very short distance.

3.1.3   The Zeeman Slower

Approximately one dimensional atomic motion is encountered in the laboratory in the form of an atomic beam. These can be produced from an atomic vapor in a region of high pressure that is allowed to move through a small opening at the end of a tube into a region of lower pressure, where the tube provides a means of collimation. As a consequence of creating a region of high pressure and a steady flux of atoms, the atoms in the beam move at thermal velocities corresponding

to a few hundred degrees Celsius. Atoms moving in atomic beam can be slowed from these velocities to those associated with a few degrees Kelvin over a distance the order of a meter through the use of Zeeman slower [36]. Firstly, this setup requires a red-detuned laser beam counter propagating against the motion of the atomic beam. Based on the size of the detuning, this laser beam will slow a certain velocity class within the atomic beam, but this velocity class will fall out of resonance once it is slowed. Further cooling is provided by placing the setup within a spatially varying magnetic field gradient (in addition to circularly polarizing the laser beam), so that as the velocity of the atomic beam changes, the energy of the resonance changes with it.

In practice, there are many variations of this setup determined by the particular experimental system that a Zeeman slower is to be a part of. The magnetic field gradient can increase or decrease as the atoms are slowed (which dictates the required polarization), the overall length of different Zeeman slowers can vary due to space, as can the size of the magnetic coils and the methods of cooling required. For a detailed discussion of the reasoning behind the specific design of our Zeeman slower, see [22].

3.1.4 The Magneto-Optical Trap (MOT)

If two counter-propagating beams of the optical molasses which are already red-detuned are also given opposite circular polarizations, the polarizations can be set relative to a magnetic field gradient that grows equally and oppositely from a zero gradient point that overlaps the intersection of the molasses beams so that an atom moving in a region of negative magnetic field gradient will also see a laser of positive circular polarization propagating towards the molasses center. In

this case, the $m_F = 1$ state will be shifted downward by the negative magnetic field gradient, and into resonance with the σ_+ light it is moving towards the zero gradient point. Propagating away from the center will be the σ_- beam that is shifted even further out of resonance with the $m_F = -1$ state by the gradient field. Likewise, an atom that stray towards a positive field gradient will encounter a σ_- beam that is shifted into resonance with its $m_F = -1$ state and forcing it back towards the point of zero gradient.

This gradient field and the introduction of circular polarization does not diminish the velocity dependent effect of the molasses, so this configuration is able to both slow and confine atoms when generalized to three dimensions. If the supplied magnetic gradient comes from pair of wire coils in an anti-Helmholtz configuration, the gradient will vanish at the coil center and grow linearly and oppositely in three dimensions, as required. Noting the presence of both optical and magnetic fields, this well known set-up is referred to as a *magneto-optical trap* (MOT) and is a powerful and widely utilized tool for cooling and trapping atoms.

In practice, a MOT cloud will form at the intersection of the molasses beams and the zero magnetic field point, typically a few millimeters in diameter and clearly visible as the atoms within continually absorb and emit photons. The energy level structure of real alkali atoms also contribute additional complications. For ^{6}Li, angular momentum addition results in three possible values for the excited state angular momentum, F'= 1/2, 3/2, 5/2, and two for the ground state, F=1/2, 3/2. These excite state splittings are unresolved, while the ground state state hyperfine splitting is 228 MHz. As a consequence, for an atom that begins in the F=3/2 ground state and absorbs a resonant photon, there is always a chance it will

make a transition to the F=1/2 ground state during spontaneous emission. If this happens, the only way the atom can continue to be cooled via radiation pressure and make transitions back to the excited state is by introducing another set of overlapping beams with a frequency tuned to the F=1/2 excited state transition. We refer to this set of beams as the "repumper beams" as their primary purpose is to repump the atoms out of the F=1/2 ground state. This set of beams has the same prioritization as the original six beams, which we label as the "MOT beams".

Unfortunately, because the MOT relies on a constant absorbtion of photons and the corresponding emissions, the trapped atoms experience small, random momentum transfers that fundamentally restrict how low of a temperature can be achieved. This lower bound for the temperature inside a MOT is given by [37]

$$T_{limit} = \frac{\hbar \Gamma}{2k_B} \, , \tag{3.2}$$

where Γ is the linewidth of the relevant optical transition. For ^{6}Li, the natural linewidth is $\Gamma/2\pi$= 5.9 MHz, corresponding to $T_{limit} = 140 \, \mu K$. To achieve lower temperatures, we rely on optical trapping methods that do not involve absorption and emission.

3.1.5   Electric Dipole Force

A laser that is tuned far from any atomic resonance can also trap and cool atoms through interactions with its oscillating electric field in place of the absorption and emission of photons. An atom in the path of such a laser beam will acquire a dipole moment proportional to the electric field of the laser, as well as an

associated potential energy given by [34]

$$U_{dipole} = -\frac{1}{2}\,\alpha\,\overline{\mathbf{E}}^2\,,\qquad(3.3)$$

where α is the dipole polarizability of the atom, $\mathbf{E}$ is the electric field of the laser and the top bar indicates that the electric field has been averaged over many optical cycles. Assuming that the magnitude of the electric field, E_0, is slowly varying, $\overline{\mathbf{E}}^2 = E_0^2/2$ and U_{dipole} is easily expressed in terms the laser intensity, $I = (c\,\epsilon_0/2)E_0^2$, in the MKS system of units as

$$U_{dipole} = -\frac{1}{2\,\epsilon_0 c}\,\alpha\,I,\qquad(3.4)$$

where ϵ_0 is the permittivity of free space and c is the speed of light. Thus, an atom will experience a potential energy that varies with position as determined by spatial distribution of the laser intensity.

3.1.6   The Far Off-resonance Dipole Trap (FORT)

By focusing a far off-resonance laser, it is possible to create both a region of high intensity and a spatial variation in that intensity that is symmetrically decreasing along each individual axis. For a positive α and a negative[1] U_{dipole}, this creates a conservative, approximately harmonic potential for trapping atoms.

In our lab, the creation of such a far off-resonance dipole trap (FORT) is achieved using a 140 watt peak power CO_2 laser at a wavelength of 10.6 μm.

---

[1]In general, α can be a positive or negative quantity, as determined by either red or blue detuning relative to the atomic resonance [38]. For the current work, we shall shall consider only a far red detuning and an attractive potential

This wavelength is nearly sixteen times longer than 670.977 nm transition in ^{6}Li, so that the rate of photon absorption is just 2 photons/hour for our conditions. While it is true that each of the two spins states of ^{6}Li that we trap have different polarizabilities, this difference is also vanishingly small for such a large detuning.

The maximum depth of dipole potential provided by our FORT varies with its geometry as well as the maximum power. At best, it is nearly 1 mK, so that the FORT must be loaded from the MOT, a process to be described later in this chapter. Once the FORT has been loaded, the MOT is extinguished, and the FORT provides a frictionless bowl for further cooling of the atoms through evaporation [34]. In a broad picture, the FORT is the last stage of confinement for our atoms before imaging. The shape of the FORT potential (along with small but important contributions from the bias magnetic field) therefore determines initial experimental conditions of the ultra-cold Fermi gas it contains. In the current work, we shall describe the use of sets of cylindrical lenses to create a beam focus that is elliptical in two directions, corresponding to a potential shape that is particularly useful for studying transport properties as the atomic cloud expands out of it. While it was mentioned that the trap shape is always approximately harmonic, determining the *exact* shape of the FORT, the magnetic potential, and the initial conditions they set is so important to our study of transport properties that a description of procedures used to do so is the entirety of Chapter 6.

3.2   Experimental Apparatus

Turning away from the general physics motivating our use of two laser system to provide beams for a Zeeman slower, MOT, and FORT, this section describes

our specific experimental apparatus. Emphasis is placed on the upgraded magnet system, the FORT shape that is elliptical along both its axial and transverse direction, and the addition of a second camera.

3.2.1 The Vacuum Chamber

Before creating an ultra-cold atomic gas, we must create an environment that is sufficiently isolated as to *allow* an ultra-cold gas. Therefore, our experiments take place inside an ultra-high vacuum chamber, the layout of which is given in Fig. 3.1. As indicated, this portion of the apparatus consists of the oven/lithium source, the Zeeman slower, and the main chamber where the MOT and FORT both form. Pressures of 3×10^{-11} Torr are maintained through the use of two sublimation pumps and two ion pumps, one of each near the main vacuum chamber, and the other two closer to what is labeled as the oven. If a procedure requires breaking this vacuum, our ability to reach these low pressures can be preserved by first filling the chamber with pure argon gas, chosen for its mass and extremely low reactivity. Once filled, argon can be continually pumped through the inside of the chamber while system is opened, as the continuous flow of argon out of any opening will prevent other gasses from entering. It is though this process that the oven region can be detached and filled with two grams of small shards of metallic ^{6}Li, the initial state of our atoms that will eventually become ultra-cold. Once the oven is reattached, the argon can be initially pumped out with a detachable roughing pump and turbo pump, before the ion pumps remove what remains.

Using wrapped nichrome wire and insulating cement on the outside of the oven, the ^{6}Li inside is heated to roughly 700° K. The output of this oven is a 6" tube with an inner diameter of 0.18", so that the exiting atomic vapor forms a collimated

Labels in figure:
Sublimation Pump, Ion Pump, Sublimation Pump, Oven, Valve, Ion Gauge, M2, CO$_2$2, P1, M1, Zeeman Slower, C1, M5, C2, S1, M4, M3, CO$_2$1, P2, Main Vacuum Chamber
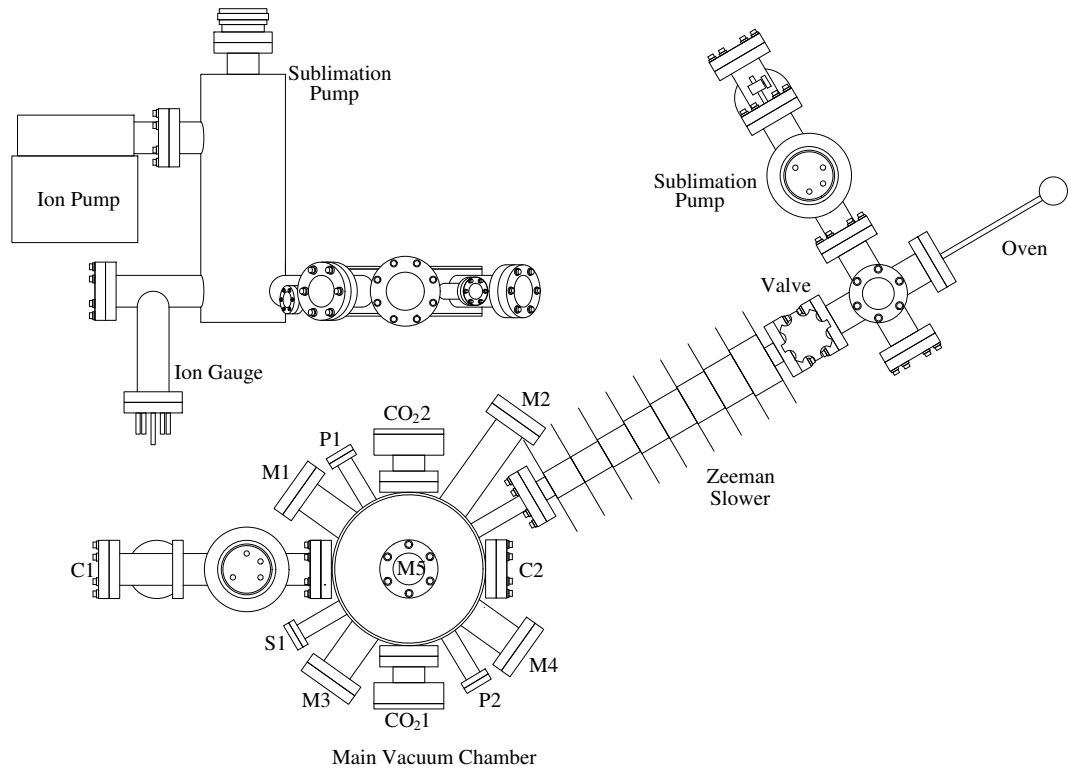
Figure 3.1: Schematic of the vacuum chamber designed by [22]. The upper left figure is a side view of the main chamber, shown below. A second ion pump between the oven and the labeled valve is omitted for simplicity.

atomic beam. The inner walls of the exit tube and oven are lined with heat-tolerant screened mesh that when coated with molten lithium, not only captures free lithium atoms that collide with it, but also provides a means for lithium to flow towards regions of the highest temperature. With this mesh in place, lithium that strikes the walls of the collimating tube does not leave the wall to further collide with more lithium atoms that could have been on a straight trajectory to successfully leave the oven. This increases the overall flux of the atomic beam for a given oven temperature. More importantly, by keeping the back of the oven at the hottest temperatures, lithium that collides with the walls can be recirculated back into the main body of the oven. This greatly increases the lifetime of the oven, so that a properly loaded oven with just 5g of ^{6}Li can last up to four years of operation without requiring a break of vacuum to refill. The oven temperature is empirically chosen to balance the need for an atomic beam of sufficient flux to load the MOT while also maintaining a reasonable background pressure. Avoiding unnecessary increases in the temperature also conserves lithium.

The atoms that successfully leave the columnating tube of the oven do so at thermal speeds of roughly 2 kilometers per second. It is with these speeds that they enter the Zeeman slower, where the atoms see a decreasing magnetic field gradient and a single σ_+ polarized slowing beam which enters at S1 in Figure3.1. Over the length of the slower (about 30 cm), a ^{6}Li atom feels a deceleration of $2 \times 10^6 \, \mathrm{m/s^2}$ as a result of radiation pressure, equivalent to two hundred thousand g's. Exiting the slower, they enter the main chamber with speeds on the order of ten meters per second.

Within the main chamber in Fig. 3.1, the six trapping beams for the MOT (each including an overlapped MOT and rempumper beam) enter though each

port labeled with an "M" prefix so that the MOT forms at the center of the main chamber, beneath M5. Note that there is a port opposite of M5, on the underside of the main chamber for the vertical beam which propagates upward. In place of coated glass, the $CO_2 1$ and $CO_2 1$ ports feature double sealed differentially pumped zinc-selenide windows to allow transmission of the CO_2 beam for the generation of the FORT, which also must overlap the MOT at the chamber center. Ports C1 and C2 allow an entrance and exit, respectively, for an resonant beam used in absorption imaging of the cloud, so that a CCD is place to the right of C2. In later sections, the generation of all of these beams shall be described, in addition to a second imaging beam that follows the path of the vertical MOT beams through M5.

When the vertical and horizontal profiles of the main chamber are compared in Fig. 3.1, a very deliberate pancake geometry can be seen in its design. In addition to providing good optical access around the side circumference, this shape allows the stacking of magnet coils on the cylinder faces above and below the main chamber that remain close to the chamber center in the vertical direction. Magnet coils surrounding the main chamber are necessary for both the MOT gradient field and the tuning of interatomic interactions. By designing the main chamber to be short in the vertical direction, the distance between the magnet coils is minimized, which substantially lowers the power required to produce a particular magnetic field value [22]. In the next section, recent upgrades to this magnet system and particularly the design of the housings used to mount them to the main chamber will be explained.

3.2.2   Upgraded Magnet Housings

The magnet system must provide not only the bias field for tuning the interaction strength of the atoms loaded into the FORT, but also the gradient field for the MOT. At the very least, their design must incorporate a means of stably mounting them above and below the vacuum chamber so that they remain stationary against any magnetic forces they produce. This ensures that the formation of each magnetic field is repeatable, and that calibrations performed one day are applicable the next. They also require efficient and reliable water cooling, as a field of 834 Gauss requires roughly 1kW of power. If this heat is not removed, the insulating coating of the magnet wires will begin to melt at around 200°C, causing immediate electrical shorts and magnet failure. Beyond these requirements, simplicity, reliability, and a compact profile that does not crowd other components on the optics table are all standard considerations that determine a more ideal design.

A simple means of accomplishing the most essential requirements of the magnet system is two identical, watertight housings mounted above and below the vacuum chamber to support and contain the magnetic coils. The chosen material for these housing has always been Delrin plastic, a reasonably heat resistent polymer with good machining properties and low water absorption. However, it is the shape of these housings, the number of coils inside, and the means of supplying the cooling water and electrical leads to the inside that has changed with different iterations of our experiment. These are the areas of the magnet system design that go beyond the basic needs of the apparatus, and have been modified over the years for the better.

In the first iteration of our magnet system, both the MOT and bais fields were

Housing Top   Housing Bottom
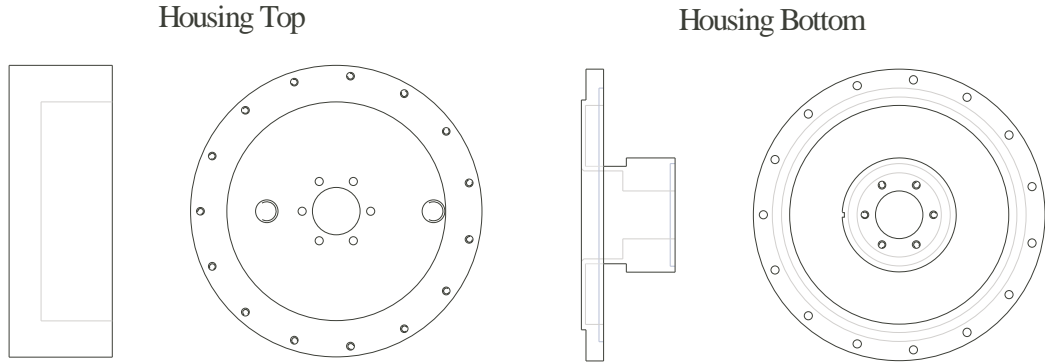
Figure 3.2: Delrin sections of the magnet housing.

provided by only a single pair of coils. As these two configurations are not needed simultaneously, it was possible to load the MOT and FORT with the two coils in a gradient configuration, followed by one of the coils reversing direction and a drastic increase in the applied voltage to create the necessary bias field. This required an electrical switching system that could withstand the high currents needed to produce 834G at the center of the vacuum chamber, prompting this single pair of coils to be replaced with two separate pairs, for a total of four coils. The primary advantage of these new housings, designed by [22], was a very compact housing interior and simple overall housing shape that is still retained in the magnet system used today.

This design consisted of two parts for each housing, shown in Fig. 3.2 and labeled as the housing bottom and housing top. Note that when mounted to the vacuum chamber, these housings are mirror images of each other over the x-z plane, so the *housing top* of the *bottom housing* is the lower most component. The interior of the housing bottom was designed with a hollow, flanged spool to be wrapped with the smaller gradient coils, while the hollow center provided optical access for the vertical MOT beams. These gradient wires were 14 gauge REA

Super Hyslik that when wound into 14 layers of 19 turns, would have an outer coil diameter matching that of the flange. This combined structure would form a new, single column for winding the much larger high field coils. To make this high field coil as stable as possible, the wire used was 8 gauge REA Therm-Amid square magnetic wire. The square cross section keeps the large wires from slipping against each other as they from 8 coil layers at 18 turns each. A water tight seal between the housing top and bottom is achieved through two circular grooves in the housing bottom, one along the lower, outer rim, and the other within the flanged spool. Each of these grooves seats a separate o-ring gasket, which seals as the two sections of the housing are screwed together. From the outside, this assembled housing appears only as a short cylinder with a centrally bored hole the diameter of the vacuum chamber windows.

While this housing design is very compact with one coil internal to the other and its simple exterior case, several choices in the way the exterior originally interfaced the water and electrical lines were problematic. Specifically, the water inlet and output ports were located on the upper surface of the housing top. The main disadvantage of this placement is the amount of space the one inch diameter water hoses occupy as they bend from a horizontal (where they travel along the table) to a vertical position where they interface with the magnet housing. For additional imaging along the vertical direction, this is very valuable space for optics. The area underneath the chamber is particularly difficult to access, and installation of optics while keeping their beam path clear of hoses was needlessly tedious. Most importantly, the introduction of two separate coils also meant two sets of input and output electrical leads for each coil, which traveled together through the very same inlet and outlet water hoses to terminals far from the

vacuum chamber. Unfortunately, electrolysis between the MOT and high field wires could eventually lead to a failure in their coatings or complete breaks, resulting in either shorts or open circuits. Removing all of the vertical imaging and MOT optics to accommodate movement of the hoses was only the first step the repair of such a design required.

Several feet of water hoses and internal coil wires led away from the chamber to an interface with the sides of additional Delrin blocks. These blocks featured two additional holes on either side of this connection leading to the housing, all of which met in the block center to serve the function of a pipe tee. Of these two additional connections, one led toward the water reservoir, and the other held a copper terminal for one end of the high field magnet wire. This terminal was designed to be large enough to have good electrical conducting properties, but as a consequence was also very difficult to locally heat. This required the terminal end inside the Delrin block to be torch brazed to the coil wire before the entire terminal was pulled through the block opening, where an o-ring gasket formed a water tight seal. The terminal end outside the block could then be wired to the high field magnet power supply. The thinner MOT magnet wire would be fed through the connection leading to the water reservoir, first passing through an additional hose length and a second Delrin block and terminal combination to interface with a separate power supply for the gradient field. This terminal connection would also require a torch braze. In total, this led to four Delrin blocks and copper terminals, all separated by hose lengths that caused a housing which could be individually praised for its compact design to instead resemble the body of a large, writhing squid creature.

Areas where the thinner MOT wires bent were particularly vulnerable to elec-

trolysis, such as those within the Delrin blocks or where their coiling stopped and started within the housing itself. Once all vertical optics were removed and the imaging calibrations ruined, attaching or replacing wires required additional accessible space around the repair area to safely use a gas torch.

Considering these issues, the current design separates the electric leads and terminals from the water hoses entirely, in addition to moving both water hoses from the housing top to the sides. Instead, four NPT threaded holes are machined through the upper surface of the housing top. Rather than attache hoses to these threads however, a male NPT to smooth PVC tubing adaptor is installed in each. These adaptors consist of three parts: a threaded base, with a male NPT end and a male PFA end (part number GAMS-182), a reusable plastic compression ring (called a gripper by the manufacturer), and a female threaded cap (part number 1213-0304) all from Parker Hennifin Corporation. Together, these components are designed to form a water tight seal between a female NPT fitting and 1/4 inch plastic tubing by forcing the compression ring against the outer diameter of the tubing as the cap is tightened. In place of plastic tubing, these fitting are used to form a water tight seal around the copper terminals, which are thus mounted to the housing top directly. Inside the magnet housing, these terminals are machined with a hole that fits snug around their associated wire, which is further secured with a perpendicular set screw. This eliminates the need for any kind of braze. The previous brands and sizes for both magnet coils are also retained.

Outside of the magnet housing, the angle at which these terminals attach to the wires leading to their respective power supplies is easily controlled with a mounting screw, so that much more space is available for mounting optics. Additionally, by mounting the water inlets and outlets on the sides of the magnet

housing, we can maintain the same flow rate provided by the bulky one inch hoses, but also keep them far out of the optical beam paths. This design also means these optics do not need to be removed if access to the housing is required. The outlet is also positioned as high as possible relative to the inlet, so that the water must fill the housing completely before exiting.

With no wires traveling through the repositioned hoses to welded terminals, we gain more space to mount and adjust optics, while greatly simplifying any hypothetical repair process. Fortunately, this ease of repair remains a hypothetical situation, as the redesign of the wiring and water circulation has also allowed the new magnet system to operate without need of repair since its implementation two years ago.

3.2.3   Dye Laser Beam Path

All of the red light near the D2 ^{6}Li resonance required for the MOT, Zeeman Slower, and absorption imaging originates from a single Coherent 899 dye laser. Though an increasingly dated piece of technology, when pumped by a (Verdi Model) at 5.5 W, this laser can provide all 800 mW at 671 nm that our experiment requires. When stabilized against a Fabry-Pérot cavity for fast frequency noise and an atomic fluoresce standard for the slower frequency drifts, the typical frequency jitter on this laser is 2-3 MHz.

The optics used for generating the Zeeman slower beam (more simply, the "slowing beam"), the MOT, repumper, and spectroscopic beam for locking to an atomic standard is unchanged from [35,39] and given in Fig. 3.3. All Acousto-optic modulators (AOs) are in a standard double pass configuration [34], so that the frequency shifts given in Table 3.1 must be doubled. During each double pass,
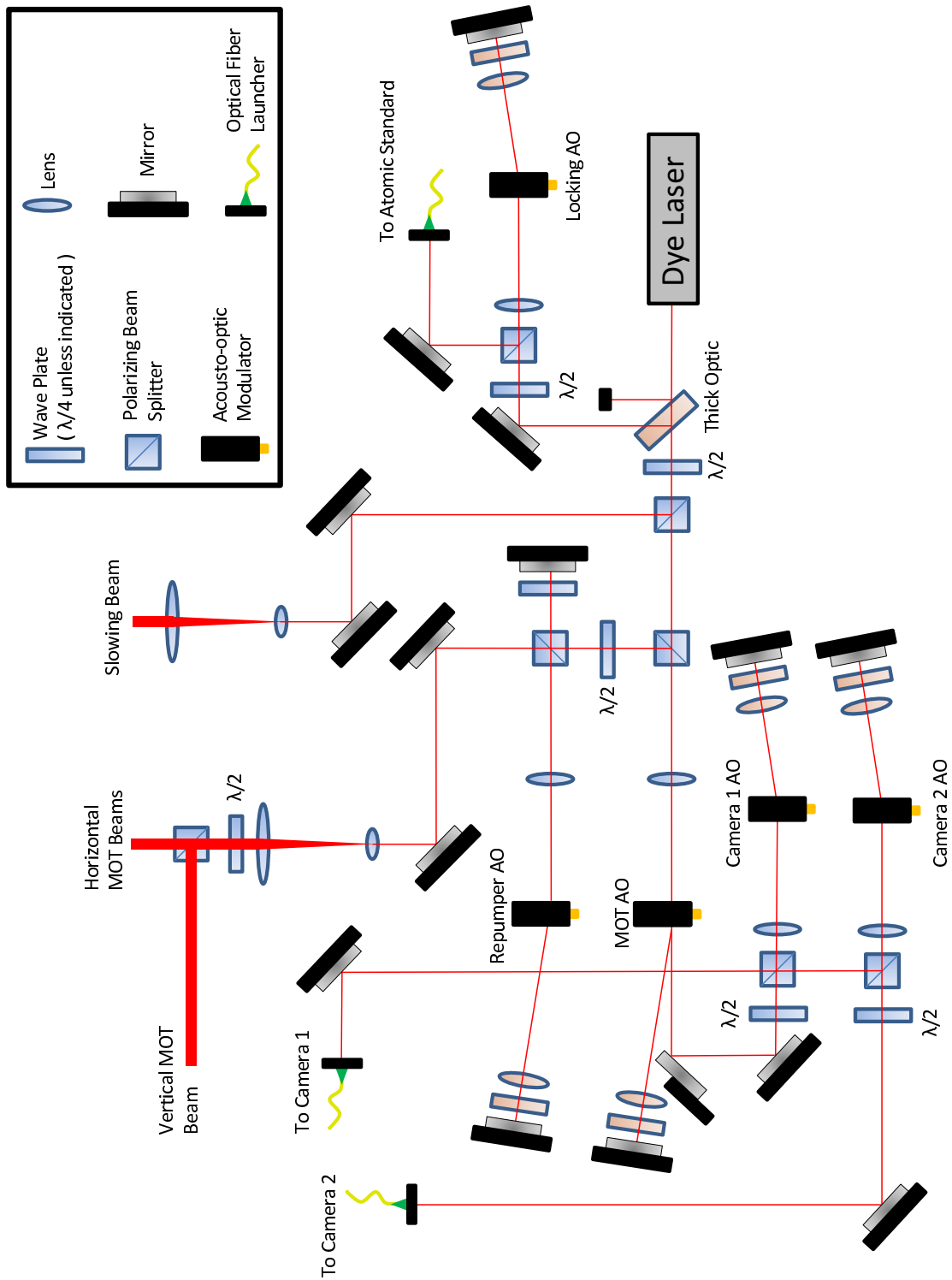
Figure 3.3: Layout of the optics for the dye laser beam path.

the linear polarization is rotated 90° by a $\lambda/4$ plate and mirror combination. Note that the locking AO between the laser output and the locking region is *upshifted*, so what comes out of the laser *downshifted* by a total of roughly 210 MHz. By adjusting the overall locking point, this is the only AO that requires daily adjustment; all others are set relative to this point.

With no additional frequency shift, 170 mW of what leaves the laser becomes the slowing beam, and the rest of the light not used for locking or the slowing beam, roughly 450 mW, becomes the MOT and repumping beams. The MOT beams are upshifted from the slowing beam frequency by 183.86 MHz, and the repumper beams are further upshifted by 203.52 MHz. The MOT and repumper beams are recombined on a polarizing beam splitter (PBS), where we empirically find that the best MOT forms for a three to one ratio in total power between the MOT and repumper at this point in the beam path.

This beam which contains both the MOT and repumper is divided up over the three dimensions of the MOT by two more PBS cubes, so that each axis contains a repumper and MOT beam of *parallel* polarization. The power in each axis is divided up equally in terms of *total* power, each containing roughly 50 mW. An emphasis is placed on total power because the vertical beam and two horizontal beams do not contain the same individual contributions of MOT beam and repumper beam power. This is a result of the MOT and repumper beams being originally recombined on a PBS, which gives them orthogonal polarizations. When this polarization is rotated with a $\lambda/2$ plate before passing another PBS so that a 1/3 of the total power goes to the vertical beam and 2/3 goes to the horizontal beams, this sets the vertical beams at a ratio of 6:1 MOT to repump power, while the horizontal beams have 1.5:1 MOT to repump power ratio.

The manner of generating light for absorbtion imaging, discussed in the following section, has required changes in our dye laser beam path. Before closing the present description of what has not changed, our continued lack of an additional rempumping beam in the Zeeman slower is worth commenting upon. We have empirically found that for our present Zeeman slower design, slowing beam power, and slight slowing beam focus, the addition of a repumping beam on the slowing beam path does not provide an increase in MOT loading. This was tested over a range of detunings and power ratios.

3.2.4 Optics Required for Imaging

Previously, the light required to image our atomic cloud on a single CCD camera was generated from a small amount of light picked off from the MOT beams. With the introduction of a second CCD camera for the purpose of imaging from two orthogonal directions, we require an additional imaging beam. In creating this beam, we wish to avoid taking more light from the MOT beams. To do this, we exploit the fact that the MOT is already shut off by the time we image atoms in the optical trap. This shut off is accompanied by turning off the MOT AO, so we generate both of our imaging beams from the zeroth order beam path of the MOT AO. This not only avoids taking additional power from the MOT, but also returns the portion of power used to create the original imaging beam.

After being well separated from the first order beam path, the zeroth order MOT beam is further divided into two beams with a $\lambda/2$ plate and PBS. These two beams travel through their AO double pass configurations before being coupled into their own fibers. These AOs and the corresponding frequency shift between these two beams are used so that we can image separate spin states with each

beam. In general, atoms that interact with one imaging beam are atoms that can not interact with the other imaging beam. If both beams were configured to image the same spin state, both images would incorrectly report a lower density of atoms simply due to the presence of the other imaging beam. This is avoided by having each imaging beam interact with a different population of atoms. A later section will discuss the process of confirming equal of atom numbers in both spin states when both cameras are used individually *and* simultaneously.

At a bias magnetic field of 834 G, where the imaging of a resonantly interacting Fermi gas takes place, the calculated frequency separation between the trapped spin states $|1\rangle$ and $|2\rangle$ is 76.2 MHz. However, the frequency shift provided by the model D323B ISOMET AO drivers that we use is 82-138 MHz. This is the reason behind each imaging beam having its own double passed AO. One of the imaging AOs is set at 124.9 MHz, and the other is adjusted to 86.27 MHz based on experimentally maximizing atom number on both images simultaneously. For a double pass, this gives a frequency separation of 77.26 MHz. For the work conducted at a finite scattering length, the bias field is adjusted as high as 986 G and as low as 720 G. At these fields, the calculated frequency separation between the trapped hyperfine states $|1\rangle$ and $|2\rangle$ are 76.46 MHz and 76.16 MHz, respectively. Even at 528 G, where the gas is non interacting, these two states are separated by 75.6 MHz. Considering these numbers compared to a natural linewidth of 5.9 MHz for the excited state, we use the same AO settings at all magnetic fields.

Emerging from their respective fiber launchers, the beam we define as camera beam 1 (CB1) enters the main chamber from the top port (M5), while camera beam 2 (CB2) enters from the side (port C1), defined in Fig. 3.1. Each beams passes through a collimating lens, so that both are collimated to a rough 2.5"

beam diameter, with about 3 mW in CB1 and 6 mW in CB2. In order to limit optical pumping during the imaging process [34], the applied light is left hand circularly polarized as defined by the direction of beam propagation relative the bias magnetic field. The lines of the bias field point from the bottom magnetic coil to the top magnetic coil, so that the positive z-axis of the magnets is also vertical axis of the main chamber. CB2 propagates through chamber from a horizontal direction, horizontally polarized orthogonal to the vertical direction so that the required σ_- light comes from a superposition of both circular polarizations. After exiting through port C2, CB2 passes through an imaging lens and arrives at CCD camera microscope objective. CB1 is applied in the path of the vertical MOT beams, so a setup that accommodates the purposes of both beams is required. A PBS replaces a mirror that would normally direct the vertical MOT beam downward into the chamber, so that CB1 may be added with a linear polarization orthogonal to the MOT beam, propagating downward against the bias field lines. In the path of both beams is a single $\lambda/4$ plate so that they each acquire circular polarization with opposite handedness. CB1 is set for right hand circular polarization, which is σ_- with respect to the bias field. So that the MOT remains functional, this requires the field of the upper MOT gradient coil be parallel to the bias field, while the bottom coil must be opposite as summarized in Fig. 3.4. Below the chamber is a Thorlabs MFF101 flip mirror, mounted with a $\lambda/4$ and mirror. With an applied TTL voltage, this allows $\lambda/4$ and mirror to move out of the vertical beam path after the MOT has loaded the FORT. With this path clear, CB1 can propagate through an imaging lens before being reflected into the microscope objective of an additional camera mounted below the chamber. Note that the motor in the flip mirror requires that it be mounted in way that the

Camera Beam 1
Horizontal Polarization

PBS

λ /4 Wave Plate

σ₋ σ₊

MOT Beam
Vertical
Polarization

Bias Magnetic Field

MOT
Magnetic
Field

Imaging Lens

λ /4 Wave Plate
Flip Mirror
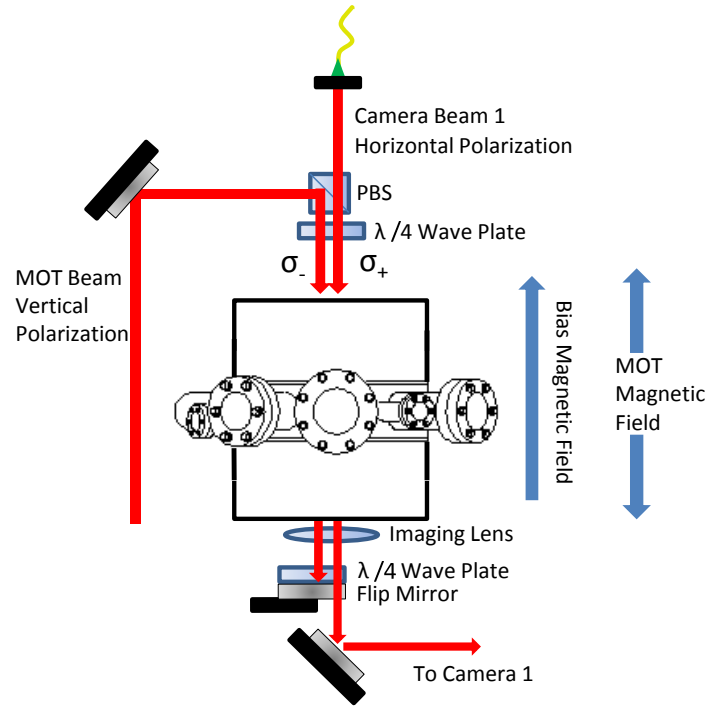
To Camera 1

Figure 3.4: Optics surrounding the main vacuum chamber for imaging with camera 1 and creating the MOT beam in the vertical direction. The indicated circular polarizations are with respect to the direction of beam propagation, which is *opposite* the direction of both the bias magnetic field for tuning the interatomic interactions and the upper coil of the MOT magnets.

presence of the strong bias field still allows it to function.

With the optics for two absorption imaging beams in place, they are applied to each spin state from a perpendicular direction using a short (10 μs), spatially uniform pulse. After being partially absorbed by the atoms, the light that reaches the CCD arrays of our cameras contains an imaged shadow of density distribution for the atomic cloud. From this shadow, all of our data is extracted.

3.2.5   CCD Camera Calibration

Extracting any information from our CCD images requires understanding a properties specific to the camera and its imaging optics. This section will briefly present the relevant results for our current set up, which uses two Andor DV434-BV cameras. A complete description of the what necessitates these calibrations can be found in [34].

Our absorption image from a single camera is a result of two consecutively taken images; one image contains the shadow of the atomic cloud (the signal shot), while a second image taken once the cloud has been destroyed by the first provides a reference shot with no atomic cloud present. From the subtraction of these two images, we must be able to associate the number of photons recorded at each pixel with the number of atoms that were present before the application of the imaging beam. This is equivalent to knowing a *column density* as a function of position on the CCD array. This column density is the three dimensional atomic density integrated along the propagation direction of the camera probe beam. As

derived in [34], it is given by:

$$n(x, z) = -\frac{1}{\sigma_R} \left\{ (1 + \delta^2) \ln \left[\frac{I_s(x, z) + (\phi - 1) I_r(x, z)}{\phi I_r(x, z)} \right] + \frac{I_s(x, z) - I_r(x, z)}{g_{cam} \, \eta_{cam} \, I_{sat}} \right\},$$
(3.5)

where $I_s(x, z)$ is the intensity distribution of the signal shot containing the cloud shadow, $I_r(x, z)$ is the intensity distribution of the reference shot, σ_R is the optical cross section of the relevant transition, δ is the imaging beam detuning, η_{cam} is the camera efficiency, g_{cam} is the camera gain, ϕ is a correction factor accounting for beam depolarization, and I_{sat} is a calculated quantity giving the number of photons per pixel in a probe pulse at the saturation intensity. Note that imaging from the side with camera 2, where the polarization of the light is a superposition of σ_+ and σ_- results in an optical cross section that is half of the value in encountered the vertical direction. The detuning δ is adjusted to be as close to zero as possible, and the camera gain and camera efficiency are properties specific to the camera used, not the positioning of the camera relative to the atomic cloud.

The conversion of an apparent image size in pixels to the size of the imaged object in microns, or simply the combined magnification of the imaging lens and camera microscope objective, changes with the placement of the camera and must be measured in order to properly calculate I_{sat} as defined above. To do this, we translate the CO_2 focusing lens just before the chamber by a known amount along the two transverse directions of the cloud while simultaneously imaging the cloud using both cameras. From the images for a single camera, we track the location in pixels of the peak density of the cloud as a function of the focusing lens position in microns. The slope of a fitted line gives the pixel size in microns at the location of the atom cloud, shown in Fig. 3.5. Combined with the known pixel size of CCD
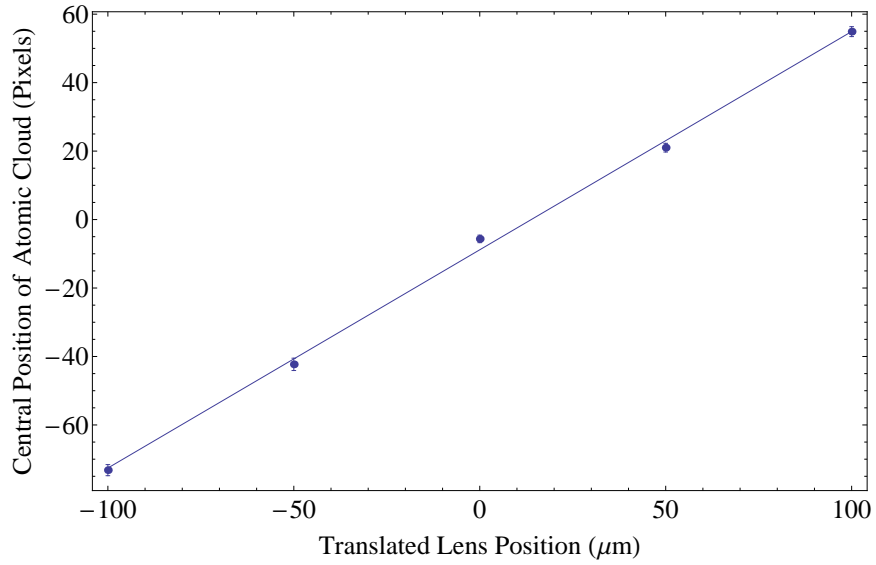
(a) Camera 1
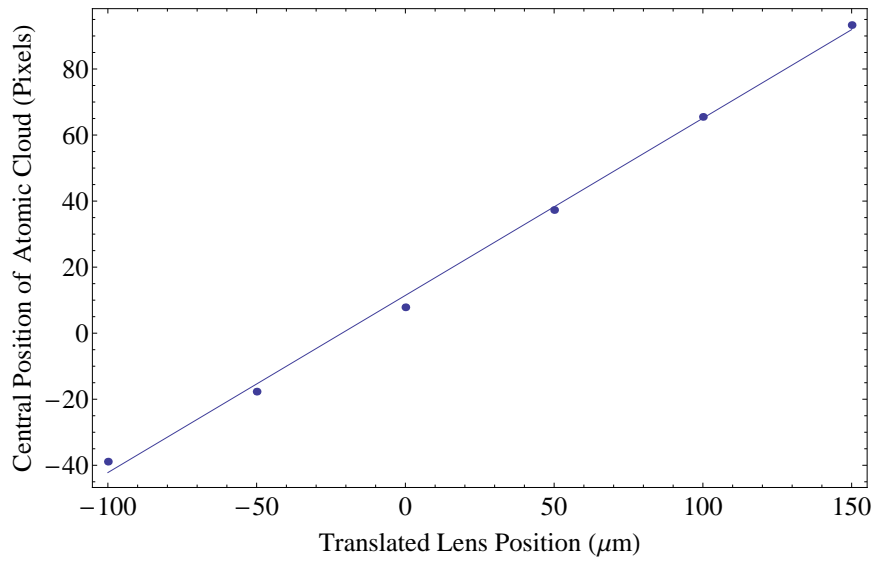
(b) Camera 2

Figure 3.5: Measurement of the pixel size in microns for the image produced by camera 1 and camera 2. The atomic cloud is translated in its radial directions by a known amount using micrometers on a focusing lens. By tacking the central position of the cloud on the pixels of the image, the above figures are created. The fitted slopes give the pixel size in microns in the trap region for each camera.

array as determined by the manufacturer (13 μm by 13 μm for our cameras), a magnification can be calculated. This value is crucial for calculating the real size of the atomic cloud, and is doubly important for the current work where we wish to compare two images of the same cloud from two different cameras. Because the calculated column density also depends on the magnification and the integral of the column density over the region of the cloud gives the total atom number, determining the magnification is also essential to determining the total number of atoms.

Once we are able to believably calculate the number of atoms imaged by each camera, we compare the two to test the balance of spin populations, minimize the detuning in each imaging beam, and check the consistency of our magnification measurement. During each experimental sequence, our spin populations are balanced with a broadband RF pulse in a magnetic field gradient [34]. Using a single camera, we image one spin state to first minimize the detuning in the imaging beam, then calculate an atom number. From image to image, we find that this number fluctuates between five and ten percent. We then image the other spin state with the same imaging beam and the same camera, adjusting the frequency of the spin balancing RF pulse. When both spin states give atom numbers that agree within ten percent without one population persisting higher or lower in total number, we treat the spin balancing to be correctly operating. We then adjust the detuning of the second camera relative to the first until they are simultaneously reporting the same atom numbers for separate spin states. Once this is set, we need only adjust the *overall* detuning of the laser on a daily basis.

3.2.6 CO$_2$ Laser Beam Path

Considering only the theory behind the operation of a far off-resonance trap, it may seem as if the CO$_2$ beam path requires just a single lens to focus the CO$_2$ laser beam at the location of the MOT. The reality, of course, is not so simple. The actual layout of CO$_2$ optics is motivated by additional considerations relating to the focal point shape, maximizing power at the focus, and precise, computer-automated control of the laser intensity. In creating a new trap shape that is elliptical in both the transverse and axial directions, the layout of these optics has undergone significant changes from what is described in prior dissertations from our group. The motivations behind using certain optics will be explained first, followed by a piece by piece description of the individual optics along the CO$_2$ beam path.

Our first consideration is maximizing the power present at the beam focus. Towards this goal, we aim to create the smallest focal point possible at the center of the main chamber. For laser beam of wavelength λ with a beam q/e^2 intensity waist w striking a diffraction limited lens of focal length f, gaussian beam optics tells us that the beam waist at the focal point w_0 will be

$$w_0 = \frac{f\,\lambda}{\pi\,w}. \tag{3.6}$$

Thus, it is advantageous to increase the beam size with an expanding telescope before it strikes our focusing lens. The initial expanded size of the beam waist is then limited only by the size of the windows on the main chamber (roughly a two and a quarter inch diameter). Eq 3.6 also indicates that the focal length of the lens should be as short as possible, which is limited by the distance from the

74

CO_2 window on the circumference of the chamber to the chamber center, which is roughly 5 inches.

Another means of increasing the intensity is by retro-reflecting the CO_2 beam back on itself, with particular care given to overlap the two foci. In practice, this triples the amount of atoms we are able to load from the FORT into the MOT compared to the focus of a single beam. However, when lowering the CO_2 power to initiate the process of *forced evaporation*, we find that pointing instability introduced by the back-going beam leads to a heating of the trapped atoms. No evidence of this heating is present when using a single beam. Thus, we require a motorized mirror (the "chopper" mirror) on the back side of the chamber to block the back-going beam when forced evaporation begins. This allows us to still take advantage of the increased loading while evaporatively cooling the atoms in a stable configuration.

Introduction of a retro-reflected beam also requires additional optics to make sure that this back-going beam does not travel all the way back to the CO_2 laser source and destroy it. In the past, this has involved an angled polarizing optic prior to the expanding telescope and a rooftop mirror on the backside of the chamber. When struck at the intersection of its two reflective faces, this rooftop mirror would rotate the polarization of the beam (which had been linear polarized by transmission through polarizing optic) 90° in addition to reflecting it, so that when the back-going beam struck the polarizing optic a second time, it was reflected harmlessly into a beam dump. However, this also created an orthogonal polarization between the forward and back-going beam at the location of the atoms. Greater intensities can be achieved if the these polarizations are parallel, so that the in-phase electric fields add constructively and to create a standing

wave.

The realization of higher intensities through the parallel polarization of the forward and back-going beam is particularly important when creating a optical trap shape that is elliptical in both the traverse and longitudinal direction. This is because an elliptical transverse direction requires an elliptical beam profile with a decreased beam waste in one direction. We achieve this by adjusting one radius of the beam profile with a simple combination of two cylindrical lenses. However, before the addition of this telescope to our optical layout, the circular beam profile was already maximized to the radius allowed by the CO_2 windows on our chamber. Therefore, the only way to create an elliptical beam profile is to make the beam waist in one transverse direction smaller, increasing the focused spot size and decreasing the overall trapping potential. This loss of intensity motivates the creation of a standing wave FORT in order to compensate, requiring not only light of the same polarization in the forward and back-going beams at the location of the atoms, but also an orthogonal relationship in the polarization of these two beams at the location of the polarization optic.

To create these polarization conditions, we use a reflective phase retarder (RPR) after our expanding telescope. When properly aligned, this optical element acts as combination of a $\lambda/4$ plate and mirror, circularly polarizing the linear forward going beam. The rooftop mirror behind the chamber is then replaced with an ordinary flat mirror, so that the back-going beam is also circularly polarized when it refocuses on the atoms. Upon striking the RPR a second time, the back-going beam becomes linearly polarized and orthogonal to the incoming beam polarization, and is then reflected from the polarization optic into a beam dump.

The installation of the RPR is non trivial, particularly in the case of an asym-

metric beam profile. On its own, this optic can not shift the phase of incoming laser light without also rotating the cross section of the beam: the 45° phase shift is produced by the optic's coating only if the surface of the RPR is 45° to the incoming beam profile in *two* planes. Reflection from such a compound angle rotates the beam profile itself 45°, which would be undetectable if the cross section was circular. Instead, the long axis of the elliptical beam profile is clearly moved 45° relative to the vertical axis of the main chamber. Thus rotated, there is no chamber window that allows a resonant imaging beam to strike the cloud from a direction perpendicular to any of the cloud axes. Correcting this rotation requires an ordinary mirror parallel to the RPR, resulting in an irregular beam path that further necessitates two additional mirrors to bring the CO_2 beam back inline with the chamber CO_2 windows. With these additional surfaces, the net gain in atom number due to the back-going beam is five times the number loaded into the forward going beam alone. Since the trap depth of the forward going beam is reduced by the beam ellipticity, the upshot is a break even in atom number compared to a circular beam profile with a back-going beam reflected from the rooftop mirror.

Finally, the CO_2 beam path must provide a means to manipulate the beam power in order to perform forced evaporation, set a final trap depth prior to expansion, or extinguish the beam entirely to initiate expansion. The optics and electronics this control requires are unchanged from previous variations of the CO_2 beam path described in earlier dissertations from our group. In summary, when the CO_2 beam is passes through a water cooled AO, an applied voltage adjusts the power (but not the direction of) a first order output beam. The AO is placed early in the beam path, but several feet from the output of the laser so

that slight expansion of the propagating beam reduces the laser intensity present on the AO crystal. Thermal lensing in the AO crystal produces an astigmatism in the beam that is corrected with a collimating cylindrical lens telescope, separate from the telescope that creates an elliptical beam profile. As the amplitude of the voltage which controls the amount of power in the first order beam is reduced (a RF signal at 40 MHz), additional cooling affects the AO crystal, causing the first order beam to change angle. In order to compensate, the amplitude of a separate voltage applied at a different frequency (32 MHZ) is increased. This keeps the first order beam traveling in a fixed direction by keeping the AO temperature constant, but also creates an additional first order beam that must be reflected safely into a beam dump.

The actual beam path is shown in Fig. 3.6 All lenses are zinc-selenide, while most mirrors, including the reflective phase retarder, are silicon. The largest 4" diameter mirrors are made of copper. The beam leaves the barrel of a Coherent DEOS LC100-NV CO_2 laser and zig-zags off of two one inch mirrors so that it expands slightly before striking the crystal of an AGM-4010BG1 AO from IntraAction Corporation. The zeroth order is deflected into a beam dump. The beam then encounters a two 1.1" diameter cylindrical lenses that form an expanding telescope. Their focal lengths are 2.0" and 5.0" respectively, so that the vertical beam waist is expanded by a factor of 2.5, setting the elliptical beam profile. Next, the wedge shaped polarization optic serves to linearly polarizes the beam before it enters a second pair of cylindrical lenses, both 1.1″ diameter with a 2.0″ FL. These lenses are arranged to form a collimating telescope, correcting the astigmatism introduced by the AO but still maintaining the elliptical profile. Just prior to this telescope, the 40 and 32 MHz first order beams have separated

78
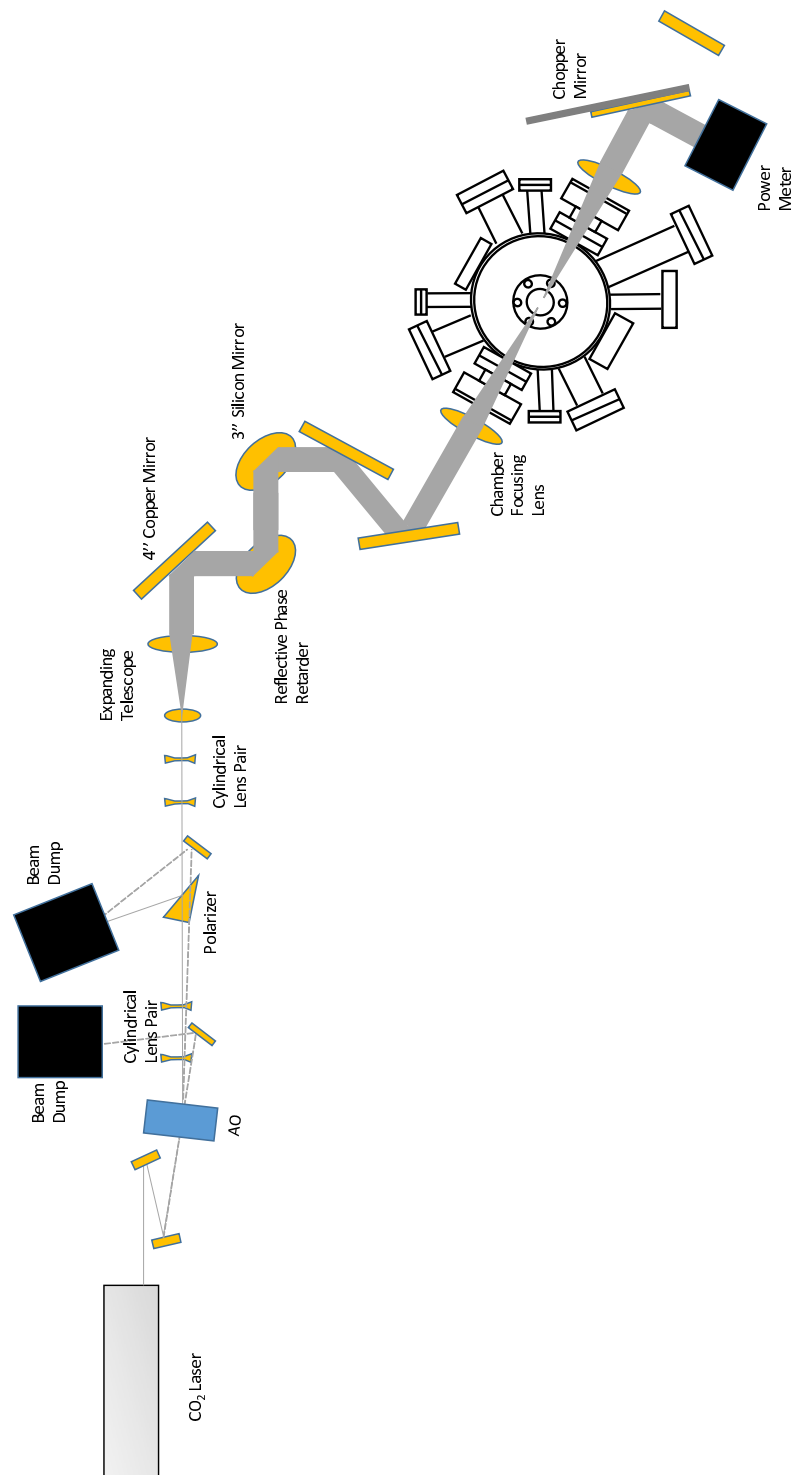
Figure 3.6: Layout of optics for the CO_2 laser beam path. Two pairs of cylindrical lenses shape the beam profile before the beam is brought to a focus at the center of the main vacuum chamber. Optical elements not to scale.

enough for a pick off mirror to send the 32 MHz beam into a beam dump. The 40 MHz beam continues to a telescope that expands the beam size for eventual focusing into the chamber, comprised of a 1.1″ diameter, 2″ FL circular lens and a 2.5″ diameter 10″ FL circular lens. This 2″ FL circular lens replaced an older lens that had a 1.1″ focal length, so that telescopes expands by a factor of 5 instead of 10, approximately. This is is tied to the decision to create the elliptical beam profile by expanding the vertical direction, rather than shrinking it. If we had shrunk one of the beam waists rather than expanded it, we could have reused the old telescope. Not wanting to push the limits of the anti-absorption coatings on the optics and risk new thermal effects, we instead choose to avoid forming and propagating an unnecessarily intense beam.

After the expanding telescope and a 4″ diameter copper mirror, the surface of the 3″ diameter RFR is set at a 45° angle relative to the incoming beam in two planes, which deflects the beam upward. The rotation of the beam profile this creates is corrected by a parallel 3″ diameter that sends the beam towards two more 4″ diameter mirrors and the final chamber focusing lens. In general, these larger 4″ inch mirrors are preferable over the 3″ mirrors due to the large projections of the beam profile created by the necessary reflections at obtuse angles. The RFR is 3″ in diameter only because this the largest size currently sold, and the parallel mirror afterwards is more easily mounted at the odd angle required than the thicker, and considerably heavier, 4″ diameter copper alternative.

The 2.5″ diameter, 7.5″ FL aspheric lens in front of the chamber finally creates the focus of the FORT at the chamber center. At the backside of the chamber, the beam is re-columnated by a second 2.5″ diameter, 7.5″ FL aspheric lens, where it either continues to the chopper mirror and terminates at a power meter, or is

retro reflected by directly striking a 3″ mirror to create the back-going beam. The second 7.5″ FL aspheric lens at the back of the chamber is crucial for assuring good overlap of the back-going beam on the original FORT focus. When the back-going beam reaches the polarizing optic, it is reflected into the same beam dump as the 32 MHz beam.

Though the laser outputs roughly 140 W, just before the chamber focusing lens we find 75 Watts in the first order beam at full power. We measure 68 W after the recollimating lens at the backside of the chamber, for an estimated 71.5 W at the trapping focus. After the chopper mirror, which is not particularly well coated against absorption, we see 64.4 W on the power meter, daily reproduced to a tenth of a Watt.

3.3   Standard Experimental Sequence

While prior sections describe the setup of our apparatus and the basic principles behind the primary components, the actual creation and imaging of an ultra-cold Fermi gas requires understanding the sequence of events during a typical experimental cycle. Broadly, our initial goal is to load as many atoms as possible into the FORT. Once this is done, the sequence will branch depending on the final interaction strength we wish to study. The final seconds are then determined by the specifics of the experiment being performed.

The sequence begins with the MOT, repumper, and slowing beams at full power and the detunings given in Table 3.1, while current is supplied to the MOT gradient coils and the Zeeman slower. The ^{6}Li oven remains on during the entire cycle, constantly churning out an atomic vapor into the Zeeman slower. The

	MOT Loading	MOT Cooling	MOT Optical Pumping
AO Name			
MOT	91.93	102.21	101.76
Repumper	113.89	112.46	Off

Table 3.1: Frequency shifts in MHz provided by the AOs during different experimental phases. Numbers given are for a single pass, while all AOs operate in a double pass configuration. The AO between the dye laser output and the locking region is set for a single pass frequency shift of roughly 105 MHz, optimized daily.

CO_2 beam is also set at full power, with the back-going beam allowed to create a standing wave. We label this configuration as the MOT loading phase, as the frequencies and intensities chosen to load the MOT with the largest number of atoms, but not necessarily the coldest. Achieving the coldest temperatures requires small detunings and low intensities, so after ten seconds, the slowing beam is shut off and the system enters the cooling phase, which lasts for 20 ms. Here, the intensity of the MOT beams is reduced by a factor of 100 with a simultaneous drop in detuning. Note that the beam path is set so that repumper beams are derived from MOT beams, therfore a drop in amplitude on the MOT AO decreases the intensity of both the MOT and repumper beams. The cooling phase frequencies are critical; empirical adjustments are required so that the detuning is as small as possible without the finite laser bandwidth allowing a frequency drift past resonance. Ultimately, it is the stability of the laser in the cooling phase that determines how many atoms are successfully loaded into the FORT. Once the cooling phase concludes, the repumper is shut off and the MOT beams remain on for an additional 500 μs, optically pumping the remaining atoms into the lowest hyperfine ground state. The gradient magnets and all remaining red beams are extinguished, leaving close to 2 million atoms in the FORT at roughly 140 μK.

With the MOT gone, the flip mirror at the base of the vertical MOT beam path clears the way for the eventual propagation of the imaging beam. The chopper mirror is also lowered to block the back-going CO_2 beam, while the bias magnets are turned on. Before tuning the interactions, the bias magnets are set to roughly 8G to give states $|1\rangle$ and $|2\rangle$ a finite energy spacing. The application of a noisy RF pulse corresponding to this energy spacing is then used to balance the population of these two states, forming a 50:50 mixture.

The bias field in then increased to 834 G for five seconds with no additional changes. In this time, the unitary collisional cross section aids the evaporative cooling process. We refer to this period as *free evaporation*, for it proceeds until equilibrated with no input from the operator. Once equilibrium is reached, we are left with roughly 450 thousand atoms per spin state, at temperatures of about 50 μK. Further cooling requires a reduction of the FORT confining potential according the *lowering curve* derived in [40], which balances efficiency with the rate of evaporation:

$$U(t) = U_0 \left(1 + \frac{t}{\tau}\right)^{-1.44}.$$
(3.7)

Both τ and the length of time over which this function determines the shape of the potential are user defined inputs. Once the lowering curve is executed, the trapping potential is re-increased to a chosen value. This final potential depth sets the energy scale for any subsequent expansion measurement. For the current work, all measurements are taken at 20% of the full laser intensity.

The magnetic field used during forced evaporation is determined by the desired final interaction of the atomic sample. In all cases, evaporation is a collisional

process that is aided by a larger collision rate. Therefore, when creating a strongly interacting Fermi gas at and around 834 G, 834 G is also the forced evaporation field. After recompression, the magnetic field can be adiabatically swept to a field between 680 G and the upper limit of our current power supply. However, sweeping the magnetic field from resonance to a value below 680 G produces a heating rate that prevents us from accessing 528 G where the gas is non-interacting [34]. The production of non-interacting gas thus requires forced evaporation at a field of 300 G before sweeping the field *upward* to 528 G.

At 300 G, the collision rate is large enough to allow evaporation, but at a very reduced rate compared to 834 G. As a result of this reduced evaporation efficiency, a forced evaporation curve that lasts up to 40 s ($\tau = 0.25\,s$) is necessary to create the coldest temperatures in a non-interacting, compared to the 3 s ($\tau = 0.028\,s$) required at 834 G. At this reduced interaction strength, the evaporation rate for the few atoms that still remain in the trap after 40 s approaches the heating rate in the main chamber due to collisions with background gases. A comparable evaporation and heating rate results only in a loss of atoms and no further reduction temperature. Thus, the energies reached after approximately 40 s at 300G is the lowest we are able to achieve in the non interacting gas.

For either a strongly interacting or non-interacting gas, the CO_2 laser is extinguished completely after recompression to 20% in order to initiate expansion. The cloud expands for a time between 400 and 2000 μs, when both imaging beams simultaneously image each spin state from a perpendicular direction, destroying the cloud in the process. Each imaging beam strikes the CCD array of their respective camera, recording the shadow cast by the cloud in images labeled as the *signal shots*. After 30 ms, the imaging beams flash again, providing images of the

84

bare beam profile with no atoms present, defined as *reference shots*. The subtraction of the signal and reference shots are recorded for each experimental cycle, while the scattered ^{6}Li of the destroyed cloud coats the walls of main chamber sublimated by titanium. More ^{6}Li enters the slower from the oven, and the cycle begins again.

Chapter 4

Hydrodynamic Theory

This chapter deals with the derivation of nearly all of the equations applied to the analysis of our data in order to quantify both transport properties and scale invariance in the expansion of a Fermi gas. Basic hydrodynamic equations will first allow us to write an exact expression for the total energy per particle of the unitary gas, and define a useful energy scale which depends only on the cloud size for a general scattering length. We will derive not only a hydrodynamic description for expansion of the mean square cloud size, but contrast this with the expansion of a mean square cloud size for an ideal, non interacting gas. Following this, we will show that the mean square cloud *radius* of both the unitary hydrodynamic case and the non interacting gas behave identically, and demonstrate that deviations from this behavior enable a measurement of the bulk viscosity and the conformal symmetry breaking pressure ΔP. The chapter concludes with a justification of using a hydrodynamic description for all data analyzed in this dissertation near a Feshbach resonance.

4.1   Hydrodynamic Equations

A simple hydrodynamic description of a fluid requires three basic equations. Euler's Equation, which is just another form for Newton's second law, a continuity equation, which is nothing but conservation of particle number, and finally an equation of state, in order to satisfy closure.

We will describe the motions of fluid elements defined to be infinitesimal densities of particles, which follow the vectors of a velocity field. Euler's equation states that

$$mn\left(\frac{\partial}{\partial t} + \mathbf{v} \cdot \nabla\right)\mathbf{v} = -\nabla P - n\nabla U_{total} + \frac{\text{dissipative forces}}{\text{unit volume}}, \qquad (4.1)$$

where P is the pressure, n is the density given as the number of atoms per unit volume, U is any external potential (here, the combined potential of the CO_2 laser and the bias magnetic field), and m is mass of a single atom. Clearly, each term has units of force per unit volume, and the equation amounts to $\mathbf{F}/V = m\frac{d\mathbf{v}}{dt}/V$. The velocity $\mathbf{v}$ in Euler's equation refers to the stream velocity represented by a velocity field. This is not the velocity of individual atoms in the trap, but the velocity with which the density evolves. For example, equilibrated atoms within the trap have kinetic energy, but the observed density would be constant; the stream velocity, and the corresponding velocity field would be zero. In such a case, Euler's equation would read:

$$0 = -\nabla P - n\nabla U_{total} + 0. \qquad (4.2)$$

This statement of force balance will later be used as a starting point to calculate

the total energy per particle of the trapped atoms in terms of the trapping potential, but will require information from the other hydrodynamic equations not yet introduced. The $\left(\frac{\partial}{\partial t} + \mathbf{v} \cdot \nabla\right)$ operator is known as the convective derivative, and here is the total time derivative of the velocity of a fluid element as it moves according to the velocity field.

A word of caution on the definition and usage of the potential energy term U_{total}. In our experimental set up, there are two external potentials: one resulting from the optical trap, and the other from the finite curvature of the magnetic field that we use to tune interactions. As the cloud sits in the trap with zero stream velocity, it feels a total potential U_{total}, which is the sum of both the optical potential U_{opt} and the magnetic bowl U_{mag}.

$$U_{mag} + U_{opt} = U_{total}. \tag{4.3}$$

The optical trap can be abruptly extinguished in order to initiate expansion and a velocity field. However, the magnetic field must remain on in order to maintain the strong interparticle interactions we wish to study. Therefore, the cloud must expand into a magnetic potential, and some stream kinetic energy will be transferred into the U_{mag} term which is then becomes a function of time[1]. In applying Euler's equation and the other hydrodynamic equations yet to be derived, we must be extremely careful in considering which potential energy terms are present and maintain consistent notation.

The form of the dissipative forces per unit volume remain to be written in the

---

[1]The magnetic field is constant in time over the timescales we perform our experiments. Its contribution to the potential energy, however, is a function of time when a stream velocity is present because the position of the atoms are now a function of time.

above equation. The form of this term well known, and the arguments behind it are well posed by Landau [14]. He reasons that internal friction in a fluid, labeled as viscosity, should only act within a fluid when different fluid elements move with different velocities, creating an internal relative motion. Therefore, viscosity dependent momentum transfers should be linear in the spatial velocity gradients for each direction. At the same time, there must exist no damping term independent of $\partial v_i / \partial x_k$, so that they all vanish when the fluid velocity is uniform. But what about uniform *rotation*? There the damping terms must also vanish, despite the presence of a velocity gradient. To fulfill all of these requirements, the damping per unit volume will be expressed as the divergence of a symmetric tensor, called the *viscous stress tensor*, labeled ε_{ij} . In general, any symmetric tensor can be written as the sum of traceless symmetric tensor and a scalar[2], and ε_{ij} takes the form of:

$$\varepsilon_{ij} \;\equiv\; \eta\,\sigma_{ij} + \zeta\sigma'\delta_{ij} \tag{4.4}$$

$$\sigma_{ij} \;\equiv\; \frac{\partial v_i}{\partial x^j} + \frac{\partial v_j}{\partial x^i} - \frac{2}{3}\delta_{ij}\nabla\cdot\mathbf{v} \tag{4.5}$$

$$\sigma' \;\equiv\; \nabla\cdot\mathbf{v}. \tag{4.6}$$

Dimensionally, they each have units of momentum over area. A natural momentum scale is $\hbar/L$ where $\hbar$ is Plank's constant and L is the interparticle spacing, so that the natural area is then L^2. Each viscosity coefficient in then expressible in terms of $\hbar$, the density $n = 1/L^3$, and a dimensionless coefficient so that

Thus, the effects of viscosity are characterized by two different viscosity coeffi-

---

[2]To see that this is true, take any n × n symmetric tensor and find its trace. Divide the trace by n, and subtract that value times the identity tensor.

89

cients. The shear viscosity, η, is a dissipative force that resists the parallel sidling of nearby fluid elements. The bulk viscosity, ζ, is a dissipative force arising from the direct collisions of fluid elements normal to their boundaries during uniform expansion or contraction. Both of these coefficients have units of momentum per area. If we wish to characterize them on the quantum scale, the natural momentum scale is $\hbar/L$ where $\hbar$ is Plank's constant and L is the interparticle spacing, so that the natural area is then L^2. Therefore, both η and ζ can be written using dimensionless proportionality constants as

$$\eta = \hbar n \, \alpha_S \tag{4.7}$$

$$\zeta = \hbar n \, \alpha_B. \tag{4.8}$$

The full form of Euler's equation necessary to describe our experiments is therefore:

$$mn \left(\partial_t + \mathbf{v} \cdot \nabla\right) v_i = -\partial_i P - n\partial_i U_{total} + \sum_j \partial_j \left(\eta \, \sigma_{ij} + \zeta \sigma' \delta_{ij}\right). \tag{4.9}$$

The second crucial hydrodynamic equation is the equation of continuity, a simple statement of conservation of particle number. Given a volume V enclosed by an area A, the rate at which the total density within V changes is opposite in sign to the rate that density flows through the boundary of A:

$$\frac{d}{dt} \int n \, dV = -\int n \, \mathbf{v} \cdot d\mathbf{A}. \tag{4.10}$$

Bringing the total time derivative on the left hand side inside the integrand requires changing it to a partial derivative, and applying the divergence theorem to

the right hand side gives:

$$\int \frac{\partial n}{\partial t} \, dV = -\int \nabla \cdot (n\,\mathbf{v}) \, dV. \tag{4.11}$$

Thus, we are left with the equation of continuity stated as:

$$\frac{\partial n}{\partial t} + \nabla \cdot (n\,\mathbf{v}) = 0. \tag{4.12}$$

Assuming the form of U_{total} is known, and that α_S and α_B are to be measured (or otherwise known), we are left to determine one velocity variable for each direction, one scaler pressure, and one scalar density. While Euler's equation is a vector equation, providing three scalar equations, the equation of continuity is a scalar equation, leaving five variables to be determined and only four equations. Conventionally, the solution to this problem is write an additional relationship between the pressure and the density, given by the equation of state (EOS). However, the EOS also introduces temperature as a variable, so in order for it to be a useful means of satisfying closure, the assumption that the system is isothermal must be made. Thus, it is through the equation of state that thermodynamic considerations become necessary to for a complete hydrodynamic description of a system.

Fortunately, the equation of state for a unitary Fermi gas is beautifully simple. Within it lies one of the most remarkable examples of how although strong interactions pose a very complicated many body problem, they also provide powerful simplifying assumptions through scale invariance and the universal hypothesis [41]. The universal hypothesis states that all local thermodynamic quantities are a function of local density and temperature *only*. Consider a small volume ΔV con-

taining ΔN atoms in equilibrium. The total density in this region $n = \Delta N / \Delta V$ will remain constant. A constant density in the region ΔV will also be accompanied by a constant associated energy, ΔE. In the universal regime, the local energy must be proportional to some universal, dimensionless function of temperature [3] labeled as f_E. The temperature and energy scales are set respectively by the local Fermi temperature, $T_F(n)$, and the local Fermi energy, $E_F(n) = k_B T_F(n)$ so that ΔE is:

$$\Delta E = \Delta N E_F(n) f_E \left[\frac{T}{T_F(n)} \right], \tag{4.13}$$

where the local Fermi energy is

$$E_F(n) = \frac{\hbar^2 (3\pi n)^{2/3}}{2m}. \tag{4.14}$$

From Eq. 4.13, the local pressure can be found through the relation

$$P = -\left(\frac{\partial \Delta E}{\partial \Delta V} \right)_{\Delta N, \Delta S}. \tag{4.15}$$

By performing this partial derivative, we should arrive at the desired expression for pressure in terms of density and temperature. However, it is not known exactly how this quantity ΔE changes with entropy, which must be kept constant in order to carry out this calculation. This motivates the use of the same arguments used

---

[3]State variables normalized by their value at a critical point are usually referred to as a reduced variable. Though the Fermi temperature is not a critical point of a phase transition, we may refer to $\theta \equiv T/T_F(n)$ as the reduced temperature.

to write ΔE to write ΔS, which takes the general form

$$\Delta S = \Delta N k_B f_S \left[\frac{T}{T_F(n)} \right]. \tag{4.16}$$

This expression reveals that in order to keep ΔS constant for the derivative in Eq. 4.15, the only variable that is independently allowed to vary in ΔE is E_F. Additionally, the only value within E_F that is not a constant is $n^{2/3}$. Therefore,

$$
\begin{aligned}
P &= -\Delta N f_E \left[\frac{T}{T_F(n)} \right] \frac{\partial E_F(n)}{\partial \Delta V} & (4.17) \\
&= -\Delta N f_E \left[\frac{T}{T_F(n)} \right] \frac{\hbar^2 (3\pi)^{2/3}}{2m} \frac{\partial n^{2/3}}{\partial \Delta V} & (4.18) \\
&= -\Delta N f_E \left[\frac{T}{T_F(n)} \right] \frac{\hbar^2 (3\pi)^{2/3}}{2m} \left(-\frac{2}{3} \right) \frac{\Delta N^{2/3}}{\Delta V^{5/3}} & (4.19) \\
&= \frac{2}{3} n E_F f_E \left[\frac{T}{T_F(n)} \right] & (4.20) \\
&= \frac{2}{3} \frac{\Delta E}{\Delta V} & (4.21) \\
P &= \frac{2}{3} \mathcal{E} & (4.22)
\end{aligned}
$$

This remarkable result for the EOS means that the energy density and pressure of a strongly interacting Fermi gas has the same relationship as the ideal, non interacting gas. A few comments on the meaning of $\mathcal{E}$ are worth noting. First, the density in an arbitrary region pertaining to this derivation was assumed to be constant. Therefore, $\mathcal{E}$ does not know anything about the stream velocity $\mathbf{v}$, which is only present when the density is flowing along a velocity field. Secondly, nowhere was a confining potential mentioned in preceding steps, and therefor $\mathcal{E}$ is the internal energy of the gas, the combined kinetic energy (the part which does not alter the density) and interaction energy only.

93

While this simple EOS has many uses and non trivial consequences, it also has failed to bring the number of equations equal to the number of variables, the very reason we set out to derive it. By revealing the relationship between pressure and energy density, not pressure explicitly in terms of density and temperature, another unknown variable was introduced. However, conservation of energy, an always reliable concept, provides the missing piece. Specifically, it provides an additional relationship between $\mathcal{E}$, $\mathbf{v}$, and U_{total}:

$$\frac{d}{dt} \int \left(n \frac{1}{2} m \mathbf{v}^2 + \mathcal{E} + n\, U_{total} \right) d^3 \mathbf{x} = 0. \qquad (4.23)$$

This expression also explicitly reiterates the definitions of $\mathbf{v}$ and $\mathcal{E}$; the kinetic energy arising from the stream velocity is not included in $\mathcal{E}$. In the same way conservation of mechanical energy is derived by integrating Newton's second law, the above statement of conservation of energy is simply another statement of Euler's equation. It is necessary to use this form only because the equation of state was not explicitly written in terms of density.

Of the hydrodynamic equations just derived, the only one specific to the unitary gas is the relation $P = \frac{2}{3}\mathcal{E}$. In the presence of a finite scattering length, Euler's equation, continuity, and energy conservation all hold. Therefore, in anticipation of later dealing with off resonant hydrodynamics and a finite scattering length, it is convenient to write the relationship between P and $\mathcal{E}$ as

$$\Delta P = P - \frac{2}{3}\mathcal{E}, \qquad (4.24)$$

a quantity which is zero for the unitary case. The calculation of ΔP off resonance will be the subject of a later chapter.

With Eq. 4.23 and Eq. 4.24, the total number of equations and variables assumed to be unknown for the unitary gas is now both six. We can now use these results to immediately derive a means for determining the total energy per particle of a unitary gas through a simple example. The novel hydrodynamic results of this chapter will then follow.

4.2 Hydrodynamic Expansion of a Mean-Square Cloud Width

All of our measurements rely on absorption images of our atomic cloud. One of the simplest numbers we can extract is a cloud width. By taking multiple pictures at different times after release form the optical trap, we can explore the cloud width as a function of time. We therefore require a general description for how this measured width should evolve based on the hydrodynamic equations derived above. More precisely, it is the *mean-square cloud size*, which we extract from the fits to our images, and aim to describe theoretically.

The photographed density profile is fit with either a two dimensional Gaussian or a zero temperature Thomas-Fermi profile, depending on the energy. For the present work, the Gaussian profile is by far the more common of the two. Both of these fits have a simple relationship between their characteristic widths and their average widths. For example, fitting a one dimensional density distribution with a Gaussian profile given by $n(x) = Ae^{-x^2/\sigma_x^2}$ would output a value for A and σ_x. If $\int n(x)dx = N$, then $A = 1/(\sigma_x \sqrt{\pi})$, and the fit value for σ_x is related to the

mean square size in the x-direction $\langle x^2 \rangle$ by:

$$\langle x^2 \rangle \;=\; \frac{1}{N} \int n\, x^2 dx = \frac{1}{N} \int \frac{1}{\sigma_x\,\pi} e^{-x^2/\sigma_x^2} x^2 dx = \frac{\sigma_x^2}{2}. \qquad (4.25)$$

We now consider how $\langle x^2 \rangle$ must evolve during expansion. To begin, we write the time derivative of $\langle x_i^2 \rangle$ for each direction $i = x, y, z$ as

$$\frac{d\langle x_i^2 \rangle}{dt} \;=\; \frac{1}{N} \int \frac{\partial n}{\partial t} x_i^2 d^3\mathbf{r}. \qquad (4.26)$$

Invoking the continuity equation gives Eq. 4.26 as:

$$\frac{d\langle x_i^2 \rangle}{dt} \;=\; \frac{1}{N} \int \frac{\partial n}{\partial t} x_i^2 d^3\mathbf{r} = \frac{1}{N} \int [-\nabla \cdot (n\mathbf{v})]\, x_i^2 d^3\mathbf{r}$$

This expression can be integrated by parts, a useful trick because the density must go to zero at an infinite distance away from the trap center:

$$\frac{1}{N} \int [-\nabla \cdot (n\mathbf{v})]\, x_i^2\, d^3\mathbf{r} \;=\; \int (n\mathbf{v}) x_i^2 \cdot d\mathbf{A} + \frac{1}{N} \int (n\mathbf{v}) \cdot \nabla\, x_i^2\, d^3\mathbf{r} \quad (4.27)$$

$$=\; \frac{1}{N} \int (n\mathbf{v}) \cdot \nabla\, x_i^2\, d^3\mathbf{r} \qquad\qquad (4.28)$$

$$=\; \frac{1}{N} \int n\, v_i\, 2x_i\, d^3\mathbf{r} \qquad\qquad (4.29)$$

$$\frac{d\langle x_i^2 \rangle}{dt} \;=\; 2\langle x_i\, v_i \rangle. \qquad\qquad\qquad (4.30)$$

The evolution of $\langle x_i\, v_i \rangle$ can be derived using the same procedures, now noting

that v_i is another variable that can change with time:

$$
\begin{aligned}
\frac{d\langle x_i v_i\rangle}{dt} &= \frac{1}{N}\int n\, x_i \frac{\partial v_i}{\partial t}\, d^3\mathbf{r} + \frac{1}{N}\int \frac{\partial n}{\partial t}\, x_i v_i\, d^3\mathbf{r} \\
&= \frac{1}{N}\int n\, x_i \frac{\partial v_i}{\partial t}\, d^3\mathbf{r} + \frac{1}{N}\int n\, \mathbf{v}\cdot\nabla(x_i v_i)\, d^3\mathbf{r} \\
&= \langle x_i(\partial_t + \mathbf{v}\cdot\nabla)v_i\rangle + \langle v_i^2\rangle.
\end{aligned}
\tag{4.31}
$$

Combining Eq. 4.30 and Eq. 4.31, we obtain,

$$
\frac{d^2}{dt^2}\frac{\langle x_i^2\rangle}{2} = \langle x_i(\partial_t + \mathbf{v}\cdot\nabla)v_i\rangle + \langle v_i^2\rangle.
\tag{4.32}
$$

The first term of the right had side of this equation looks like the convective derivative of a velocity component multiplied by the position component in the same direction. The same term would appear if we took a density averaged product of Euler's equation with a position component, prompting us to write:

$$
\begin{aligned}
\frac{1}{N}\int n\, x_i(\partial_t + \mathbf{v}\cdot\nabla)v_i\, d^3\mathbf{r} &= \frac{1}{N m}\int x_i(-\partial_i P - n\,\partial_i U_{total})\, d^3\mathbf{r} \\
&\quad + \frac{1}{N m}\sum_j \int x_i\partial_j(\eta\,\sigma_{ij} + \zeta_B\,\sigma'\,\delta_{ij})\, d^3\mathbf{r}.
\end{aligned}
$$

The pressure, trapping potential, and viscosity terms on the right hand side must all approach zero an infinite distance from the trap, so integrating by parts gives:

$$
\langle x_i(\partial_t + \mathbf{v}\cdot\nabla)v_i\rangle = \frac{1}{Nm}\int P\, d^3\mathbf{r} - \frac{1}{m}\langle x_i\partial_i U_{total}\rangle - \frac{1}{Nm}\int(\eta\,\sigma_{ii} + \zeta_B\,\sigma')\, d^3\mathbf{r}
\tag{4.33}
$$

Writing the viscosity coefficients as $\eta \equiv \alpha_S\,\hbar\, n$ and $\zeta_B \equiv \alpha_B\,\hbar\, n$, we arrive at,

$$
\langle x_i(\partial_t + \mathbf{v}\cdot\nabla)v_i\rangle = \frac{1}{Nm}\int P\, d^3\mathbf{r} - \frac{1}{m}\langle x_i\partial_i U_{total}\rangle - \frac{\hbar}{m}\langle \alpha_S\,\sigma_{ii} + \alpha_B\,\sigma'\rangle,
\tag{4.34}
$$

where

$$\langle \alpha_S \, \sigma_{ii} + \alpha_B \, \sigma' \rangle \equiv \frac{1}{N} \int n \left(\alpha_S \, \sigma_{ii} + \alpha_B \, \sigma \right) d^3 \mathbf{r}. \tag{4.35}$$

Now, by taking Eq. 4.34 (derived from the continuity equation) and combining it with Eq. 4.32 (independently derived from Euler's equation), we then obtain for one direction x_i,

$$\frac{d^2}{dt^2} \frac{\langle x_i^2 \rangle}{2} = \frac{1}{Nm} \int P \, d^3 \mathbf{r} + \langle v_i^2 \rangle - \frac{1}{m} \langle x_i \partial_i U_{total} \rangle - \frac{\hbar}{m} \langle \alpha_S \, \sigma_{ii} + \alpha_B \, \sigma' \rangle. \tag{4.36}$$

Eq. 4.36 therefore determines the evolution of the mean square cloud radii along each axis, $\langle x_i^2 \rangle$, which depends on the conservative forces arising from the scalar pressure and the trap potential, as well as the dissipative forces arising from the shear and bulk viscosity.

In applying these equations to our experimental system, it is worth mentioning that these equations are derived under the basic assumption that a single fluid is present. However, a strongly interacting Fermi gas is able to undergo a phase transition where a superfluid can form at the trap center, surrounded by a normal fluid component at the edges. In this two fluid regime, it is a reasonable question to ask how well a single fluid model could hope to explain the expansion dynamics. As noted in Ref. [42], both the superfluid and the normal fluids move together in expansion, making a system that follows the behavior of an overall one component fluid. Indeed, it takes considerable effort to intentionally excite relative motion between the superfluid and normal fluids [43]. Having not attempted these additional steps in our experiments, we are well justified in applying the single fluid model to our exploration of the unitary gas above, below, and around the superfluid transition.

4.3 Scaling Solution of a Mean Square Cloud Width

Having found an equation for the evolution of $\langle x_i^2 \rangle$ in the form of Eq. 4.36, we make two simple assumptions in order to find a solution. The first assumption comes from looking back at the form of Euler's equation:

$$mn \left(\partial_t + \mathbf{v} \cdot \nabla \right) v_i = -\partial_i P - n \partial_i U_{total} + \sum_j \partial_j \left(\eta \, \sigma_{ij} + \zeta \sigma' \delta_{ij} \right). \qquad (4.37)$$

For our experiments, we know that the form of the potential is going to be close to harmonic, and therefore $\partial_i U_{total}$ will be linear in the spatial coordinate, x_i. Looking at the left hand side of Euler's equation, this also implies that the velocity field is linear in the spatial coordinate to the same degree that $\partial_i U_{total}$ is. This assumption, and the simplification it provides is the primary reason that we choose to work with a harmonic trap with an anharmonic correction term rather than an exact form of the potential.

The second simplification is the assumption of a *scaling* solution, or rather a density that changes by a *scale transformation*. As a specific example, this means that if the cloud forms a Gaussian density profile in the trap, this density profile will remain Gaussian once released; the cloud width will simply increase as the central simultaneously decreases to conserve total atom number. Likewise, a near ground state gas that has a zero temperature Thomas-Fermi profile will maintain this shape as it expands once the trap has been shut off. More precisely, for an initial Gaussian or Thomas-Fermi profile with a characteristic width in the ith direction given by $\sigma_i(t = 0)$, this width at time t will grow to $\sigma(t) = b_i(t)\sigma_i(0)$,
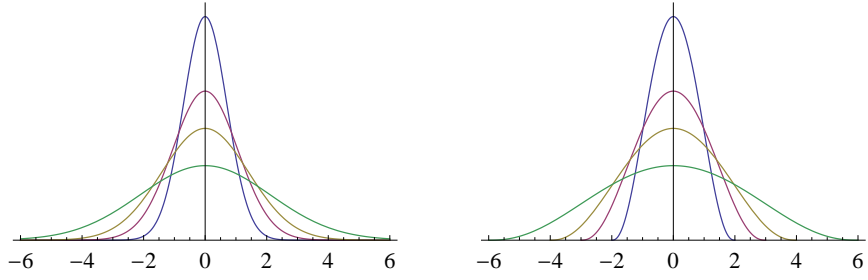
Figure 4.1: Scaled evolution of a one dimensional Gaussian distribution (left) a and zero-temperature Thomas-Fermi distribution (right). The subtle differences between the two types of distributions are most apparent where the tails of each approach zero. The expressions for each are given by $\frac{N}{2\sqrt{\pi}\,[b_x(t)\sigma_x(0)]}\,e^{-x^2/b_x^2(t)\sigma_x^2(0)}$ and $\frac{8N}{5\,\pi\,[b_x(t)\,\sigma_x(0)]}\left(1 - \frac{x^2}{b_x^2(t)\sigma_x^2(0)}\right)^{5/2}$ respectively. Four density profiles of each distribution are plotted for values of $b_x(t) = 1, 1.5, 2$, and 3.

where $b_i(t)$ is a time dependent scale factor with initial conditions $b_i(0) = 1$ and $\dot{b}_i(0) = 0$. The normalization of these density profiles both go as $1/\sigma_x$ for 1d so a $1/b_x$ is necessary factor in the amplitude. Since a width σ_i goes inversely to x_i, multiplying σ_i by b_i is the same as dividing x_i by b_i. We can therefore take what we have learned from these two 1d distributions and generalize the idea of a scaled density solution to an arbitrary three dimensional density. If the initial equilibrium density of the trapped cloud is given by $n_0(x, y, z)$, then the density at all later times is given by:

$$n(\mathbf{r}, t) = \frac{n_0(x/b_x, y/b_y, z/b_z)}{\Gamma(t)} \tag{4.38}$$

$$\Gamma(t) \equiv b_x b_y b_z, \tag{4.39}$$

where $\Gamma(t)$ is defined to be the *volume scale factor*.

The combination of these two approximations has important consequences. Since one assumption deals with the velocity field and the other with the density,

the continuity equation 4.12 which relates the two is good starting point. It can be trivially used to show that for a linear velocity field ($\mathbf{v} = \alpha_x x \,\hat{i} + \alpha_y y \hat{j} + \alpha_z z \hat{k}$) and a scaled density of the above form gives $\alpha_i = \dot{b}_i/b_i$ or $v_i = x_i \dot{b}_i/b_i$.

Having previously noted that $\langle x_i^2 \rangle$ is proportional to σ_i^2 we note that $\langle x_i^2 \rangle = \langle x_i^2 \rangle_0 \, b_i^2(t)$, and $\langle v_i^2 \rangle = \langle x_i^2 \rangle \dot{b}_i^2/b_i^2 = \langle x_i^2 \rangle_0 \dot{b}_i^2(t)$, where $\langle x_i^2 \rangle_0$ is the mean-square cloud radius of the trapped cloud in the ith direction, just before release. Combining this with $\frac{d^2}{dt^2}\frac{\langle x_i^2 \rangle}{2} = \langle x_i^2 \rangle_0 \dot{b}_i^2(t) + \langle x_i^2 \rangle_0 \, b_i \ddot{b}_i$, the evolution of $\langle x_i^2 \rangle$ (Eq. 4.36) in the scaling approximation with a linear velocity field becomes:

$$\langle x_i^2 \rangle_0 \, b_i \ddot{b}_i = \frac{1}{Nm} \int P \, d^3\mathbf{r} - \frac{\hbar}{m}\langle \alpha_S \, \sigma_{ii} + \alpha_B \nabla \cdot \mathbf{v} \rangle - \frac{1}{m}\langle x_i \partial_i U_{total} \rangle. \qquad (4.40)$$

The goal now becomes finding a way to write the right hand side of this equation in terms of $b_i(t)$ and its time derivatives. Performing this process on the volume integral of the pressure is lengthly, but generally straight forward. It will involve the equation of state (written generally in terms of ΔP), significant manipulation of the conservation of energy equation, and finally Euler's equation in the case of equilibrated force balance to write initial conditions.

To determine the evolution equation for the pressure integral at all scattering lengths, we start with the general equation of state in the form of $P = \frac{2}{3}\mathcal{E} + \left(P - \frac{2}{3}\mathcal{E}\right) = \frac{2}{3}\mathcal{E} + \Delta P$, integrated over volume to write

$$\frac{1}{N}\int P d^3\mathbf{r} = \frac{2}{3}\frac{1}{N}\int \mathcal{E}d^3\mathbf{r} + \frac{1}{N}\int \Delta P d^3\mathbf{r}. \qquad (4.41)$$

Separately, energy conservation (4.23) allows us to write an additional relation

101

for $\mathcal{E}$ and P by explicitly evaluating the time derivative:

$$\frac{d}{dt} \int \left(n \frac{1}{2} m \mathbf{v}^2 + \mathcal{E} + n\, U_{total} \right) d^3\mathbf{r} = 0. \tag{4.42}$$

Performing the time derivative of this equation and generating a more compact form requires a bit of algebra. Beginning with the simplest term first, the potential energy term gives:

$$
\begin{aligned}
\frac{d}{dt} \int n\, U_{total}\, d^3\mathbf{r} &= \int n \frac{\partial U_{total}}{\partial t} d^3\mathbf{r} + \int U_{total} \frac{\partial n}{\partial t} d^3\mathbf{r} && (4.43) \\
&= \int n \frac{\partial U_{total}}{\partial t} d^3\mathbf{r} + \int U_{total} \left[-\nabla \cdot (n\mathbf{v}) \right] d^3\mathbf{r} && (4.44) \\
&= \int n \frac{\partial U_{total}}{\partial t} d^3\mathbf{r} + \int (n\mathbf{v}) \cdot \nabla U_{total}\, d^3\mathbf{r}, && (4.45)
\end{aligned}
$$

where we obtain this expression using the usual tricks of continuity and integration by parts. The progression of the stream velocity requires a few more involved steps, but begins by using the same methods as above.

$$
\begin{aligned}
\frac{d}{dt} \int n \frac{1}{2} m \mathbf{v}^2 d^3\mathbf{r} &= \frac{1}{2} m \left(\int \mathbf{v}^2 \frac{\partial n}{\partial t} d^3\mathbf{r} + 2 \int n\mathbf{v} \cdot \frac{\partial \mathbf{v}}{\partial t} d^3\mathbf{r} \right) && (4.46) \\
&= \frac{1}{2} m \left(\int \mathbf{v}^2 \left[-\nabla \cdot (n\mathbf{v}) \right] d^3\mathbf{r} + 2 \int n\mathbf{v} \cdot \frac{\partial \mathbf{v}}{\partial t} d^3\mathbf{r} \right) && (4.47) \\
&= \frac{1}{2} m \left(\int (n\mathbf{v}) \cdot \mathbf{v}^2 d^3\mathbf{r} + 2 \int n\mathbf{v} \cdot \frac{\partial \mathbf{v}}{\partial t} d^3\mathbf{r} \right) && (4.48) \\
&= m \int n\mathbf{v} \cdot (\mathbf{v} \cdot \nabla)\mathbf{v}\, d^3\mathbf{r} + mn \int \mathbf{v} \cdot \frac{\partial \mathbf{v}}{\partial t} d^3\mathbf{r} && (4.49) \\
&= m \int n\mathbf{v} \cdot \frac{\partial \mathbf{v}}{\partial t} + \mathbf{v} \cdot (\mathbf{v} \cdot \nabla)\mathbf{v}\, d^3\mathbf{r} && (4.50)
\end{aligned}
$$

This integrand in the last line looks the left side of Euler's equation Eq. 4.9,

dotted with velocity, so we make the replacement with the right hand side:

$$m \int n\mathbf{v} \cdot \frac{\partial \mathbf{v}}{\partial t} + \mathbf{v} \cdot (\mathbf{v} \cdot \nabla)\mathbf{v} \, d^3\mathbf{r} \tag{4.51}$$

$$= \int \mathbf{v} \cdot (-\nabla P - n\nabla U_{total}) + \sum_j v_i \partial_j \left(\eta \, \sigma_{ij} + \zeta \sigma' \delta_{ij} \right) d^3\mathbf{r} \tag{4.52}$$

The above pressure term is easily integrated by parts to give $\int P(\nabla \cdot \mathbf{v})d^3\mathbf{r}$, and the potential term will eventually cancel with a term opposite in sign in the expression for $\frac{d}{dt} \int n \, U_{total} \, d^3\mathbf{r}$, so no further changes to it are necessary.

However, the $\int \sum_j v_i \partial_j \left(\eta \, \sigma_{ij} + \zeta \sigma' \delta_{ij} \right) d^3\mathbf{r}$ term requires a bit more discussion. First, what is its physical meaning? Every term we are evaluating in this energy conservation equation has units of energy per unit time, while the integrands have units of energy per unit time per unit volume. This term is then some rate of energy transfer that results from non zero viscosity coefficients, or rather from the presence of frictional forces. Therefore, this term must represents a frictional heating rate resulting from the viscosity dissipating directed kinetic energy. We will label this term as $-\dot{Q}$, fist integrating it by parts and treating the viscosity coefficients as zero at infinity to produce:

$$\dot{Q} = -\int \sum_{ij} v_i \partial_j \left(\eta \, \sigma_{ij} + \zeta \sigma' \delta_{ij} \right) d^3\mathbf{r} = \int \sum_{ij} (\partial_i v_j) \left(\eta \, \sigma_{ij} + \zeta \sigma' \delta_{ij} \right) d^3\mathbf{r} \tag{4.53}$$

$$\equiv \int \dot{q} \, d^3\mathbf{r}, \tag{4.54}$$

where $\dot{q} = \sum_{ij}(\partial_i v_j) \left(\eta \, \sigma_{ij} + \zeta \sigma' \delta_{ij} \right)$. For the next series of manipulations it is

worth reiterating the definitions of σ_{ij} and σ' as

$$\sigma_{ij} \equiv \frac{\partial v_i}{\partial x^j} + \frac{\partial v_j}{\partial x^i} - \frac{2}{3}\delta_{ij}\nabla \cdot \mathbf{v}$$

$$\sigma' \equiv \nabla \cdot \mathbf{v},$$

and that σ_{ij} is symmetric and traceless. Because $\sum_{ij}(\partial_i v_j)(\eta\,\sigma_{ij} + \zeta\sigma'\delta_{ij}) = \sum_{ij}(\partial_j v_i)(\eta\,\sigma_{ij} + \zeta\sigma'\delta_{ij})$ we can write $\sum_{ij}(\partial_i v_j)(\eta\,\sigma_{ij} + \zeta\sigma'\delta_{ij})$ as $\frac{1}{2}\sum_{ij}(\partial_i v_j + \partial_j v_i)(\eta\,\sigma_{ij} + \zeta\sigma'\delta_{ij})$. Additionally, the tracelessness of σ_{ij} combined with the summation over i and j means that a scaler term (such as another $\frac{2}{3}\delta_{ij}\nabla \cdot \mathbf{v}$ term) can multiplied by σ_{ij} and summed over ij to produce no additional effect. This is useful because it allows us to arrive at a more compact expression in the form of:

$$
\begin{aligned}
\dot{q} &= \sum_{ij}(\partial_i v_j)(\eta\,\sigma_{ij} + \zeta\sigma'\delta_{ij}) \\
&= \sum_{ij}(\partial_i v_j)(\eta\,\sigma_{ij}) + \zeta\sigma'^2 \\
&= \sum_{ij}\frac{1}{2}(\partial_i v_j + \partial_j v_i)(\eta\,\sigma_{ij}) + \zeta\sigma'^2 \\
&= \sum_{ij}\frac{1}{2}(\partial_i v_j + \partial_j v_i - \frac{2}{3}\delta_{ij}\nabla \cdot \mathbf{v})(\eta\,\sigma_{ij}) + \zeta\sigma'^2 \\
\dot{q} &= \sum_{ij}\frac{1}{2}\eta\,\sigma_{ij}^2 + \zeta\sigma'^2
\end{aligned}
\tag{4.55}
$$

. Finally, combining all of these energy per unit time terms gives the following expression:

$$\frac{d}{dt}\int d^3\mathbf{r}\,\mathcal{E} + \int d^3\mathbf{r}\,(\nabla \cdot \mathbf{v})\,P + \int d^3\mathbf{r}\,n\,\frac{\partial U_{total}}{\partial t} = \dot{Q}. \tag{4.56}$$

104

Just after release of the cloud, the trap potential is constant in time, and the last term in Eq. 4.56 vanishes. Using $P = \frac{2}{3}\mathcal{E} + \Delta P$, Eq. 4.56 yields

$$\frac{d}{dt}\int \mathcal{E}\, d^3\mathbf{r} + \frac{2}{3}\int (\nabla \cdot \mathbf{v})\,\mathcal{E}\, d^3\mathbf{r} = \dot{Q} - \int (\nabla \cdot \mathbf{v})\,\Delta P d^3\mathbf{r}. \qquad (4.57)$$

As we intend to explore small deviations from the scale invariant regime, the last term on the right of Eq. 4.57 can be evaluated using suitable approximations, as discussed in the chapter dealing with the calculation of ΔP.

Another consequence of the scaling solution is the relationship $\nabla \cdot \mathbf{v} = \dot{\Gamma}/\Gamma$, a quantity that is independent of the spatial coordinates and can move outside of the volume integrals. With this substitution, Eq. 4.57 reduces to

$$\frac{d}{dt}\int \mathcal{E}\, d^3\mathbf{r} + \frac{2}{3}\frac{\dot{\Gamma}}{\Gamma}\int \mathcal{E}\, d^3\mathbf{r} = \dot{Q} - \frac{\dot{\Gamma}}{\Gamma}\int \Delta P d^3\mathbf{r}. \qquad (4.58)$$

The left hand side of this equation can be turned into the time derivative of a single term by first multiplying both sides by $\Gamma^{2/3}$:

$$\Gamma^{2/3}\frac{d}{dt}\int \mathcal{E}\, d^3\mathbf{r} + \frac{2}{3}\frac{\dot{\Gamma}}{\Gamma^{1/3}}\int \mathcal{E}\, d^3\mathbf{r} = \Gamma^{2/3}\dot{Q} - \frac{\dot{\Gamma}}{\Gamma^{1/3}}\int \Delta P d^3\mathbf{r}$$

$$\frac{d}{dt}\left(\Gamma^{2/3}\int \mathcal{E}\, d^3\mathbf{r}\right) = \Gamma^{2/3}\dot{Q} - \frac{\dot{\Gamma}}{\Gamma^{1/3}}\int \Delta P d^3\mathbf{r}$$

$$\Gamma^{2/3}\int \mathcal{E}\, d^3\mathbf{r} - \Gamma^{2/3}(t=0)\int \mathcal{E}_0\, d^3\mathbf{r} = \int_0^t \Gamma^{2/3}\dot{Q}dt - \int_0^t \frac{1}{\Gamma^{1/3}}\frac{d\Gamma}{dt}\int \Delta P d^3\mathbf{r}\, dt$$

$$\int \mathcal{E}d^3\mathbf{r} = \frac{\int \mathcal{E}_0\, d^3\mathbf{r} + \int_0^t \Gamma^{2/3}\,\dot{Q}dt - \int_1^{\Gamma(t)} \frac{1}{\Gamma^{1/3}}\int \Delta P d^3\mathbf{r}\, d\Gamma}{\Gamma^{2/3}} \qquad (4.59)$$

We have thus found the volume integral of the energy density at time t after release of the cloud in terms of the initial condition $\int \mathcal{E}_0\, d^3\mathbf{r}$, having used $\Gamma(t=0) = 1$.

Although this relation can be used to determine the evolution of $\int P\,d^3\mathbf{r}$ in general, it is particularly well-suited to a perturbative treatment of $\Delta P = P - \frac{2}{3}\mathcal{E}$ in the near scale-invariant regime.

To determine the volume integral of the initial internal energy, $\int \mathcal{E}_0\,d^3\mathbf{r}$, we note that before release from the optical trap and the onset of expansion, the equilibrium density is determined by the balance between the outward force arising from the equilibrium pressure P_0 and the inward restoring force of the total potential,

$$\nabla P_0 + n(\mathbf{r})\nabla U_{total}(\mathbf{r}) = 0. \tag{4.60}$$

This statement of force balance is equivalent to Euler's equation with no stream velocity. When a dot product of both sides of Eq. 4.60 is taken with $\mathbf{r}$ and integrated over volume, the surface term of the pressure once again vanishes when integrated by parts to produce:

$$3\int P_0\,d^3\mathbf{r} \;=\; \int n(\mathbf{r})\mathbf{r}\cdot\nabla U_{total}(\mathbf{r})d^3\mathbf{r} \tag{4.61}$$

$$=\; \langle \mathbf{r}\cdot\nabla U_{total}\rangle_0. \tag{4.62}$$

This volume of the integral of the initial pressure is a crucial initial condition, warranting its own definition,

$$\widetilde{E} = \langle \mathbf{r}\cdot\nabla U_{total}\rangle_0, \tag{4.63}$$

the importance of which will be discussed in Chapter 6. Inserting the relationship between the initial internal energy density and a general pressure term, $\mathcal{E}_0 =$

$\frac{3}{2}P_0 - \frac{3}{2}\Delta P_0$, we find

$$\frac{1}{N}\int \mathcal{E}_0\, d^3\mathbf{r} = \frac{1}{2}\,\langle \mathbf{r}\cdot\nabla U_{total}\rangle_0 - \frac{3}{2N}\int \Delta P_0\, d^3\mathbf{r}. \tag{4.64}$$

Using Eq. 4.64 to eliminate $\int \mathcal{E}_0\, d^3\mathbf{r}$ and taking $\langle \mathbf{r}\cdot\nabla U_{total}\rangle_0$ as the energy scale, we determine the time-dependent volume integral of the pressure in Eq. 4.41: $\frac{1}{N}\int Pd^3\mathbf{r} = \frac{2}{3}\frac{1}{N}\int \mathcal{E}d^3\mathbf{r} + \frac{1}{N}\int \Delta P d^3\mathbf{r}$ as,

$$\frac{1}{N}\int Pd^3\mathbf{r} = \frac{\langle \mathbf{r}\cdot\nabla U_{total}\rangle_0}{3\,\Gamma^{2/3}}\left[1 + C_Q(t) + C_F(t) - C_F(0) - C_P(t)\right]. \tag{4.65}$$

Here, the effect of heating on the pressure integral is given by $C_Q(t)$, which is determined from Eq. 4.59,

$$\dot{C}_Q(t) \equiv \frac{\Gamma^{2/3}(t)\frac{2\dot{Q}}{N}}{\langle \mathbf{r}\cdot\nabla U_{total}\rangle_0}, \tag{4.66}$$

with the initial condition $C_Q(0) = 0$. Using the definition of the heating rate, Eq. 4.55, with the velocity field $v_i = x_i\,\dot{b}_i/b_i$, where $\partial_j v_i = \delta_{ij}\dot{b}_i/b_i$ is spatially constant, it is straightforward to obtain

$$\frac{2\dot{Q}}{N} = \hbar\,\bar{\alpha}_S\sum_i \sigma_{ii}^2 + 2\hbar\,\bar{\alpha}_B\frac{\dot{\Gamma}^2}{\Gamma^2}. \tag{4.67}$$

The trap averaged-viscosity coefficients, which appear in Eq. 4.67, are defined by

$$\bar{\alpha}_S(a) \;\equiv\; \int \eta/(N\hbar)\, d^3\mathbf{r} \tag{4.68}$$

$$\bar{\alpha}_B(a) \;\equiv\; \int \zeta_B/(N\hbar)\, d^3\mathbf{r}. \tag{4.69}$$

In the general case of a finite scattering length a, the trap-averaged viscosity coefficients are dependent on both the scattering length and time. The form of this dependence will be discussed in Chapter 5, along with all other terms in the hydrodynamic equations that vary with a finite scattering length. Additionally in Eq. 4.67, we note that

$$\frac{\dot{\Gamma}}{\Gamma} = \frac{\dot{b}_x}{b_x} + \frac{\dot{b}_y}{b_y} + \frac{\dot{b}_z}{b_z} \tag{4.70}$$

and

$$\sigma_{ii} = 2\frac{\dot{b}_i}{b_i} - \frac{2}{3}\frac{\dot{\Gamma}}{\Gamma}, \tag{4.71}$$

so that we may write,

$$\sum_i \sigma_{ii}^2 = 4\sum_i \frac{\dot{b}_i^2}{b_i^2} - \frac{4}{3}\frac{\dot{\Gamma}^2}{\Gamma^2}. \tag{4.72}$$

Explicitly expanding this compact result in terms of expansion factors gives:

$$\sum_i \sigma_{ii}^2 = \frac{8}{3}\left(\frac{\dot{b}_x^2}{b_x^2} + \frac{\dot{b}_y^2}{b_y^2} + \frac{\dot{b}_z^2}{b_z^2} - \frac{\dot{b}_x}{b_x}\frac{\dot{b}_y}{b_y} - \frac{\dot{b}_x}{b_x}\frac{\dot{b}_z}{b_z} - \frac{\dot{b}_y}{b_y}\frac{\dot{b}_z}{b_z}\right). \tag{4.73}$$

The effect of $\Delta P = P - \frac{2}{3}\mathcal{E}$ on the pressure integral (arising from last term in Eq. 4.41) is determined by

$$C_F(t) \equiv \frac{\Gamma^{2/3}(t)\frac{3}{N}\int \Delta P\, d^3\mathbf{r}}{\langle \mathbf{r}\cdot\nabla U_{total}\rangle_0}. \tag{4.74}$$

Finally, the last term in Eq. 4.59 gives

$$C_p(t) \equiv \frac{2\int_1^{\Gamma(t)} \frac{d\Gamma}{\Gamma^{1/3}}\frac{1}{N}\int \Delta P\, d^3\mathbf{r}}{\langle \mathbf{r}\cdot\nabla U_{total}\rangle_0}. \tag{4.75}$$

With Eq. 4.65 for the volume integral of the pressure, Eq. 4.40 yields our

central result for the scale factor evolution,

$$\ddot{b}_i = \frac{\overline{\omega_i^2}}{\Gamma^{2/3}b_i}\left[1 + C_Q(t) + C_F(t) - C_F(0) - C_p(t)\right]$$
$$-\frac{\hbar\left(\bar{\alpha}_S\,\sigma_{ii} + \bar{\alpha}_B\frac{\dot{\Gamma}}{\Gamma}\right)}{m\langle x_i^2\rangle_0 b_i} - \frac{\langle x_i\partial_i U_{mag}\rangle}{m\langle x_i^2\rangle_0 b_i}. \quad (4.76)$$

In Eq. 4.76, the only remaining time dependent part of U_{total} is the magnetic potential, Eq. 4.3, as we are interested in expansion of the cloud after the optical part of the potential is extinguished. Further, we define the mean ballistic oscillation frequency of the total potential in the ith direction[4], which need not be harmonic,

$$\overline{\omega_i^2} \equiv \frac{\langle x_i\partial_i U_{total}\rangle_0}{m\langle x_i^2\rangle_0} = \frac{\langle \mathbf{r}\cdot\nabla U_{total}\rangle_0}{3m\langle x_i^2\rangle_0}. \quad (4.77)$$

Here the second form follows from force balance in equilibrium, $\partial_i p + n\partial_i U_{total} = 0$. Multiplying by x_i and integrating by parts requires that $\langle x_i\partial_i U_{total}\rangle_0$ is the same for all directions.

While Eq. 4.76 represents the general scaling solution for both on and off resonance, a method to calculate ΔP has yet to be introduced. For now, it is instructive to set ΔP to zero and study the scaling solution in the unitary case. $\Delta P = 0$ means $C_F(t) = C_F(0) = C_p(t) = 0$ and we have

$$\ddot{b}_i = \frac{\overline{\omega_i^2}}{\Gamma^{2/3}b_i}\left[1 + C_Q(t)\right] - \frac{\hbar\left(\bar{\alpha}_S\,\sigma_{ii} + \bar{\alpha}_B\frac{\dot{\Gamma}}{\Gamma}\right)}{m\langle x_i^2\rangle_0 b_i} - \frac{\langle x_i\partial_i U_{Mag}\rangle}{m\langle x_i^2\rangle_0 b_i} \quad (4.78)$$

$$\dot{C}_Q(t) = \frac{\Gamma^{2/3}(t)}{\langle \mathbf{r}\cdot\nabla U_{total}\rangle_0}\left(\hbar\,\bar{\alpha}_S\sum_i\sigma_{ii}^2 + 2\hbar\,\bar{\alpha}_B\frac{\dot{\Gamma}^2}{\Gamma^2}\right), \quad (4.79)$$

---

[4]The reason for this relationship will become clear in the Chapter 6. For now, treat it only as a definition.

With or without ΔP, Mathematica easily determines a numerical solution for the expansion factors b_i, given the initial conditions $b_i(0) = 0$ and $\dot{b}_i(0) = 0$ and the measured parameters characterizing the confining potential. As described below, the shear viscosity α_S is best used a fit parameter to mean square widths expressed as an *aspect ratio*, while the much smaller α_B and a suitable approximation for ΔP are determined by fitting $\langle \mathbf{r}^2 \rangle$ to the data, which is the subject of a following section. Before delving into $\langle \mathbf{r}^2 \rangle$, however, we will first briefly look at the scaling solution of a noninteracting gas.

4.4   Scaling Solution of a Non-Interacting Gas

Having determined the form of the scaling solution for hydrodynamic expansion, it is worth noting the contrast with a scaling solution for the expansion of a noninteracting gas. This derivation is handled in depth in [34], and will only be presented here only in summary. The derivation begins with a system of equations using a relaxation approximation, which gives the expansion factors b_i as

$$\ddot{b}_i + \frac{1}{b_i\,m\,\langle \tilde{x}_i^2 \rangle} \left[\left\langle \tilde{x}_i \frac{\partial U_{EV}(b_x\tilde{x}, b_y\tilde{y}, b_z\tilde{z})}{\partial \tilde{x}_i} \right\rangle - \theta_i \left\langle \tilde{x}_i \frac{\partial U_{EQ}(\tilde{x}, \tilde{y}, \tilde{z})}{\partial \tilde{x}_i} \right\rangle \right] = 0 \quad (4.80)$$

$$\dot{\theta}_i + 2\,\theta_i \frac{\dot{b}_i}{b_i} = -\frac{1}{\tau_R} \left(\theta_i - \bar{\theta} \right). \quad (4.81)$$

where τ_R is the relaxation time, related to the characteristic time between collisions of two particles in the gas, $\bar{\theta} = (\theta_x + \theta_y + \theta_z)/3$, and $\theta_i = \theta_i(t)$ give an effective temperature in the ith direction. The two potential terms U_{EQ} and U_{EV} refer to potential energy terms under equilibrium and potential energy terms which evolve with time, respectively. In our system, U_{EQ} is thus the initial confining poten-

tial energy, initial optical plus initial magnetic, and U_{EV} would be the magnetic potential energy which grows as the atoms expand. The tilde in $\tilde{x}_i$ is meant to indicate an initial size, so that $\langle \tilde{x}_i^2 \rangle = \langle x_i^2 \rangle_0$ in our notation. However, $\tilde{x}_i$ is useful here to distinguish the time dependent behavior in U_{EV} from the equilibrium behavior in U_{EQ}. In the noninteracting limit, the gas is collisionless, and $\tau_R \to \infty$ [5]. In this case, the second equation yields $\theta_i = 1/b_i^2$, so that we have a single equation to consider:

$$\ddot{b}_i + \frac{1}{b_i\, m\, \langle \tilde{x}_i^2 \rangle} \left[\left\langle \tilde{x}_i \frac{\partial U_{EV}(b_x \tilde{x}, b_y \tilde{y}, b_z \tilde{z})}{\partial \tilde{x}_i} \right\rangle - \frac{1}{b_i^2} \left\langle \tilde{x}_i \frac{\partial U_{EQ}(\tilde{x}, \tilde{y}, \tilde{z})}{\partial \tilde{x}_i} \right\rangle \right] = 0. \quad (4.82)$$

As before, $b_i(t)$ have exactly the same meaning in terms of how an initial density scales in time, and are subject to the same initial conditions as the hydrodynamic case. Neglecting the effects of the magnetic bowl, $\langle x_i \partial_i U_{total} \rangle_0 \to \langle x_i \partial_i U_{Opt} \rangle_0$, and once extinguished to initiate expansion, $U_{EV} = 0$ and we have:

$$\ddot{b}_i - \frac{1}{m\, b_i^3\, \langle \tilde{x}_i^2 \rangle} \langle x_i \partial_i U_{total} \rangle_0 = 0. \quad (4.83)$$

Where $\left\langle \tilde{x}_i \frac{\partial U_{EQ}(\tilde{x}, \tilde{y}, \tilde{z})}{\partial \tilde{x}_i} \right\rangle$ has been written as $\langle x_i \partial_i U_{total} \rangle_0$ to be consistent with the notation we adopted in the derivation of the scaling solution for the hydrodynamic system. Now, the definition for what we have earlier labeled the mean ballistic

---

[5]The relaxation approximation is also capable of deriving the hydrodynamic equations at unitarity by allowing τ to approach zero. Any small, but finite τ in this case can be shown to be related to shear viscosity. However, the relaxation approximation does not contain any information about bulk viscosity or a finite ΔP when a finite scattering length is introduced by tuning away from resonance. It is for these reasons that we derive expansion factors for the strongly interacting case with a full hydrodynamic treatment in the previous section

oscillation frequency becomes clear. For if we neglect the magnetic bowl, we have

$$\overline{\omega_i^2} \equiv \frac{\langle x_i \partial_i U_{total} \rangle_0}{m \langle x_i^2 \rangle_0} \quad \rightarrow \quad \frac{\langle x_i \partial_i U_{Opt} \rangle_0}{m \langle x_i^2 \rangle_0} = \frac{\langle \mathbf{r} \cdot \nabla U_{Opt} \rangle_0}{3m \langle x_i^2 \rangle_0} \tag{4.84}$$

$$\ddot{b}_i - \frac{\overline{\omega_i^2}}{b_i^3} = 0, \tag{4.85}$$

and $b_i(t)$ then evolves according to:

$$b_i(t) = \sqrt{1 + (\omega_i\, t)^2} \tag{4.86}$$

$$b_i^2(t) = 1 + (\omega_i\, t)^2, \tag{4.87}$$

for the initial conditions $\dot{b}_i(0) = 0$ and $b_i(0) = 1$. We find that $b_i(t)^2$ evolves as a simple quadratic in time, so that

$$\langle x_i^2 \rangle = b_i^2(t)\langle x_i^2 \rangle_0 = \langle x_i^2 \rangle_0 + (\omega_i\, t)^2 \, \langle x_i^2 \rangle_0. \tag{4.88}$$

This relation is easy to alternative derive without Eq. 4.82. If a non-interacting gas is confined in a potential U that is extinguished at time $t = 0$ to initiate expansion, then the ith gas particle with initial position $\mathbf{r}_{i0}$ will have a time dependent position given by $\mathbf{r}_i = \mathbf{r}_{i0} + \mathbf{v}_{i0}\, t$. If we look at a mean square width of the cloud in the x direction, where the average is taken over the density distribution, we have that

$$\langle x^2 \rangle = \langle x^2 \rangle_0 + \langle v_x^2 \rangle_0\, t^2, \tag{4.89}$$

where terms the are first order in velocity, $\propto \langle v_x \rangle_0 = 0$, vanish in the averaging process. The form of Eq. 4.89 is the reason why "ballistic expansion" is used

112

to describe the behavior of the non interacting gas upon release from an optical trap. This simply refers to the presence of a constant velocity: whatever velocity a density elements has when the trap is extinguished is the velocity it will maintain during expansion. The cloud width therefore grows as a constant velocity times time, and the widths squared grows as a constant times time squared. In contrast, the velocity of hydrodynamic system will continue to evolve while the cloud expands, due to internal pressure and viscous forces.

Note that that the effect of the time dependent magnetic potential energy was neglected in the above derivation for the sake of demonstrating simple quadratic scaling with time. In order to properly account for its contribution to the expansion factors, we return to the relaxation approximation and now observe a case where $\left\langle \tilde{x}_i \frac{\partial U_{EV}(b_x \tilde{x}, b_y \tilde{y}, b_z \tilde{z})}{\partial \tilde{x}_i} \right\rangle$ is no longer zero, but rather equal to:

$$U_{EV}(b_x \tilde{x}, b_y \tilde{y}, b_z \tilde{z}) = \frac{m}{2} \left(-\omega_{x\,mag}^2 b_x^2 \tilde{x}^2 + \omega_{y\,mag}^2 b_y^2 \tilde{y}^2 + \omega_{z\,mag}^2 b_z^2 \tilde{z}^2 \right), \quad (4.90)$$

where this form of the magnetic potential will be derived in chapter 6. Note only that we treat the magnetic bowl as being exactly harmonic, with no bars over its oscillation frequency, unlike the optical potential.

Not only does the magnetic bowl create a non zero potential energy that evolves with time as the gas expands, it also contributes an additional term to the equilibrium potential. This $\frac{\langle \mathbf{r} \cdot \nabla U_{mag} \rangle_0}{3m \langle x_i^2 \rangle_0}$ simply adds to the optical potential, giving the following system of equations for the expansion factors of a non interacting

gas released from an optical potential into a magnetic bowl:

$$\ddot{b}_x - \omega_{mx}^2\, b_x - \frac{\bar{\omega}_{x\,opt}^2 - \omega_{x\,mag}^2}{b_x^3} \;=\; 0 \tag{4.91}$$

$$\ddot{b}_y + \omega_{my}^2\, b_y - \frac{\bar{\omega}_{y\,opt}^2 + \omega_{y\,mag}^2}{b_y^3} \;=\; 0 \tag{4.92}$$

$$\ddot{b}_z + \omega_{mz}^2\, b_z - \frac{\bar{\omega}_{z\,opt}^2 + \omega_{z\,mag}^2}{b_z^3} \;=\; 0. \tag{4.93}$$

In the presence of the magnetic potential, these equations still admit a closed form solution of the form

$$b_i^2(t) = 1 + \frac{\bar{\omega}_{i\,opt}^2}{\omega_{i\,mag}^2} \sin^2(\omega_{i\,mag}t). \tag{4.94}$$

It is apparent from the results of this section that the expansion factors behave very differently in the hydrodynamic case then they would in the absence of interparticle interactions. Observable examples of these differences are given in the following section.

4.5   Hydrodynamic Expansion

Qualitatively, the difference between the expansion of a hydrodynamic cloud and that of a non interacting cloud is most apparent when an *aspect ratio* for an initial anisotropic density distribution is compared. The introductory chapter of this dissertation presented the concept of *elliptic flow* as the signature of hydrodynamic behavior when an aspect ratio is examined. Here, we shall demonstrate this using numerical solutions to the equations given above.

We define an aspect ratio of the cloud as the ratio of two characteristic widths

from two directions. For example, the x-y aspect ratio is defined to be $\sigma_x(t)/\sigma_y(t)$, or equivalently $\sqrt{\langle x^2\rangle/\langle y^2\rangle}$. For a cigar shaped, elliptical cloud, we choose to always define the aspect ratio with the initially smaller width in the numerator, so that the aspect ratio begins with a value less than one. This is because the way the aspect ratio will grow towards a value of one is sensitive to both shear viscosity and distinguishing ballistic and hydrodynamic expansion.

Consider the non-interacting gas, where the mean square width in the ith direction grows according to Eq. 4.89. If we consider the x-y aspect ratio, we have

$$\sqrt{\frac{\langle x^2\rangle}{\langle y^2\rangle}} = \sqrt{\frac{\langle x^2\rangle_0 + \langle v_x^2\rangle_0\, t^2}{\langle y^2\rangle_0 + \langle v_y^2\rangle_0\, t^2}}. \tag{4.95}$$

Because the average initial velocity is the same in all directions, at large times the aspect ratio in ballistic flow asymptotes at unity. No matter the starting shape of a ballistic cloud, it will end as a sphere. When this happens, the radius will continue to increase in size, but the aspect ratio will remain fixed at unity.

On the other hand, the aspect ratio of an initially elliptical, hydrodynamic cloud will always reach a value of unity. Neglecting viscosity, Eq.4.78 for the hydrodynamic expansion factor in one direction is

$$\ddot{b}_i = \frac{\overline{\omega_i^2}}{\Gamma^{2/3}b_i}. \tag{4.96}$$

Qualitatively, $\overline{\omega_i^2}$ is set by the confining potential, so that a larger $\overline{\omega_i^2}$ corresponds to both a higher pressure gradient and a narrower initial width according to the hydrodynamic equations which led to the derivation of Eq.4.78. For a larger $\overline{\omega_i^2}$, Eq. 4.96 indicates there will be a greater acceleration of $\ddot{b}_i$. Therefore, a smaller

115

initial width will grow according to a expansion factor possessing a larger acceleration, allowing it to eventually overtake the size of an initially larger direction. Observation of this elliptic flow pattern provided the first evidence for the creation of the first strongly interacting Fermi gas in 2002 [7].

Aspect ratios described by the hydrodynamic expansion factors in Eq.4.78 have additional important properties that are not obvious without graphing their numerical solutions. For instance, at long enough times, the elliptical flow of hydrodynamic system will also saturate the aspect a nearly constant value, although *this value will always be greater than unity*, signifying the narrow direction overtaking what was initially the larger cloud width. Additionally, it can be shown numerically that by properly choosing the ratio of the trapping frequencies that establish the initial aspect ratio, this saturation point can occur at longer or shorter times. The correlation is found to be that the closer the trapping frequencies (or equivalently, the closer the initial sizes) the sooner the aspect ratio will saturate to a final value.

The aspect ratio of an expanding hydrodynamic cloud is also sensitive to the shear viscosity $\bar{\alpha}_S$ of the system. If shear viscosity is present, momentum will be transferred *out of* the more quickly expanding direction and *into* the more slowly expanding direction. This slows the time dependent growth of the aspect ratio by both lowering its numerator and increasing its denominator, making it a powerful means of measuring the shear viscosity. Exploiting this allowed the first measurement of the shear viscosity in a unitary Fermi gas within the high temperature regime [5].

For the present work, we note a numerical result that if the saturation of the aspect ratio is observable, a non zero shear viscosity also causes the aspect

ratio to saturate to a smaller value. Experimentally, we are limited in the time after release from the optical trap that we can reliably observe. As the cloud expands, it becomes more diffuse, lowering our signal to noise ratio. Additionally, continued expansion will approach the finite boundaries of our image. Therefore, if the saturation of the aspect ratio occurs at later times, it will not be observable. The saturation of the aspect ratio is not seen in either Ref. [7] or Ref. [5], as both experiments used trapping frequencies that differed by a factor of nearly 30 to 1.

In our current experimental setup, the ellipticity of the cloud in both its longitudinal and transverse directions create two very different aspect ratios that we have the option of studying. Using the orientation of the cloud established in the previous chapter, we label the x-y aspect ratio as the *transverse aspect ratio*, and the x-z aspect ratio as the *longitudinal aspect ratio*. Numerical simulations indicate that we are able to observe the saturation of the aspect ratio in the transverse direction where the frequencies differ only by a factor of 2.7, but not in the longitudinal direction where the differ by a factor of 33 (a longitudinal aspect ratio similar to previous experiments in Refs. [5, 7]). This also means we are not only able to clearly observe the viscosity lowering the saturation value of the transverse aspect ratio, but only the slowed growth of the longitudinal aspect ratio. As a result, we extract a measurement the shear viscosity from the study of the transverse aspect ratio, where its effect is more pronounced. Examples of how these predicted aspect ratios differ, including the saturation of one but not the other, as well as the effect of shear viscosity on both, are given in Figure 4.2.

In closing this discussion of aspect ratios, note that if the initial shape of the trap was not elliptical, we would have a comparatively boring aspect ratio to study. Both a non interacting gas and strongly interacting gas released from a spherical
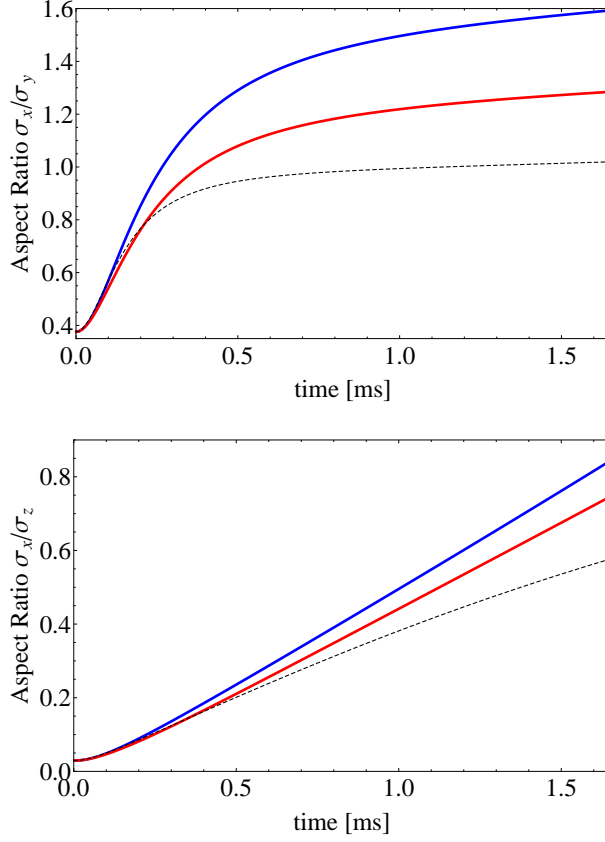
Figure 4.2: Calculated aspect ratios as a function of time after release from an optical trap using a numerical solution to Eq. 4.78, with trap oscillation frequencies matching our experimental conditions. In blue, an input energy of 1.25 in E/E_F units and zero viscosity. In red, an input energy of $E/E_F = 1.25$ and $\bar{\alpha}_S$ equal to 2. The top plot shows the transverse aspect ratio while the lower plot shows one of the longitudinal aspect ratios. While the presence of viscosity creates a notable change in both cases, the effect is greater overall and at earlier times in the transverse direction. The results for a ballistic gas released from the same optical trap are given as dotted lines.

trap would maintain their spherical shape. Additionally, the spherical expansion of the hydrodynamic case would experience no effect of shear viscosity, as any momentum transfer would be completely isotropic. The creation of a spherical trap is also incredibly difficult, if not impossible, experimentally. However, the experimental observation of a *spherical quantity*, given by mean square cloud radius, is possible if *all three* widths of the trap are known.

4.6 Expansion of the Mean-Square Cloud Radius

Having found the scaled solution for each direction at and around unitarity, as well the non interacting regime, there is a clear difference in the evolution of the aspect ratio starting from an elliptical trap. However, in this section it shall be demonstrated that there is particular scalar quantity in the expansion dynamics that behaves exactly the same in both the non interacting and unitary case, regardless of any initial asymmetry in the shape. This quantity is the *mean square cloud radius*, $\langle \mathbf{r}^2 \rangle = \langle x^2 \rangle + \langle y^2 \rangle + \langle z^2 \rangle$. Remarkably, this derivation can be carried out without assuming a form of the velocity field, as was necessary in the case of the scaled solution. We make only the assumption that a single fluid is present, and begin with equation 4.36, the general evolution of the mean square cloud radii along each axis, $\langle x_i^2 \rangle$, which depends on the conservative forces arising from the scalar pressure and the trap potential, as well as the viscous forces arising from the shear and bulk viscosity:

$$\frac{d^2}{dt^2} \frac{\langle x_i^2 \rangle}{2} = \frac{1}{Nm} \int P \, d^3 \mathbf{r} + \langle v_i^2 \rangle - \frac{1}{m} \langle x_i \partial_i U_{total} \rangle - \frac{\hbar}{m} \langle \alpha_S \, \sigma_{ii} + \alpha_B \, \sigma' \rangle. \quad (4.97)$$

When this equation is summed over all three directions, the shear viscosity term vanishes, since σ_{ij} is traceless, yielding

$$\frac{d^2}{dt^2}\frac{\langle \mathbf{r}^2 \rangle}{2} = \frac{3}{Nm}\int P d^3\mathbf{r} + \langle \mathbf{v}^2 \rangle - \frac{1}{m}\langle \mathbf{r}\cdot\nabla U_{total}\rangle - \frac{3\hbar}{m}\langle \alpha_B \nabla\cdot\mathbf{v}\rangle. \qquad (4.98)$$

Using the general equation of state $P = \frac{2}{3}\mathcal{E} + \Delta P$ for the pressure integral gives:

$$\begin{aligned}
\frac{d^2}{dt^2}\frac{\langle \mathbf{r}^2 \rangle}{2} &= \frac{2}{Nm}\int \mathcal{E}\, d^3\mathbf{r} + \langle \mathbf{v}^2 \rangle + \frac{3}{Nm}\int \left(P - \frac{2}{3}\mathcal{E}\right) d^3\mathbf{r} \\
&\quad - \frac{1}{m}\langle \mathbf{r}\cdot\nabla U_{total}\rangle - \frac{3\hbar}{m}\langle \alpha_B \nabla\cdot\mathbf{v}\rangle.
\end{aligned} \qquad (4.99)$$

Further manipulation of this equation is very simple mathematically, but requires extreme care in distinguishing the extinguishable optical potential from the ever present magnetic potential. Because we are looking for an evolution of $\langle \mathbf{r}^2 \rangle$ after release from the optical trap, the above equation proceeds from time $t \geq 0^+$ where the $\mathbf{r}\cdot\nabla U_{total}$ term will abruptly change from U_{total} to U_{mag}. To avoid future confusion in this derivation, we will immediately rewrite Eq. 4.99 as

$$\begin{aligned}
\frac{d^2}{dt^2}\frac{\langle \mathbf{r}^2 \rangle}{2} &= \frac{2}{Nm}\int \mathcal{E}\, d^3\mathbf{r} + \langle \mathbf{v}^2 \rangle + \frac{3}{Nm}\int \left(P - \frac{2}{3}\mathcal{E}\right) d^3\mathbf{r} \\
&\quad - \frac{1}{m}\langle \mathbf{r}\cdot\nabla U_{mag}\rangle - \frac{3\hbar}{m}\langle \alpha_B \nabla\cdot\mathbf{v}\rangle.
\end{aligned} \qquad (4.100)$$

To rewrite the first two terms of this equation, we invoke energy conservation followed by force balance, which requires an equilibrium relationship at $t = 0^-$ just *before* release from the trap. In this situation, U_{total} is the relevant potential energy, not simply U_{mag}.

Beginning this process, we use energy conservation to eliminate $\langle \mathbf{v}^2 \rangle$ from

Eq. 4.100. To do so, we note that just after release there is an initial internal energy per particle given by $\int \mathcal{E}(t = 0^+)d^3\mathbf{r}$ and some initial magnetic potential energy. As time progresses, this internal energy will drop, the stream velocity will increase, and the magnetic potential energy will also increase.

$$\frac{1}{N}\int \mathcal{E}_0\, d^3\mathbf{r} + \langle U_{mag}\rangle_0 = \frac{1}{N}\int \mathcal{E}d^3\mathbf{r} + \frac{1}{2}m\langle \mathbf{v}^2\rangle + \langle U_{mag}\rangle \tag{4.101}$$

$$\frac{2}{Nm}\int \mathcal{E}d^3\mathbf{r} + \langle \mathbf{v}^2\rangle = \frac{2}{Nm}\int \mathcal{E}_0\, d^3\mathbf{r} + \frac{2}{m}\langle U_{mag}\rangle_0 - \frac{2}{m}\langle U_{mag}\rangle. \tag{4.102}$$

We now use force balance to write the initial condition on the pressure which we will relate to $\frac{1}{N}\int \mathcal{E}_0\, d^3\mathbf{r}$ using $\mathcal{E}_0 = \frac{3}{2}P_0 - \frac{3}{2}\Delta P$. The initial condition on the pressure requires $t = 0^-$ *before* release from the trap, where the stream velocity $\mathbf{v} = 0$. Eq. 4.98 then gives the volume integral of the initial pressure as

$$\frac{3}{N}\int P_0\, d^3\mathbf{r} = \langle \mathbf{r}\cdot\nabla U_{total}\rangle_0, \tag{4.103}$$

which depends on U_{total}, not just U_{mag}. When Eq. 4.103 is combined with the general equation of state for the the initial energy and pressure, we have

$$\frac{1}{N}\int \mathcal{E}_0\, d^3\mathbf{r} = \frac{3}{2N}\int P_0\, d^3\mathbf{r} - \frac{3}{2N}\int \left(P - \frac{2}{3}\mathcal{E}\right)_0 d^3\mathbf{r}.$$

$$\frac{1}{N}\int \mathcal{E}_0\, d^3\mathbf{r} = \frac{1}{2}\langle \mathbf{r}\cdot\nabla U_{total}\rangle_0 - \frac{3}{2N}\int \left(P - \frac{2}{3}\mathcal{E}\right)_0 d^3\mathbf{r}$$

$$\frac{2}{Nm}\int \mathcal{E}_0\, d^3\mathbf{r} = \frac{1}{m}\langle \mathbf{r}\cdot\nabla U_{total}\rangle_0 - \frac{3}{Nm}\int \left(P - \frac{2}{3}\mathcal{E}\right)_0 d^3\mathbf{r}. \tag{4.104}$$

Thus, we find $\frac{2}{Nm}\int \mathcal{E}d^3\mathbf{r} + \langle\mathbf{v}^2\rangle$ to be given by

$$\frac{2}{Nm}\int \mathcal{E}d^3\mathbf{r} + \langle\mathbf{v}^2\rangle = \frac{1}{m}\langle\mathbf{r}\cdot\nabla U_{total}\rangle_0$$
$$-\frac{3}{Nm}\int \Delta P_0 \, d^3\mathbf{r} + \frac{2}{m}\langle U_{mag}\rangle_0 - \frac{2}{m}\langle U_{mag}\rangle \qquad (4.105)$$

Inserting these terms into Eq. 4.100 we obtain our central result for $\langle\mathbf{r}^2\rangle$ and the study of scale invariance,

$$\frac{d^2}{dt^2}\frac{\langle\mathbf{r}^2\rangle}{2} = \frac{1}{m}\langle\mathbf{r}\cdot\nabla U_{total}\rangle_0 + \frac{2}{m}\langle U_{mag}\rangle_0 - \frac{2}{m}\langle U_{mag}\rangle - \frac{1}{m}\langle\mathbf{r}\cdot\nabla U_{mag}\rangle$$
$$-\frac{3\hbar}{m}\langle\alpha_B \nabla\cdot\mathbf{v}\rangle + \frac{3}{Nm}\int \Delta P \, d^3\mathbf{r} - \frac{3}{Nm}\int \Delta P_0 \, d^3\mathbf{r}. (4.106)$$

We will write this in a more compact form by defining

$$\langle\mathbf{r}\cdot\nabla U_{total}\rangle_0 = \langle\mathbf{r}\cdot\nabla U_{opt}\rangle_0 + \langle\mathbf{r}\cdot\nabla U_{mag}\rangle_0 \qquad (4.107)$$

$$\Delta U_{mag} \equiv 2\langle U_{mag}\rangle_0 + \langle\mathbf{r}\cdot\nabla U_{mag}\rangle_0 - 2\langle U_{mag}\rangle - \langle\mathbf{r}\cdot\nabla U_{mag}\rangle. \qquad (4.108)$$

Although U_{opt} deviates from purely harmonic behavior at finite energies, U_{mag} does not[6]. Treating U_{mag} as harmonic allows ΔU_{mag} to be equivalently written as:

$$\Delta U_{mag} = 4\langle U_{mag}\rangle_0 - 4\langle U_{mag}\rangle. \qquad (4.109)$$

---

[6]See Chapter 6

Using these definitions, Eq. 4.106 is:

$$\frac{d^2}{dt^2}\frac{m\langle \mathbf{r}^2\rangle}{2} = \langle \mathbf{r}\cdot\nabla U_{opt}\rangle_0 + \frac{3}{N}\int [(\Delta P)-(\Delta P)_0]d^3\mathbf{r} - 3\,\hbar\,\langle \alpha_B\,\nabla\cdot\mathbf{v}\rangle + \Delta U_{mag}.$$

(4.110)

A remarkable property of this result arises for the case of the unitary gas, where $\Delta P = 0$ and $\alpha_B = 0$. Neglecting the effect of the magnetic bowl gives:

$$\frac{d^2}{dt^2}\langle \mathbf{r}^2\rangle = \frac{2}{m}\langle \mathbf{r}\cdot\nabla U_{opt}\rangle_0 \tag{4.111}$$

$$\langle \mathbf{r}^2\rangle = \langle \mathbf{r}^2\rangle_0 + \frac{1}{m}\langle \mathbf{r}\cdot\nabla U_{opt}\rangle_0 t^2 \tag{4.112}$$

for the initial conditions $\langle \mathbf{r}^2\rangle_0$ and $\partial_t\langle \mathbf{r}^2\rangle_0 = 0$. This is exactly the behavior found for the scaling solution of the *non-interacting* gas when the magnetic bowl was neglected. Despite largest possible difference in interaction strengths and aspect ratios demonstrate obviously different dynamics, $\langle \mathbf{r}^2\rangle_0$ behaves in precisely the same way in both the unitary and non-interacting gas. Eq. 4.112 is also completely independent of shear viscosity, indicating momentum conservation: slowing the expansion of one width speeds up the others by the exact amount required to maintain a total radius with quadratic temporal behavior.

It is the scale invariance of the unitary and non-interacting gas which allows the thermodynamic properties of both systems to be expressed in terms of only by only the density and the temperature. It is for this reason that $P = (2/3)\mathcal{E}$ in both regimes, and that $\Delta P = 0$. By requiring scale invariance a more advanced treatment of hydrodynamics, it can also be shown theoretically that $\alpha_B = 0$ of the unitary gas is exactly zero at all temperatures [20]. Therefore, it is the scale invariance of the unitary gas which makes this striking similarity in the behavior

of $\langle \mathbf{r}^2 \rangle_0$ possible. Using Eq. 4.112, it is possible to detune the interactions away from the unitary gas, observe deviations from quadratic temporal behavior, and demonstrate conformal symmetry breaking.

The relation given by Eq. 4.112 also allows for completely arbitrary trapping frequencies; it remains valid even for the optical trap used in the present work that is elliptical in two directions. By simply choosing different combinations of measured widths, we can study shear viscosity through the transverse aspect ratio, or bulk viscosity and scale invariance through the mean square cloud size.

4.7   Validity of a Hydrodynamic Model

For the unitary gas, the above hydrodynamic treatment is valid throughout the superfluid and normal fluid regimes. Even near the superfluid transition temperature, where both a normal fluid and superfluid may be present, the two fluids move together in expansion [44] so that the single fluid model we have thus far assumed is valid. However, for a study of the shear viscosity off resonance, particularly below resonance where a finite molecular fraction can exist, the use of a single fluid model requires additional justification. If the temperature is low enough, dimer molecules can condense into a BEC, and a two fluid model would be required to describe the expansion of the BEC and the uncondensed molecules and atoms surrounding it. We will avoid this complication by working in the normal fluid regime, where a molecular condensate is not observed, and a single fluid description remains applicable.

On the opposite end of the temperature spectrum, a finite molecular fraction below resonance could also cause our hydrodynamic description to become invalid

at high temperatures. In this regime, the gas is becoming more diffuse, lowering its initial density. Not only is the scattering length finite, but the size of the wavevector k is also increasing with temperature, both of which cause a drop in the collisional cross section. All of these factors raise the question of whether the cloud would be better treated as being made up ballistically expanding particles, constituting a failure of hydrodynamics. Within this section, it will be argued that hydrodynamics remains a valid description of the off resonant regimes studied in this dissertation. A few of the necessary relations that follow will be stated without derivation, as their full justification will be given in the following chapter where they are central to the topics discussed.

For a general system, the applicability of hydrodynamics can be characterized by the Knudsen number, K_n, a dimensionless ratio defined to be

$$K_n = \frac{\lambda_{mfp}}{L}, \tag{4.113}$$

where λ_{mfp} is the collisional mean free path, and L is some characteristic length scale of the system under consideration. A small K_n corresponds to good hydrodynamics. For example, if λ_{mfp} is the mean free path of molecules within the lower atmosphere and L is the size of an aircraft, the Knudsen number says that hydrodynamics a valid description of air flowing over a wing.

Assuming that our system below resonance is made up of a normal fluid mixture of atoms and molecules, the cloud will expand as a single fluid if K_n is small for all species present. When constructing a relevant Knudsen number, we assume the worst case for each quantity, that is, the value that would make the Knudsen number the largest. In choosing an appropriate λ_{mfp} to calculate,

we shall note that if a two-component Fermi gas near a Feshbach resonance has a scattering length between spin-up and spin-down atoms given by a, then the molecule-molecule scattering length is given by $0.6a$ [45], while the molecule-atom scattering length is $1.2a$ [46]. We expect a small molecular fraction at high temperature, so molecule-atom collisions are far more probable than those between two molecules. Thus, from the remaining two cross scattering lengths, we choose the smaller atom-atom scattering length to obtain a more conservative estimate of the Knudsen number.

We calculate a mean free path, defined by

$$\lambda_{mfp} = \frac{1}{n_\uparrow \, \sigma} \, , \tag{4.114}$$

where $n_\uparrow = n_0/2$ is the central density in one spin state in a 50-50 mixture. We must first determine a cross section from the scattering length. Here, a conservative estimate would require a *smaller* cross section, so we take σ to be the average *transport* cross section (a comparatively smaller cross section through suppressed forward scattering), used in Ref. [47] to estimate the shear viscosity and denoted by $\bar{\sigma}_{trans}$. To calculate this quantity, we use the s-wave cross section $\sigma(k) = 4\pi a^2/(1 + k^2 a^2)$ and integrate it over a Maxwell-Boltzmann distribution of relative wave vectors k. However, following Ref. [47] this Maxwell-Boltzmann distribution is multiplied by a factor of k^5 to obtain the transport cross section $\sigma_{transpsort}$. Additionally, because the energy in the Boltzmann factor is the relative kinetic energy of two colliding atoms, E is given by $(\hbar k)^2/(2\mu_m)$, where μ_m is the reduced mass given by $\mu_m = m/2$ for two atoms with equal mass m. By including the normalization of this distribution, the transport cross section given

by:

$$\bar{\sigma}_{trans} = \frac{\int_0^\infty \frac{4\pi a}{1+k^2 a^2} e^{-\frac{\hbar^2 k^2}{m k_B T}} 4\pi k^7 dk}{\int_0^\infty e^{-\frac{\hbar^2 k^2}{m k_B T}} 4\pi k^7 dk} \tag{4.115}$$

$$= \frac{2\lambda_T^2}{3} F(q), \tag{4.116}$$

where $\lambda_T = h/\sqrt{2\pi m k_B T}$ is the thermal wavelength, and $F(q) \equiv \frac{1}{2} \int_0^\infty \frac{dy\, y^3\, e^{-y}}{y+q^2}$, with $q = \lambda_T/(|a|\sqrt{2\pi})$. In the limit of low temperature and a finite scattering length, where $\lambda_T >> |a|$, this quantity becomes

$$\bar{\sigma}_{trans} \to \frac{\lambda_T^2}{3} \int_0^\infty \frac{dy\, y^3\, e^{-y}}{q^2} = 4\pi a^2. \tag{4.117}$$

In the resonant case, $F(q) \to \frac{1}{2} \int_0^\infty \frac{dy\, y^3\, e^{-y}}{y} = 1$, so that

$$\bar{\sigma}_{trans} \to \frac{2\,\lambda_T^2}{3}. \tag{4.118}$$

If, on the other hand, we had chosen to calculate the calculate the average resonant cross section $4\pi/k^2$ using a standard Maxwell-Boltzmann distribution with a degneracy factor of $4\pi k^2$, the resonant cross section would be given as

$$\frac{\int_0^\infty \frac{4\pi}{k^2} e^{-\frac{\hbar^2 k^2}{m k_B T}} 4\pi k^2 dk}{\int_0^\infty e^{-\frac{\hbar^2 k^2}{m k_B T}} 4\pi k^2 dk} = 4\,\lambda_T^2. \tag{4.119}$$

This result is a factor of 6 larger than the resonant value of $\bar{\sigma}_{trans}$ given above, which would lead to a smaller Knudsen number if used in its calculation. This indicates that $\bar{\sigma}_{trans}$ is indeed the cross section we want to use in order to conservatively estimate K_n. For an appropriate length scale in K_n, we will take L to be

the smallest diameter of the cloud, $2R_x$, where R_x is the radius of the x-direction. Putting this all together, the Knudsen number for our system is estimated as

$$K_n = 1/\left(\frac{n_0}{2}L\,\bar{\sigma}_{trans}\right).\tag{4.120}$$

The expression for n_0 the initial density at the trap center, will be explicitly derived in Chapter 5 as Eq.5.84. For now, the result is simply stated as

$$n_0 = \frac{E_F^3}{(2\pi)^{3/2}\hbar^3}\frac{3^{1/2}m^{3/2}}{E^{3/2}}.\tag{4.121}$$

Combining this with relations given in Chapter 6, $m\omega_x^2 R_x^2 = 2k_B T$, $E = 3k_B T$, and $E_F = (3N\omega_x\omega_y\omega_z)^{1/3} \equiv k_B T_{FI}$ (Fermi energy of an ideal gas at the trap center), some lengthly but simple algebra gives the Knudsen number at the cloud center, just after release from the trap as:

$$K_n = \frac{\sqrt{\pi}}{2(3N\lambda_x)^{1/3}F(q)}\left(\frac{E}{E_F}\right)^2,\tag{4.122}$$

where $q \equiv \frac{1}{k_{FI}|a|}\sqrt{\frac{6E_F}{E}}$ and $\lambda_x \equiv \omega_y\omega_z/\omega_x^2$. While the above quantity denotes the *intial* Knudsen number, k_{FI} (and therefore q), as well as the Fermi energy are density dependent quantities. As a consequence of the density decrease during expansion, the Knudsen number itself varies with the expansion time of the cloud. For the unitary gas, this actually leads to a decrease in the Knudsen number during expansion, so that the cloud becomes *more* hydrodynamic. In the following chapter, we demonstrate that an *adiabatic approximation* in the expansion of the resonant gas causes the the temperature $T \propto n^{2/3}$, as T/T_F is required to stay constant if entropy to be conserved. Thus, the initial unitary Knudsen number

128

where $q = 0$ and $F(q) = 0$ is

$$K_n(0) = \frac{1}{(n_0/2)\,\sigma}\frac{1}{L} \rightarrow \frac{3}{(n_0)\,2}\frac{1}{\lambda_T^2}\frac{1}{R_x}.$$ (4.123)

We know from Eq.4.121 that $n_0 \propto E_F^3 \propto (n^{2/3})^3$, so that n_0 evolves as $1/\Gamma^2$. The temperature dependence of λ_T dictates that $\lambda_T^2 \propto 1/T \propto n^{-2/3}$, while R_x grows by a factor of b_x during expansion. Thus, for the resonant gas, the Knudsen number decreases during expansion as

$$K_n(t) = \frac{K_n(0)\,\Gamma^{1/3}(t)}{b_x(t)}.$$ (4.124)

In the case of a finite scattering length, the Knudsen number only decreases with expansion initially, but this decrease stops when the temperature drops below a certain value where $\lambda_T > |a|$. As shown above, in this limit the cross section becomes $4\pi a^2$, and then the Knudsen number can only increase as the density decreases. The size of this increase must be quantified in order to justify our hydrodynamic description. To do so, we first assume that the dimer fraction remains constant as the cloud expands, as changing the molecular population requires three-body collisions, which occur with negligible probability during the expansion time. We then plot the time dependent scaling of Eq.4.122 for our highest energy $\widetilde{E}/E_F = 1.6$ in Fig. 4.3. Note the lowest curve showing the unitary gas continuing to become hydrodynamic for longer expansion times. The top two curves are a bit worrisome for a proponent of hydrodynamics, but not only do they represent by far the worst case, hydrodynamics may also still be applicable the behavior of the gas at later times is determined by the early expansion times where the gas is clearly hydrodynamic. We can simulate such a scenario using
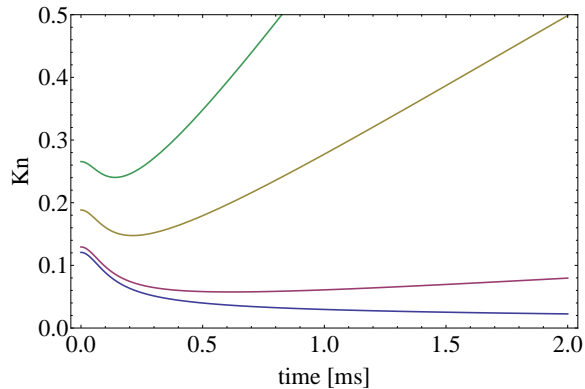
Figure 4.3: Knudsen number at the cloud center as a function of expansion time for different scattering lengths a at an energy $\widetilde{E}/E_F = 1.6$. Curves from top to bottom for $1/(k_{FI}|a|) = 0.9, 0.6, 0.2, 0$, respectively.

the relaxation model given by Eq.4.80 and Eq.4.81. This allows the numerical simulation of a transverse aspect ratio which is hydrodynamic for $t \leq 0.5\,ms$, where it is switched to being non-interacting for all later times. The comparison between such a curve and one that simulates hydrodynamics for all times is given in Fig. 4.4. The difference is negligible. Even in the worst case scenario of hydrodynamics failing at later times, the expansion behavior at all times appears to be determined by the short times where a hydrodynamic description is valid. Moving forward, we can confidently apply the hydrodynamic equations derived thus far to all data which will be presented in this dissertation.
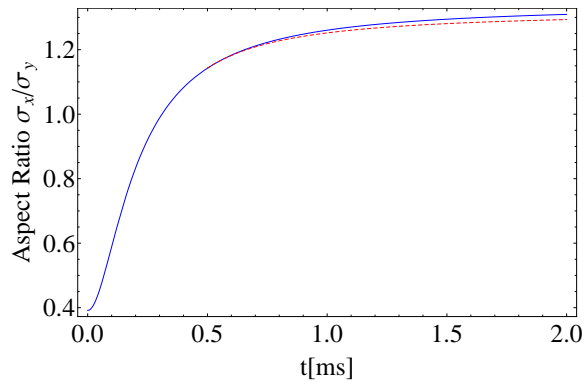
Figure 4.4: Breakdown of hydrodynamic expansion: Aspect ratio versus time for $\widetilde{E}/E_F = 1.6$ where the viscosity coefficient $\alpha_{S0} \simeq 3.0$. Blue solid curve: Hydrodynamic theory; Red dashed curve: Ballistic expansion with initial conditions set by the hydrodynamic theory at 0.5 ms.

Chapter 5

Conformal Symmetry Breaking

A familiar example of a conformally symmetric system, or one without an intrinsic length scale, is a non-interacting ideal gas. If initially confined in a potential U that is extinguished at time $t = 0$ to allow expansion into free space, the ith gas particle with initial position $\mathbf{r}_{i0}$ will have a time dependent position given by a ballistic trajectory $\mathbf{r}_i = \mathbf{r}_{i0} + \mathbf{v}_{i0} t$ so that the mean square radius $\langle \mathbf{r}^2 \rangle = \langle \mathbf{x}^2 \rangle + \langle \mathbf{y}^2 \rangle + \langle \mathbf{z}^2 \rangle$ of the entire gas obeys:

$$\langle \mathbf{r}^2 \rangle = \langle \mathbf{r}^2 \rangle_0 + \langle \mathbf{v}^2 \rangle_0 \, t^2 \tag{5.1}$$

$$\frac{d^2}{dt^2} \frac{m}{2} \langle \mathbf{r}^2 \rangle = \langle \mathbf{r} \cdot \nabla U \rangle_0, \tag{5.2}$$

where the virial theorem for a trapped cloud yields $m\langle \mathbf{v}^2 \rangle_0 = \langle \mathbf{r} \cdot \nabla U \rangle_0$ [21]. In comparison, the expansion of $\langle \mathbf{r}^2 \rangle$ into free space for a general single component hydrodynamic system behaves as (Eq.4.110):

$$\frac{d^2}{dt^2} \frac{m}{2} \langle \mathbf{r}^2 \rangle = \langle \mathbf{r} \cdot \nabla U \rangle_0 + \frac{3}{N} \int [(\Delta P) - (\Delta P)_0] d^3\mathbf{r} - 3\, \hbar \, \langle \alpha_B \, \nabla \cdot \mathbf{v} \rangle \tag{5.3}$$

where $\Delta P = P - \frac{2}{3}\mathcal{E}$ is a change in the equation of state from the ideal (*and unitary*) gas relation $P = \frac{2}{3}\mathcal{E}$ and α_B is the bulk viscosity coefficient. Therefore,

it is through ΔP and α_B that conformal symmetry breaking manifests in the hydrodynamic expansion of the scalar mean square cloud raidus.

To measure either ΔP or α_B as the only free parameter in an expansion experiment, a theory that determines the other is necessary. Alternatively, the size of both can be estimated from a simple model up to a dimensionless coefficient, followed by a simultaneous two parameter fit to data. Towards this end, the determination of ΔP and the trap averaged α_B in terms of measurable quantities are primary results of this chapter. For additional studies of transport properties when scale invariance is broken, a treatment of a general shear viscosity coefficient that includes a dependence on a finite length scale is also presented.

The finite length scale that breaks scale invariance in our system is a_S, the s-wave scattering length. We therefore expect that ΔP should be a function of a_S, in addition to the density and temperature. We shall find this relationship by treating the pressure in the high temperature limit, where the fugacity $z \approx n\lambda_T^3$ is small, n being the density and λ_T is the thermal wavelength. This allows a series expansion of both the pressure and $(2/3)\mathcal{E}$ in either $n\lambda_T^3$ or the fugacity, to determine $\Delta P = P - (2/3)\mathcal{E}$. Proceeding with a fugacity expansion, ΔP will be found in terms of $\partial B_z/\partial T$, where B_2 is the second order expansion coefficient. The value of B_2 can then be related to the s-wave partial wave phase shift of an ultra cold Fermi gas near a Feshbach resonance [48, 49].

Through dimensional analysis, a general form of the viscosity coefficients can also be written as a function of density, temperature, and the scattering length, up to dimensionless constants. For the bulk viscosity, this dimensionless constant has been predicted recently [24], while the shear viscosity will be shown to require two dimensionless coefficients.

Before beginning these derivations, it is worth commenting on the validity of the high temperature limit when applied to experiments on an ultra cold gas. As reasoned in [48], as long as a phase change is avoided, the thermodynamic functions in the high temperature regime are analytically continuations (in T and n) of those in the degenerate regime. With this in mind, we now turn to a high temperature expansion of the equation of state in terms of the fugacity [48].

5.1   Fugacity Expansion of ΔP

The fugacity, defined as $z = e^{\mu/k_B T}$, is found in many different distribution functions in statistical mechanics. When these distributions appear the integrands of averaged quantities, z provides a useful series expansion variable, provided that the temperature is high so that the chemical potential is large and negative. A high temperature expansion up to second order in the fugacity will be our first step in writing an expression for ΔP. Before beginning this process, useful physical insight into the definition of fugacity and its intended use in the calculation of ΔP comes from a simple example.

Consider the pressure for the non-interacting Fermi gas. Beginning with the grand partition function

$$\mathcal{Z} \;=\; e^{-\Omega/k_B T} = \sum_{\text{microstates}} e^{(\mu N - E)/k_B T}, \tag{5.4}$$

$$\tag{5.5}$$

we have that

$$\Omega = -k_B T \ln \mathcal{Z} \;\; = \;\; -k_B T \ln \left(\sum_{\text{microstates}} e^{(\mu N - E)/k_B T} \right), \tag{5.6}$$

where N is the total number of particles in a microstate, $E = E(N)$ is the energy of the microstate, and Ω is the grand potential defined as

$$\Omega = U - TS - \mu N. \tag{5.7}$$

From the Gibbs free energy $G \equiv U + PV - TS = \mu N$, the grand potential is simply $\Omega = U - TS - \mu N = -PV$. For non-interacting fermions, each single-particle state can be treated as an independent thermodynamic system, with possible number $N = 0, 1$ and respective energies $E(N) = 0, \varepsilon$. Since each particle has the same properties, the grand partition function is then expressible as a product so that the grand potential is:

$$P_\uparrow V = k_B T \ln \left(\prod_i \left[1 + e^{(\mu N - \varepsilon_i)/k_B T} \right] \right), \tag{5.8}$$

where $P_\uparrow$ indicates the presence of only one spin component, in this case spin up. If the infinite product over possible energies is brought outside the natural log term, it becomes an infinite sum that can be evaluated as an integral weighted by the appropriate density of states $D(\varepsilon)d\varepsilon = V\,d^3\mathbf{p}/h^3 = (2m)^{3/2} 2\pi \varepsilon^{1/2} V / h^3 d\varepsilon$. This gives the pressure of a one-component non-interacting Fermi gas as:

$$P_\uparrow = k_B T \frac{1}{h^3} (2m)^{3/2} 2\pi \int_0^\infty \ln \left[1 + e^{(\mu - \varepsilon)/k_B T} \right] \varepsilon^{1/2} d\varepsilon, \tag{5.9}$$

Recognizing the factor $z = e^{\mu/k_B T}$ within the integrand, we substitute the fugacity in addition to the change of variables $q = \varepsilon/k_B T$ so that

$$P_\uparrow = \frac{k_B T}{\lambda_T^3} \frac{2}{\sqrt{\pi}} \int_0^\infty \ln\left(1 + z\, e^{-q}\right) q^{1/2} dq, \tag{5.10}$$

where $\lambda_T \equiv \frac{h}{\sqrt{2\pi m k_B T}}$ is the thermal wavelength. By making additional substitutions $v = (2/3)\, q^{3/2}$ and $u = \ln\left(1 + z\, e^{-q}\right)$, we may integrate by parts to get:

$$P_\uparrow = \frac{k_B T}{\lambda_T^3} \frac{2}{\sqrt{\pi}} \frac{2}{3} \int_0^\infty \frac{z\, e^{-q}}{1 + z\, e^{-q}}\, q^{3/2} dq. \tag{5.11}$$

This integral is now expressible in terms of a power series in the fugacity:

$$
\begin{aligned}
P_\uparrow &= \frac{k_B T}{\lambda_T^3} \frac{4}{3\sqrt{\pi}} \int_0^\infty z\, e^{-q} \sum_{l=0}^\infty \left(-z\, e^{-q}\right)^l q^{3/2} dq && (5.12) \\
&= \frac{k_B T}{\lambda_T^3} \frac{4}{3\sqrt{\pi}} \sum_{l=0}^\infty (-1)^l\, z^{l+1} \int_0^\infty e^{-(l+1)q}\, q^{3/2} dq && (5.13) \\
&= \frac{k_B T}{\lambda_T^3} \frac{4}{3\sqrt{\pi}} \sum_{l=0}^\infty (-1)^l\, z^{l+1} \frac{1}{(l+1)^{5/2}} \int_0^\infty e^{-y}\, y^{3/2} dy. && (5.14)
\end{aligned}
$$

In the last line, the substitution $y = (l+1)q$ is made so that the remaining integral is the gamma function $\Gamma(5/2) = \frac{3}{2}\frac{\sqrt{\pi}}{2}$. Thus, we have that the pressure of a single component ideal fermi gas is

$$P_\uparrow = \frac{k_B T}{\lambda_T^3} \sum_{k=0}^\infty \frac{(-1)^{k+1}\, z^k}{k^{5/2}}. \tag{5.15}$$

From this expression for the pressure, the density can be quickly found from the

Gibbs-Duhem relation, $dP = n\,d\mu + s\,dT$, so that

$$n_\uparrow = \left(\frac{\partial P_\uparrow}{\partial \mu}\right)_T = \frac{k_B T}{\lambda_T^3} \sum_{k=0}^{\infty} \frac{(-1)^{k+1}}{k^{5/2}} k\, z^{k-1} \frac{\partial z}{\partial \mu} \tag{5.16}$$

$$= \frac{k_B T}{\lambda_T^3} \sum_{k=0}^{\infty} \frac{(-1)^{k+1}}{k^{5/2}} k\, z^{k-1} \frac{z}{k_B T} \tag{5.17}$$

$$= \frac{1}{\lambda_T^3} \sum_{k=0}^{\infty} \frac{(-1)^{k+1} z^k}{k^{3/2}} . \tag{5.18}$$

In the high temperature limit, the expansion up to second order is:

$$P_\uparrow = \frac{k_B T}{\lambda_T^3} \left(z - \frac{1}{2^{5/2}} z^2\right) = \frac{k_B T}{\lambda_T^3} \left(z - B_2^0 z^2\right) \tag{5.19}$$

$$n_\uparrow = \frac{1}{\lambda_T^3} \left(z - \frac{1}{2^{3/2}} z^2\right) = \frac{1}{\lambda_T^3} \left(z - 2\, B_2^0 z^2\right) . \tag{5.20}$$

The factor of $2^{-5/2}$ in front of the pressure's quadratic fugacity term is defined as *the coefficient B_2^0* for a non-interacting Fermi gas.

In general, the pressure and density can be expanded in the fugacity for any high temperature gas of arbitrary interactions and statistics, defining a *cluster expansion* for the a single species gas in the grand canonical ensemble [49]:

$$\frac{P}{k_B T} = \frac{1}{\lambda_T^3} \sum_{l=1}^{\infty} B_l z^l \tag{5.21}$$

$$n = \frac{1}{\lambda_T^3} \sum_{l=1}^{\infty} l B_l z^l . \tag{5.22}$$

From this definition, a general B_2 represents the lowest order deviation from the behavior of an ideal gas and begins to characterize interactions between particles. It will be the highest order that we concern ourselves with in the present problem,

so that writing ΔP becomes an issue of writing B_2[1]. Note also the first order result of the density, $z = n \lambda_T^3$, indicates that the fugacity estimates the number of particles in a cubic space of edge length λ_T. In the high temperature limit, it is therefore a quantity less than one until the system approaches degeneracy.

Moving away from the example of the non-interacting Fermi gas, we now begin the process of finding B_2 as the first step in writing $\Delta P = P - \frac{2}{3}\mathcal{E}$ for a strongly interacting Fermi gas near a Feshbach resonance. Our experiments do not involve a single spin population, but rather a 50-50 mixture of spin-up and spin-down atoms, so we shall redefine P and n (with no up arrow) to be the total pressure $P = P_\uparrow + P_\downarrow$ and the total density $n = n_\uparrow + n_\downarrow = \frac{\partial P}{\partial \mu}$,

$$P = P_\uparrow + P_\downarrow = \frac{2\,k_B T}{\lambda_T^3}\left(z - B_2 z^2\right) \tag{5.23}$$

$$n = n_\uparrow + n_\downarrow = \frac{2}{\lambda_T^3}\left(z - 2B_2 z^2\right). \tag{5.24}$$

We may write the energy density $\mathcal{E} = U/V$ and divide the grand potential $\Omega = -PV = U - TS - \mu N$ by volume to arrive at:

$$\mathcal{E} = Ts + \mu n - P, \tag{5.25}$$

where s is the entropy density. Thus, to find $\mathcal{E}$ we must first find the entropy density and the chemical potential from the pressure.

Returning to the Gibbs-Duhem relation, $dP = n\,d\mu + s\,dT$, we may find s from the derivative of the pressure, Eq.5.23, with respect to temperature at fixed

---

[1] B_2 is sometimes defined as the expansion coefficient for the second order density [50, 51], not the fugacity. This definition is arbitrary, especially up to second order, where it can be shown for $\frac{P}{kTn} = \sum_{l=1}^{\infty} A_l(T)(n\lambda_T^3)^{l-1}$ and $\frac{P}{k_B T} = \frac{1}{\lambda_T^3}\sum_{l=1}^{\infty} B_l z^l$ that $B_2 = -A_2$ [2]

138

μ, where z, λ_T and B_2 are temperature dependent. This gives

$$
\begin{aligned}
s &= \left(\frac{\partial P}{\partial T}\right)_\mu = \frac{5}{2}\frac{P}{T} + \frac{2k_B T}{\lambda_T^3}\frac{\partial}{\partial T}(z - B_2 z^2)\Big|_\mu \\
&= \frac{5}{2}\frac{P}{T} + \frac{2k_B T}{\lambda_T^3}(1 - 2B_2 z)\left(\frac{\partial z}{\partial T}\right)\Big|_\mu - \frac{2k_B T}{\lambda_T^3}z^2\frac{\partial B_2}{\partial T}.
\end{aligned}
\tag{5.26}
$$

From the definition of $z = e^{\mu/k_B T}$, we have $\frac{\mu}{k_B T} = \ln(z)$, and

$$
\left(\frac{\partial z}{\partial T}\right)_\mu = -\frac{\mu}{k_B T^2}e^{\mu/k_B T} = -\frac{z}{T}\ln(z).
\tag{5.27}
$$

Using this result and the full expression for P in s gives:

$$
\begin{aligned}
s &= \frac{5}{2}\frac{P}{T} - \frac{2k_B}{\lambda_T^3}(1 - 2B_2 z)\, z \ln(z) - \frac{2k_B T}{\lambda_T^3}z^2\frac{\partial B_2}{\partial T} \tag{5.28} \\
&= \frac{5}{2}\frac{2k_B}{\lambda_T^3}(z - B_2 z^2) - \frac{2k_B}{\lambda_T^3}(z - 2B_2 z^2)\ln(z) - \frac{2k_B T}{\lambda_T^3}z^2\frac{\partial B_2}{\partial T} \tag{5.29}
\end{aligned}
$$

Noting the relation $\frac{n\lambda_T^3}{2} = z - 2B_2 z^2$ from Eq. 5.24, we make the substitution

$$
\begin{aligned}
z - B_2 z^2 &= z - 2B_2 z^2 + B_2 z^2 \tag{5.30} \\
z - B_2 z^2 &\simeq \frac{n\lambda_T^3}{2} + B_2\left(\frac{n\lambda_T^3}{2}\right)^2 + O\left(\left(n\lambda_T^3\right)^3\right), \tag{5.31}
\end{aligned}
$$

139

so that:

$$
\begin{aligned}
s &= \frac{5}{2}\frac{2k_B}{\lambda_T^3}\left(\frac{n\lambda_T^3}{2}+B_2 z^2\right) - k_B n \ln(z) - \frac{2k_B T}{\lambda_T^3} z^2 \frac{\partial B_2}{\partial T} \\
&= \frac{5}{2}\frac{2k_B}{\lambda_T^3}\left[\frac{n\lambda_T^3}{2}+B_2\left(\frac{n\lambda_T^3}{2}\right)^2\right] - k_B n \ln(z) - \frac{2k_B T}{\lambda_T^3}\left(\frac{n\lambda_T^3}{2}\right)^2 \frac{\partial B_2}{\partial T} \\
&= \frac{5}{2}k_B n\left[1+B_2\left(\frac{n\lambda_T^3}{2}\right)\right] - k_B n \ln\left(\frac{n\lambda_T^3}{2}+2B_2 z\right) - \frac{2k_B T}{\lambda_T^3}\left(\frac{n\lambda_T^3}{2}\right)^2 \frac{\partial B_2}{\partial T} \\
&= \frac{5}{2}k_B n + \frac{5}{4}k_B n B_2(n\lambda_T^3) - k_B n \ln\left(\frac{n\lambda_T^3}{2}\right) - 2k_B n B_2\left(\frac{n\lambda_T^3}{2}\right) - \frac{2k_B T}{\lambda_T^3}\left(\frac{n\lambda_T^3}{2}\right)^2 \frac{\partial B_2}{\partial T} \\
&= \frac{5}{2}k_B n + \frac{1}{4}k_B n B_2(n\lambda_T^3) - k_B n \ln(n\lambda_T^3) + k_B n \ln(2) + \frac{1}{2}k_B n T\,(n\lambda_T^3)\frac{\partial B_2}{\partial T} \\
&= k_B n\left[\frac{5}{2}+\ln(2)-\ln(n\lambda_T^3)\right] + k_B n\left(\frac{B_2}{4}-T\frac{\partial B_2}{\partial T}\frac{1}{2}\right)(n\lambda_T^3) \qquad (5.32)
\end{aligned}
$$

where $\ln(z) \simeq \ln(n\lambda_T^3/2 + 2B_2 z^2) \approx \ln(n\lambda_T^3/2) + 2B_2 z^2 2/n\lambda_T^3 = \ln(n\lambda_T^3/2) + 2B_2(n\lambda_T^3/2)$. The first term is now the familiar Sackur-Tetrode result, while the second term is the B_2 dependent correction.

The chemical potential is found using

$$
\mu/k_B T = \ln(z) = \ln(n\lambda_T^3/2) + 2B_2(n\lambda_T^3/2), \qquad (5.33)
$$

so that results for the entropy density and chemical potential can be inserted into Eq 5.25 to complete our B_2 dependent derivation for the energy density, $\mathcal{E}(n,T)$:

$$
\mathcal{E} = \frac{3}{2}n k_B T\left\{1+(n\lambda_T^3)\left[\frac{B_2}{2}-\frac{1}{3}T\frac{\partial B_2}{\partial T}\right]\right\}. \qquad (5.34)
$$

The pressure itself is given by Eq.5.23, which can be written in terms of the

140

density

$$P \ = \ \frac{2\,k_B T}{\lambda_T^3}\,(z - B_2 z^2) \tag{5.35}$$

$$P \ = \ \frac{2\,k_B T}{\lambda_T^3}\left[\frac{n\lambda_T^3}{2} - B_2\left(\frac{n\lambda_T^3}{2}\right)^2\right] \tag{5.36}$$

$$P \ = \ n k_B T\left(1 - \left(n\lambda_T^3\right)\frac{B_2}{2}\right), \tag{5.37}$$

so that we finally obtain ΔP,

$$\Delta P = P - \frac{2}{3}\mathcal{E} = \frac{1}{3}n k_B T\left(T\,\frac{\partial B_2}{\partial T}\right)(n\lambda_T^3). \tag{5.38}$$

We see that ΔP vanishes unless B_2 is temperature dependent.

5.2 Calculation of B_2

The above form of ΔP does not yet contain an obvious dependence on the scattering length, which must therefore be contained in B_2. Reference [48] gives an explicit expression for the second cluster expansion coefficient of a two component Fermi gas near a Feshbach resonance. However, with different forms of B_2 floating around the literature based on arbitrary factors in the expansion, we need to first check consistency between our definitions. Reference [48] defines the density for a two-component Fermi gas up to second order in the fugacity as:

$$n = \frac{2}{\lambda_T^2}(z - 2^{-3/2}z^2 + 2\sqrt{2}\,b_2 z^2). \tag{5.39}$$

In our notation, the density for a two component, non-interacting Fermi gas was defined by Eq.5.24 be:

$$n = \frac{2}{\lambda_T^2}(z - 2^{-3/2}z^2) = \frac{2}{\lambda_T^2}(z - 2B_2^0 z^2). \tag{5.40}$$

Thus, [48] uses b_2 to distinguish the general second order expansion in fugacity from the second order fugacity of the non-interacting Fermi gas. We need only recognize that

$$B_2 = 2^{-5/2} - \sqrt{2}\, b_2 \tag{5.41}$$

to write ΔP in the notation of Reference [48] as:

$$\Delta P = -\frac{\sqrt{2}}{3} n k_B T \left(T \frac{\partial b_2}{\partial T} \right) (n\lambda_T^3). \tag{5.42}$$

Reference [48] then gives b_2 as:

$$b_2 = \sum_b e^{|E_b|/k_B T} + \sum_l \gamma_l \int_0^\infty \frac{dk}{\pi} \frac{d\delta_l(k)}{dk} e^{-\frac{\hbar^2 k^2}{m K_B T}} \gamma_l \tag{5.43}$$

where E_b is the energy of the two body (molecular) bound state, $\gamma_l = 2l + 1$ and $\delta_l(k)$ is the lth partial wave phase shift. For s-wave scattering where $l = 0$,

$$b_2 = \sum_b e^{|E_b|/k_B T} + \int_0^\infty \frac{dk}{\pi} \frac{d\delta_0(k)}{dk} e^{-\frac{\hbar^2 k^2}{m K_B T}}. \tag{5.44}$$

The scattering length will then enter into b_2 through the bound state energy and the derivative of the phase shift. From the definition of the s-wave phase

scattering length in terms of the s-wave phase shift, Eq.2.14, we have

$$\delta_0(k) = -\tan^{-1}(ka_s) \tag{5.45}$$

$$\frac{\partial \delta_0(k)}{\partial k} = -\frac{a_s}{1 + k^2 a_s^2}. \tag{5.46}$$

Since a bound state only exists on the BEC side of resonance where the scattering length is positive, we will place a heaviside theta function $\Theta[a]$ in front of the Σ_b term, indicating that this contribution should be zero when the scattering length is negative and no bound state is present. Additionally, we are only interested in one singlet bound state, which is responsible for the Feshbach resonance. Hence, there should be only one term in the Σ_b summation, with binding energy given by $E_b = \hbar^2/m\,a_s^2$. Last, the function $a_s = -sign[a_s]\mid a_s\mid$ will also be placed in front of the integral, accounting for the odd function of a_s in the integrand. This will yield a single compact expression applicable to both the BEC and BCS side in the form of

$$b_2 = \Theta(a_s)\, e^{\frac{\hbar^2}{m\,a_s^2 k_B T}} - sign(a_s)\frac{1}{\pi}\int_0^\infty \frac{\mid a_s\mid}{1 + k^2 a_s^2} e^{-\frac{\hbar^2 k^2}{m k_B T}} dk. \tag{5.47}$$

Since

$$\lambda_T = \frac{h}{\sqrt{2\pi m k_B T}} = \sqrt{2\pi}\sqrt{\frac{\hbar^2}{m k_B T}}, \tag{5.48}$$

We will make the substitution

$$\frac{\hbar^2}{m k_B T} = \frac{\lambda_T^2}{2\pi} \tag{5.49}$$

143

so that

$$b_2 = \Theta(a_s) \, e^{\frac{\lambda_T^2}{2\pi a_s^2}} - sign(a_s) \frac{1}{\pi} \int_0^\infty \frac{\mid a_s \mid}{1 + k^2 a_s^2} \, e^{-\frac{\lambda_T^2 k^2}{2\pi}} \, dk. \tag{5.50}$$

The integral is evaluated with a change of variables $q = k \mid a_s \mid \geq 0$,

$$b_2 = \Theta(a_s) \, e^{\lambda_T^2/2\pi a_s^2} - sign(a_s) \frac{1}{\pi} \int_0^\infty \frac{1}{1 + q^2} \, e^{\frac{-\lambda_T^2 q^2}{2\pi a_s^2}} \, dq. \tag{5.51}$$

Using

$$x = \frac{\lambda_T}{\sqrt{2\pi} \mid a_s \mid}, \tag{5.52}$$

we have

$$b_2(x) = \Theta(a_s) \, e^{x^2} - sign(a_s) F(x), \tag{5.53}$$

where

$$F(x) = \frac{1}{\pi} \int_0^\infty \frac{1}{1 + q^2} \, e^{-x^2 q^2} \, dq. \tag{5.54}$$

The integral $F(x)$ can be evaluated to give:

$$F(x) = \frac{e^{x^2}}{2} [1 - \mathrm{erf}(\mid x \mid)], \tag{5.55}$$

where erf(x) is the error function, $\mathrm{erf}(x) = \frac{2}{\sqrt{\pi}} \int_0^x e^{-t^2} dt$. Thus,

$$b_2(x) \;=\; e^{x^2} \Theta(a_s) - \frac{sign(a_s)}{2} e^{x^2} [1 - \mathrm{erf}(\mid x \mid)] \tag{5.56}$$

144

where $x = \frac{\lambda_T}{|a_s|\sqrt{2\pi}}$, as defined in Eq.5.52.

5.3   Evaluation of $\frac{1}{N}\int \Delta P\, d^3\mathbf{r}$

Having have found an expression for b_2 and hence ΔP, we need only evaluate the volume integrals of ΔP that appear in our hydrodynamic equations and relate the result to experimentally convenient quantities. Thus, this section will derive an expression for

$$\frac{1}{N}\int \Delta P\, d^3\mathbf{r} = -\frac{1}{N}\int \frac{\sqrt{2}}{3} n k_B T \left(T\frac{\partial b_2}{\partial T}\right)(n\lambda_T^3)\, d^3\mathbf{r}, \tag{5.57}$$

where we have used Eq 5.42 for ΔP. Treating our atomic cloud as having a uniform temperature and scattering length, the only spatially varying contribution to the volume integral is the density. Eq.5.57 is then

$$\frac{1}{N}\int \Delta P\, d^3\mathbf{r} = -\frac{2\sqrt{2}}{3} k_B T \left(T\frac{\partial b_2}{\partial T}\right)\frac{1}{N}\int n\left(\frac{n\lambda_T^3}{2}\right) d^3\mathbf{r}. \tag{5.58}$$

From the lowest order of the series for z given in equation Eq.5.24, $n\lambda_T^3/2$ is the fugacity so that

$$\bar{z} = \frac{1}{N}\int n\left(\frac{n\lambda_T^3}{2}\right) d^3\mathbf{r} \tag{5.59}$$

is the *trap averaged fugacity*. To evaluate $\bar{z}$, we assume a three dimensional gaussian density, the shape most appropriate for the high temperature limit we

have assumed:

$$n = n(\mathbf{r}, t) = \frac{N}{\pi^{3/2}\sigma_x(t)\,\sigma_y(t)\,\sigma_z(t)} \exp\left[-\frac{x^2}{\sigma_x^2(t)} - \frac{y^2}{\sigma_y^2(t)} - \frac{z^2}{\sigma_z^2(t)}\right], \quad (5.60)$$

Here $\sigma_i(t)$ is the $1/e$ width in the ith direction and t is the expansion time. As discussed in Chapter4, these time dependent widths are related to their initial values through the expansion factors $b_i(t)$ so that $\sigma_i(t) = b_i(t)\,\sigma_i(0)$. The trap averaged fugacity is then:

$$
\begin{aligned}
\bar{z} &= \frac{1}{N}\int n\left(\frac{n\lambda_T^3}{2}\right)d^3\mathbf{r} \\
&= \frac{\lambda_T^3}{2N}\left(\frac{N}{\pi^{3/2}\sigma_x(t)\,\sigma_y(t)\,\sigma_z(t)}\right)^2 \int_{-\infty}^{\infty}\exp\left[-\frac{2x^2}{\sigma_x^2(t)} - \frac{2y^2}{\sigma_y^2(t)} - \frac{2z^2}{\sigma_z^2(t)}\right]d^3\mathbf{r} \\
&= \frac{\lambda_T^3}{2N}\left(\frac{N}{\pi^{3/2}\sigma_x(t)\,\sigma_y(t)\,\sigma_z(t)}\right)^2 \left(\frac{\pi}{2}\right)^{3/2}\sigma_x(t)\,\sigma_y(t)\,\sigma_z(t) \\
&= \frac{\lambda_T^3}{2^{5/2}}\frac{N}{\pi^{3/2}\sigma_x(t)\,\sigma_y(t)\,\sigma_z(t)}\,.
\end{aligned}
\quad (5.61)
$$

The widths appearing in $\bar{z}$ are not the only quantities in ΔP that vary with expansion time. The temperature, which explicitly appears in the expression for ΔP as well as entering $\bar{z}$ through the thermal wavelength, also changes during expansion. Since ΔP is a small perturbation to the unitary gas equation of state $P = (2/3)\mathcal{E}$, we shall evaluate ΔP with the approximation that the temperature evolves *adiabatically* and write the associated entropy density using assumptions applicable to the unitary gas. Invoking the same dimensional arguments used to write the entropy per particle of the unitary gas in Eq.4.16, we write the entropy

ΔS of a small volume ΔV that contains ΔN atoms as:

$$\Delta S = \Delta N k_B f_S \left[\frac{T}{T_F(n)} \right], \tag{5.62}$$

where f_S is a dimensionless function of density and temperature, and the temperature is scaled by the local Fermi temperature $T_F(n)$. For ΔS to remain constant, $T/T_F(n)$ must be constant and $T \propto n^{2/3}$. Since the time dependent density decreases with expansion time as $n(t) = n(0)/\Gamma(t)$ where $\Gamma(t) = b_x(t) \, b_y(t) \, b_z(z)$ is the volume scale factor, the temperature evolves as $T = T_0 \, \Gamma(t)^{-2/3}$, where T_0 is the initial in-trap temperature.

The thermal wavelength is $\lambda_T \propto T^{-1/2}$, so it is related to an initial value by

$$\lambda_T = \lambda_{T0} \, \Gamma(t)^{1/3}. \tag{5.63}$$

The expansion time dependence of λ_T provides the missing relation needed to write $\bar{z}$ during expansion in terms of an initial value. When this is done, we find that

$$\bar{z} \; = \; \frac{\lambda_T^3}{2^{5/2}} \frac{N}{\pi^{3/2} \sigma_x(t) \, \sigma_y(t) \, \sigma_z(t)} \tag{5.64}$$

$$= \; \frac{\lambda_{T0}^3 \, \Gamma(t)}{2^{5/2}} \frac{N}{\pi^{3/2} \, \Gamma(t) \, \sigma_x(0) \, \sigma_y(0) \, \sigma_z(0)} \tag{5.65}$$

$$= \; \frac{\lambda_{T0}^3}{2^{5/2}} \frac{N}{\pi^{3/2} \, \sigma_x(0) \, \sigma_y(0) \, \sigma_z(0)} \tag{5.66}$$

$$= \; \frac{\lambda_{T0}^3}{2^{5/2}} \, n_0 \,, \tag{5.67}$$

where $n_0 = \frac{N}{\pi^{3/2} \, \sigma_x(0) \, \sigma_y(0) \, \sigma_z(0)}$, the initial density at the trap center. This result indicates that $\bar{z}$ is an adiabatic invariant, independent of the expansion time under

the assumption that the temperature evolves adiabatically after release from the trap.

The variable within b_2 that we have defined to be $x \equiv \frac{\lambda_T}{|a_s|\sqrt{2\pi}}$ is also related to the thermal wavelength and therefore the temperature. Since $x \sim \lambda_T \sim T^{-1/2}$, x will be related to an initial x_0 by

$$x = x_0 \Gamma(t)^{1/3} \tag{5.68}$$

$$x_0 \equiv \frac{\lambda_{T_0}}{|a_s|\sqrt{2\pi}} \tag{5.69}$$

$$\lambda_{T0} = \frac{h}{\sqrt{2\pi m k_B T_0}}. \tag{5.70}$$

We also note that the temperature dependence of b_2 through x gives the quantity $T\frac{\partial b_2}{\partial T} = T\frac{\partial b_2(x)}{\partial T}$ in ΔP. Using $\frac{dx}{dT} = -\frac{1}{2}\frac{x}{T}$

$$T\frac{\partial b_2(x)}{\partial T} = T\frac{dx}{dT}b_2'(x) \tag{5.71}$$

$$= -\frac{x}{2}b_2'(x). \tag{5.72}$$

Combining these results for $\bar{z}$ with the time evolution of the temperature, the volume integral of ΔP, Eq.5.58 is

$$\frac{1}{N}\int \Delta P\, d^3\mathbf{r} = -\frac{2\sqrt{2}}{3}k_B T\left(T\frac{\partial b_2}{\partial T}\right)\frac{1}{N}\int n\left(\frac{n\lambda_T^3}{2}\right)d^3\mathbf{r} \tag{5.73}$$

$$= \frac{\sqrt{2}}{3}\frac{k_B T_0}{\Gamma(t)^{2/3}}x\, b_2'(x)\frac{\lambda_{T0}^3}{2^{5/2}}n_0. \tag{5.74}$$

In place of an initial temperature, we prefer to work in terms of an initial energy, which can be found directly from an initial cloud size. Since ΔP is perturbation to $(2/3)\mathcal{E}$, in order to estimate T_0 in the high temperature limit, we

148

can take the initial pressure $P_0(\mathbf{r}) \approx n k_B T_0$. Prior to expansion of the atomic cloud, force balance relates the density of the atomic cloud within the potential U_{total} to the initial pressure via Eq.4.62:

$$3 \int P_0(\mathbf{r}) d^3\mathbf{r} = \int n(\mathbf{r}) \mathbf{r} \cdot \nabla U_{total}(\mathbf{r}) d^3\mathbf{r} \tag{5.75}$$

$$3 k_B T_0 \int n(\mathbf{r}) d^3\mathbf{r} = \int n(\mathbf{r}) \mathbf{r} \cdot \nabla U_{total}(\mathbf{r}) d^3\mathbf{r} \tag{5.76}$$

$$3 k_B T_0 N = \int n(\mathbf{r}) \mathbf{r} \cdot \nabla U_{total}(\mathbf{r}) d^3\mathbf{r} \tag{5.77}$$

$$3 \, k_B T_0 = \langle \mathbf{r} \cdot \nabla U_{total} \rangle_0 \tag{5.78}$$

Having defined $\widetilde{E} = \langle \mathbf{x} \cdot \nabla U_{total} \rangle_0$, the initial temperature is approximated by

$$\frac{k_B T_0}{E_F} = \frac{1}{3} \frac{\widetilde{E}}{E_F}, \tag{5.79}$$

where E_F is the Fermi energy, allowing us to work in dimensionless units by introducing a natural energy scale.

The Fermi energy is also related to k_{FI}, the Fermi wave vector of an ideal gas at the trap center, by

$$\frac{(\hbar \, k_{FI})^2}{2m} = E_F. \tag{5.80}$$

k_{FI} shall be used as scale of inverse length to make a dimensionless quantity when multiplying the s-wave scattering length a_s that appears in $x = \frac{\lambda_{T_0}}{|a_s|\sqrt{2\pi}} \Gamma(t)^{1/3}$ so that

$$x_0 = \frac{\lambda_{T_0}}{|\, a_s \,| \, \sqrt{2\pi}} = \frac{\hbar}{|\, a_s \,| \, \sqrt{m \, k_B T_0}} \frac{k_{FI}}{k_{FI}} = \frac{\sqrt{6}}{|\, k_{FI} \, a_s \,|} \left(\frac{E_F}{\widetilde{E}} \right)^{1/2}, \tag{5.81}$$

where $k_{FI} = |k_{FI}|$ is always positive.

Further simplification of $\frac{1}{N} \int \Delta P \, d^3\mathbf{r}$ will come from also writing n_0, the initial density of the trap center, in terms of $\widetilde{E}/E_F$. We will start by relating the in trap widths $\sigma_i(0)$ to E_{harm}, the total energy per particle in the harmonic unitary case Eq.6.16,

$$
\begin{aligned}
E_{harm} &\equiv 3m\omega_x^2 \langle x^2 \rangle_0 = 3m\omega_y^2 \langle y^2 \rangle_0 = 3m\omega_z^2 \langle z^2 \rangle_0 &\text{(5.82)}\\
&= 3m\omega_x^2 \frac{\sigma_x(0)^2}{2} = 3m\omega_y^2 \frac{\sigma_y(0)^2}{2} = 3m\omega_z^2 \frac{\sigma_z(0)^2}{2}. &\text{(5.83)}
\end{aligned}
$$

Note also $E_{harm} = \widetilde{E}$ for the unitary gas in a harmonic trap [52]. We shall use the $E_{harm} = \widetilde{E}$ relation here also, again applying unitary relations to the correction to the unitary equation of state that ΔP defines. This allows n_0 to be written as:

$$
\begin{aligned}
n_0 &= \frac{N}{\pi^{3/2}\,\sigma_x(0)\,\sigma_y(0)\,\sigma_z(0)} \\
&= \frac{N}{\pi^{3/2} \left(\frac{2\widetilde{E}}{3m\,\omega_x^2}\right)^{1/2} \left(\frac{2\widetilde{E}}{3m\,\omega_y^2}\right)^{1/2} \left(\frac{2\widetilde{E}}{3m\,\omega_z^2}\right)^{1/2}} \\
&= \frac{N\, 3^{3/2}\, m^{3/2} \omega_x\, \omega_y\, \omega_z}{(2\pi)^{3/2}\,\widetilde{E}^{3/2}} \\
&= \frac{(3\,N\,\omega_x\,\omega_y\,\omega_z\,\hbar^3)3^{1/2}\, m^{3/2}}{(2\pi)^{3/2}\hbar^3\,\widetilde{E}^{3/2}} \\
n_0 &= \frac{E_F^3}{(2\pi)^{3/2}\hbar^3}\frac{3^{1/2}m^{3/2}}{\widetilde{E}^{3/2}}, &\text{(5.84)}
\end{aligned}
$$

where we have used $E_F \equiv (3N)^{1/3}\hbar\,\omega_x\,\omega_y\,\omega_z$. With this relationship for n_0, the

trap averaged fugacity is given by

$$
\begin{aligned}
\bar{z} &= \frac{1}{2^{5/2}} n_0 \lambda_{T0}^3 \\
&= \frac{9}{4\sqrt{2}} \left(\frac{E_F}{\widetilde{E}} \right)^3 \left(\frac{\widetilde{E}}{3k_B T_0} \right)^{3/2} \\
\bar{z} &= \frac{9}{4\sqrt{2}} \left(\frac{E_F}{\widetilde{E}} \right)^3,
\end{aligned}
\tag{5.85}
$$

where we have used $\widetilde{E}/3k_B T_0 = 1$ in the high temperature limit.

With the above expressions for n_0 and T_0 in terms of $\widetilde{E}$ we arrive at the primary result of this section for the volume integral of ΔP:

$$
\frac{1}{N} \int \Delta P \, d^3\mathbf{r} = \frac{\widetilde{E}}{\Gamma^{1/3}} \frac{\sqrt{6}}{4} \left(\frac{E_F}{\widetilde{E}} \right)^{7/2} \frac{1}{\mid k_{FI} a \mid} b_2'(x). \tag{5.86}
$$

It is now simply a matter of inserting $b_2{'}(x)$ into this result to obtain the ΔP dependent terms in the equations for the scaling solution and $\langle \mathbf{r}^2 \rangle$.

For additional studies of expansion dynamics when the scattering length is finite, Chapter 4 derives not only the effect of ΔP on $\langle \mathbf{r}^2 \rangle$, but also the scaling solution in terms of the expansion factors $b_i(t)$. We now restate the two ΔP dependent terms found in the scaling solution, Eq. 4.74 and Eq. 4.74, in addition to the single ΔP dependent term in the $\langle \mathbf{r}^2 \rangle$ equation, Eq. 4.112, given respectively by:

$$
C_F(t) - C_F(0) \equiv \frac{\Gamma^{2/3}(t) \frac{3}{N} \int \Delta P \, d^3\mathbf{r}}{\langle \mathbf{r} \cdot \nabla U_{total} \rangle_0} - \frac{\frac{3}{N} \int \Delta P_0 \, d^3\mathbf{r}}{\langle \mathbf{r} \cdot \nabla U_{total} \rangle_0} \tag{5.87}
$$

$$
C_p(t) \equiv \frac{2 \int_1^{\Gamma(t)} \frac{d\Gamma}{\Gamma^{1/3}} \frac{1}{N} \int \Delta P \, d^3\mathbf{r}}{\langle \mathbf{r} \cdot \nabla U_{total} \rangle_0} \tag{5.88}
$$

151

and

$$\frac{3}{N} \int [\Delta P - \Delta P_0] \, d^3\mathbf{r}. \tag{5.89}$$

When all three of these terms are inspected together, it is found that they all depend not on ΔP, but rather on the *difference* between ΔP and an initial ΔP_0. Thus, any static contribution to ΔP has no effect on any of these terms.

Ignoring the static parts of ΔP allows further simplification of Eq. 5.86 through manipulation of $b_2(x)$, given by Eq. 5.56:

$$b_2(x) = e^{x^2}\Theta(a_s) - \frac{-sign(a_s)}{2} \, e^{x^2}[1 - \text{erf}(\mid x \mid)] \tag{5.90}$$

where the first term depends on a Boltzmann factor with a molecular state binding energy for $a_s > 0$, giving a heaviside theta function. There is no molecular contribution for $a_s < 0$. This molecular term also contains a temperature, which the careful reader may expect to adiabatically evolve according to $T = T_0 \Gamma(t)^{-2/3}$. As $\Gamma(t)$ increases with time, this would cause the factor $e^{x^2} = e^{|E_b|/k_B T}$ to diverge at longer times. However, this Boltzmann factor, by definition, must also be related to the molecular population, or simply the probability of a molecule being present. In order for the molecular population to change, three body or higher order interactions are necessary. As the probability of these interactions are vanishingly small during the ms time scale of the expansion, it will be assumed that the molecular term does not change from its initial value, and need not be considered in a calculation of $\Delta P - \Delta P_0$. For our purposes, we therefore

approximate:

$$b_2(x) \simeq -\frac{sign(a_s)}{2} e^{x^2} \mathrm{erfc}(x) \tag{5.91}$$

$$b_2{}'(x) \simeq sign(a_s) \left(\frac{1}{\sqrt{\pi}} - x\, e^{x^2} \mathrm{erfc}(x) \right), \tag{5.92}$$

where $\mathrm{erfc}(x) \equiv 1-\mathrm{erf}(x)$. We note in Eq. 5.86 that $sign(a_s)/ \mid k_{FI}\, a_s \mid = 1/k_{FI}\, a_s$.
By defining

$$b_2{}'(x) = sign(a_s) f_2{}'(x) \tag{5.93}$$

$$f_2{}'(x) = \frac{1}{\sqrt{\pi}} - x\, e^{x^2} \mathrm{erfc}(x). \tag{5.94}$$

The first two ΔP dependent terms given above are then:

$$C_F(t) \equiv \frac{\Gamma^{2/3}(t)\frac{3}{N}\int \Delta P\, d^3\mathbf{r}}{\widetilde{E}} = \frac{3\sqrt{6}}{4}\left(\frac{E_F}{\widetilde{E}}\right)^{7/2}\frac{1}{k_{FI}\, a_s}\Gamma^{2/3}\, f_2'(x) \tag{5.95}$$

$$C_F(0) \equiv \frac{\frac{3}{N}\int \Delta P_0\, d^3\mathbf{r}}{\widetilde{E}} = \frac{3\sqrt{6}}{4}\left(\frac{E_F}{\widetilde{E}}\right)^{7/2}\frac{1}{k_{FI}\, a_s}\, f_2'(x_0). \tag{5.96}$$

$C_p(t)$ is slightly more involved, requiring the evaluation of an integral over $\Gamma(t)$,

$$C_p(t) \equiv \frac{2\int_1^{\Gamma(t)}\frac{d\Gamma}{\Gamma^{1/3}}\frac{1}{N}\int \Delta P\, d^3\mathbf{r}}{\widetilde{E}} \tag{5.97}$$

$$= \frac{2\sqrt{6}}{4}\left(\frac{E_F}{E}\right)^{7/2}\frac{1}{k_{FI}a}\int_1^{\Gamma(t)}\frac{1}{\Gamma^{2/3}}f_2{}'(x)\, d\Gamma. \tag{5.98}$$

Using the expression for the time dependence of x given by $x = x_0\Gamma^{-2/3}$, we substitute x with the dummy variable x' so that this integral evaluates to

$$\frac{3}{x_0}\int_{x_0}^{x} f_2{}'(x')dx' = \frac{3}{x_0}[f_2(x) - f_2(x_0)], \tag{5.99}$$

153

yielding

$$C_p(t) = \frac{3}{2} \left(\frac{E_F}{E} \right)^3 [f_2(x) - f_2(x_0)]. \tag{5.100}$$

Finally, for the ΔP dependent term in the $\langle \mathbf{r}^2 \rangle$ equation, we have that:

$$\frac{3}{N} \int [\Delta P - \Delta P_0] \, d^3 \mathbf{r}$$

$$= \frac{\widetilde{E}}{m} \frac{3\sqrt{6}}{4} \left(\frac{E_F}{\widetilde{E}} \right)^{7/2} \frac{1}{k_{FI} \, a_s} [\Gamma^{-1/3} f_2{}'(x) - f_2{}'(x_0)]. \tag{5.101}$$

In closing, note that $f(x)$ is an even function of x, and therefore an even function of a_S. The conformal symmetry breaking pressure is thus odd function of $1/a_s$ given by factor $\frac{1}{k_{FI} \, a_s}$ above.

5.4   Determining the Bulk Viscosity

A finite scattering length produces not only a finite ΔP, but also the possibility of a finite bulk viscosity. While the scattering length may change sign on either side of resonance, the bulk viscosity must always remain positive. As defined, a negative viscosity coefficient would be analogous to a frictional force which assisted motion, an entirely unphysical situation. We also know that the bulk viscosity must vanish in the scale-invariant regime, where $|a_s| \to \infty$. Hence, to leading order in a_s, the bulk viscosity must scale as $1/(k_F \, a_s)^2$, where $k_F = (3\pi^2 n)^{1/3}$ is the *local* Fermi wave vector. Recalling the form of the bulk viscosity

coefficient as defined by Eq.4.8, to leading order in $1/a_S$ it takes the general form

$$\zeta(a_s) \quad = \quad \hbar\, n\, \alpha_B \tag{5.102}$$

$$= \quad \hbar\, n\, \frac{1}{(k_F\, a_s)^2} f_B \left[\frac{T}{T_F(n)} \right], \tag{5.103}$$

where f_B is a dimensionless function of the reduced temperature $\theta \equiv T/T_F(n)$. Invoking the same adiabatic approximation discussed and applied in the evaluation of ΔP, we require $T/T_F(n)$ be a constant in order to conserve entropy. Therefore, f_B is temporally constant and we need only consider how n and k_F evolve in time. Since $n = n(0)\Gamma(t)^{-1}$ and $k_F \propto n^{1/3}$, it follows that $\alpha_B(t)$ is related to an initial value $\alpha_B(0)$ by

$$\alpha_B(t) = \alpha_B(0)\, \Gamma^{2/3}(t). \tag{5.104}$$

Taking the trap average of the above equation defines $\overline{\alpha}_B(t)$, where

$$\overline{\alpha}_B(t) \quad \equiv \quad \frac{1}{N} \int \alpha_B(t)\, n\, d^3\mathbf{r} \tag{5.105}$$

$$= \quad \frac{1}{N} \int \alpha_B(0)\, \Gamma^{2/3}(t)\, n\, d^3\mathbf{r} \tag{5.106}$$

$$\overline{\alpha}_B(t) \quad = \quad \overline{\alpha}_B(0)\, \Gamma^{2/3}(t), \tag{5.107}$$

since $\Gamma(t)$ is spatially constant.

The fact the α_B varies as $1/(k_F\, a_s)^2$ raises an important question regarding our ability to measure α_B when a finite ΔP is also present. In the previous section, we used a high temperature expansion up to second order in the fugacity to produce a from of ΔP that is an odd function of $1/a_s$. If higher order terms in ΔP that vary as $1/(k_F\, a_s)^2$ are considered, how large are these contributions compared to

the size the bulk viscosity? We shall now demonstrate that the bulk viscosity is the *only* contribution to the behavior of $\langle \mathbf{r}^2 \rangle$ that varies as $1/(k_F \, a_s)^2$, as the $1/(k_F \, a_s)^2$ contribution to the volume integral of $\Delta P - \Delta P_0$ generally vanishes.

Using dimensional arguments similar to those above, we write a general $1/(k_F \, a_s)^2$ dependent contribution to ΔP as

$$\Delta P_2 = n E_F(n) \frac{1}{(k_F \, a_s)^2} \, f_{P_2} \left[\frac{T}{T_F(n)} \right], \tag{5.108}$$

where f_{P_2} is a dimensionless function of the reduced temperature. We know that f_{P_2} is temporally constant in the adiabatic approximation, and that $E_F(n)/(k_F \, a_s)^2 = \hbar^2/(2 \, m \, a_s^2)$ is spatially and temporally constant. To find the contribution of this term to $\langle \mathbf{r}^2 \rangle$, we first evaluate the volume integral of ΔP_2,

$$\int \Delta P_2 \, d^3\mathbf{r} \;\; = \;\; \frac{\hbar^2}{2 \, m \, a_s^2} \frac{1}{N} \int f_{P_2}(\theta) n \, d^3\mathbf{r} \tag{5.109}$$

$$= \;\; \frac{\hbar^2}{2 \, m \, a_s^2} \langle f_{P_2}(\theta) \rangle \tag{5.110}$$

Although an infinitesimal volume element grows in size during expansion, the number of atoms within each volume element is constant. Therefore, $\langle f_{P_2}(\theta) \rangle$ is also temporally constant. With no time dependence, the contribution of ΔP_2 will vanish in the difference of $\int \Delta P - \Delta P_0 d^3\mathbf{r}$. Hence, there is no part of $\int \Delta P - \Delta P_0 d^3\mathbf{r}$ that scales as $1/(k_F \, a_s)^2$ to consider in our analysis.

The form of $\bar{\alpha}_B(0)$ that shall be assumed for comparison to our data is derived theoretically in reference [24]. The predicted form of bulk viscosity given in reference [24] is for the case of the high temperature and second order in the fugacity z, consistent with the assumptions in the form of ΔP derived above. In

this limit, reference [24] gives ζ as

$$\zeta \;=\; \widetilde{c}_B \left(\frac{\lambda_T}{a_s}\right)^2 \frac{\hbar}{\lambda_T^3} z^2 \tag{5.111}$$

$$\widetilde{c}_B \;=\; \frac{1}{24\pi\sqrt{2}}. \tag{5.112}$$

As above, we shall approximate the fugacity as $z = n\,\lambda_T^3/2$. Writing $\zeta = \alpha_B(t)\hbar\,n$ gives

$$\alpha_B(t) \;=\; \widetilde{c}_B \left(\frac{\lambda_T}{a_s}\right)^2 \frac{n\,\lambda_T^3}{4}. \tag{5.113}$$

Using the same relationships used in the derivation of ΔP, we write λ_T as $\lambda_T = \lambda_{T0}\Gamma^{1/3}$ and $\lambda_{T0}/a_s = (\sqrt{12\pi}/k_{FI}a_s)(E_F/\widetilde{E})^{1/2}$ so that

$$\alpha_B(t) \;=\; \widetilde{c}_B \frac{12\pi}{(k_{FI}\,a_s)^2} \Gamma^{2/3} \left(\frac{E_F}{\widetilde{E}}\right) \frac{z}{2}. \tag{5.114}$$

Taking the trap average of 5.114, the fugacity is the only quantity that is density dependent, so that

$$\bar{\alpha}_B(t) \;=\; \widetilde{c}_B \frac{12\pi}{(k_F\,a_s)^2} \Gamma^{2/3} \left(\frac{E_F}{\widetilde{E}}\right) \frac{\bar{z}}{2} \tag{5.115}$$

$$\bar{\alpha}_B(t) \;=\; c_B \Gamma^{2/3} \left(\frac{E_F}{\widetilde{E}}\right)^4, \tag{5.116}$$

where c_B is defined as

$$c_B = \frac{9}{32}\frac{1}{(k_{FI}a_s)^2}. \tag{5.117}$$

and $\bar{z}$ is given by Eq.5.85 in the previous section. Above, Eq.5.107 shows that

$\bar{\alpha}_B(t)$ is related to $\bar{\alpha}_B(0)$ by $\bar{\alpha}_B(t) = \bar{\alpha}_B(0)\,\Gamma^{2/3}(t)$, so that

$$\bar{\alpha}_B(0) \;=\; c_B\left(\frac{E_F}{\widetilde{E}}\right)^4. \qquad\qquad (5.118)$$

We therefore have expressions for both ΔP and $\bar{\alpha}_B(0)$ in the high temperature limit. To determine the validity of the each prediction, we fit the expansion data using two parameters, a scale factor λ_P for the ΔP terms and a scale factor ΔB for the predicted $\bar{\alpha}_B(0)$. For work in the unitary gas, the measured expansion of $\langle \mathbf{r}^2 \rangle$ matches the non-interacting gas so closely that we assume that $\Delta P = 0$ and fit only $\bar{\alpha}_B(0)$.

5.5 Determining the Shear Viscosity Off Resonance

Recall that the trap averaged shear viscosity coefficient defined by Eq.4.68 and Eq. 4.7 in Chapter 4,

$$\eta \;=\; \hbar\, n\, \alpha_s$$
$$\bar{\alpha}_S \;\equiv\; \int \eta/(N\hbar)\, d^3\mathbf{r}.$$

For the resonant case, $\bar{\alpha}_S$ is a dimensionless function of the reduced temperature, $\theta \equiv T/T_F(n)$. In the adiabatic approximation used to derive ΔP and $\bar{\alpha}_B(0)$, this makes $\bar{\alpha}_S$ temporally constant throughout the expansion, as θ is an adiabatic invariant. In this section, we will derive a more general, time dependent expression for $\bar{\alpha}_S(a_s)$ when the scattering length is finite.

Like the bulk viscosity coefficient treated above, α_s is a dimensionless function of the reduced temperature θ. Unlike the bulk viscosity, α_s is non-zero for the unitary gas where $1/(k_F\, a_s) = 0$, so the simplest general α_s must be the *sum* of two terms: one that is independent of the scattering length that corresponds to unitary case, and an additional part that varies as a function of $1/(k_F\, a_s)$ so it will vanish when $a_s = \infty$, similar to the behavior of α_B above. We make the assumption that the a_s dependent term will be an even function of the scattering length, symmetric across the value found in the unitary gas. This leads to a general expression for α_s given by

$$\alpha_s = \alpha_{S0}(\theta) + \frac{1}{(k_F a_s)^2}\, f_2(\theta), \tag{5.119}$$

where the first term is the contribution at resonance, the second term is the finite a_s correction, and α_{S0} and f_2 are both dimensionless functions of θ. Once again, we note that θ is independent of time in the adiabatic approximation, so that the resonant contribution is temporally constant. Since $n = n(0)\Gamma(t)^{-1}$ and $k_F \propto n^{1/3}$ we define the scattering length dependent part of the shear viscosity in terms of an inial value α_{S2} so that

$$f_2(\theta)/(k_F a_s)^2 = \alpha_{S2}\, \Gamma^{2/3}(t). \tag{5.120}$$

After integrating over the trap density, we arrive at our central result for the

general form of the trap averaged shear viscosity coefficient:

$$\bar{\alpha}_S \equiv \int \eta/(N\hbar) \, d^3\mathbf{r} \tag{5.121}$$

$$= \frac{1}{N} \int n \, \alpha_s \, d^3\mathbf{r} \tag{5.122}$$

$$\bar{\alpha}_S = \bar{\alpha}_{S0} + \bar{\alpha}_{S2} \, \Gamma^{2/3}(t). \tag{5.123}$$

For the resonant gas, $\bar{\alpha}_{S2}$ is set to zero and we fit the expansion of the transverse aspect ratio to extract self consistent values of $\bar{\alpha}_{S0}$ and the initial mean square cloud size in the z-direction, $\langle z^2 \rangle_0$. For measurements of the shear viscosity off resonance, we fit the expansion of the traverse aspect ratio self to find self consistent values of $\langle z^2 \rangle_0$ and $\bar{\alpha}_{S2}$, using the value of $\bar{\alpha}_{S0}$ found for the same initial cloud size in the unitary case. Hence, the determination of $\bar{\alpha}_{S0}$ in the unitary gas serves not only as a reference for the bulk viscosity, but is also a necessary input into Eq.5.123 in order to measure $\bar{\alpha}_{S2}$ when a finite scattering length is present.

Chapter 6

Characterization of the Confining Potential

In studying the expansion of a strongly interacting ultra-cold Fermi gas, the importance of understanding the potential from which it expands can not be overstated. In our experimental setup, the gas is prepared in the combined potential of a focused CO_2 laser beam and the potential generated by the curvature in the bias magnetic field that tunes the interatomic interactions. When the gas is initially confined, the equilibrium density is determined by the balance between the outward pressure force and the inward restoring force of these two potentials. Therefore, determining the initial atomic density from an absorption image will also give the initial pressure, provided that the shape of the total potential is known. When the optical potential is removed, the initial pressure drives the gas outward, creating the density expansion from which we measure viscosity coefficients and changes in the equation of state. The accuracy of these measurements are thus dependent on our determination of the initial pressure, and hence our characterization of the confining potentials.

This chapter will introduce a new method for characterizing the shape of the optical potential using the scale invariant expansion of a non-interacting gas. We begin by establishing the geometry of our atomic cloud, and the coordinate sys-

tem we adopt to describe it. In order to create confinement, the total potential must have a minimum at the cloud center, and, to lowest order, it is quadratic and hence harmonic. In this approximation, the total potential is then expressible in terms of the measured oscillation frequency of a trapped atom. Further accuracy in characterizing the confining potential is then determined by our ability to estimate (or measure) the higher order *anharmonic corrections*. We derive an exact relationship between the pressure, mean square cloud width, and the total confining potential, demonstrating that the volume integrated pressure is expressible in terms of an oscillation frequency and mean square cloud size for a single axis of the cloud.

Next, we discuss the measurement of the oscillation frequencies associated with the magnetic potential by creating a collective sloshing motion of the atomic cloud within it. Following this, the advantages and disadvantages of *parametric resonance*, our prior method for measuring the optical trap oscillation frequencies, are covered in detail. For the accuracy required in the current work, parametric resonance must be supplemented with a new technique that uses the expansion of the mean square cloud radius, $\langle \mathbf{r}^2 \rangle = \langle x^2 \rangle + \langle y^2 \rangle + \langle z^2 \rangle$, in the non-interacting gas to determine the anharmonic correction to the optical potential in terms of the initial mean square cloud size. For the unitary gas, where an exact relationship between the confining potential and total energy per particle is known, we determine the energy given our measured anharmonic correction and cloud width.
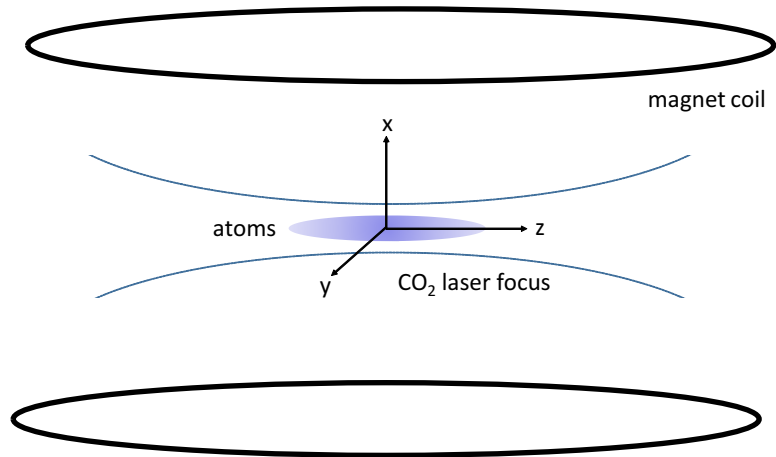
Figure 6.1: Orientation of the optical and magnetic potentials, objects not to scale. The atom cloud, in red, forms a tri-axial ellipsoid with a 1.0:2.7:33 (x:y:z) aspect ratio at the focus of a CO_2 laser beam, blue curves, that propagates along the z-axis with an elliptical beam cross section. The interatomic interactions are tuned with an applied magnetic field, created by two magnetic coils, cylindrically symmetric about the x-axis, in black. Curvature in this bias field produces a magnetic potential energy.

6.1 Basic Geometry of the Confining Potentials

Our ultra cold gas of ^{6}Li atoms is formed at the focus of CO_2 laser beam. The atoms are polarized by the field and attracted to the regions of highest intensity, so that the shape of confining potential matches the intensity distribution of the beam shape. The restoring force on the atoms in then proportional to the gradient of the beam intensity. We label this optical potential as U_{opt}. As given in Fig.6.1, the direction of beam propagation is designated to be the z-axis.

As the beam approaches its focus, the spatial variation of the intensity is slowest in the direction of propagation, so that the z-direction is the most weakly confined. Using a columnating cylindrical lens telescope, the beam profile in the x-y plane is adjusted to have a 2.7:1 aspect ratio, creating a potential that

is asymmetric in all three directions. The intensity variation from the focus to beam edge in the the x and y-directions are much greater than z-direction, creating a stronger confining force and an atomic cloud in the shape of a tri-axial ellipsoid, with with a 1.0:2.7:33 (x:y:z) aspect ratio. The longest width of the cloud, resulting from the smallest restoring force z-direction, is roughly 220 μm.

For a perfect Gaussian beam, the intensity at the beam focus is [53]:

$$I(x, y, z) = \frac{I_0}{1 + (z/\sigma_z)^2} \exp\left(-\frac{x^2}{\sigma_x^2} - \frac{y^2}{\sigma_z^2}\right).$$ (6.1)

When combined with Eq. 3.4: $U_0 = \alpha_0 I_0 / (2 \epsilon_0 c)^2$, the potential energy of an atom with static polarizability α_0 in such a laser field is:

$$U_{dip}(x, y, z) = -\frac{U_0}{1 + (z/\sigma_z)^2} \exp\left(-\frac{x^2}{\sigma_x^2} - \frac{y^2}{\sigma_z^2}\right),$$ (6.2)

where this potential is labeled U_{dip} (as opposed to U_{opt}) to distinguish that this is an idealized representation of a possible optical potential, but not necessarily the exact potential for the atoms in our trap. However, Eq.6.2 does illustrate that even in an ideal case, U_{opt} is not harmonic. A mean harmonic potential energy can be written simply in terms of the mean square cloud size and the oscillation frequency of the confined atoms. However, due to the presence of potential terms higher order than quadratic in the form of U_{opt}, the oscillation frequency of an atom confined in our trap will require an *anharmonic correction*, which itself depends on the mean square cloud size.

In order to tune the atomic interactions, two coils of wire produce a bias magnetic field and an associated magnetic potential, denoted by U_{mag}. As shown in Fig.6.1, the axis of symmetry for the magnet coils is in the x-direction. This

magnetic potential is more than three orders of magnitude weaker than the optical potential in the x and y-directions, but accounts for roughly ten percent of the confining potential in the axial-direction. As we shall see below, the cloud size in the z-direction is particularly important, so the precise contribution of the magnetic potential must also be carefully determined. Note that while the largest dimension of the atomic cloud is 220 μm, the radius of the two magnets coils is on the order of 20 cm, and they sit about 5 cm above and below the cloud. The magnetic potential can therefore be treated as quadratically varying in x,y, and z, at all energies, as described below.

From the sum of these two potentials, we define a total potential for the trapped atoms as

$$U_{total} = U_{opt} + U_{mag}, \tag{6.3}$$

where U_{opt} will require an energy dependent anharmonic correction and U_{mag} will not. Although U_{opt} can be extinguished to initiate expansion, the bias magnetic field, and therefore U_{mag}, must remain, so that the resonant collisional interactions the bias field produces are present throughout the expansion process. Hence, determining U_{mag} is important not only for its contribution to the initial cloud size in the axial direction, but also for the finite amount of internal energy the cloud loses during expansion in exchange for magnetic potential energy.

6.2 The Energy Scale $\widetilde{E} = \langle \mathbf{r} \cdot \nabla U_{total}(\mathbf{r}) \rangle_0$

Before release from the optical trap and the onset of expansion, the equilibrium density is determined by the balance between the outward force arising from the

equilibrium pressure P_0 and the inward restoring force of the total potential,

$$\nabla P_0 + n(\mathbf{r})\nabla U_{total}(\mathbf{r}) = 0. \tag{6.4}$$

This is a vector equation, corresponding to three scalar equations of the form

$$\frac{\partial P_0}{\partial x_i} + n(\mathbf{r})\frac{\partial U_{total}(\mathbf{r})}{\partial x_i} = 0, \tag{6.5}$$

where $x_i = x, y, z$, the component in the ith direction. Multiplying each side by x_i and integrating over volume gives:

$$\int x_i \frac{\partial P_0}{\partial x_i} \, d^3\mathbf{r} + \int x_i \, n(\mathbf{r})\frac{\partial U_{total}(\mathbf{r})}{\partial x_i} d^3\mathbf{r} = 0 \tag{6.6}$$

When the pressure term is integrated by parts, we have

$$\int \frac{\partial}{\partial x_i}(x_i P_0) \, d^3\mathbf{r} - \int P_0 \frac{\partial x_i}{\partial x_i} \, d^3\mathbf{r} + \int x_i \, n(\mathbf{r})\frac{\partial U_{total}(\mathbf{r})}{\partial x_i} d^3\mathbf{r} = 0 \tag{6.7}$$

By noting that the pressure is zero an infinite distance from the trap, the first term on the left vanishes, leaving

$$\int P_0 \, d^3\mathbf{r} = \int x_i \, n(\mathbf{r})\frac{\partial U_{total}(\mathbf{r})}{\partial x_i} d^3\mathbf{r} \tag{6.8}$$

$$\frac{1}{N}\int P_0 \, d^3\mathbf{r} = \left\langle x_i \frac{\partial U_{total}(\mathbf{r})}{\partial x_i} \right\rangle_0. \tag{6.9}$$

By explicitly comparing the three equations that Eq. 6.9 represents, we have

$$\left\langle x\frac{\partial U_{total}}{\partial x} \right\rangle_0 = \left\langle y\frac{\partial U_{total}}{\partial y} \right\rangle_0 = \left\langle z\frac{\partial U_{total}}{\partial z} \right\rangle_0. \tag{6.10}$$

166

Similarly, if the three equations in Eq. 6.8 are summed, we can write a single integral volume on the right hand side and arrive at the energy scale of the system that we shall define as $\widetilde{E}$:

$$3 \int P(\mathbf{r})\, d^3\mathbf{r} \;=\; \int n(\mathbf{r})\mathbf{r} \cdot \nabla U_{total}(\mathbf{r}) d^3\mathbf{r} \tag{6.11}$$

$$\frac{3}{N} \int P_0(\mathbf{r})\, d^3\mathbf{r} \;=\; \langle \mathbf{r} \cdot \nabla U_{total}(\mathbf{r}) \rangle_0 \tag{6.12}$$

$$\widetilde{E} \;\equiv\; \langle \mathbf{r} \cdot \nabla U_{total}(\mathbf{r}) \rangle_0 = 3 \left\langle x_i \frac{\partial U_{total}(\mathbf{r})}{\partial x_i} \right\rangle_0 . \tag{6.13}$$

Eq. 6.13 allows $\widetilde{E}$ to be determined from a width and potential gradient for a single direction.

Due to its relation to the initial pressure, Eq. 6.12, the quantity $\widetilde{E} \equiv \langle \mathbf{r} \cdot \nabla U_{total}(\mathbf{r}) \rangle_0$ appears in every equation that governs expansion of the atomic cloud. For an initial in-trap mean square cloud size $\langle x_i^2 \rangle_0$, where $x_i = x, y, z$ the coordinate in the ith direction, the mean square cloud size is given at a later expansion time t by $\langle x_i^2 \rangle = b_i^2(t) \langle x_i^2 \rangle_0$, where $b_i(t)$ is found from (Eq.4.76):

$$\ddot{b}_i = \frac{\langle \mathbf{r} \cdot \nabla U_{total} \rangle_0}{3m \langle x_i^2 \rangle_0} \frac{1}{\Gamma^{2/3} b_i} \left[1 + C_Q(t) + C_F(t) - C_F(0) - C_p(t) \right]$$

$$- \frac{\hbar \left(\bar{\alpha}_S\, \sigma_{ii} + \bar{\alpha}_B\, \frac{\dot{\Gamma}}{\Gamma} \right)}{m \langle x_i^2 \rangle_0 b_i} - \frac{\langle x_i \partial_i U_{mag} \rangle}{m \langle x_i^2 \rangle_0 b_i}, \tag{6.14}$$

$\widetilde{E}$ also plays a central role in expansion of the means square cloud radius, (Eq.4.110):

$$\frac{d^2}{dt^2} \frac{m \langle \mathbf{r}^2 \rangle}{2} = \langle \mathbf{r} \cdot \nabla U_{Opt} \rangle_0 + \frac{3}{N} \int \left[(\Delta P) - (\Delta P)_0 \right] d^3\mathbf{r} - 3\,\hbar\, \langle \alpha_B\, \nabla \cdot \mathbf{v} \rangle + \Delta U_{mag}. \tag{6.15}$$

For a resonantly interacting trapped cloud, which obeys the virial theorem and has an equation of state $P = (2/3)\mathcal{E}$, the total internal energy per particle

is $E_{int} = 3/(2N) \int P_0 \, d^3\mathbf{r} = (1/2)\langle \mathbf{r} \cdot \nabla U_{total}(\mathbf{r})\rangle_0$, so that the total energy per particle for the trapped cloud is

$$E = \langle U_{total}\rangle_0 + \frac{1}{2}\langle \mathbf{r} \cdot \nabla U_{total}(\mathbf{r})\rangle_0. \tag{6.16}$$

If U_{total} were harmonic, then $\langle U_{total}\rangle_0 = \frac{1}{2}\langle \mathbf{r} \cdot \nabla U_{total}(\mathbf{r})\rangle_0$ and the total energy per particle of the unitarity gas in a harmonic trap is exactly $E_{harm} = \widetilde{E}$. Combined with Eq. 6.10, the unitary gas in a harmonic trap also allows $E_{harm} \equiv 3m\omega_x^2\langle x^2\rangle_0 = 3m\omega_y^2\langle y^2\rangle_0 = 3m\omega_z^2\langle z^2\rangle_0$.

$\widetilde{E}$ and the initial density profile are the most crucial initial conditions in our study of expansion. Therefore, it is the need to determine $\widetilde{E}$ from the initial density profile that makes the characterization of U_{total} so important to our experiments. Before proceeding with the characterization of U_{total}, we note an important issue relating to the initial density in the next section.

6.3   The Importance of the Axial Direction

The optical (and total) potential gradient is weakest in the axial direction (the dimension along the z-axis) of our trap, and this has several important consequences. First, the weakest confining force makes the axial direction the largest initial dimension of the cloud. A typical size in the axial direction is roughly 220 μm, while the initial size in the x-direction is barely 7 μm. Because of the small sizes in the radial direction, when we attempt to image the initial density profile of the cloud with a camera resolution limited to 6 μm, the image is spoiled by a large diffraction pattern. Therefore, the initial density can not be measured directly. Instead, initial mean square sizes $\langle x_i^2\rangle_0$ are determined from the appli-

cation of calculated expansion factors $b_i(t)$ to widths imaged after the cloud has expanded to a larger size, so that $\langle x_i^2 \rangle_0 = \langle x_i^2 \rangle / b_i^2(t)$.

Second, the weakest confining force in the axial direction also establishes the smallest initial pressure gradient, so that the z-width experiences the slowest expansion once the optical trap is extinguished. After 600 μs of expansion time, the x-width will increase by roughly a factor of ten, so that a diffraction pattern will no longer be present when the cloud is imaged. In that same amount of time, the z-width will have expanded by less than one percent. Clearly, a fit to the z-width from such an image is nearly its in-trap value. If a model dependent expansion factor is applied to that measured width to calculate an initial width, a ten percent mistake in that calculation is less than a 0.1% error in what is reported as the initial z-width. Eq. 6.10, $\left\langle x \frac{\partial U_{total}}{\partial x} \right\rangle_0 = \left\langle y \frac{\partial U_{total}}{\partial y} \right\rangle_0 = \left\langle z \frac{\partial U_{total}}{\partial z} \right\rangle_0 = \widetilde{E}/3$, presents us with of choice of initial mean sizes and potential gradients to use when calculating $\widetilde{E}$, and it is for the above reason that we choose the z-direction. However, this decision requires that $\partial U_{total}/\partial z$ be determined to the same level of accuracy as $\langle z^2 \rangle_0$. Thus, in characterizing the confining potential, we are particularly interested in the gradient of the total potential in the z-direction.

6.4 Oscillation Frequencies of the Confining Potentials

If the total confining potential is treated as harmonic,

$$U_{total} = \frac{1}{2}m\,\omega_x^2\,x^2 + \frac{1}{2}m\,\omega_y^2\,y^2 + \frac{1}{2}m\,\omega_z^2\,z^2, \tag{6.17}$$

where m is the mass of ^{6}Li, we need only determine the oscillation frequencies of the confined atoms in order to characterize the potential. Considering that the total potential is a sum of optical and magnetic contributions, a harmonic form provides that total oscillation frequency is expressible as a simple sum of quadratures. In the ith direction, we have that

$$\omega_i^2 = \omega_{i\,opt}^2 + \omega_{i\,mag}^2. \tag{6.18}$$

The size of the magnet coils (20 cm) creating the magnetic potential relative to the size of atomic cloud (220 μm) means that U_{mag} is harmonic for all initial cloud sizes, so that $\omega_{i\,mag}^2$ is independent $\langle x_i^2 \rangle$. This is not the case for the optical potential.

Within the optical potential, deviations from a harmonic shape cause the atoms to experience an *energy dependent* oscillation frequency. Consider the optical potential in the x-direction, assumed to arise from the radial intensity profile of a Gaussian beam given by

$$U(x) \;=\; U_0 \left(1 - \exp\left[-\frac{x^2}{\sigma_x^2} \right] \right) \tag{6.19}$$

$$\;=\; U_0 \left(1 - \exp\left[-\frac{m\,\omega_{x\,opt}^2\,x^2}{2\,U_0} \right] \right), \tag{6.20}$$

where the energy is referenced to the potential minimum $-U_0$. Hence, $\sigma_x^2 = 2U_0/m\,\omega_{x\,opt}^2$ is chosen so that when the above from is Taylor expanded,

$$U(x) \approx \frac{1}{2}\,m\,\omega_{x\,opt}^2\,x^2 + \dots. \tag{6.21}$$

Then, the quadratic term is the familiar form of the harmonic oscillator by con-
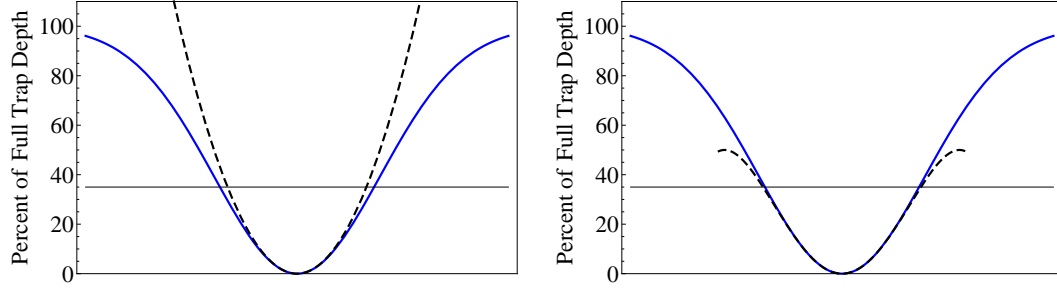
Figure 6.2: Anharmonicity in Gaussian optical potential. Two approximations to the potential shape are given by the dashed lines. The Gaussian potential is $U_0 \left(1 - \exp\left[-x^2 m / \omega_{x\,opt}^2 2U_0\right]\right)$ so that its harmonic approximation is $\frac{1}{2}m\,\omega_{x\,opt}^2\,x^2$ by construction, where U_0 is the total depth of the trap. The frequency $\omega_{x\,opt}$ represents the highest allowed frequency for vanishingly small energies at the bottom of the well. The dashed line on the left gives a purely harmonic approximation to this shape, while the dashed line on the right is given by $\frac{1}{2}m\,\omega_{x\,opt}^2\,x^2 - m^2\omega_{x\,opt}^4 x^4/(8\,U_0)$, including a fourth order term. The horizontal line marks an energy corresponding to thirty five percent the total trap depth, where the harmonic approximation is already deviating from the actual, weaker potential. U_0, m, and $\omega_{x\,opt}$ are the same in both cases.

struction.

Shown in Fig. 6.2, $\omega_{x\,opt}$ is the harmonic potential for low energy atoms near the bottom of the well. Higher energy atoms are able to explore the upper regions of the potential, where they will start to see a smaller potential gradient and a weaker confining force. The higher they go, the more anharmonicity is present and the smaller the oscillation frequency becomes relative to $\omega_{x\,opt}$. Considering higher energies and greater distances from the trap center, the decrease of the oscillation frequency can be written in terms of displacement from the potential minimum by including higher order terms in the expansion of the potential. For

this model potential, the energy dependent frequency is $\bar{\omega}_{x\,opt}$ where,

$$\frac{1}{2}m\,\omega_{x\,opt}^2\,x^2 - \frac{m^2\omega_{x\,opt}^4 x^4}{8U_0} = \frac{1}{2}m\,x^2\left(\omega_{x\,opt}^2 - \frac{m\omega_{x\,opt}^4 x^2}{4U_0}\right) \tag{6.22}$$

$$= \frac{1}{2}m\,\bar{\omega}_{x\,opt}^2 x^2, \tag{6.23}$$

so that

$$\bar{\omega}_{x\,opt}^2 = \omega_{x\,opt}^2\left(1 - \frac{m\omega_{x\,opt}^2}{4U_0}x^2\right). \tag{6.24}$$

The potential in Eq.6.23 is plotted in Fig.6.2, showing a more accurate representation to its true shape for atoms at thirty five percent trap depth when the fourth order term is included compared to that predicted by the harmonic approximation.

Generalizing this example, our notation now defines $\omega_{i\,opt}$, without the overhead bar, as the oscillation frequency of the lowest energy atoms in the optical potential that move a vanishingly small distance from the potential minimum. Atoms that move a finite distance from the bottom of the optical trap in the ith direction oscillate with a frequency $\bar{\omega}_{i\,opt}$ that decreases as function of the squared displacement. For an initial mean square size of our atomic cloud $\langle x_i^2\rangle_0$ that also expresses the averaged square displacement of atoms from the potential minimum, we define a general form of the average optical trap oscillation frequency given by:

$$\bar{\omega}_{i\,opt}^2 = \omega_{i\,opt}^2 h_A[\langle x_i^2\rangle_0] = \omega_{i\,opt}^2\left(1 - \lambda\langle x_i^2\rangle_0\right), \tag{6.25}$$

where $h_A[\langle x_i^2\rangle_0]$ is the *anharmonic correction factor*, and λ is a positive constant.

As defined, $h_A[\langle x_i^2 \rangle_0]$ is always less than unity.

In previous dissertations from our group, $\bar{\omega}_{i\,opt}^2$ has been measured at a single low energy where λ is small, so that $\omega_{i\,opt}$ and λ are then calculated from some assumed form of the potential. This will remain our method for measuring the oscillation frequencies in the x and y-directions. However, for the accuracy required in the current work, both $\omega_{z\,opt}^2$ and $h_A[\langle z^2 \rangle_0]$ will need to be directly measured using new techniques.

In contrast to the optical trap vibration frequencies, the oscillation frequencies associated with harmonic magnetic potential are energy independent, as found above. This makes the form of the magnetic potential comparatively easier to characterize, and we will discuss that measurement before moving onto the optical trap.

6.5   Measurement of the Oscillation Frequencies in the Magnetic Potential

The geometry our magnets (Fig.6.1) allows for the measurement of single oscillation frequency to describe the magnetic potential in all three directions. The large size of the magnet coils relative to the atomic cloud creates a harmonic potential for initial energies of the confined atoms, and elementary magnetostatics relates the oscillation frequency of a single direction to the remaining two.

With the origin placed at the center of the atomic cloud, the bore of the magnet is along the x-direction, causing the magnetic field to decrease as the origin is approached along the x-axis. The radial direction of the magnet is in the z-y plane, where the field increases towards the origin. Following [34], the spin

173

states we trap are high field seekers, and the potential must be repulsive in the x-direction, and attractive in the z and y direction so that

$$U_{mag} = -\frac{1}{2}m\,\omega^2_{x\,mag}\,x^2 + \frac{1}{2}m\,\omega^2_{y\,mag}\,y^2 + \frac{1}{2}m\,\omega^2_{z\,mag}\,z^2. \tag{6.26}$$

The magnetic dipole moment of an atom, $\boldsymbol{\mu}$, will align itself with the local magnetic field direction so that $U_{mag} = -\boldsymbol{\mu}\cdot\mathbf{B} = -\mid\boldsymbol{\mu}\mid\mid\mathbf{B}\mid = -\mu\,\mathrm{B}$. Noting the elementary relation $\nabla^2\mathbf{B} = 0$ and taking the axis of $\mathbf{B}$ to be in the x-direction gives:

$$\nabla^2\mathbf{B} = \nabla^2\mathrm{B}\,\hat{x} = \nabla^2\left(\frac{-U_{mag}}{\mu}\right)\hat{x} = 0. \tag{6.27}$$

Inserting the the form of U_{mag} from Eq. 6.26 into Eq. 6.27 yields

$$-\omega^2_{x\,mag} + \omega^2_{y\,mag} + \omega^2_{z\,mag} = 0. \tag{6.28}$$

The cylindrical symmetry of the magnets demands $\omega_{z\,mag} = \omega_{y\,mag}$, and therefore

$$\omega^2_{x\,mag} = 2\,\omega^2_{z\,mag}, \tag{6.29}$$

so that the magnetic potential is expressible in terms of single harmonic frequency,

$$\omega^2_{mag} = \omega^2_{z\,mag} = \omega^2_{y\,mag} = \frac{1}{2}\,\omega^2_{x\,mag}. \tag{6.30}$$

For a typical experiment, the minimum of the optical potential is carefully aligned on top of the magnetic potential minimum, and the imaging camera is focused on the atomic cloud. Keeping the camera position fixed, we begin this
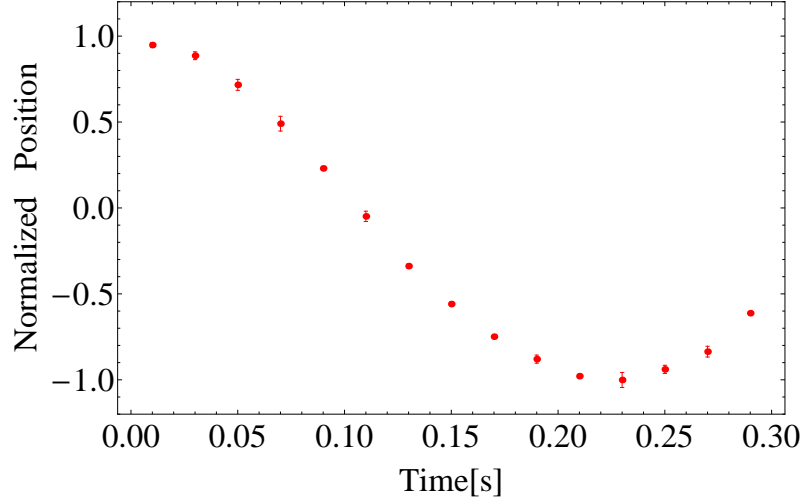
Figure 6.3: Measured position of the central density of the atomic cloud vs time after release from a shallow optical trap which has been moved off of the magnetic bowl center in the attractive y-direction. The magnets are producing a field of 834 Gauss. Though only a portion of one oscillation is visible in the plot, the frequency is found within a quarter of one hertz to be $\omega_{mag\,834} = 2\pi \times 21.5(0.25)$ Hz.

measurement of ω_{mag}^2 by adjusting the focusing lens of the CO_2 beam so that the optical trap is moved off center of the magnetic bowl in the z-y plane, as close to edge of the cameras CCD array as possible, while still maintaining the ability to fit a Gaussian profile to the cloud in our analysis. We then create and cool a new resonantly interacting cloud of atoms at this position, and release it from a shallow depth of the optical trap. The released atoms move under the influence of the attractive part of the magnetic bowl in the y-direction, and the density distribution will start to oscillate about the origin. We colloquially refer to this oscillation as a slosh mode, as the atoms collectively slosh back and forth about the potential minimum in the same way water might slosh in the bottom of a swung bucket. By taking pictures of the cloud at different times after release from the shallow optical trap, we can create a plot of the position of central density as a

function of time (Figure 6.3). The cloud will expand while it oscillates, but this does not prevent the accurate determination of its central position. The resulting plot is a portion of a sine curve, and a sinusoidal fit gives ω_{mag} at 834 Gauss to be $\omega_{mag\,834} = 2\pi \times 21.5(0.25)$ Hz.

For our measurements of transport coefficients at different interaction strengths, we command the same laser power so that the optical trap is unchanged, but the oscillation frequency of the magnetic potential will change as a function of the magnetic field that controls the interactions. Assuming U_{mag} is linear in the applied bias field B and quadratic in ω_{mag}, we write ω_{mag} at an arbitrary magnetic field as

$$\omega_{mag} = \omega_{mag\,834}\sqrt{\frac{B(G)}{834}} = 21.5(0.25)\sqrt{\frac{B(G)}{834}}, \tag{6.31}$$

in terms of the oscillation frequency measured at 834 G.

6.6 Parametric Resonance

In the past, $\bar{\omega}_{i\,opt}$ has been determined using parametric resonance [34]. Starting with a weakly interacting gas evaporability cooled at 300 G, the laser intensity is modulated at single percent amplitude for the particular trap depth being characterized. After waiting one second for the gas to reach thermal equilibrium, the optical trap is extinguished and the cloud size is measured. This process is repeated as a function of modulation frequency for a fixed expansion time. Dithering the laser intensity corresponds to a small variation in the spring constant for an atom confined in the optical potential, so that each atom will act as a classical parametric oscillator. Unlike a driven oscillator, where an outside

force directly drives the system, a parametric oscillation results from the periodic variation of one of the oscillator's parameters. A familiar example is a pendulum that oscillates due to variations in its length. Just as a resonance occurs in the perimetrically oscillating pendulum when its length is varied at a frequency twice its natural frequency (corresponding to an effective push at both of its turning points), the most energy is coupled into the gas when the laser intensity is varied at twice the oscillation frequency of the total potential. Since energy is proportional to the cloud width squared, a spectrum of cloud widths plotted against the modulation frequency of the laser intensity produces a peak at twice the total oscillator frequency of the combined optical and magnetic potentials. Since the excitation is performed in the weakly interacting regime, the energy coupled into one of the trap axes will cause all three of the trap widths to increase through collisional cross relaxation. It is therefore not necessary to favor a particular width of the cloud when analyzing the spectrum of a particular parametric frequency.

For the trap used in the present work, which is elliptical in both the axial and radial directions, there are three distinct frequency peaks to be found using this method. The results of these experiments performed at 300 G with an optical trap produced by twenty percent of our full CO_2 laser power is given in Fig 6.4-6.6, where radial widths of the absorption image are plotted as a function of drive frequency applied for the same duration and amplitude at each point. A Gaussian curve is then fit to each spectrum to extract a central frequency.
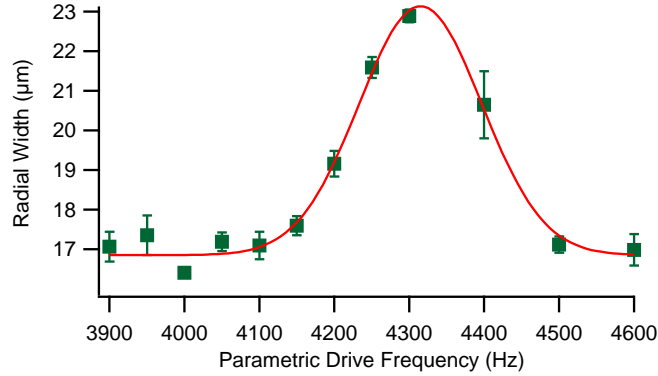
Figure 6.4: Plot of the radial cloud width as a function of parametric excitation frequency. The total potential characterized is the combination of the optical trap depth at 20% of its maximum value and the magnetic bowl produced by a 300 Gauss magnetic field. This spectrum provides the parametric response of the total trapping potential in the x-direction. Solid squares are experimental data, while the red curve is a gaussian fit to the data. The peak is centered at 4215.1(4)Hz
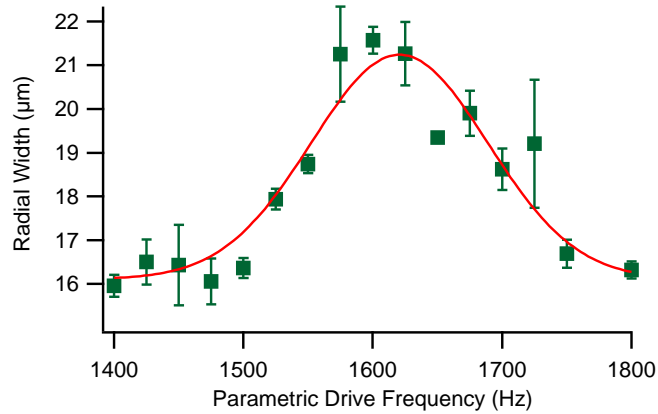
Figure 6.5: Plot of the radial cloud width as a function of parametric excitation frequency. The total potential characterized is the combination of the optical trap depth at 20% of its maximum value and the magnetic bowl produced by a 300 Gauss magnetic field. This spectrum provides the parametric response of the total trapping potential in the y-direction. Solid squares are experimental data, while the red curve is a gaussian fit to the data. The peak is centered at 1620.7(5)Hz
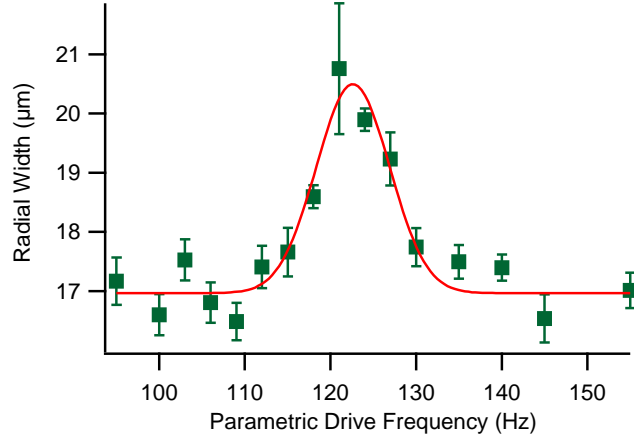
Figure 6.6: Plot of the radial cloud width as a function of parametric excitation frequency. The total potential characterized is the combination of the optical trap depth at 20% of its maximum value and the magnetic bowl produced by a 300 Gauss magnetic field. This spectrum provides the parametric response of the total trapping potential in the z-direction. Solid squares are experimental data, while the red curve is a gaussian fit to the data. The peak is centered at 122.62(0.4)Hz

6.6.1 Anharmonic Corrections to the Parametric Frequencies

A higher starting energy before dithering the laser intensity will cause atoms to oscillate in more anharmonic regions of optical trap, where the potential is more slowly varying than in the region closer to the potential minimum. This lowers the central frequency of the observed peak in a parametric resonance experiment. This behavior is demonstrated in Fig.6.7.

The parametric spectra shown in Fig.6.7 are for the axial direction, where the contribution of the magnetic bowl is not negligible. Thus, from the definition of an anharmonic oscillation frequency of the optical trap given in Eq.6.25,

$$\bar{\omega}_{i\,opt}^2 = \omega_{i\,opt}^2 h_A[\langle x_i^2 \rangle_0] = \omega_{i\,opt}^2 \left(1 - \lambda \langle x_i^2 \rangle_0 \right), \tag{6.32}$$
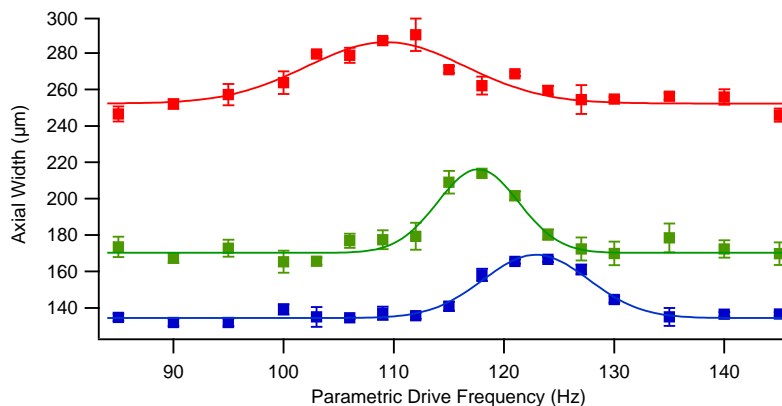
Figure 6.7: Spectra for parametric excitation of the combined optical potential at twenty percent of full laser power and the magnetic bowl produced by 300 Gauss in the z-direction for three different starting energies. Every displayed point is taken at the same time after release from the trap, and the larger baseline widths correspond to more energy present before the excitation. The location of the peak is clearly shifted to a lower frequency for higher initial widths, given by the baseline value of each spectrum. The central values of the peaks are 122.92(0.46), 117.66(0.36), and 109.3(0.7). The lowest energy data point in this figure is the same data as that shown in Figure 6.6, except here the axial direction is plotted as opposed to the radial. That the radial direction gave a frequency of 122.62(0.4)Hz and the axial 122.92(0.5) is a convincing demonstration that one direction does not need to be favored over another in the analysis.

the central frequency ω_p of the measured peak in the parametric spectrum in the z-direction is given by

$$\omega_p = 2\sqrt{\bar{\omega}_{z\,opt}^2 + \omega_{mag}^2} = 2\sqrt{\omega_{z\,opt}^2\left(1 - \lambda\langle x_i^2\rangle_0\right) + \omega_{mag}^2} \ . \tag{6.33}$$

In an attempt to find $\omega_{z\,opt}$, we start with the parametric frequency measured at the lowest initial mean square cloud size where the anharmonic correction should be small, and divide by two to get the total frequency. We subtract the square of the magnetic frequency at 300 G to arrive at $\bar{\omega}_{z\,opt} = 2\pi \times 59.9(0.3)$ Hz.

To calculate how anharmonicity affects the measured parametric response, we start with the scaling solution for the non-interacting gas given by Eq.4.82:

$$\ddot{b}_i + \frac{1}{b_i\,m\,\langle x_i^2\rangle_0}\left[\left\langle x_i\frac{\partial U_{opt}}{\partial x_i}\right\rangle - \frac{1}{b_i^2}\left\langle x_i\frac{\partial U_{opt}}{\partial x_i}\right\rangle_0\right] = 0. \tag{6.34}$$

Here, U_{opt} appears in place of U_{total} to set the initial potential because the magnetic contribution to the measured parametric frequency has already been subtracted above. Because the resulting dynamics will be an oscillation and not an expansion, we replace the expansion factors b_i with $b_i \to 1 + \epsilon(t)$ where $\epsilon \ll 1$. Thus, $\epsilon_i(t)$ represents the time dependent amplitude of oscillation.

Making the simplify assumption that the actual shape of the optical potential is a Gaussian, so that $U_{opt} = U_0\left(1 - \exp\left[-\frac{x^2}{\sigma_x^2} - \frac{y^2}{\sigma_y^2} - \frac{z^2}{\sigma_z^2}\right]\right)$, where $\sigma_i^2 =$

$2U_0/m\,\omega_{i\,opt}^2$, and Taylor expansion up to quartic order arrives gives:

$$U_{opt} = \frac{1}{2}m\omega_{x\,opt}^2\,x^2 + \frac{1}{2}m\omega_{y\,opt}^2\,y^2 + \frac{1}{2}m\omega_{z\,opt}^2\,z^2 - \frac{m^2\omega_{x\,opt}^4\,x^4\omega_{y\,opt}^4\,y^4}{4\,U_0}$$
$$- \frac{m^2\omega_{x\,opt}^4\,x^4\omega_{z\,opt}^4\,z^4}{4\,U_0} - \frac{m^2\omega_{y\,opt}^4\,y^4\omega_{z\,opt}^4\,z^4}{4\,U_0}$$
$$- \frac{m^2\omega_{x\,opt}^4\,x^4}{8\,U_0} - \frac{m^2\omega_{y\,opt}^4\,y^4}{8\,U_0} - \frac{m^2\omega_{z\,opt}^4\,z^4}{8\,U_0}, \quad (6.35)$$

where the harmonic term takes the familiar form by construction. This potential term is inserted into Eq. 6.34, where the brackets specify the usual average over they density. By also assuming a gaussian form of the density, the appropriate distribution for a cloud in the high temperature limit, we may exploit simple relationships between the averaged second order widths and the averaged fourth order widths. For a normalized gaussian density, $n_G(x) = N/(\sqrt{\pi}\sigma_x)\exp[-x^2/\sigma_x^2]$, $\langle x^2 \rangle = \frac{1}{N}\int x^2\,n_G(x)\,dx = \sigma_x^2/2$. Similarly,

$$\langle x_i \rangle^4 = 3\langle x_i \rangle^2 \quad (6.36)$$

$$\langle x_i^2 x_j^2 \rangle = \langle x_i^2 \rangle \langle x_j^2 \rangle, \quad (6.37)$$

with $x_i = x, y, z$, the dimension in the i-direction and $j \neq k \neq i$ are the remaining dimensions.

When making the substitution, $b_i(t) \rightarrow 1 + \epsilon_i(t)$, we note that for small oscillations $\epsilon_i \ll 1$ it is only necessary to keep terms which are first order in ϵ_i. For the ith direction, this gives:

$$\ddot{\epsilon}_i + 4\,\omega_{i\,opt}^2\left[\epsilon_i\left(1 - \frac{9}{2}\frac{\langle x_i^2 \rangle}{\sigma_i^2} - \frac{\langle x_j^2 \rangle}{\sigma_j^2} - \frac{\langle x_k^2 \rangle}{\sigma_k^2}\right) - \epsilon_j\frac{\langle x_j^2 \rangle}{2\,\sigma_j^2} - \epsilon_k\frac{\langle x_k^2 \rangle}{2\,\sigma_k^2}\right] = 0, \quad (6.38)$$

182

where $j \neq k \neq i$. For a purely harmonic potential, Eq. 6.38 reduces to $\ddot{\epsilon}_i + 4\omega_{i\,opt}^2 \epsilon_i = 0$, correctly predicting the frequency $\sqrt{4\omega_{i\,opt}^2} = 2\omega_{i\,opt}$, as we would expect for the maximum response of a perimetrically driven oscillator. We further simplify Eq. 6.38 using additional quadratic approximations in the quartic correction terms. 6.38. From Eq. 6.10, we have that $3\left\langle x\frac{\partial U_{total}}{\partial x}\right\rangle_0 = 3\left\langle y\frac{\partial U_{total}}{\partial y}\right\rangle_0 = 3\left\langle z\frac{\partial U_{total}}{\partial z}\right\rangle_0 = \widetilde{E}$, which in the harmonic limit for the unitary or non-interacting gas is the total energy per particle, E_{harm}:

$$E_{harm} \equiv 3m\omega_{x\,opt}^2\langle x^2\rangle = 3m\omega_{y\,opt}^2\langle y^2\rangle = 3m\omega_{z\,opt}^2\langle z^2\rangle. \tag{6.39}$$

In the anharmonic correction terms, we can use the harmonic relation implied by Eq. 6.10 that $\omega_{x\,opt}^2\langle x^2\rangle = \omega_{y\,opt}^2\langle y^2\rangle = \omega_{z\,opt}^2\langle z^2\rangle$, after first recognizing that each σ_i can be related to its corresponding ω_i though U_0. Eq.6.38 then reduces to:

$$\ddot{\epsilon}_i + 4\omega_i^2\left[\epsilon_i\left(1 - \frac{13}{12}\frac{E_{harm}}{U_0}\right) - \epsilon_j\frac{1}{12}\frac{E_{harm}}{U_0} - \epsilon_k\frac{1}{12}\frac{E_{harm}}{U_0}\right] = 0. \tag{6.40}$$

To apply this expression for energy dependent shifts in the measured parametric frequency due to the anharmonicity of a gaussian potential, we calculate E_{harm} from the measured z-frequency, and the take the width measured of the baseline of the parametric spectrum on either side of the peak as $\langle z^2\rangle$, extrapolated to its in trap value using expansion factors also calculated from the measured frequencies. The trap depth is calculated [39] using the static polarizability of ^{6}Li, the measured x and y parametric frequencies, and the measured laser power of 14.3 W, 20% of the maximum 71.5 W.

While there is coupling to ϵ_j and ϵ_k in Eq. 6.40 for ϵ_i, the coupling coefficients are an order of magnitude less than the correction factor in front of ϵ_i. Therefore,

this coupling can be neglected, and the anharmonic correction to the measured parametric frequency ($\omega_{i\,measured} = \bar{\omega}_{i\,opt}$) for a Gaussian potential is related to the harmonic frequency $\omega_{i\,opt}$:

$$\omega_{i\,opt}^2 \approx \frac{\bar{\omega}_{i\,opt}^2}{1 - \frac{13}{12}\frac{E_{harm}}{U_0}}, \tag{6.41}$$

or

$$\bar{\omega}_{i\,opt}^2 \approx \omega_{i\,opt}^2 \left(1 - \frac{13}{4}\frac{m}{U_0}\langle z^2\rangle_0\right). \tag{6.42}$$

The anharmonic correction found above is a calculated quantity specific to the assumed form of the potential. Further, it only relates $\bar{\omega}_{i\,opt}$ to $\omega_{i\,opt}$ in a *parametric resonance* experiment; this equation does not relate $\bar{\omega}_{i\,opt}$ to $\omega_{i\,opt}$ for a general *expansion* experiment, where expansion factors are related to the form of the optical potential differently than what is given by Eq. 6.34. To find the correction to $\widetilde{E}$ that determines expansion from a gaussian potential, we insert the quartic order approximation to the gaussian potential given in Eq. 6.35 into $3\left\langle z\frac{\partial U_{opt}}{\partial z}\right\rangle_0$, arriving at

$$\widetilde{E} \simeq E_{harm}\left(1 - \frac{E_{harm}}{U_0}\right) \tag{6.43}$$

where E_{harm} is defined by Eq. 6.39.

6.6.2   Limitations of Parametric Resonance

When the results of the previous section are applied to our analysis of the expansion of $\langle \mathbf{r}^2 \rangle$, which is discussed in detail in Chapter 7, we find that the equation

is very sensitive to the ω_z, at the sub percent level. These small mistakes in ω_z directly translate into falsely observed conformal symmetry breaking effects. This is cause to take a serious look at the limitations inherent to using parametric resonance to determine ω_z. Additionally, the anharmonic correction was calculated from an assumed potential, and that assumption is worth questioning.

First, we were presented with different parametric spectra of ω_z that shifted central frequencies as a function of energy. We chose the $\bar{\omega}_z$ from the lowest energy data, so that it would be as close to the harmonic value as possible before applying the correction. However, because we must prepare the gas in the weakly interacting regime, the lower collision rate severely limits the efficiency of evaporation. Thus, to achieve the energy of the lowest energy parametric resonance data in the z-direction, the lowering time of the evaporation curve was already 40 seconds. Increasing the lowering time further does little to additionally cool the gas, as the background heating rate begins to match the decreased evaporation rate that occurs at these longer times. This (qualitative) higher limit on the temperature preceeding a parametric resonance experiment makes the value of the harmonic frequency always a calculated value, that requires an assumed form of the potential.

Second, a gaussian may have been the incorrect shape to use in the derivation of the anharmonic correction. A better description of the intensity distribution of a focused laser along its axis of propagation would be a Lorenztian, so that U_{opt} is given by Eq. 6.2. The parametric oscillator equation for the z-direction, a modified form of Eq. 6.34 would then be:

$$\ddot{\epsilon}_z + 4\,\omega_z^2 \left[-\epsilon_x \frac{1}{12} \frac{E_{harm}}{U_0} - \epsilon_y \frac{1}{12} \frac{E_{harm}}{U_0} + \epsilon_z \left(1 - \frac{11}{6} \frac{E_{harm}}{U_0} \right) \right] = 0. \quad (6.44)$$

which indeed doubles the size of the anharmonic correction in the z-direction. However, Eq. 6.2 is not strictly correct either. For instance, σ_x and σ_y themselves should be z-dependent, as the radial spot sizes should increase away from the focus in order to conserve power. The issue of two Rayleigh lengths could also be raised, as the trap intentionally lacks cylindrical symmetry. It must be asked what there is gain is from continually trying to fine tune assumptions about the trap shape, when a more appropriate measurement technique could potentially avoid these issues entirely.

The extreme sensitivity of $\langle \mathbf{r}^2 \rangle$ to $\bar{\omega}_z$ and $h_A[\langle z^2 \rangle_0]$ makes the procedure assuming a potential shape inadequate. Conversely, if $\langle \mathbf{r}^2 \rangle$ is studied as a function $\langle z^2 \rangle_0$ for other systems that are known to be scale invariant, we would have an extremely sensitive measurement of $h_A[\langle z^2 \rangle_0]$. Therefore, in order to precisely and accurately determine the harmonic frequencies and anharmonic corrections for the resonantly interacting gas in the normal fluid phase, we use the behavior of two other scale invariant systems. First, the unitary superfluid where $\langle z^2 \rangle_0$ is small and the anharmonic correction factor is negligible will determine the harmonic $\omega_{z\,opt}^2$. Following this, measurements of $\langle \mathbf{r}^2 \rangle$ for a range of higher energies in the non-interacting gas will determine $h_A[\langle z^2 \rangle_0]$.

6.7 $\omega_{z\,opt}^2$ from the Unitary Superfluid

We determine the total axial harmonic oscillation frequency, given by $\omega_z(B) = \sqrt{\omega_{z\,opt}^2 + \omega_{mag}^2(B)}$, from several sets of aspect ratio data taken at 834 G for energies $E/E_F \simeq 0.50$ close to the ground state. As a consequence, the cloud size and $\langle z^2 \rangle_0$ reach our smallest achievable values, where the anharmonic correction

factor can be neglected. The gas is also nearly a pure superfluid at these energies, so we can assume that the bulk viscosity, shear viscosity and ΔP are negligible. By measuring *both* aspect ratios σ_x/σ_z and σ_y/σ_z as a function of time after release, we determine that $\omega_z(834\,G) = 2\pi \times 64.3(0.4)$ Hz and $\omega_{z\,opt} = 2\pi \times 60.6(0.4)$ after the magnetic contribution is subtracted.

This method of determining $\omega_{z\,opt}$ from the unitary superfluid is possible because we have already measured $\omega_x = 2\pi \times 2210(4)$ Hz and $\omega_y = 2\pi \times 830(2)$ using parametric resonance and the gaussian anharmonic corrections described above. Therefore, parametric resonance is still necessary for determining the oscillation frequencies in the radial directions, but must be supplemented with this additional technique for the accuracy required in the axial direction.

6.8 The Anharmonic Correction from the Mean Square Cloud Radius

From measurements of scale invariance in the strongly interacting gas, we find that Eq. 4.112, $\langle \mathbf{r}^2 \rangle = \langle \mathbf{r}^2 \rangle_0 + \frac{t^2}{m} \langle \mathbf{r} \cdot \nabla U_{opt} \rangle_0$, is extremely sensitive to the anharmonic correction in $\widetilde{E} = \langle \mathbf{r} \cdot \nabla U_{opt} \rangle_0$. We therefore determine the anharmonic correction from the expansion of $\langle \mathbf{r}^2 \rangle$ in the non-interacting gas, an independent scale invariant system.

Having found $\omega_{z\,opt}$ from measurements of unitary superfluid described above, we first define the relationship between $\widetilde{E}$ and the anharmonic correction to the optical oscillation frequency in the z-direction, $h_A[\langle z^2 \rangle_0]$. Starting from the defi-

nition $\widetilde{E} \equiv \langle \mathbf{r} \cdot \nabla U_{total}(\mathbf{r}) \rangle$, we note:

$$\langle \mathbf{r} \cdot \nabla U_{total}(\mathbf{r}) \rangle_0 = \langle \mathbf{r} \cdot \nabla U_{opt}(\mathbf{r}) \rangle_0 + \langle \mathbf{r} \cdot \nabla U_{mag}(\mathbf{r}) \rangle_0 \qquad (6.45)$$

$$= 3 \left\langle z \frac{\partial U_{total}}{\partial z} \right\rangle_0, \qquad (6.46)$$

so that

$$\langle \mathbf{r} \cdot \nabla U_{opt}(\mathbf{r}) \rangle_0 = 3 \left\langle z \frac{\partial U_{total}}{\partial z} \right\rangle_0 - \langle \mathbf{r} \cdot \nabla U_{mag}(\mathbf{r}) \rangle_0 \qquad (6.47)$$

$$\langle \mathbf{r} \cdot \nabla U_{opt}(\mathbf{r}) \rangle_0 = 3 \left\langle z \frac{\partial U_{opt}}{\partial z} \right\rangle_0 + 3 \left\langle z \frac{\partial U_{mag}}{\partial z} \right\rangle_0 - \langle \mathbf{r} \cdot \nabla U_{mag}(\mathbf{r}) \rangle_0. \quad (6.48)$$

We can simplify Eq.6.48 by comparing the relative sizes of the magnetic restoring forces and the initial cloud size in each direction. The spatial derivative of the magnetic potential is relatively similar in each direction, as the total magnetic potential, Eq. 6.26, is $U_{mag} = (1/2) \, m \, \omega_{mag}^2 (z^2 + y^2 - 2x^2)$. However, the initial size in the z-direction is more than an order of magnitude larger than for the x and y-directions. Therefore, we have that

$$\langle \mathbf{r} \cdot \nabla U_{mag}(\mathbf{r}) \rangle \simeq \left\langle z \frac{\partial U_{mag}}{\partial z} \right\rangle_0 = m \omega_{mag}^2 \langle z^2 \rangle_0. \qquad (6.49)$$

Then,

$$\langle \mathbf{r} \cdot \nabla U_{opt}(\mathbf{r}) \rangle = 3 \left\langle z \frac{\partial U_{opt}}{\partial z} \right\rangle_0 + 3 \left\langle z \frac{\partial U_{mag}}{\partial z} \right\rangle_0 - \langle \mathbf{r} \cdot \nabla U_{mag}(\mathbf{r}) \rangle$$

$$= 3 \left\langle z \frac{\partial U_{opt}}{\partial z} \right\rangle_0 + 2 \left\langle z \frac{\partial U_{mag}}{\partial z} \right\rangle_0$$

$$= 3 \left\langle z \frac{\partial U_{opt}}{\partial z} \right\rangle_0 + 2 \, m \omega_{mag}^2 \langle z^2 \rangle_0 . \qquad (6.50)$$

It is noteworthy and counterintuitive that this *optical* energy scale depends on the *addition* of a *magnetic* term.

We now define the anharmonic correction to the optical trap oscillation frequency in the z-direction $h_A[\langle z^2 \rangle_0]$ in terms of $\left\langle z \frac{\partial U_{opt}}{\partial z} \right\rangle_0$ so that

$$\left\langle z \frac{\partial U_{opt}}{\partial z} \right\rangle_0 = m\omega_{z\,opt}^2 h_A[\langle z^2 \rangle_0]\langle z^2 \rangle_0. \tag{6.51}$$

Using this in Eq. 6.50 then gives:

$$\frac{\langle \mathbf{r} \cdot \nabla U_{opt}(\mathbf{r}) \rangle_0}{m} = 3\,\omega_{z\,opt}^2 h_A[\langle z^2 \rangle_0]\langle z^2 \rangle_0 + 2\,\omega_{mag}^2 \langle z^2 \rangle_0. \tag{6.52}$$

To measure $\langle \mathbf{r}^2 \rangle = \langle \mathbf{r}^2 \rangle_0 + \frac{\langle \mathbf{r} \cdot \nabla U_{opt} \rangle_0}{m} t^2$ in the non-interacting gas, and hence $h_A[\langle z^2 \rangle_0]$, we first evaporatively cool the gas in the weakly interacting regime at 300G and sweep the magnetic field to 528 G, where the scattering length is zero. The optical trap is then extinguished to initiate expansion. As elaborated upon in Chapter7, we take images of the cloud from each camera as a function of time after release from the optical trap, calculate a column density, and fit a two dimensional gaussian to each image to produce a measured width for the x,y, and z direction. From the squared sum of these widths, we create plots of $\langle \mathbf{r}^2 \rangle$ as a function of time. To the resulting curve, we perform a one parameter fit of the form

$$\langle \mathbf{r}^2 \rangle_0 + c_1 t^2, \tag{6.53}$$

to determine c_1. This requires first a determination of $\langle \mathbf{r}^2 \rangle_0$.

To determine the initial mean square radius of the cloud, $\langle \mathbf{r}^2 \rangle_0$, we note that

$\langle z^2 \rangle_0$ well approximates $\langle \mathbf{r}^2 \rangle_0$ for our trap geometry through the relationship

$$\langle \mathbf{r}^2 \rangle_0 = \langle z^2 \rangle_0 \left(1 + \frac{\omega_z^2}{\omega_x^2} + \frac{\omega_z^2}{\omega_y^2} \right), \tag{6.54}$$

where $1 - \omega_z^2/\omega_x^2 - \omega_z^2/\omega_y^2 = 0.9931 \approx 1$, using only the harmonic values of the oscillation frequencies. To find $\langle z^2 \rangle_0$, we rely on the expansion factor $b_z^2(t) = \langle z^2 \rangle / \langle z^2 \rangle_0$ for the ballistic gas given by Eq.4.82, which becomes

$$\ddot{b}_z + \omega_{mz}^2 \, b_z - \frac{\omega_{z\,opt}^2 \, h_A[\langle z^2 \rangle_0] + \omega_{mz}^2}{b_z^3} = 0. \tag{6.55}$$

from $\overline{\omega}_{z\,opt}^2 = \omega_{z\,opt}^2 \, h_A[\langle z^2 \rangle_0]$. Note that we only need a single equation because there is no coupling to $b_x(t)$ and $b_y(t)$ in a non-interacting gas. Because Eq. 6.55 is itself dependent on $\langle z^2 \rangle_0$, we shall require an iterative procedure to produce self consistent values of $\langle z^2 \rangle_0$ and $b_z(t)$. To begin this process, we initially set $h_A[\langle z^2 \rangle_0] = 1$, so that $\overline{\omega}_{z\,opt}$ is given by $\omega_{z\,opt} = 2\pi \times 60.6(0.4)$ Hz, the value measured from the aspect ratio of the unitary superfluid. Because every measured mean square size in the z-direction is expected to have expanded from the same $\langle z^2 \rangle_0$, we may calculate $\langle z^2 \rangle_0$ from the error weighted average of every measured z-width divided by the appropriate expansion factor.

An example of measured $\langle \mathbf{r}^2 \rangle$ data and the one parameter fit function $\langle \mathbf{r}^2 \rangle_0 + c_1 t^2$ is shown in Fig. 6.8. We have from Eq. 6.52 in the previous section that

$$c_1 = \frac{\langle \mathbf{r} \cdot \nabla U_{opt}(\mathbf{r}) \rangle_0}{m} = 3\,\omega_{z\,opt}^2 h_A[\langle z^2 \rangle_0]\langle z^2 \rangle_0 + 2\,\omega_{mag}^2 \langle z^2 \rangle_0, \tag{6.56}$$
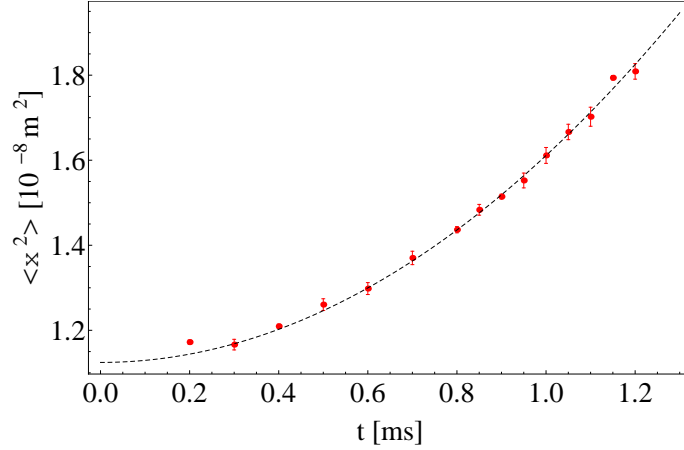
Figure 6.8: Expansion of the mean square cloud size, $\langle \mathbf{r}^2 \rangle$, of a non-interacting gas at 528 G. The time dependent effect of the magnetic potential has a negligible effect on the resulting curvature. The dotted line shows a simple fit function given by $\langle \mathbf{r}^2 \rangle_0 + c_1 t^2$, where c_1 is the only fitted parameter and $\langle \mathbf{r}^2 \rangle_0$ using expansion factors applied to every data point.

allowing us relate $h_A[\langle z^2 \rangle_0]$ to c_1 by

$$h_A[\langle z^2 \rangle_0] = \frac{c_1}{3\,\omega_{z\,opt}^2 \langle z^2 \rangle_0} - \frac{2\,\omega_{mag}^2}{3\,\omega_{z\,opt}^2}. \tag{6.57}$$

or

$$3\,\omega_{z\,opt}^2 h_A[\langle z^2 \rangle_0] = \frac{c_1}{\langle z^2 \rangle_0} - 2\,\omega_{mag}^2 \langle z^2 \rangle_0. \tag{6.58}$$

After performing multiple measurements of c_1 for different values of $\langle z^2 \rangle_0$, we plot the right side of Eq. 6.58 as a function of $\langle z^2 \rangle_0$. To the resulting collection of points, we assume a linear form $h_A[\langle z^2 \rangle_0] \simeq 1 - \lambda_1 \langle z^2 \rangle_0$, and fit the function $3\omega^2(1 - \lambda_1 \langle z^2 \rangle_0)$ with ω and λ_1 as two fit parameters. The value of λ_1 is then inserted into Eq. 6.55 and the result converges after a few iterations to $\lambda_1 =$
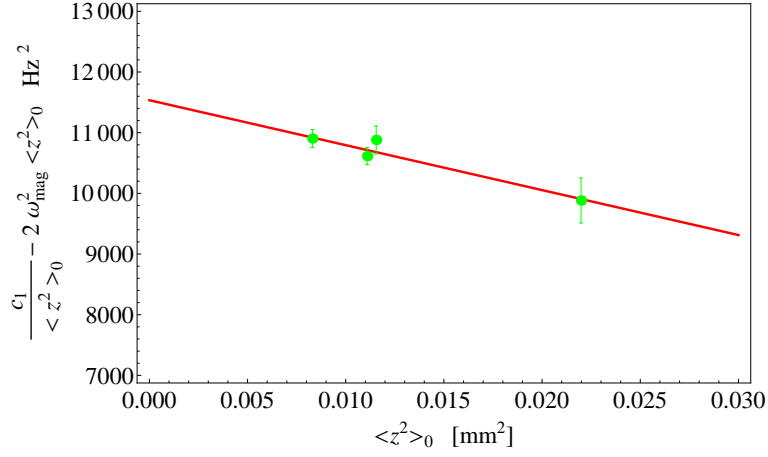
Figure 6.9: In green, $\frac{c_1}{\langle z^2 \rangle_0} - 2\,\omega_{mag}^2 \langle z^2 \rangle_0$ as a function of $\langle z^2 \rangle_0$ for four sets of data measuring $\langle \mathbf{r}^2 \rangle$ in the expansion of a non interacting Fermi gas at 528 G. The red line is a two parameter fit of the form $3\omega(1 - \lambda_1 \langle z^2 \rangle_0)$, with ω and λ_1 as the fit parameters. The fit value $\lambda_1 = 9.3(1.1) \times 10^6$ $1/\mu\mathrm{m}^2$ determines our anharmonic correction $h_A[\langle z^2 \rangle_0] \simeq 1 - \lambda_1 \langle z^2 \rangle_0$.

$9.3(1.1) \times 10^{-6}/\mu\mathrm{m}^2$, which determines $h_A[\langle z^2 \rangle]$. The final fit to $\frac{c_1}{\langle z^2 \rangle_0} - 2\,\omega_{mag}^2 \langle z^2 \rangle_0$ is shown in Fig. 6.9. We find that the intercept for $\langle z^2 \rangle_0 = 0$ is fit by $\omega = 2\pi \times 62(0.61)$ Hz, a reasonable estimate for the harmonic value of $\omega_{z\,opt}$, but differing by 2 Hz from the value found in the unitary superfluid, a much more accurate means of directly determining $\omega_{z\,opt}$.

With $h_A[\langle z^2 \rangle_0]$ determined, we now state our primary result of this chapter; the anharmonic correction to $\widetilde{E}$ and the optical trap oscillation frequency in the z-direction from Eq. 6.51 and Eq. 6.46,

$$\left\langle z \frac{\partial U_{opt}}{\partial z} \right\rangle_0 = m\omega_{z\,opt}^2 h_A[\langle z^2 \rangle_0]\langle z^2 \rangle_0 \tag{6.59}$$

$$\widetilde{E} = 3\left\langle z \frac{\partial U_{total}}{\partial z} \right\rangle_0 = 3m\omega_{z\,opt}^2 h_A[\langle z^2 \rangle_0]\langle z^2 \rangle_0 + 3m\omega_{mag}^2 \langle z^2 \rangle_0 \tag{6.60}$$

$$\bar{\omega}_{z\,opt}^2 = h_A[\langle z^2 \rangle_0]\,\omega_{z\,opt}^2, \tag{6.61}$$

192

where $\omega_{z\,opt}^2 = 2\pi \times 60.6(0.4)$ Hz and $h_A[\langle z^2 \rangle_0] = 1 - \lambda_1 \langle z^2 \rangle_0$, and $\lambda_1 = 9.3(1.1) \times 10^6/\mu m^2$.

To add the anharmonic correction to all of the equations that determine the expansion factors, we need to make additional consistency assumptions. We have measured the anharmonic correction to the z-direction *only*, and must therefore assume how to correct the frequencies in the x and y direction. The simplest assumption is that they also require the same correction factor $h_A[\langle z^2 \rangle_0]$, and this is the approximation that we shall use. More complex treatments are certainly reasonable, as we have already seen that a potential that is truly Lorentzian would require twice as much anharmonic correction as a Gaussian shape. Perhaps the x and y directions are both Gaussian, while the z direction is Lorentzian, so that the radial frequencies should only be corrected by $(1/2)h_A[\langle z^2 \rangle_0]$. Such considerations are not necessary: this particular example produces no noticeable effect in any measured quantity, changing both our measured values of bulk and shear viscosity by roughly 1/10 of their associated error bars. In general, these quantities are so insensitive to the x and y frequencies because $\langle \mathbf{r}^2 \rangle$ depends on $\widetilde{E}$ and $\langle \mathbf{r}^2 \rangle_0 \approx \langle z^2 \rangle$, both of which require only $\overline{\omega}_z^2$, while the shear viscosity is measured via an aspect *ratio* of the x and y direction, so any anharmonic correction shared by both $\overline{\omega}_z^2$ and $\overline{\omega}_y^2$ will cancel. Thus, we treat the two radial frequencies as

$$\overline{\omega}_x^2 = \overline{\omega}_{x\,opt}^2 = \omega_{x\,opt}^2 h_A[\langle z^2 \rangle_0] \tag{6.62}$$

$$\overline{\omega}_y^2 = \overline{\omega}_{y\,opt}^2 = \omega_{y\,opt}^2 h_A[\langle z^2 \rangle_0] \,. \tag{6.63}$$

To demonstrate the sensitivity of $\langle \mathbf{r}^2 \rangle$ to the anharmonic correction factor,
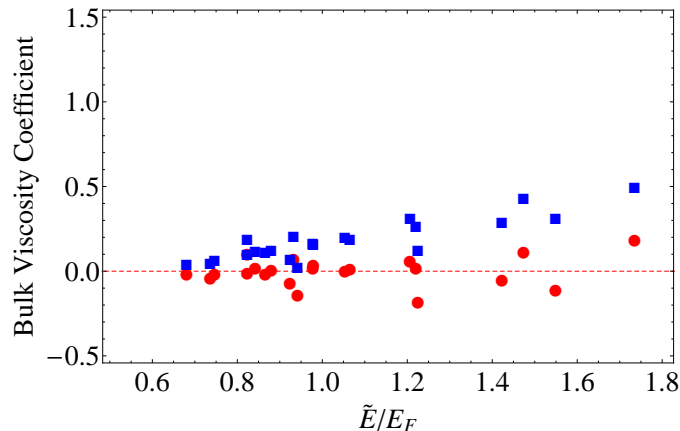
Figure 6.10: Effect of the anharmonic correction on the measured bulk viscosity, in units of $\hbar n$. Red dots (with correction); Blue squares (without correction).

in Fig. 6.10 we plot the bulk viscosity in the unitary gas, analyzed[1] with the value for $h_A[\langle z^2\rangle_0]$ found above (in red) and $h_A[\langle z^2\rangle_0] = 0$ (in blue). When no anharmonic correction is used, we find a bulk viscosity that grows with increasing energy. This trend vanishes once the measurements of the anharmonicity in the confining potential are applied.

6.9 Unitary Energy

For the unitary gas, the total energy per particle obeys the virial theorem and is given by Eq. 6.16,

$$E = \langle U_{total}\rangle_0 + \frac{1}{2}\langle \mathbf{r}\cdot\nabla U_{total}\rangle_0. \tag{6.64}$$

Our anharmonic correction is determined for $\widetilde{E} = \langle \mathbf{r}\cdot\nabla U_{total}\rangle_0$, which we must relate to the anharmonic correction for $\langle U_{total}\rangle_0$. We accomplish this using a

---

[1]See Chapter 7 for the details of this analysis

general form for the optical potential.

We shall assume only that the optical potential is symmetric about its minimum, and that the spatial variation is separable. Specifically, we require that the potential can be written as

$$U_{opt} = U_0 \left(1 - f_x \left[\frac{x^2}{\sigma_x^2} \right] f_y \left[\frac{y^2}{\sigma_y^2} \right] f_z \left[\frac{z^2}{\sigma_z^2} \right] \right), \tag{6.65}$$

where f_i is a dimensionless function of x_i^2/σ_i^2 and σ_i^2 is the characteristic width of ith direction. The constant U_0 gives the full trap depth and has dimensions of energy. If this function is Taylor expanded up to fourth order, it must be of the form

$$
\begin{aligned}
U_{opt} &= \frac{1}{2} m\, \omega_{xh}^2\, x^2 + \frac{1}{2} m\, \omega_{yh}^2\, y^2 + \frac{1}{2} m\, \omega_{zhopt}^2\, z^2 \\
&\quad - \frac{m^2\, \omega_{xh}^2 \omega_{yh}^2\, x^2\, y^2}{4U_0} - \frac{m^2\, \omega_{xh}^2\, \omega_{zhopt}^2\, x^2\, z^2}{4U_0} - \frac{m^2\, \omega_{yh}^2 \omega_{zhopt}^2\, y^2\, z^2}{4U_0} \\
&\quad - \lambda_x \frac{m^2 \omega_{xh}^4\, x^4}{8U_0} - \lambda_y \frac{m^2 \omega_{yh}^4\, y^4}{8U_0} - \lambda_z \frac{m^2 \omega_{zhopt}^4\, z^4}{8U_0} \quad \dots \; ,
\end{aligned}
\tag{6.66}
$$

where ω_{ih} is the harmonic frequency in the ith direction, and λ_x, λ_y, and λ_z are dimensionless constants. The first three harmonic terms take the above form by construction, so that the additional terms are deviations from the familiar form of a harmonic potential. As a consequence, $(1/2)\, m\, \omega_{ih}^2 = U_0/\sigma_i^2$. The fourth order *cross terms* come from the *products* of the chosen form of these harmonic terms, so that the cross terms will be the same for all separable potentials given by Eq. 6.65. Only fourth order terms, which are functions of only one direction, depend explicitly on the form of the potential, and this form is contained in the constants given by λ_i. We shall proceed by finding an expression for $\widetilde{E}$ in terms of

the Taylor expansion given by Eq.6.66, and compare this to the measured result,

$$\widetilde{E} \;=\; \langle \mathbf{r} \cdot \nabla U_{total} \rangle_0 = \langle \mathbf{r} \cdot \nabla U_{opt} \rangle_0 + \langle \mathbf{r} \cdot \nabla U_{mag} \rangle_0 \tag{6.67}$$

$$=\; 3\, m\, \omega_{zopt}^2 \langle z^2 \rangle_0 (1 - \lambda_1 \langle z^2 \rangle_0) + 3\, m\, \omega_{z\,mag}^2 \langle z^2 \rangle_0 \tag{6.68}$$

$$=\; 3\, m\, \omega_{zopt}^2 \langle z^2 \rangle_0 - 3\, m\, \omega_{zopt}^2 \langle z^2 \rangle_0 \lambda_1 \langle z^2 \rangle_0 + 3\, m\, \omega_{z\,mag}^2 \langle z^2 \rangle_0 \tag{6.69}$$

$$=\; 3\, m\, \omega_{zopt}^2 \langle z^2 \rangle_0 - A.N. + 3\, m\, \omega_{z\,mag}^2 \langle z^2 \rangle_0, \tag{6.70}$$

where we define the anharmonic correction term, $A.N. = 3\, m\, \omega_{zopt}^2 \langle z^2 \rangle_0 \lambda_1 \langle z^2 \rangle_0$, which allows an easier comparison between the equations for $\widetilde{E}$ and E to be derived from Eq.6.66. These two expressions will reveal a simple relationship between an anharmonic correction to E and the anharmonic correction to $\widetilde{E}$ that we have already measured.

From Eq. 6.66, $\langle \mathbf{r} \cdot \nabla U_{opt} \rangle$ is given by

$$
\begin{aligned}
\langle \mathbf{r} \cdot \nabla U_{opt} \rangle_0 \;=\;& m\, \omega_{xh}^2\, \langle x^2 \rangle_0 + m\, \omega_{yh}^2\, \langle y^2 \rangle_0 + m\, \omega_{zopt}^2\, \langle z^2 \rangle_0 \\
& - \frac{m^2\, \omega_{xh}^2 \omega_{yh}^2\, \langle x^2 y^2 \rangle_0}{U_0} - \frac{m^2\, \omega_{xh}^2\, \omega_{zhopt}^2\, \langle x^2 z^2 \rangle_0}{U_0} - \frac{m^2\, \omega_{yh}^2 \omega_{zhopt}^2\, \langle y^2 z^2 \rangle_0}{U_0} \\
& - \lambda_x \frac{m^2 \omega_{xh}^4\, \langle x^4 \rangle_0}{2U_0} - \lambda_y \frac{m^2 \omega_{yh}^4\, \langle y^4 \rangle_0}{2U_0} - \lambda_z \frac{m^2 \omega_{zhopt}^4\, \langle z^4 \rangle_0}{2U_0} \;\cdots\; . \tag{6.71}
\end{aligned}
$$

To compare this result to Eq. 6.68, we must first add a magnetic term, given by $\langle \mathbf{r} \cdot \nabla U_{mag} \rangle_0 = m\, \omega_{z\,mag} \langle z^2 \rangle_0$. Two additional magnetic terms will come from the first line of Eq. 6.71, assuming $\omega_{xh}^2 \langle x^2 \rangle_0 = \omega_{yh}^2 \langle y^2 \rangle_0 = (\omega_{zopt}^2 + \omega_{zmag}^2) \langle z^2 \rangle_0$, so that

$$m\, \omega_{xh}^2\, \langle x^2 \rangle_0 + m\, \omega_{yh}^2\, \langle y^2 \rangle_0 + m\, \omega_{zopt}^2\, \langle z^2 \rangle_0 \tag{6.72}$$

$$=\; 3\, m\, \omega_{zopt}^2\, \langle z^2 \rangle_0 + 2\, m\, \omega_{zmag}^2\, \langle z^2 \rangle_0 \tag{6.73}$$

In this form, Eq. 6.71 and the addition of $\langle \mathbf{r} \cdot \nabla U_{mag} \rangle_0$ yields:

$$
\begin{aligned}
\langle \mathbf{r} \cdot \nabla U_{total} \rangle_0 \;=\; & 3\,m\,\omega_{zopt}^2\,\langle z^2 \rangle_0 + 3\,m\,\omega_{zmag}^2\,\langle z^2 \rangle_0 \\
& - \frac{m^2\,\omega_{xh}^2\omega_{yh}^2\,\langle x^2\,y^2 \rangle_0}{U_0} - \frac{m^2\,\omega_{xh}^2\,\omega_{zhopt}^2\,\langle x^2\,z^2 \rangle_0}{U_0} - \frac{m^2\,\omega_{yh}^2\omega_{zhopt}^2\,\langle y^2\,z^2 \rangle_0}{U_0} \\
& - \lambda_x \frac{m^2\omega_{xh}^4\,\langle x^4 \rangle_0}{2U_0} - \lambda_y \frac{m^2\omega_{yh}^4\,\langle y^4 \rangle_0}{2U_0} - \lambda_z \frac{m^2\omega_{zhopt}^4\,\langle z^4 \rangle_0}{2U_0} \quad \ldots \; .
\end{aligned}
\tag{6.74}
$$

Comparing to Eq. 6.70 provides an expression for the anharmonic correction given by:

$$
\begin{aligned}
A.N. \;=\; & 3\,m\,\omega_{zopt}^2\langle z^2 \rangle_0 \lambda_1 \langle z^2 \rangle_0 \\
=\; & \frac{m^2\,\omega_{xh}^2\omega_{yh}^2\,\langle x^2\,y^2 \rangle_0}{U_0} + \frac{m^2\,\omega_{xh}^2\,\omega_{zhopt}^2\,\langle x^2\,z^2 \rangle_0}{U_0} + \frac{m^2\,\omega_{yh}^2\omega_{zhopt}^2\,\langle y^2\,z^2 \rangle_0}{U_0} + \\
& \lambda_x \frac{m^2\omega_{xh}^4\,\langle x^4 \rangle_0}{2U_0} + \lambda_y \frac{m^2\omega_{yh}^4\,\langle y^4 \rangle_0}{2U_0} + \lambda_z \frac{m^2\omega_{zhopt}^4\,\langle z^4 \rangle_0}{2U_0} \quad \ldots \;,
\end{aligned}
\tag{6.75}
$$

When the Taylor expansion of Eq.6.66 is used to derive the form of E, we find first that

$$
\langle U_{opt} \rangle_0 + \frac{1}{2}\,\langle \mathbf{r} \cdot \nabla U_{opt} \rangle_0 =
\tag{6.76}
$$

$$
\begin{aligned}
& m\,\omega_{xh}^2\,\langle x^2 \rangle_0 + m\,\omega_{yh}^2\,\langle y^2 \rangle_0 + m\,\omega_{zopt}^2\,\langle z^2 \rangle_0 \\
& - \frac{3}{4}\frac{m^2\,\omega_{xh}^2\omega_{yh}^2\,\langle x^2\,y^2 \rangle_0}{U_0} - \frac{3}{4}\frac{m^2\,\omega_{xh}^2\,\omega_{zhopt}^2\,\langle x^2\,z^2 \rangle_0}{U_0} - \frac{3}{4}\frac{m^2\,\omega_{yh}^2\omega_{zhopt}^2\,\langle y^2\,z^2 \rangle_0}{U_0} \\
& - \frac{3}{4}\lambda_x \frac{m^2\omega_{xh}^4\,\langle x^4 \rangle_0}{2U_0} - \frac{3}{4}\lambda_y \frac{m^2\omega_{yh}^4\,\langle y^4 \rangle_0}{2U_0} - \frac{3}{4}\lambda_z \frac{m^2\omega_{zhopt}^4\,\langle z^4 \rangle_0}{2U_0} \quad \ldots \;,
\end{aligned}
\tag{6.77}
$$

where the difference from $\langle \mathbf{r} \cdot \nabla U_{opt} \rangle_0$ is a factor of 3/4 in the anharmonic correction terms *only*. The full expression of E, Eq. 6.64, including the magnetic potential,

197

then gives

$$\langle U_{total}\rangle_0 + \frac{1}{2}\,\langle \mathbf{r} \cdot \nabla U_{total}\rangle_0 = 3\,m\,\omega_{zopt}^2\,\langle z^2\rangle_0 \quad + \quad 3\,m\,\omega_{zmag}^2\,\langle z^2\rangle_0 \qquad (6.78)$$

$$- \frac{3}{4}\,A.N. \qquad (6.79)$$

This factor of $3/4$ in front of the anharmonic correction term (which depends on an already determined value of λ_1) is the central result for writing the energy of the unitary gas when the anharmonic correction is measured for $\widetilde{E}$, without requiring a specific form of the potential. Comparison to the form of $\widetilde{E}$ requires that if we have successfully measured

$$\widetilde{E} = 3\,m\,\omega_{zopt}^2\langle z^2\rangle_0(1 - \lambda_1\langle z^2\rangle_0) + 3\,m\,\omega_{z\,mag}^2\langle z^2\rangle_0 \qquad (6.80)$$

then for the general potential of Eq. 6.65, the total energy per particle for the unitary gas is

$$E = 3\,m\,\omega_{zopt}^2\langle z^2\rangle_0 \left(1 - \frac{3}{4}\lambda_1\langle z^2\rangle_0\right) + 3\,m\,\omega_{z\,mag}^2\langle z^2\rangle_0 \qquad (6.81)$$

This expression will allow transport coefficients in the unitary regime to be measured as a function of our best estimate of the true energy per particle, not simply the energy scale $\widetilde{E}$. Off resonance, where a finite scattering length prevents a simple expression for E, $\widetilde{E}$ remains our best characterization of the energy scale.

Chapter 7

Data Analysis and Results

This chapter describes the analysis and results of four different experiments. Throughout all four, we image the hydrodynamic expansion of an ultra cold Fermi gas from two perpendicular directions following release from a anisotropic optical trap in the shape of a tri-axial ellipsoid with a 1.0 : 2.7 : 33 (x:y:z) aspect ratio for a range of interactions strengths.

First, we observe an elliptic flow pattern in the expanding x-y aspect ratio $\sqrt{\langle x^2 \rangle / \langle y^2 \rangle}$ of the unitary gas that is highly sensitive to the shear viscosity η, allowing the measurement of small shear viscosities at low energies previously unaccessible in expansion experiments [5, 6]. We find that the shear viscosity grows from -0.02(4)$\hbar n$ in the superfluid regime, to 3.39(32)$\hbar n$ at a total energy per particle $E = 1.70(4)E_F$, where E_F is the Fermi energy of an ideal gas at the trap center and n is the density.

Next, we observe that the mean square cloud radius $\langle \mathbf{r}^2 \rangle = \langle x \rangle^2 + \langle y \rangle^2 + \langle z \rangle^2$ of the resonantly interacting gas expands ballistically, identical to a non-interacting gas. This is in contrast to the aspect ratio, which expands hydrodynamically with an energy dependent shear viscosity. Such behavior is a consequence of scale invariance, and a demonstration that the equation of state $P = 2/3\,\mathcal{E}$ and local thermal equilibrium are maintained throughout expansion. Quantitatively

examining the expansion of $\langle \mathbf{r}^2 \rangle$, we also find that the energy-averaged unitary bulk viscosity is consistent with zero, $0.00(0.04)\hbar\, n$.

Third, we tune the interaction strength away from resonance, where we observe conformal symmetry breaking as $\langle \mathbf{r}^2 \rangle$ deviates from ballistic flow. Our analysis finds that the primary contribution to this behavior is a change in the equation of state $\Delta P = P - 2/3\,\mathcal{E}$, rather then the emergence of a finite bulk viscosity.

Finally, we study the shear viscosity as a function of energy and interaction strength $1/(k_{FI}a)$, where a is the s-wave scattering length and k_{FI} is the Fermi wave vector for an ideal gas at the trap center. At low energy, the minimum is less than the resonant value and is significantly shifted toward the BEC side of resonance, to $1/(k_{FI}a) = 0.2$. This suggests that a Bose-Fermi mixture permits a lower shear viscosity and higher collision rate then the resonantly interacting Fermi gas.

7.1 Geometry of the Atomic Cloud

Before presenting results, we remind the reader of the geometry of our atomic cloud relative to the two cameras that image it, discussed in Chapter 3. The cloud is prepared in an asymmetric optical trap with a $1.0 : 2.7 : 33$ (x:y:z) aspect ratio. In addition to the optical trap, there exists a finite potential from the bias magnetic field that tunes the atomic interactions, so that the total potential that sets the initial cloud size is:

$$U_{total} = \frac{1}{2}\, m\, \omega_x^2\, h_A[\langle z^2 \rangle_0] x^2 + \frac{1}{2}\, m\, \omega_y^2 h_A[\langle z^2 \rangle_0]\, y^2$$
$$+ \frac{1}{2}\, m\, \left(\omega_{z\,opt}^2 h_A[\langle z^2 \rangle_0] + \omega_{z\,mag}^2 \right) z^2. \quad (7.1)$$

Measured according to the techniques described in Chapter 6, the harmonic oscil-lator frequencies of the optical trap are $\omega_x = 2\pi \times 2210(4)$ Hz, $\omega_y = 2\pi \times 830(2)$ Hz, and $\omega_{z\,opt} = 2\pi \times 60.6(0.4)$ Hz. The anharmonic correction for the optical frequencies is $h_A[\langle z^2 \rangle_0] = 1 - \lambda_1 \langle z^2 \rangle_0$, where $\langle z^2 \rangle_0$ is the initial mean square cloud size in the z-direction and $\lambda_1 = 9.3(1.1) \times 10^{-6}/\mu m^2$. The oscillator frequency of the magnetic potential at 834 G is $\omega_{z\,mag}^2 = 2\pi \times 64.03(0.4)$ Hz. The magnetic po-tential is a non-negligible contribution to the total potential in the the z-direction only.

While the optical potential can be extinguished to initiate expansion, the mag-netic potential must persist to maintain the atomic interactions. This remaining magnetic potential is expressible in terms of a single frequency, ω_{mag},

$$U_{mag} = -\frac{1}{2}m\,2\omega_{mag}^2\,x^2 + \frac{1}{2}m\,\omega_{mag}^2\,y^2 + \frac{1}{2}m\,\omega_{mag}^2\,z^2. \tag{7.2}$$

The magnetic potential does not require an anharmonic correction.

As shown in Figure 7.1, an absorbtion image of the y-z plane is recorded by camera-1, while the image of the x-z plane is recorded by camera-2. We refer to the z-direction as the axial direction, while x and y are radial directions. The ratio of one of the radial cloud widths to the axial cloud widths is a longitudinal aspect ratio, while the ratio of the x-width to the y-width is the transverse aspect ratio.

7.2 Measurement of the Mean-Square Cloud Size

In order to quantify expansion dynamics, we must know the mean-square widths of the atomic cloud $\langle x_i^2 \rangle$, where $x_i = x, y, z$, the coordinate in the ith direction,
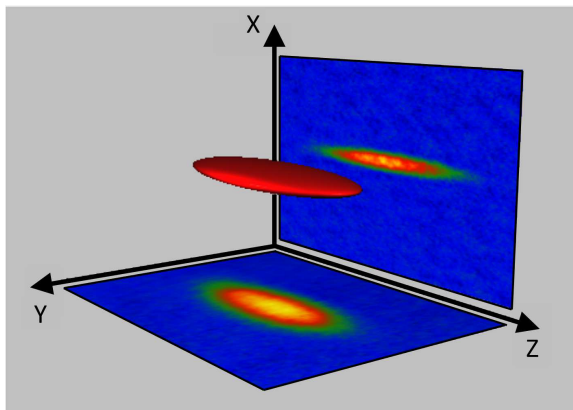
Figure 7.1: Two CCD cameras are used to image the density profile of the expanding cloud, providing widths of all three dimensions. The cloud is released from an asymmetric optical trap with a $1.0 : 2.7 : 33$ (x:y:z) aspect ratio, where the y-z plane is imaged by camera-1 and the x-z plane is imaged by camera-2. The images shown have been cropped to focus on the density profile of the cloud; an actual image is about three times wider, with additional pixels on either side of the cloud in the z-direction.

as a function of the *expansion time t*, or equivalently, *time after release* from the optical trap. After the conclusion of automated data taking described in Chapter 3, we are typically left with six to ten images from each camera for every time point after release. For the current work, we take roughly fourteen time points for a combined total of nearly two hundred and eighty images. We shall treat the methods of image acquisition as established experimental techniques [34]. From these images, our first task is to associate the number of photons recorded at each pixel of the cameras CCD (charged coupled device) array with a number of atoms, turning the image into *column density* distribution according to the methods in [34]. A column density is simply a three dimensional density with one direction integrated out, (in this case, the direction normal to the plane of the camera) with units of atom number per unit area, so that numerically integrating

the column density pixel by pixel produces a total atom number. Because these two dimensional CCD images are representations of three dimensional atomic clouds, all of our information about the density of atomic sample must come from this column density.

For all but the lowest energy points, a two-dimensional gaussian fit of the form

$$n(y, z) = B + A \exp\left[-\frac{y^2}{\sigma_y^2} - \frac{z^2}{\sigma_z^2}\right], \tag{7.3}$$

is applied to each column density from camera-1, where A, B, σ_x, and σ_z are fit coefficients for the x-z plane. To each column density from camera-2, we perform an identical fit in the x-z plane:

$$n(x, z) = B + A \exp\left[-\frac{x^2}{\sigma_x^2} - \frac{z^2}{\sigma_z^2}\right]. \tag{7.4}$$

The fit values of σ_i are what we label as the cloud width in the ith-direction for the expansion time corresponding to that image. A two-dimensional gaussian fit is favored over a one-dimensional fit due to finite size of the CCD array: as the strongly interacting cloud expands in the initially narrow transverse direction, it approaches the boundaries of the image. If a one dimensional gaussian fit is performed on such a distribution, the baseline produced by the fitting function is not adequately accurate, as the true baseline may be outside the image. If the baseline is incorrect, the fit values of σ_i will also be incorrect. The axial direction of the cloud, however, starts comparably large, but also expands very little, maintaining sufficient distance from the edge of the CCD array to fit an accurate baseline and width. By using a two-dimensional fit, there is only one baseline for both dimensions, so that if the density distribution is near the camera

edge in the radial direction, the larger region between the axial limits of the cloud and the CCD array edge will create a stable baseline for fitting to both the axial and radial width.

Though accurate baselines are necessary to fit the widths given by σ_x, σ_y, and σ_z, once we have these widths we no longer use the fit baselines B values and the amplitude A values. For each image, we are then left with two widths from the two dimensional fit and an atom number. For each release time point, the average and standard deviation of the corresponding ten data points are found. To avoid confusion, we call each averaged width as a function of time a data point, and the number of points used to create that average to be the number of trials. The associated error bar is then taken to be standard deviation divided by the square root of the number of trials. Additionally, the atom number from every image for every release time point is averaged together to create an average atom number for the data run.

Of course, not every picture that comes back from the automated data run is ideal. Drifts in the dye laser frequency, poor optical trap loading, or off-resonant imaging can produce images that should not be averaged with the rest. In order to eliminate these points, our fitting routine has the option to reject points based on the value of the atom number and/or widths compared to the standard deviation of all widths for that time point or the overall atom number. Depending on the stability of the system for that particular data run, we are typically able to keep all points within two sigma for each parameter. The fitting routine will automatically adjust the value of the number of trials used to calculate the error bar for a data point if an image for that time point had to be rejected.

Both cameras image the z-direction, and comparison of the extracted z-widths

TOF (μs)	z-width 1	z-width 2
400	222.71	227.80
600	224.80	227.54
800	225.86	226.82
1000	224.98	226.21
1200	224.36	223.90
1400	228.13	227.30
1500	226.62	226.47
1600	227.06	226.36
1700	227.91	226.79
1800	223.77	223.27
1900	228.15	225.11
2000	229.58	226.00

Table 7.1: Comparison of the measured z-widths (ω_z) for different times of flight (TOF) after release from the optical trap taken from camera-1 and camera-2 for a typical experimental sequence. Agreement within one percent is found between this comparison.

from each image of the same cloud produces an experimentally comforting agreement within one percent (see Table 7.1). A discussion of the measurement of each camera's magnification that makes this agreement possible can be found in Chapter3. As we have no reason to favor one camera's measurement of σ_z over the other, the two z-widths for each cloud are averaged together.

The assumption that the atomic cloud density is gaussian also provides a simple relationship between the measured widths σ_i and the mean square cloud size $\langle x_i^2 \rangle$. For a three dimensional gaussian density given by

$$n = \frac{N}{\pi^{3/2}\sigma_x\,\sigma_y\,\sigma_z} \exp\left[-\frac{x^2}{\sigma_x^2} - \frac{y^2}{\sigma_y^2} - \frac{z^2}{\sigma_z^2}\right], \qquad (7.5)$$

a mean square cloud size in the ith direction is:

$$\langle x_i^2 \rangle \ = \ \frac{1}{N} \int x_i^2 n \, d^3\mathbf{r} = \frac{\sigma_i^2(t)}{2} \tag{7.6}$$

The ratio of the widths can be taken to look at aspect ratios of the expanding cloud, while all three mean square cloud sizes can be summed to produce the mean square cloud radius, $\langle \mathbf{r}^2 \rangle$. For fitting purposes, these quantities are then plotted as a function of expansion time.

7.3 Initial Mean Square Cloud Size and the Energy Scale

There is one crucial time point for mean square cloud sizes that we can not directly image, and it is one of our largest experimental limitations. We are unable to measure cloud widths within the trap, a result of our camera's resolution being limited to six microns. Even though the in trap σ_z is well within this resolution, the small in-trap radial sizes are not. Due to the finite aperture of the imaging system, attempts to image the initial cloud results in a detraction pattern so large that no width can be properly characterized. The consequences of this adds many steps to our analysis procedure, but these steps are not individually complicated.

Since the initial cloud widths (and a corresponding energy scale) are not directly imaged, they must be calculated by dividing measurable widths by known. These expansion factors are generally viscosity dependent, while viscosity is in turn a function of energy, which is directly proportional to the initial mean square size. Thus, we require an iterative procedure to produce self consistent values of

the viscosity and the initial cloud size.

The initial cloud size is related to the energy scale of the expanding cloud, defined by Eq. 6.13:

$$\widetilde{E} = \langle \mathbf{r} \cdot \nabla U_{total}(\mathbf{r}) \rangle_0. \tag{7.7}$$

As the z-direction is confined with the weakest potential, it also expands the least when released. This makes its calculated in-trap value the least sensitive to model dependent expansion factors, and therefore the preferred width to relate to the energy. However, energy does not depend on mean square cloud size alone. To accurately measure the energy, we must determine the frequency of the potential in the z-direction with the same certainty as the z-width[1]. Once this is accomplished, we relate $\widetilde{E}$ to an initial z-width via:

$$\langle \mathbf{x} \cdot \nabla U_{total}(\mathbf{x}) \rangle_0 = 3 \left\langle z \frac{\partial U_{total}}{\partial z} \right\rangle_0, \tag{7.8}$$

and Eq. 6.61 defines,

$$
\begin{aligned}
\left\langle z \frac{\partial U_{total}}{\partial z} \right\rangle_0 &= \left\langle x \frac{\partial U_{total}}{\partial x} \right\rangle_0 = \left\langle y \frac{\partial U_{total}}{\partial y} \right\rangle_0 \\
&= \left\langle x \frac{\partial U_{opt}}{\partial x} \right\rangle_0 = \left\langle y \frac{\partial U_{opt}}{\partial y} \right\rangle_0 \\
&= m(\omega_{zopt}^2 h_A[\langle z^2 \rangle_0] + \omega_{z\,mag}^2)\langle z^2 \rangle_0, \tag{7.9}
\end{aligned}
$$

where $U_{total} = U_{opt} + U_{mag}$, used above to reiterate that the magnetic potential is negligible compared to the optical potential in the x and y directions.

---

[1]With special emphasis on $\omega_{z\,opt}$, the procedure for measuring all trap frequencies is the subject of Chapter 6.

Since the shear viscosity dependent expansion factors are used to determine $\langle z^2 \rangle_0$ and therefore $\widetilde{E}$, we proceed with a description of shear viscosity measurement, starting with the unitary (resonant) case.

7.4   Measurement of Unitary Shear Viscosity

In order to measure shear viscosity, we fit a scaling model for the expansion factors to the cloud's transverse aspect ratio as a function of time after release. We begin with the calculation of expansion factors. We first need to write the evolution equations that govern them in terms of measured quantities. This process will be very similar to the way the equations for the ideal gas expansion factors were treated in Chapter 6, as we use the same consistency arguments for writing the optical potential terms as a function of the anharmonic correction factor $h_A[\langle z^2 \rangle_0]$ and the measured harmonic frequencies, as well relate all initial widths to $\langle z^2 \rangle_0$. The equations for the expansion factors in the unitary regime are derived in Chapter 4 and found to be:

$$\ddot{b}_i = \frac{\overline{\omega_i^2}}{\Gamma^{2/3}b_i}[1 + C_Q(t)] - \frac{\hbar\left(\bar{\alpha}_S\,\sigma_{ii} + \bar{\alpha}_B\,\frac{\dot{\Gamma}}{\Gamma}\right)}{m\langle x_i^2 \rangle_0 b_i} - \frac{\langle x_i \partial_i U_{Mag}\rangle}{m\langle x_i^2 \rangle_0 b_i} \quad (7.10)$$

$$\dot{C}_Q(t) = \frac{\Gamma^{2/3}(t)}{\langle \mathbf{x} \cdot \nabla U_{total}\rangle_0}\left(\hbar\,\bar{\alpha}_S \sum_i \sigma_{ii}^2 + 2\hbar\,\bar{\alpha}_B\,\frac{\dot{\Gamma}^2}{\Gamma^2}\right), \quad (7.11)$$

As defined above, Eq. 7.8 and Eq. 7.9 give:

$$\langle \mathbf{x} \cdot \nabla U_{total}(\mathbf{x})\rangle_0 = 3\left\langle z\frac{\partial U_{total}}{\partial z}\right\rangle_0 = m(\omega_{zopt}^2 h_A[\langle z^2 \rangle_0] + \omega_{z\,mag}^2)\langle z^2 \rangle_0. \quad (7.12)$$

We also assume that the necessary anharmonic correction to the optical frequency is the same for each direction, so that

$$\bar{\omega}_z^2 = \omega_{z\,opt}^2\, h_A[\langle z^2\rangle_0] + \omega_{z\,mag}^2 \tag{7.13}$$

$$\bar{\omega}_x^2 = \omega_x^2\, h_A[\langle z^2\rangle_0] \tag{7.14}$$

$$\bar{\omega}_y^2 = \omega_y^2\, h_A[\langle z^2\rangle_0]. \tag{7.15}$$

To find the initial mean square cloud sizes in the x and y direction, we relate them to the initial z-width using the total effective harmonic frequencies:

$$\bar{\omega}_z^2\, \langle z^2\rangle_0 = \bar{\omega}_y^2\, \langle y^2\rangle_0 = \bar{\omega}_x^2\, \langle x^2\rangle_0. \tag{7.16}$$

This allows all expansion factors to be written in terms of the initial z-widths and the harmonic frequencies as:

$$\ddot{b}_z = -\omega_{z\,mag}^2\, b_z + \frac{\omega_{zopt}^2 h_A[\langle z^2\rangle_0] + \omega_{z\,mag}^2}{\Gamma^{2/3} b_z}[1 + C_Q(t)] - \frac{\hbar\left(\bar{\alpha}_S\,\sigma_{ii} + \bar{\alpha}_B\,\frac{\dot{\Gamma}}{\Gamma}\right)}{b_z m \langle z^2\rangle_0}$$

$$\ddot{b}_x = 2\omega_{z\,mag}^2\, b_x + \frac{\omega_x^2 h_A[\langle z^2\rangle_0]}{\Gamma^{2/3} b_x}[1 + C_Q(t)] - \frac{\hbar\left(\bar{\alpha}_S\,\sigma_{ii} + \bar{\alpha}_B\,\frac{\dot{\Gamma}}{\Gamma}\right)\omega_x^2 h_A[\langle z^2\rangle_0]}{b_x\, m(\omega_{zopt}^2 h_A[\langle z^2\rangle_0] + \omega_{z\,mag}^2)\langle z^2\rangle_0}$$

$$\ddot{b}_y = -\omega_{z\,mag}^2\, b_y + \frac{\omega_y^2 h_A[\langle z^2\rangle_0]}{\Gamma^{2/3} b_y}[1 + C_Q(t)] - \frac{\hbar\left(\bar{\alpha}_S\,\sigma_{ii} + \bar{\alpha}_B\,\frac{\dot{\Gamma}}{\Gamma}\right)\omega_y^2 h_A[\langle z^2\rangle_0]}{b_y\, m(\omega_{zopt}^2 h_A[\langle z^2\rangle_0] + \omega_{z\,mag}^2)\langle z^2\rangle_0}$$

$$\dot{C}_Q(t) = \frac{\Gamma^{2/3}}{3m(\omega_{zopt}^2 h_A[\langle z^2\rangle_0] + \omega_{z\,mag}^2)\langle z^2\rangle_0}\left(\hbar\bar{\alpha}_S\sum_i \sigma_{ii}^2 + 2\hbar\bar{\alpha}_B\,\frac{\dot{\Gamma}^2}{\Gamma^2}\right)$$

$$\sum_i \sigma_{ii}^2 = \frac{8}{3}\left(\frac{\dot{b}_x^2}{b_x^2} + \frac{\dot{b}_y^2}{b_y^2} + \frac{\dot{b}_z^2}{b_z^2} - \frac{\dot{b}_x\,\dot{b}_y}{b_x\,b_y} - \frac{\dot{b}_x\,\dot{b}_z}{b_x\,b_z} - \frac{\dot{b}_y\,\dot{b}_z}{b_y\,b_z}\right)., \tag{7.17}$$

and $\Gamma(t) = b_x(t)\, b_y(t)\, b_z(t)$ is the volume scale factor.

Our iterative procedure begins by first setting $\bar{\alpha}_S$ and $\bar{\alpha}_B$ equal to zero and

$h_A[\langle z^2 \rangle_0]$ equal to one, and numerically solving for $b_x(t)$, $b_y(t)$, and $b_z(t)$ with the initial conditions $b_x(0) = b_y(0) = b_z(0) = 1$, and $\dot{b}_x(0) = \dot{b}_y(0) = \dot{b}_z(0) = C_Q(0) = 0$. Removing the viscosity coefficients and the anharmonic correction factors removes the energy dependence from the expansion factors and creates an initial guess for b_z which does not itself depend on $\langle z^2 \rangle_0$. We then divide each $\langle z(t)^2 \rangle$ (where t is the expansion time corresponding to that measured width) by the corresponding $b_z^2(t)$ to produce a calculated $\langle z^2 \rangle_0$ from *every* measured z-width, as all widths must expand from the same initial value. Using the z-width at every time greatly improves the statistics compared to that obtained using a single time point, giving a more accurate estimate of the initial width. All of these values for $\langle z^2 \rangle_0$ are then averaged (with the appropriate weight given to each point based on the error bar) to produce a single $\langle z^2 \rangle_0$ for that data set.

This value of $\langle z^2 \rangle_0$ now allows the inclusion of the anharmonic correction factor $h_A[\langle z^2 \rangle_0]$ and the viscosity dependent terms, where $\bar{\alpha}_S$ and $\bar{\alpha}_B$ are still unknown. To determine $\bar{\alpha}_S$, we set the much smaller $\bar{\alpha}_B$ equal to zero and use $\bar{\alpha}_S$ given by Eq. 5.123:

$$\bar{\alpha}_S = \bar{\alpha}_{S0} + \bar{\alpha}_{S2}\,\Gamma^{2/3}(t). \tag{7.18}$$

For the unitary gas, $\bar{\alpha}_{S2} = 0$, so $\bar{\alpha}_{S0}$ is equivalent to $\bar{\alpha}_S$. We then use $\bar{\alpha}_{S0}$ as the single χ^2 fitting parameter to plots of the measured transverse aspect ratio as a function of time[2].

Once a fitted value for $\bar{\alpha}_{S0}$ has been extracted from the transverse aspect ratio, the expansion factors are recalculated using this value of $\bar{\alpha}_{S0}$ as an *input*, along

---

[2]See Chapter 4 for a discussion of why the transverse aspect ratio is preferred over a longitudinal aspect ratio when quantifying a shear viscosity coefficient.

with the initial calculation of $\langle z^2 \rangle_0$. These new expansion factors will produce a new value for $\langle z^2 \rangle_0$ when applied to each measured $\langle z^2 \rangle$, therefore changing the size of the anharmonic correction factor and the value of $\bar{\alpha}_{S0}$ returned from the fit to the transverse aspect ratio. This new $\bar{\alpha}_{S0}$ is used to recalculate the expansion factors, and this procedure continues until it produces a z-width that agrees with the z-width that the previous cycle to within 3 significant figures. At this point, the cycle stops and we are left with self-consistent values of $\langle z^2 \rangle_0$ and $\bar{\alpha}_{S0}$.

Before reporting these values below, we first present samples of transverse aspect ratio data taken in the unitary gas, given as the top four curves in Figure 7.2. For comparison, the aspect ratio of the non interacting gas at 528 G is also shown, which never exceeds a value of one. This indicates the formation of a circular cloud, and a lack of interactions as described in Section 4.5. The unitary gas curves, in contrast, all reach an aspect ratio larger than one, demonstrating the elliptic flow also discussed in Chapter 4. If viscosity is neglected, Eq. 7.10 for the hydrodynamic expansion factors gives $\ddot{b}_i = \bar{\omega}_i^2/(\Gamma^{2/3}b_i)$, indicating that the initially smaller direction with the larger $\bar{\omega}_i^2$ will have a larger acceleration and surpass the initially larger direction in its final size. However, the observed decrease in the value that the aspect ratio reaches for the higher energies in the unitary gas data indicates that the shear viscosity increases with increasing energy. A smaller aspect ratio corresponds to the more rapidly expanding direction losing more of its translational energy, which is instead transferred to the more slowly expanding, initially larger direction. This larger transfer of momentum as a function of energy is the result of increased shear viscosity.
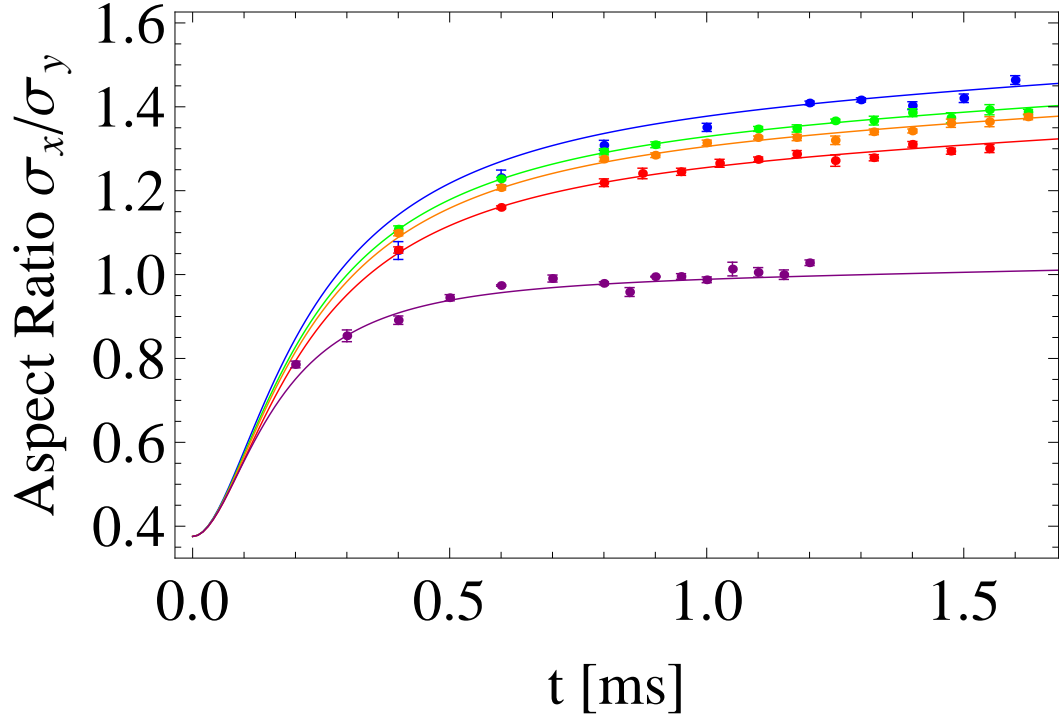
Figure 7.2: Transverse aspect ratio σ_x/σ_y versus time after release from an optical trap, demonstrating elliptic hydrodynamic flow. Top to bottom: Resonantly interacting gas at $834\,G$, $E = 0.66\,E_F$, $E = 0.89\,E_F$, $E = 1.17\,E_F$, $E = 1.46\,E_F$, ballistic gas at $528\,G$, $E = 1.78\,E_F$. Top four solid curves: Hydrodynamic theory with the shear viscosity as the only fit parameter; Lower solid curve: Ballistic theory with no free parameters. Error bars denote statistical fluctuations.

## 7.5 Results of the Unitary Shear Viscosity Measurement

For the unitary gas, where exact expressions for many thermodynamic quantities are known, we may plot $\bar{\alpha}_{S0}$ as a function of $\widetilde{E}$, the energy per particle E, or the temperature T. Though $\widetilde{E}$ is the only energy scale required in the hydrodynamic equations necessary to determine $\bar{\alpha}_{S0}$, E can be calculated directly from the measured value of $\langle z^2 \rangle_0$ using the formula given by Eq. 6.81,

$$E = 3\,m\,\omega_{zopt}^2 \langle z^2 \rangle_0 \left(1 - \frac{3}{4} \lambda_1 \langle z^2 \rangle_0 \right) + 3\,m\,\omega_{z\,mag}^2 \langle z^2 \rangle_0 \tag{7.19}$$

where the anharmonic correction $\left(1 - \frac{3}{4} \lambda_1 \langle z^2 \rangle_0 \right)$ requires the same λ_1 used in $h_A[\langle z^2 \rangle_0]$. Additionally, previous measurements of the entropy as a function of E in the unitary regime [54, 55] allow knowledge of the temperature through the relation $T = \partial E / \partial S$, presenting a third option for how $\bar{\alpha}_{S0}$ can be displayed. Below, we shall discuss all three.

First, we plot $\bar{\alpha}_{S0}$ in Fig. 7.3 as a function of E/E_F, where $E_F = (3N)^{1/3} \hbar \bar{\omega}$ is the Fermi energy of an ideal gas at the trap center. With a typical total number of atoms $N \simeq 2.5 \times 10^5$, and $\bar{\omega} \equiv (\omega_x \omega_y \omega_z)^{1/3}$, $E_F \simeq k_B \times 2.0\,\mu\text{K}$. We identify the normal fluid data points that fall within $0.6 < E/E_F < 2.0$, which include all but the three lowest energy points. Note that for these three data points, the viscosity appears to decrease very rapidly as the energy decreases, likely the result of an increasing, zero viscosity superfluid component. For the remaining normal fluid points, we fit a function of the form

$$c_1 E/E_F + c_3 (E/E_F)^3, \tag{7.20}$$
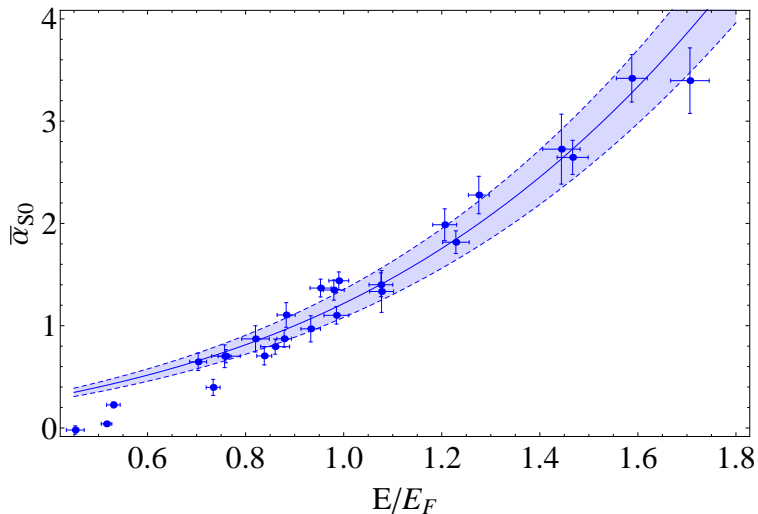
Figure 7.3: Density averaged shear viscosity, $\bar{\alpha}_{S0}$, defined by Eq. 7.18, of the unitary Fermi gas (834 G) versus energy E for $E/E_F < 2.0$. $\bar{\alpha}_{S0}$ is the trap-averaged shear viscosity coefficient from the fit using Eq. 7.17 and the iterative procedure described in the main text. The solid blue curve shows the fit $0.66\, E/E_F + 0.56\, (E/E_F)^3$ to the normal fluid $0.6 < E/E_F < 2.0$ data (we exclude the three lowest energy points, in the superfluid regime). The dashed lines enclosing the shaded region denote the range arising from the uncertainty in the fit coefficients.

and find $c_1 = 0.66(0.08)$ and $c_3 = 0.56(0.06)$. This curve is given in Figure 7.3, along with a shaded region showing the range allowed by the fit coefficient error bars.

This data immediately invites comparison to previously measured values for $\bar{\alpha}_{S0}$ given in [5], where $\bar{\alpha}_{S0}$ was measured with two separate techniques for two separate energy regimes. For $E/E_F > 2$, the $\bar{\alpha}_{S0}$ values reported in Ref. [5] were extracted from fits to the *longitudinal* aspect ratio for a *cylindrically symmetric* trap that was 50 times deeper than the trap presently used. For $E/E_F < 2.5$ the viscosity was determined from a separate study of collective mode damping. Thus, the present work is the first measurement of shear viscosity in the low energy
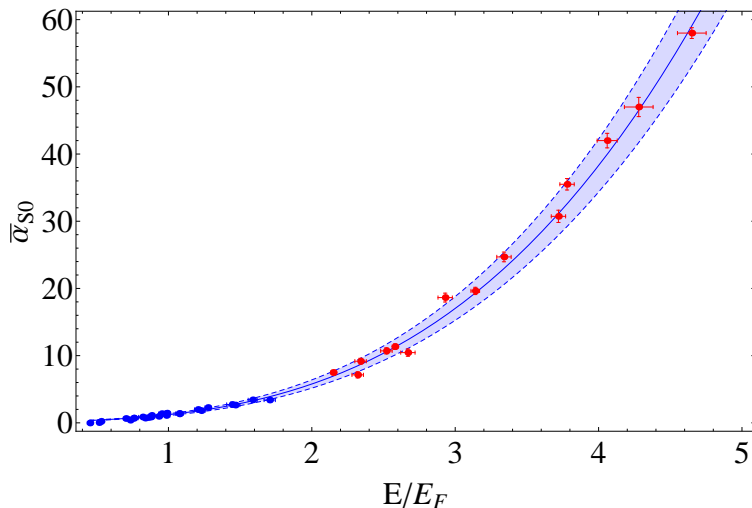
Figure 7.4: Density averaged shear viscosity, $\bar{\alpha}_{S0}$, of the unitary Fermi gas as a function of energy E. Blue circles for $E/E_F < 2.0$ show data from fits to the transverse aspect ratio presented in this dissertation. Red circles for $E/E_F > 2.0$ show data from Ref. [5]. The solid curve shows that the fit $0.66\,E/E_F + 0.56\,(E/E_F)^3$, obtained using only the low energy $0.6 < E/E_F < 2.0$ data, is in very good agreement with the high energy $E/E_F > 2.0$ data. The dashed lines denote the range arising from the uncertainty in the fit coefficients.

regime using expansion of the gas, the advantages of which will be discussed below.

To compare to the high energy data of Ref. [5], we use the *same* values found above for c_1 and c_3 to extrapolate the fitted curve all the way up to an E/E_F of 5. On this curve we place all of the expansion data given in Ref. [5] as red data points, shown in Figure 7.4. The excellent agreement between the two is prime example of universal scaling. Despite the difference in trap depths and the different aspect ratios used to study the different clouds, the whole energy range is well characterized by the fit to the present low energy data.

The low energy expansion data from the present work is compared to previous low energy viscosity data obtained from collective mode damping [5] in Figure
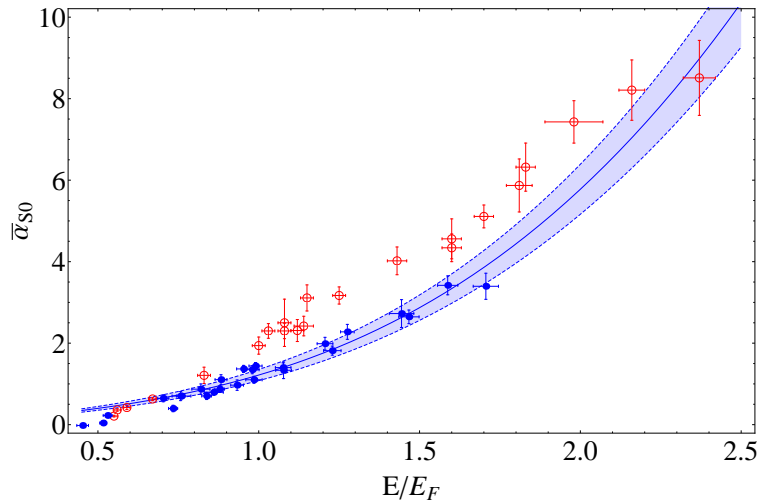
Figure 7.5: Shear viscosity coefficient $\bar{\alpha}_{S0}$ for a resonantly interacting Fermi gas versus energy. Blue solid circles from measurement of the transverse aspect ratio versus time after release (present work). Red open circles from collective mode damping, Ref. [5]. The solid curve shows the fit $0.66\, E/E_F + 0.56\, (E/E_F)^3$, as discussed above and shown in the previous two figures.

7.5. Aside from the very lowest energy data points, the collective mode damping data is systematically higher. To explain this, we consider damping effects beyond shear viscosity that could occur in a collective oscillation. One important difference between collective modes and expansion techniques is that expansion process occurs over a relatively long time scale compared to period of collective oscillation. In a collective mode performed at higher energies, the thermalization rate is comparable to or less than the collective oscillation frequency. This causes a breakdown of hydrodynamics, and more ballistic behavior that results in greater damping. Additionally, if a ballistic component were to be present at the cloud edge, it would repeatedly interact with the hydrodynamic part during each oscillation cycle, or even vibrate out of phase.

Next, the present values of $\bar{\alpha}_{S0}$ are displayed in Figure 7.6 as function of the
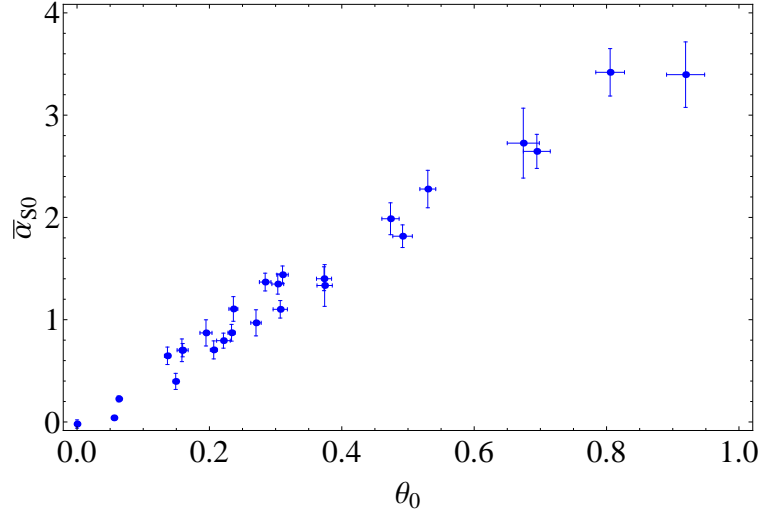
Figure 7.6: Shear viscosity coefficient $\bar{\alpha}_{S0}$ for a resonantly interacting Fermi gas versus reduced temperature θ_0 at the trap center.

initial reduced temperature at the trap center

$$\theta_0 \equiv \frac{T}{T_F(n_0)} = \frac{T}{T_{FI}} \left(\frac{n_I}{n_0}\right)^{2/3}, \tag{7.21}$$

where n_0 is the density at the trap center, $T_F(n_0)$ is the local Fermi temperature at the trap center given by $T_F(n_0) = \hbar^2 \left(3\pi^2 n_0\right)^{2/3}/(2mk_B)$, and $T_{FI} = E_F/k_B = T_F(n_I)$ is the Fermi temperature of an ideal gas with density n_I at the trap center. T/T_{FI} is determined from the temperature calibration in Ref [6].

Finally, the numerical values of $\bar{\alpha}_{S0}$, E/E_F, and $T/T_F(n_0)$ used to produce Fig 7.3-7.6 are given in Table 7.2.

	E/E_F	$T/T_F(n_0)$	$\bar{\alpha}_{S0}$
1	0.452(18)	0.000(2)	-0.02(4)
2	0.526(10)	0.056(2)	0.040(7)
3	0.530(14)	0.063(2)	0.23(3)
4	0.703(17)	0.137(5)	0.65(8)
5	0.733(14)	0.149(4)	0.39(8)
6	0.757(13)	0.158(4)	0.70(11)
7	0.760(30)	0.159(8)	0.70(6)
8	0.820(28)	0.195(9)	0.79(7)
9	0.837(15)	0.206(5)	0.87(8)
10	0.860(30)	0.221(10)	0.79(7)
11	0.879(14)	0.233(5)	0.87(8)
12	0.883(18)	0.236(6)	1.11(12)
13	0.933(20)	0.270(8)	0.97(13)
14	0.953(22)	0.284(9)	1.37(8)
15	0.980(21)	0.303(9)	1.35(9)
16	0.985(25)	0.307(10)	1.10(8)
17	0.990(20)	0.310(8)	0.97(13)
18	1.07(2)	0.373(11)	1.37(8)
19	1.08(2)	0.374(11)	1.35(9)
20	1.21(2)	0.474(13)	1.99(16)
21	1.23(3)	0.492(15)	1.81(11)
22	1.28(2)	0.530(14)	2.27(18)
23	1.44(4)	0.674(24)	2.72(34)
24	1.47(3)	0.694(24)	2.65(16)
25	1.59(3)	0.805(21)	3.41(23)
26	1.70(4)	0.919(29)	3.39(32)

Table 7.2: The total energy per particle E/E_F, the temperature $T/T_F(n_0)$, where n_0 is the density at the cloud center, and the shear viscosity coefficient $\bar{\alpha}_{S0}$ for a resonantly interacting Fermi gas.

7.6 Observation of Scale Invariance in the Expansion of a Unitary Fermi Gas

Although the transverse aspect ratio of unitary gas exhibits elliptical, hydrodynamic flow and a significantly energy dependent shear viscosity, we now demonstrate that the mean square cloud *radius* of the gas expands identically to a non-interacting gas.

For a non-interacting gas confined in a potential U that is extinguished at t=0 to allow expansion into free space, the mean square radius of the entire gas obeys the ballistic result Eq. 5.2:

$$\langle \mathbf{r}^2 \rangle = \langle \mathbf{r}^2 \rangle_0 + \frac{t^2}{m} \langle \mathbf{r} \cdot \nabla U \rangle_0. \tag{7.22}$$

In our experimental system, we extinguish the optical potential, so that $\langle \mathbf{r}^2 \rangle$ for a single component hydrodynamic system expands according to Eq. 4.110

$$\frac{d^2}{dt^2} \frac{m \langle \mathbf{r}^2 \rangle}{2} = \langle \mathbf{r} \cdot \nabla U_{Opt} \rangle_0 + \frac{3}{N} \int [(\Delta P) - (\Delta P)_0] d^3 \mathbf{r} - 3 \hbar \langle \alpha_B \nabla \cdot \mathbf{v} \rangle, \tag{7.23}$$

which reduces to the scale invariant, ballistic result[3]

$$\langle \mathbf{r}^2 \rangle = \langle \mathbf{r}^2 \rangle_0 + \frac{t^2}{m} \langle \mathbf{r} \cdot \nabla U_{opt} \rangle_0, \tag{7.24}$$

provided that there is a zero bulk viscosity coefficient α_B, and no deviation from the ideal gas equation of state $P = (2/3)\mathcal{E}$ so that $\Delta P = P - (2/3)\mathcal{E} = 0$.

---

[3]Note that in Eq. 7.23 we have neglected the the one percent effect on $\langle \mathbf{r}^2 \rangle$ originating from a finite change in magnetic potential energy during expansion given by ΔU_{mag}. This has been properly accounted for in the data, and how this is done will be explained in the next section.

Eq. 7.24 is dependent on the initial cloud size and energy. However, we may remove these dependencies and compare different scale invariant systems beginning from different initial cloud sizes by arranging Eq. 7.24 to give

$$m[\langle \mathbf{r}^2 \rangle - \langle \mathbf{r}^2 \rangle_0]/\langle \mathbf{r} \cdot \nabla U_{opt} \rangle_0 = t^2, \tag{7.25}$$

motivating the definition

$$\tau^2(t) \equiv m[\langle \mathbf{r}^2 \rangle - \langle \mathbf{r}^2 \rangle_0]/\langle \mathbf{r} \cdot \nabla U_{opt} \rangle_0. \tag{7.26}$$

Through Eq. 7.26, we construct a quantity that is independent of the initial energy, and should obey $\tau^2(t) = t^2$ provided that the system is scale invariant.

We demonstrate scale invariant behavior by plotting $\tau^2(t)$ for different energies in Figure 7.7, which includes a reprint of Figure 7.2 to emphasize that both graphs display different combinations of mean square cloud widths generated from *the same data*, including the non interacting gas. In contrast to the aspect ratio curve, which varies substantially with energy and shear viscosity as described above, the combined $\tau^2(t)$ lies on a single t^2 curve with a $\chi^2 = 1.1$ using no free parameters. The aspect ratio data provides a crucial comparison. First, it serves as a reminder that the unitary system is indeed hydrodynamic, as the aspect ratio exhibits elliptic flow. If the mean square cloud radius data were presented alone, one would incorrectly conclude that the system is simply ballistic, and the t^2 scaling is trivial. The aspect ratio shows that this is not the case. Second, comparison of these two plots shows that shear viscosity does not spoil scale invariance. Mechanically, the momentum that shear viscosity removes from the rapidly expanding x-direction is redistributed among the other two directions such
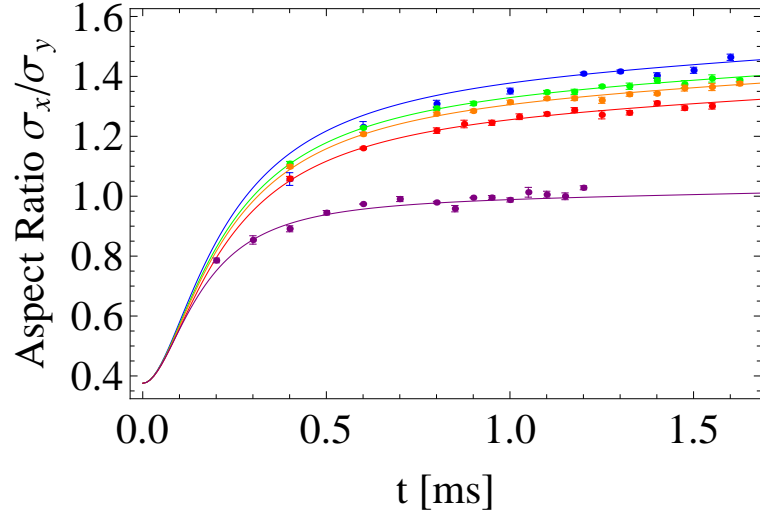
(a) Transverse aspect ratio σ_x/σ_y, from Fig. 7.2
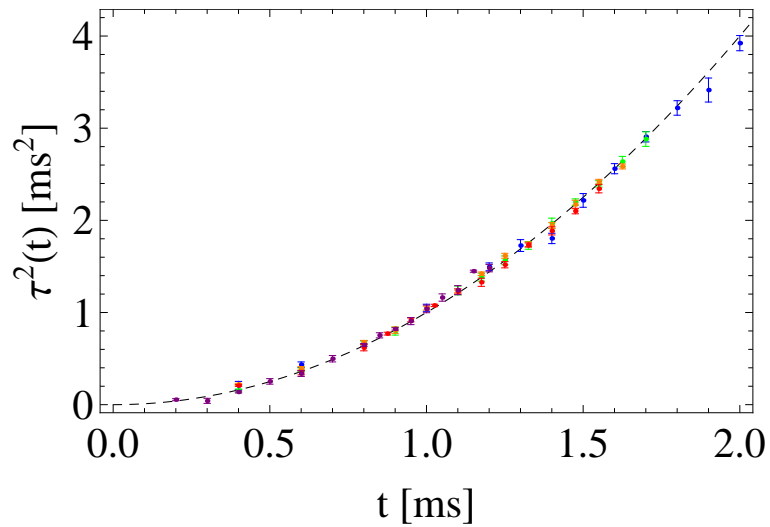
(b) $\tau^2(t) \equiv m(\langle \mathbf{r}^2 \rangle - \langle \mathbf{r}^2 \rangle_0)/\langle \mathbf{r} \cdot \nabla U \rangle_0$

Figure 7.7: Scale invariant expansion of a resonantly interacting Fermi gas. Experimental values of $\tau^2(t) \equiv m[\langle \mathbf{r}^2 \rangle - \langle \mathbf{r}^2 \rangle_0]/\langle \mathbf{r} \cdot \nabla U \rangle_0$ versus time t after release, for the same data as in Fig. 7.2 collapse onto a single curve, demonstrating universal t^2 scaling. Data shown is from the resonantly interacting gas at $834\,G$, $E = 0.66\,E_F$, $E = 0.89\,E_F$, $E = 1.17\,E_F$, $E = 1.46\,E_F$, and the ballistic gas at $528\,G$, $E = 1.78\,E_F$. Dashed curve $\tau^2(t) = t^2$, as predicted by Eq. 7.26. Note that the noninteracting gas data is included in both figures.

that the t^2 scaling is maintained.

In Chapter 4, the equation of state for the resonantly interacting Fermi was demonstrated to be identical to the non interacting gas result, $P = (2/3)\mathcal{E}$. One crucial assumption that went into this derivation for the unitary gas was a condition of local thermal equilibrium. For the unitary gas data to collapse onto a single $\tau^2(t)$ curve with the non interacting gas demonstrates that $\Delta P = 0$ throughout expansion, indicating that local thermal equilibrium and the equation of state $P = (2/3)\mathcal{E}$ maintained in the expansion process.

7.7 Measurement of the Unitary Bulk Viscosity

Theoretically, the bulk viscosity is predicted to vanish in the scale invariant regime, [24,44,56,57], consistent with the bulk viscosity frequency sum rule, which vanishes when $\Delta P = 0$ [58]. Having qualitatively demonstrated scale invariance above, we now assume that the explicit ΔP term in the mean square cloud radius expansion equation is zero, attributing any conformal symmetry breaking effect to the bulk viscosity as single fit parameter.

Starting with general equation for the time evolution of $\langle \mathbf{r}^2 \rangle$, Eq. 4.110,

$$\frac{d^2}{dt^2} \frac{m \langle \mathbf{r}^2 \rangle}{2} = \langle \mathbf{x} \cdot \nabla U_{Opt} \rangle_0 + \frac{3}{N} \int [(\Delta P) - (\Delta P)_0] d^3\mathbf{x} - 3\,\hbar\,\langle \alpha_B \nabla \cdot \mathbf{v} \rangle + \Delta U_{Mag}.$$

(7.27)

we first set ΔP to 0. As before, we take $\langle \mathbf{x} \cdot \nabla U_{Opt} \rangle_0 = m(3\,\omega_{zopt}^2 h_A[\langle z^2 \rangle_0] + 2\omega_{z\,mag}^2)\langle z^2 \rangle_0$. As reasoned in Chapter 5, we take $\bar{\alpha}_B$ to be a time dependent quantity given by Eq. 5.107 $\overline{\alpha}_B = \overline{\alpha}_B(t) = \overline{\alpha}_B(0)\,\Gamma^{2/3}(t)$ and $\nabla \cdot \mathbf{v}$ to be position

independent and equal to $\dot{\Gamma}/\Gamma$ (see Chapter 4) so that

$$3\,\hbar\,\langle\alpha_B\,\nabla\cdot\mathbf{v}\rangle = 3\,\hbar\,\overline{\alpha}_B(0)\,\Gamma^{2/3}\frac{\dot{\Gamma}}{\Gamma}. \tag{7.28}$$

Given by Eq. 4.109, we write ΔU_{mag} (a one percent effect on the expansion of $\langle\mathbf{r}^2\rangle$) in terms of the initial cloud sizes and expansion factors where the potential is time dependent:

$$
\begin{aligned}
\Delta U_{Mag} &= 4\langle U_{Mag}\rangle_0 - 4\langle U_{Mag}\rangle \tag{7.29}\\
&= 4\left(-\frac{1}{2}\langle x^2\rangle_0\,2\,\omega_{mag}^2 + \frac{1}{2}\langle y^2\rangle_0\,\omega_{mag}^2 + \frac{1}{2}\langle z^2\rangle_0\,\omega_{mag}^2\right)\\
&\quad - 4\left(-\frac{1}{2}\langle x^2\rangle_0\,2\,\omega_{mag}^2\,b_x^2(t) + \frac{1}{2}\langle y^2\rangle_0\,\omega_{mag}^2\,b_y^2(t) + \frac{1}{2}\langle z^2\rangle_0\,\omega_{mag}^2\,b_z^2(t)\right).
\end{aligned}
$$

We then insert Eq. 7.30 into

$$\frac{d^2}{dt^2}\frac{m\langle\mathbf{r}^2\rangle}{2} = \Delta U_{mag}, \tag{7.30}$$

which is numerically solved and subtracted from the data. The evolution equation for $\langle\mathbf{r}^2\rangle$ which we will fit to unitary data is then:

$$\frac{d^2}{dt^2}\frac{m\langle\mathbf{r}^2\rangle}{2} = m\left(3\,\omega_{zopt}^2 h_A[\langle z^2\rangle_0] + 2\omega_{z\,mag}^2\right)\langle z^2\rangle_0 - 3\,\hbar\,\overline{\alpha}_B(0)\,\Gamma^{2/3}\frac{\dot{\Gamma}}{\Gamma}. \tag{7.31}$$

with the initial conditions $\langle\mathbf{r}^2\rangle_0 = \langle x^2\rangle_0 + \langle y^2\rangle_0 + \langle z^2\rangle_0$ and $d/dt\langle\mathbf{r}^2\rangle = 0$, so that $\overline{\alpha}_B(0)$ is the only fit parameter.

A fit to $\langle\mathbf{r}^2\rangle$ using $\overline{\alpha}_B(0)$ as the only fit parameter is possible because fits to the transverse aspect ratio aspect ratio *of the same data* have already provided self-consistent values for $\langle z^2\rangle_0$, b_x, b_y, and b_z. Although the expansion factors

are shear viscosity dependent, they only come into the $\langle \mathbf{r}^2 \rangle$ evolution if ω_{mag} and $\overline{\alpha}_B(0)$ are finite. Thus, the measurement of the shear viscosity not only provides a comparison between the relative sizes of $\overline{\alpha}_B$ and $\overline{\alpha}_S$, but also determines the perturbative effects ΔU_{mag} and $\dot{\Gamma}/\Gamma$ in the bulk viscosity term.

7.8 Results of the Unitary Bulk Viscosity Measurement

The resulting values of $\overline{\alpha}_B(0)$ are shown in Figure 7.8 as a function of $\widetilde{E}/E_F$ along with $\bar{\alpha}_{S0}$ for comparison. Even with ΔP assumed to be zero and all conformal symmetry breaking effects attributed to the bulk viscosity, we find bulk viscosity remains zero over the full energy range studied. A weighted averaged of all the bulk viscosity data shown in Fig. 7.8 gives $\overline{\alpha}_B(0) = 0.00(0.04)$, further quantifying the degree to which the expansion is scale invariant.

The error reported in the energy averaged value of bulk viscosity includes both statistical and systematic contributions to the uncertainty. By an order of magnitude, the dominant contribution to the systematic uncertainty of the bulk viscosity measurement is the uncertainty z-direction trapping frequency, $\overline{\omega}_z = \sqrt{\omega_{z\,opt}^2 \, h_A[\langle z^2 \rangle_0] + \omega_{mag}^2}$. For this reason, the new methods used to determine $\omega_{z\,opt}$ from the aspect ratio of an expanding superfluid and $h_A[\langle z^2 \rangle_0]$ from the $\langle \mathbf{r}^2 \rangle$ expansion of a non-interacting gas, the subjects of Chapter 6, are crucial to our measurement of bulk viscosity.

In the time since this data was taken at 834 G, new measurements of the magnetic field value corresponding to the Feshbach resonance place it at a value of 832 G [30]. Using the form of ΔP that is derived in the high temperature limit
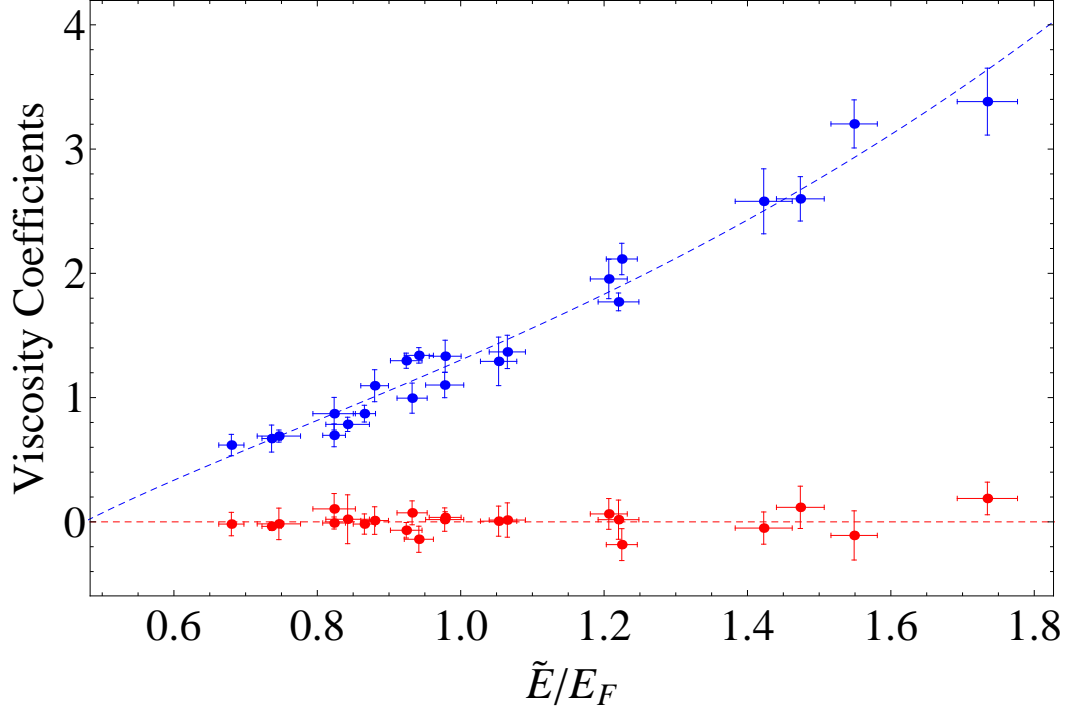
Figure 7.8: Measurement of bulk and shear viscosity for a scale-invariant Fermi gas. In blue, the trap-averaged shear viscosity coefficient $\int d^3\mathbf{r}\,\eta/(N\hbar) \equiv \bar{\alpha}_S$ versus energy $\widetilde{E}/E_F$. In red, the trap-averaged bulk viscosity coefficient $\overline{\alpha}_B(0)$ where $\int d^3\mathbf{r}\,\zeta_B/(N\hbar) \equiv \bar{\alpha}_B = \overline{\alpha}_B(0)\Gamma^{2/3}(t)$ versus energy. Bars denote statistical error. (Dashed curves added to guide the eye.) The data shown corresponds only to the normal fluid regime. Three data points below the superfluid transition temperature shown in the previous section dealing with shear viscosity results are neglected.

within Chapter5, we find that a difference in 2G produces systematic change in the value of $\overline{\alpha}_B(0)$ of 0.005, an order of magnitude less than our total error estimate given above.

Considering these possible error sources, our null result for the bulk viscosity is two orders of magnitude more stringent than a previous estimate by our group based on a consistency argument [6]. This previous argument was based on the expansion of the longitudinal aspect ratio for a relatively high, single energy at $E/E_F \simeq 3.3$ where $\alpha_S \simeq 25$. It was found that a χ^2 fit to the shear viscosity was minimized for a value of $\overline{\alpha}_B(0) = 0$, where negative values of $\overline{\alpha}_B(0)$ were not considered. However, careful examination shows the uncertainty in this estimate was $\simeq 4.0$.

7.9 Measurement of Conformal Symmetry Breaking

A qualitative comparison of $\tau^2(t)$ for data taken above, below, and on resonance is given in Figure 7.9. While a difference in the curvature appears to exist, the procedure described above for the resonant case will require significant modification in order to properly attribute the observed effect to ΔP, the bulk viscosity, or some combination of the two.

Off resonance, the analysis techniques described for the on resonant case can not be applied. As in the resonant case, we do not know the the initial z-width. Unlike the resonant case, we also have a finite ΔP. Previously, we could use a known scaling solution that allows us to iteratively find an initial z-width along with the shear viscosity. While we know how to include the effects of bulk viscosity
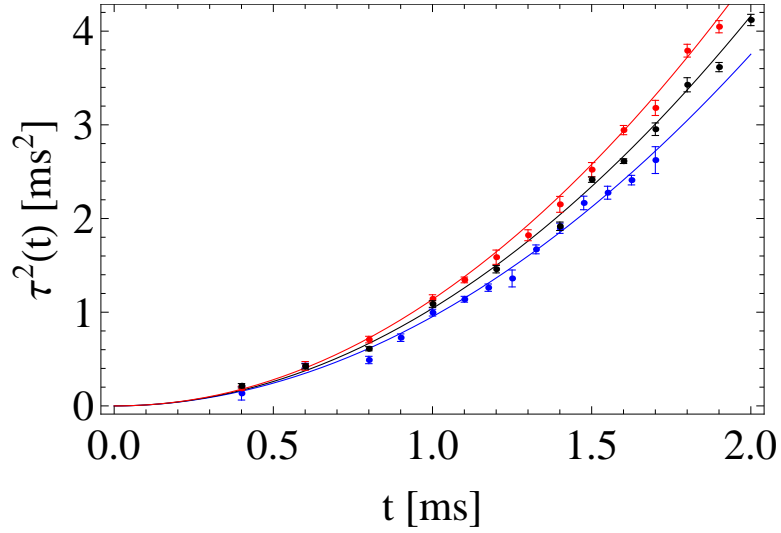
Figure 7.9: Conformal symmetry breaking in the expansion for a Fermi gas near a Feshbach resonance. The data are the experimental values of $\tau^2(t) \equiv m[\langle \mathbf{r}^2 \rangle - \langle \mathbf{r}^2 \rangle_0]/\langle \mathbf{r} \cdot \nabla U \rangle_0$ for $\widetilde{E}/E_F \simeq 1.0$, versus time t after release. Solid curves are the predictions using Eq. 4.110 with $\overline{\alpha}_B(0) = 0$, where the pressure change ΔP is approximated using the second virial coefficient without any free parameters. Top: $1/(k_{FI}a_S) = -0.59$; Center: $1/(k_{FI}a_S) = 0$; Bottom: $1/(k_{FI}a_S) = +0.61$.

and ΔP in the expansion factors, we can not hope to iteratively find $\langle z^2 \rangle_0$ through expansion factors consistent with not only with an unknown shear viscosity, but also the unknown bulk viscosity and ΔP. To find $\langle z^2 \rangle_0$ in a more general way, we instead perform a two parameter fit to the $\langle \mathbf{r}^2 \rangle_0$ data of the form

$$\langle \mathbf{r}^2 \rangle = c_0 + c_1 t^2 \tag{7.32}$$

with both c_1 and c_0 as fit parameters. Independent of the expansion factors, the fitted c_0 provides a value for $\langle \mathbf{r}^2 \rangle_0$, which for our trap geometry also well approximates $\langle z^2 \rangle_0$ through the relationship

$$\langle \mathbf{r}^2 \rangle_0 = \langle z^2 \rangle_0 \left(1 + \frac{\omega_z^2}{\omega_x^2} + \frac{\omega_z^2}{\omega_y^2} \right), \tag{7.33}$$

where $1 - \omega_z^2/\omega_x^2 - \omega_z^2/\omega_y^2 = 0.993 \approx 1$. From $\langle z^2 \rangle_0$, a value for $\langle \mathbf{r} \cdot \nabla U_{Opt} \rangle_0/m$ can be calculated.

This method allows us to determine both $\langle \mathbf{r}^2 \rangle_0$, the initial condition for the equation

$$\frac{d^2}{dt^2} \frac{m \langle \mathbf{r}^2 \rangle}{2} = \langle \mathbf{x} \cdot \nabla U_{Opt} \rangle_0 + \frac{3}{N} \int [(\Delta P) - (\Delta P)_0] d^3 \mathbf{x} - 3\hbar \langle \alpha_B \nabla \cdot \mathbf{v} \rangle + \Delta U_{Mag}, \tag{7.34}$$

and the quantity $\langle \mathbf{x} \cdot \nabla U_{Opt} \rangle_0$ without the use of expansion factors. For a known ΔU_{mag} and a scale invariant system where $\Delta P = \alpha_B = 0$ the values of $\langle \mathbf{r}^2 \rangle_0$ and $\langle \mathbf{r} \cdot \nabla U_{Opt} \rangle_0/m$ should determine the behavior of $\langle \mathbf{r}^2 \rangle$ exactly. If we treat the unitary gas as the zeroth order system that ΔP, $3\hbar \langle \alpha_B \nabla \cdot \mathbf{v} \rangle$, and ΔU_{Mag} are all perturbations to, then we are justified using the unitary gas expansion factors within these three additional terms *only*. In doing so, we may determine their

individual contributions to the total deviation from scale invariant flow.

A central idea of this technique is that both $\langle \mathbf{r}^2 \rangle_0$ and $\langle \mathbf{r} \cdot \nabla U_{Opt} \rangle_0 / m$ can be found from $c_0 = \langle \mathbf{r}^2 \rangle_0 \simeq \langle z^2 \rangle_0$. However, relating $\langle z^2 \rangle_0$ to $\langle \mathbf{r} \cdot \nabla U_{Opt} \rangle_0 / m$ requires $\bar{\omega}_z^2$. Within the analysis of the bulk viscosity in the unitary gas, it was shown that $\bar{\omega}_z^2 = \omega_{z\,opt}^2 \, h_A[\langle z^2 \rangle_0] + \omega_{mag}^2$, emphasized as containing the anharmonic correction factor $h_A[\langle z^2 \rangle_0]$, is the primary contribution to systematic errors in the measurement of bulk viscosity. Depending on the sizes of new systematic errors introduced by determining $\langle z^2 \rangle_0$ from c_1, it is not clear that the same anharmonic correction should be applicable to this new fitting procedure. Therefore, we first apply the $\langle \mathbf{r}^2 \rangle = c_0 + c_1 t^2$ fitting technique to the unitary data, where the $\langle \mathbf{r}^2 \rangle$ expansion has been separately characterized using the techniques described in the previous sections, so that the relationship between c_1 and c_0 in the unitary gas will establish a reference for anharmonically correcting the data taken at a finite scattering length.

We will start with definition of $h_A[\langle z^2 \rangle_0]$ given in Chapter 6 by Eq. 6.57:

$$h_A[\langle z^2 \rangle_0] \equiv \frac{c_1}{3\,\omega_{z\,opt}^2 \langle z^2 \rangle_0} - \frac{2}{3} \frac{\omega_{mag}^2}{\omega_{z\,opt}^2}. \tag{7.35}$$

In Chapter6, this equation determined the anharmonic correction we have used thus far by studying the values of c_1 and $\langle z^2 \rangle_0$ in the non-interacting gas at 528 G. This definition is particularly useful because the $2\omega_{mag}^2 / 3\omega_{opt}^2$ removes the primary[4] effect of the bias magnetic field, leaving only anharmonicity to change $h_A[\langle z^2 \rangle_0]$ from a value of one at 528 G. A key difference, however, is that $\langle z^2 \rangle_0$

---

[4]The effect of ΔU_{mag} on the expansion of $\langle \mathbf{r}^2 \rangle$ is a one percent effect, compared to the roughly eight percent effect of $2\omega_{mag}^2 / 3\omega_{z\,opt}^2$ on the expansion of $\langle \mathbf{r}^2 \rangle$ at 834 G. At 528 G, the effect of ΔU_{mag} is less than a tenth of a percent.

was determined from expansion factors, where it will now be determined from c_0. We will also generalize $h_A[\langle z^2 \rangle_0]$ to all magnetic fields and make the field we are using explicit by defining

$$h_A[B, \langle z^2 \rangle_0] \equiv \frac{c_1[B]}{3\,\omega_{z\,opt}^2 \langle z^2 \rangle_0} - \frac{2}{3} \frac{\omega_{mag}^2[B]}{\omega_{z\,opt}^2}. \tag{7.36}$$

This expression clarifies that, in general, c_1 is a magnetic field dependent quantity not only through ΔU_{mag}, but also through the conformal symmetry breaking that the magnetic field dependent scattering length produces. With this in mind, to every unitary data set we fit $\langle \mathbf{r}^2 \rangle = c_0 + c_1 t^2$, determine $\langle z^2 \rangle_0$ from c_0, and using the known value of $\omega_{z\,opt}^2$ and ω_{mag}^2 as inputs, calculate values for $h_A[834, \langle z^2 \rangle_0]$. To all of these calculated $h_A[834, \langle z^2 \rangle_0]$ values, we fit a line to obtain a continuous $h_A[834, \langle z^2 \rangle_0]$ as a function of $\widetilde{E}$. We can now characterize the curvature of $\langle \mathbf{r}^2 \rangle$ as a function of time at any field through the ratio,

$$Q_B \equiv \frac{h_A[B, \langle z^2 \rangle_0]}{h_A[834, \langle z^2 \rangle_0]}. \tag{7.37}$$

which is 1 at 834 G by construction.

We can predict how Q_B should vary from a value of unity off-resonance by performing double time integrals on Eq. 5.101,

$$\frac{3}{N} \int [\Delta P - \Delta P_0]\, d^3\mathbf{x} = \lambda_P \frac{\widetilde{E}}{m} \frac{3\sqrt{6}}{4} \left(\frac{E_F}{\widetilde{E}} \right)^{7/2} \frac{1}{k_F a} [\Gamma^{-1/3} f_2{}'(x) - f_2{}'(x_0)]. \tag{7.38}$$

and Eq 5.118

$$3\,\hbar\,\langle\alpha_B\,\nabla\cdot\mathbf{v}\rangle \;=\; \lambda_B\,3\,\hbar\,\bar\alpha_B(0)\,\Gamma^{2/3}\frac{\dot\Gamma}{\Gamma} \tag{7.39}$$

$$\bar\alpha_B(0) \;=\; \frac{9}{32}\frac{1}{(k_{FI}a_s)^2}\left(\frac{E_F}{\widetilde{E}}\right)^4. \tag{7.40}$$

where λ_P and λ_B are added as dimensionless fit parameters. Note that λ_P and λ_B are the *only* fit parameters, as every other quantity is derived from theory described in Chapter 5. As stated, unitary expansion factors are used in these expressions to write the volume scale factor $\Gamma(t) = b_x(t)\,b_y(t)\,b_z(t)$. We are now able to perform a two parameter fit to the measured quantity Q_B given by Eq. 7.37 at 986 G and 760 G, with λ_P and λ_B as the fitting parameters.

## 7.10 Results of the Conformal Symmetry Breaking Analysis

We first establish a bench mark for the use of the $\langle\mathbf{r}^2\rangle = c_0 + c_1 t^2$ fits by presenting the ratio Q_B for the resonantly interacting gas in Figure 7.10. It is clear from the fluctuations around the value of one that the there is noise inherent in the $\langle\mathbf{r}^2\rangle = c_0 + c_1\,t^2$ method. This is simply the result of a two parameter $c_0 = \langle\mathbf{r}^2\rangle_0 \simeq \langle z^2\rangle$ and c_1 fit, as opposed to finding a fixed $\langle\mathbf{r}^2\rangle_0$ and $\langle z^2\rangle$ through the scaling solution in the unitary case and fitting c_1 only.

For fields of 760 G and 986 G, which correspond to $1/(k_F a_s) = +0.61$ and $1/(k_F a_s) = -0.59$, respectively, we also plot Q_B in Fig. 7.11. While this data has similar noise to the unitary Q_B data, it is also clear that that the red data at $1/(k_F a_S) = -0.59$ is consistently above the unitary data, while the blue data
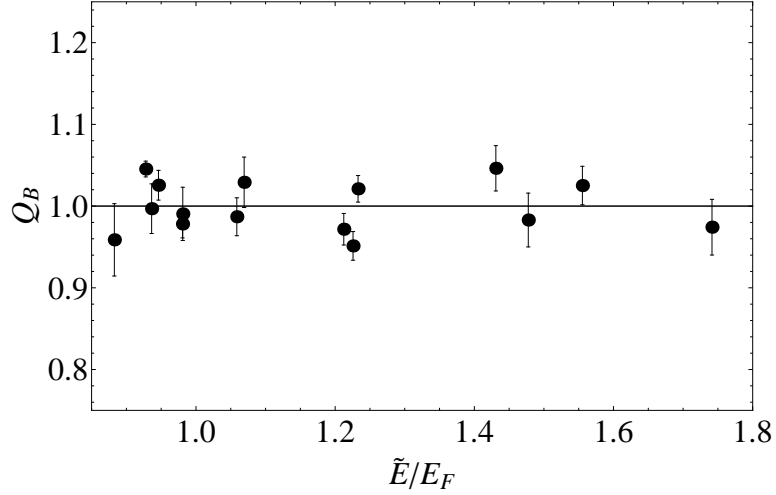
Figure 7.10: Q_B, given by Eq. 7.37, as a function of $\widetilde{E}/E_F$ for a resonantly interacting Fermi gas. The black dots are obtained from the fit to individual expansion curves to determine Q_B using $\langle \mathbf{r}^2 \rangle = c_0 + c_1\, t^2$ fits. The black horizontal line denotes the ideal value of unity.

at $1/(k_F a_s) = +0.61$ is consistently below, and even about a the unitary value of $Q_B = 1$. Note that Eq. 7.38 given above, which gives the effect of a finite ΔP on the expansion of $\langle \mathbf{r}^2 \rangle$, was shown in Chapter 5 to be an *odd* function of $1/(k_F a_s)$. Thus, Fig. 7.11 is a qualitative indication that a finite ΔP accounts for the majority of the deviation from scale invariant behavior, as a nonzero bulk viscosity (an even function of $1/a_s$), should shift both sets of finite a_s data downwards. The scaling parameters λ_p and λ_B, used to compare to expressions for ΔP and the bulk viscosity term derived in Chapter 5 are also shown for different sizes and their respective effects on Q_B in Fig. 7.11. The dashed lines show a predicted Q_B which includes $\lambda_p = 1$ and $\lambda_B = 0$, while the dotted lines show a Q_B for $\lambda_p = 1$ but a $\lambda_B = 1$. It therefor appears that a larger downward shift of both data sets is required to match the predicted value of bulk viscosity. However, the noise on the individual data points does not allow for a definitive statement
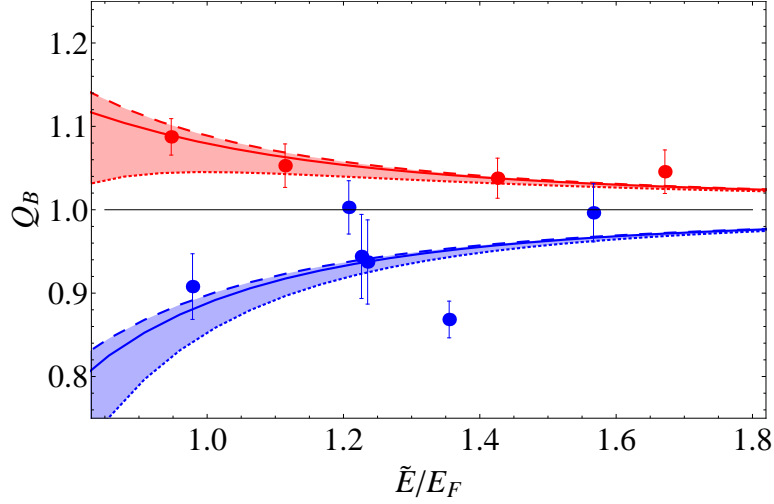
Figure 7.11: Contributions of a change to the equation of state ΔP and the bulk viscosity ζ_B to conformal symmetry breaking as a function of energy in an expanding Fermi gas. The data is fit with $\langle \mathbf{r}^2 \rangle = c_0 + c_1 t^2$ to produce the ratio Q_B (Eq. 7.37) and shown for the resonantly interacting gas $1/(k_{FI}a_S) = 0$ (black line-theory), for $1/(k_{FI}a_S) = -0.59$ (top, red dots) and for $1/(k_{FI}a_S) = +0.61$ (bottom, blue dots). Solid curves top and bottom show the best fit, where $\lambda_p = 1.07(0.25)$ and $\lambda_B = 0.20(0.55)$, see Fig. 7.12. The dashed (dotted) curves show the predictions for $\lambda_p = 1.07$ and $\lambda_B = 0$ ($\lambda_B = 1$), to illustrate the effect of the bulk viscosity.

from this graph alone.

For a more quantitative study of λ_B and λ_p, the χ^2 contour plot for the two parameter fit of λ_B and λ_p to the data are given in Figure 7.12. From this plot, it is determined that the best fit to the data is given by a value of $\lambda_p = 1.07(0.25)$ and $\lambda_B = 0.20(0.55)$. These values of λ_B and λ_p are additionally displayed in Fig. 7.11 as solid lines. It therefore appears that the bulk viscosity measured with this technique is smaller than predicted for the high temperature limit [24]. While this measured value is consistent with zero, its upper limit also places a constraint on the maximum value within the range of the predicted by [24]. Because the ΔP model adequately describes the data, this analysis indicates that the observed breaking of scale invariance is dominated by the finite scattering length directly changing the equation of state. It is also noteworthy that the expression used for ΔP that was derived in Chapter 5 in the *high temperature limit* is so consistent with data taken at $E/E_F \simeq 1$.

7.11 Measurement of the Shear Viscosity for a Finite Scattering Length

For a general scattering length, we previously derived a general form of the trap averaged shear viscosity given by Eq.5.123 to second order in $1/(k_F a_s)$:

$$\bar{\alpha} = \bar{\alpha}_{S0} + \bar{\alpha}_{S2} \, \Gamma^{2/3}(t), \tag{7.41}$$

where the second term represents a deviation away from the unitary value of $\bar{\alpha}_{S0}$ which we measured above. Off resonance, our goal is to measure $\bar{\alpha}_{S2}$ as a function
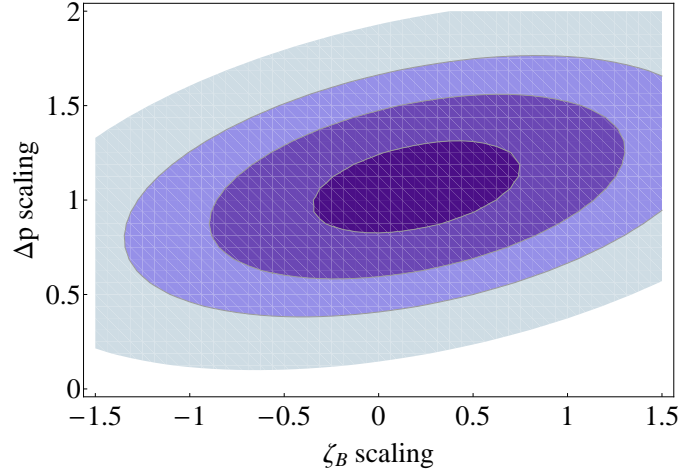
Figure 7.12: Contour plot of χ^2 for all of the off-resonance data as a function of λ_B and λ_p. The data shown in Fig. 7.11 are compared to the high temperature forms of α_B and ΔP using two scaling parameters, λ_p for Δp and λ_B for the bulk viscosity.

of scattering length and the energy scale $\widetilde{E}$ (or equivalently $\langle z^2 \rangle_0$).

Following the procedure used for the unitary gas exactly, all of the shear viscosity information will come from self consistent, iterative fits to the transverse aspect ratio for $\bar{\alpha}$ and $\langle z^2 \rangle_0$. Unlike the mean square cloud size, the transverse aspect ratio is insensitive to ΔP for the conditions of our experiment, so any change to the unitary equation of state can be neglected entirely. Thus, the only additional step in parameterizing the general shear viscosity requires that $\bar{\alpha}_{S0}$ already be known as a function of $\langle z^2 \rangle_0$ for the resonant case. We are then able to input $\bar{\alpha}_{S0}(\langle z^2 \rangle_0)$ and find $\bar{\alpha}_{S2}$.

To utilize our measurement of $\bar{\alpha}_{S0}$ in the unitary gas for the study of $\bar{\alpha}_{S2}$, we simply refit the above values of $\bar{\alpha}_{S0}$ as a function of $\widetilde{E}/E_F$. From this fit, we obtain $\bar{\alpha}_{S0}(\widetilde{E}) = 0.69(0.08)\,\widetilde{E}/E_F + 0.63(0.06)\,(\widetilde{E}/E_F)^3$. Neglecting ΔP in our determination of $\bar{\alpha}_{S0}$ is justified by the following numerical simulation using the

235

full hydrodynamic scaling solution in the general case of a finite scattering length. By including the anharmonic correction and expressing each width in terms of $\langle z^2 \rangle_0$ as in Eq.7.17, comparison to Eq.~refeq:6.1e given in Chapter 4 as:

$$\ddot{b}_i = \frac{\overline{\omega_i^2}}{\Gamma^{2/3} b_i} [1 + C_Q(t) + C_F(t) - C_F(0) - C_p(t)]$$

$$- \frac{\hbar \left(\bar{\alpha}_S \, \sigma_{ii} + \bar{\alpha}_B \, \frac{\dot{\Gamma}}{\Gamma} \right)}{m \langle x_i^2 \rangle_0 b_i} - \frac{\langle x_i \partial_i U_{Mag} \rangle}{m \langle x_i^2 \rangle_0 b_i}, \quad (7.42)$$

in addition to Eq. 5.95, Eq. 5.96 and Eq. 5.100 from Chapter 5 for $C_F(t)$, $C_F(0)$, and $C_p(t)$, respectively, give the general scaling solution as:

$$\ddot{b}_z = -\omega_{z\,mag}^2 \, b_z + \frac{\omega_{zopt}^2 h_A[\langle z^2 \rangle_0] + \omega_{z\,mag}^2}{\Gamma^{2/3} b_z} [1 + C_Q(t) + C_F(t) - C_F(0) - C_p(t)]$$

$$- \frac{\hbar \left(\bar{\alpha}_S \, \sigma_{ii} + \bar{\alpha}_B \, \frac{\dot{\Gamma}}{\Gamma} \right)}{b_z m \langle z^2 \rangle_0} \quad (7.43)$$

$$\ddot{b}_x = 2\,\omega_{z\,mag}^2 \, b_x + \frac{\omega_x^2 \, h_A[\langle z^2 \rangle_0]}{\Gamma^{2/3} b_x} [1 + C_Q(t) + C_F(t) - C_F(0) - C_p(t)]$$

$$- \frac{\hbar \left(\bar{\alpha}_S \, \sigma_{ii} + \bar{\alpha}_B \, \frac{\dot{\Gamma}}{\Gamma} \right) \omega_x^2 \, h_A[\langle z^2 \rangle_0]}{b_x \, m (\, \omega_{zopt}^2 h_A[\langle z^2 \rangle_0] + \omega_{z\,mag}^2) \langle z^2 \rangle_0} \quad (7.44)$$

$$\ddot{b}_y = -\omega_{z\,mag}^2 \, b_y + \frac{\omega_y^2 \, h_A[\langle z^2 \rangle_0]}{\Gamma^{2/3} b_y} [1 + C_Q(t) + C_F(t) - C_F(0) - C_p(t)]$$

$$- \frac{\hbar \left(\bar{\alpha}_S \, \sigma_{ii} + \bar{\alpha}_B \, \frac{\dot{\Gamma}}{\Gamma} \right) \omega_y^2 \, h_A[\langle z^2 \rangle_0]}{b_y \, m (\, \omega_{zopt}^2 h_A[\langle z^2 \rangle_0] + \omega_{z\,mag}^2) \langle z^2 \rangle_0} \quad (7.45)$$

$$\dot{C}_Q(t) = \frac{\Gamma^{2/3} \left(\hbar \, \bar{\alpha}_S \sum_i \sigma_{ii}^2 + 2\hbar \, \bar{\alpha}_B \frac{\dot{\Gamma}^2}{\Gamma^2} \right)}{3m(\, \omega_{zopt}^2 h_A[\langle z^2 \rangle_0] + \omega_{z\,mag}^2)\langle z^2 \rangle_0} \tag{7.46}$$

$$\sum_i \sigma_{ii}^2 = \frac{8}{3} \left(\frac{\dot{b}_x^2}{b_x^2} + \frac{\dot{b}_y^2}{b_y^2} + \frac{\dot{b}_z^2}{b_z^2} - \frac{\dot{b}_x \, \dot{b}_y}{b_x \, b_y} - \frac{\dot{b}_x \, \dot{b}_z}{b_x \, b_z} - \frac{\dot{b}_y \, \dot{b}_z}{b_y \, b_z} \right) \tag{7.47}$$

$$C_F(t) \equiv \frac{\Gamma^{2/3}(t) \frac{3}{N} \int \Delta P \, d^3\mathbf{x}}{\widetilde{E}} = \frac{3\sqrt{6}}{4} \left(\frac{E_F}{\widetilde{E}} \right)^{7/2} \frac{1}{k_F a} \, \Gamma^{2/3} \, f_2'(x) \tag{7.48}$$

$$C_F(0) \equiv \frac{\frac{3}{N} \int \Delta P_0 \, d^3\mathbf{x}}{\widetilde{E}} = \frac{3\sqrt{6}}{4} \left(\frac{E_F}{\widetilde{E}} \right)^{7/2} \frac{1}{k_F a} \, f_2'(x_0) \tag{7.49}$$

$$C_p(t) \equiv \frac{2 \int_1^{\Gamma(t)} \frac{d\Gamma}{\Gamma^{1/3}} \frac{1}{N} \int \Delta P \, d^3\mathbf{x}}{\langle \mathbf{x} \cdot \nabla U_{total} \rangle_0} = \frac{3}{2} \left(\frac{E_F}{\widetilde{E}} \right)^3 [f_2(x) - f_2(x_0)]. \tag{7.50}$$

where $f_2(x)' = sign(a) \left(\frac{1}{\sqrt{\pi}} - x \, e^{x^2} \text{erfc}(x) \right)$, $x = x_0 \Gamma^{1/3}(t)$, and $x_0 = \frac{\sqrt{6}}{|k_F a|} \left(\frac{E_F}{\widetilde{E}} \right)^{1/2}$ (Eq. 5.94, Eq. 5.68, and Eq. 5.81). Using the measured values for the trap frequencies, the anharmonic correction, and a zero bulk viscosity, we choose an $\widetilde{E}/E_F$ and the associated values of $\langle z^2 \rangle_0$ and $\bar{\alpha}_{S0}$ from the unitary measurement to create transverse aspect ratio curves for arbitrary values of $\bar{\alpha}_{S2}$. Examples are shown in Figures 7.13 and 7.14. According to these calculated curves, the size of ΔP estimated in the high temperature limit has a very small effect on the transverse aspect ratio compared to a finite $\bar{\alpha}_{S2}$. For this reason, we neglect the model dependent ΔP entirely and use the same equations for the expansion factors as used in the unitary gas (Eq.7.17) to determine $\bar{\alpha}_{S2}$ and $\langle z^2 \rangle_0$ from fits of the aspect ratio at a general scattering length.

In the unitary gas, the scaling solution depends on $\langle z^2 \rangle_0$ through the anharmonic correction. This simply requires an iterative to produce self consistent values of the expansion factors, $\langle z^2 \rangle_0$, and $\bar{\alpha}_{S0}$. The scaling solution for the off resonant gas is additionally dependent on $\langle z^2 \rangle_0$ through $\bar{\alpha}_{S0}(\widetilde{E})$ based on the fit of $\bar{\alpha}_{S0}$ as a function $\widetilde{E}$ in the unitary gas. We may then fit the transverse aspect ratio
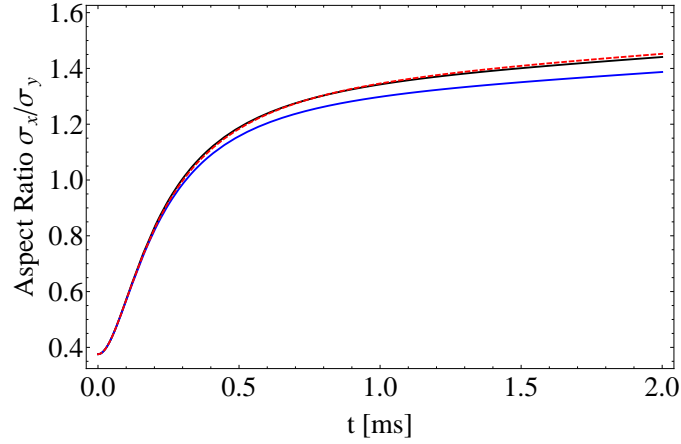
Figure 7.13: Transverse aspect ratio σ_x/σ_y for $1/(k_{FI}a) = +0.6$ (below resonance) as a function of time after release, calculated using Eq. 7.42 with $\widetilde{E}/E_F = 1.0$, $\bar{\alpha}_{S0} = 1.2$. Black solid line: $\bar{\alpha}_{S2} = 0$, $C_F(t) = C_F(0) = C_p(t) = 0$; Red dashed line: $\bar{\alpha}_{S2} = 0$, $C_F(t)$, $C_F(0)$, and $C_p(t)$ determined from Eqs. 7.48-7.50, showing a negligibly small effect of ΔP. Blue solid line: $\bar{\alpha}_{S2} = 0.2$, $C_F(t) = C_F(0) = C_p(t) = 0$, showing a significant effect of a finite $\bar{\alpha}_{S2}$.
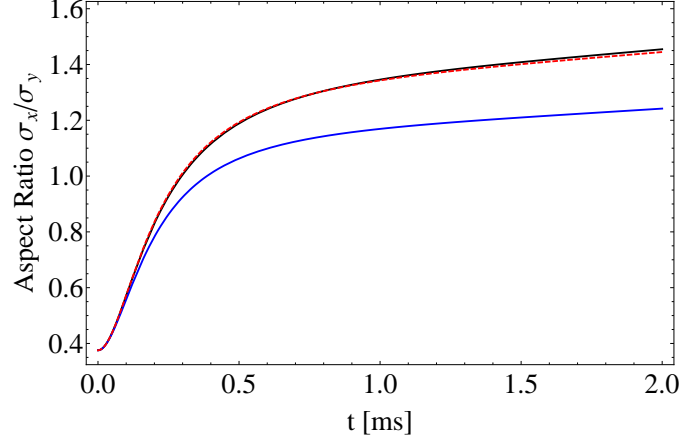
Figure 7.14: Transverse aspect ratio σ_x/σ_y for $1/(k_{FI}a) = -0.6$ (above resonance) as a function of time after release, calculated using Eq. 7.42 with $\widetilde{E}/E_F = 1.0$, $\bar{\alpha}_{S0} = 1.2$. Black solid line: $\bar{\alpha}_{S2} = 0$, $\Delta P = 0$; Red dashed line: $\bar{\alpha}_{S2} = 0$, $C_F(t)$, $C_F(0)$, and $C_p(t)$ determined from Eqs. 7.48- 7.50, showing a negligibly small effect of ΔP; Blue solid line: $\bar{\alpha}_{S2} = 0.9$, $C_F(t) = C_F(0) = C_p(t) = 0$, showing a significant effect of a finite $\bar{\alpha}_{S2}$.

of off-resonant data. with $\bar{\alpha}_S$ as the only free parameter with an iterative proce-
dure, finding self consistent values of $\bar{\alpha}_S$ and $\langle z^2 \rangle_0$. Values of $\bar{\alpha}_{S2}$ are extracted
from six different values of $1/(k_{FI}a) = -0.61, -0.33, -0.01, 0.23, 0, 0.58, 0.86$ and
a range of $\widetilde{E}$ values. For each $1/(k_{FI}a)$, the value of $\bar{\alpha}_{S2}$ as a function of $\widetilde{E}$ is then
fit with a line. Once determined, this line estimates $\bar{\alpha}_{S2}$ as a continuous function
$\widetilde{E}$, allowing us to compare values of $\bar{\alpha}_{S2}$ for different values of $1/(k_{FI}a)$, but the
same $\widetilde{E}$.

7.12 Results of the Shear Viscosity for a Finite Scattering Length Analysis

The simultaneously measured values of $\bar{\alpha}_{S2}$ and $\widetilde{E}$ are given in Fig. 7.15 for six
different interaction strengths. The linear fits to $\bar{\alpha}_{S2}$ as a function of $\widetilde{E}$ are also
shown, in addition to dotted lines indicating the uncertainty in the linear fit
function as a result of the uncertainty in $\bar{\alpha}_{S2}$ and $\widetilde{E}$. The different graphs are
grouped in their respective columns by sign of the scattering length, so that data
taken on the BEC side, with a positive scattering length, is on the left. The
data from the BCS side is arranged in the right column. In the time since this
experiment was performed, a new measurement [30] has found the location of the
Feshbach resonance in ^{6}Li at 832 G, rather than 834 G. This has no effect on
our measured viscosities, as ΔP is neglected, but we do label the 834 G data as
$1/(k_{FI}a) = -0.01$, as opposed to $1/(k_{FI}a) = 0.00$.

In acknowledgment of a new measurement that gives the location of Feshbach
resonance [30] at 832 G, what was thought to resonant data when this experiment
was performed is relabeled as $1/(k_{FI}a) = -0.01$, as it was taken a magnetic field
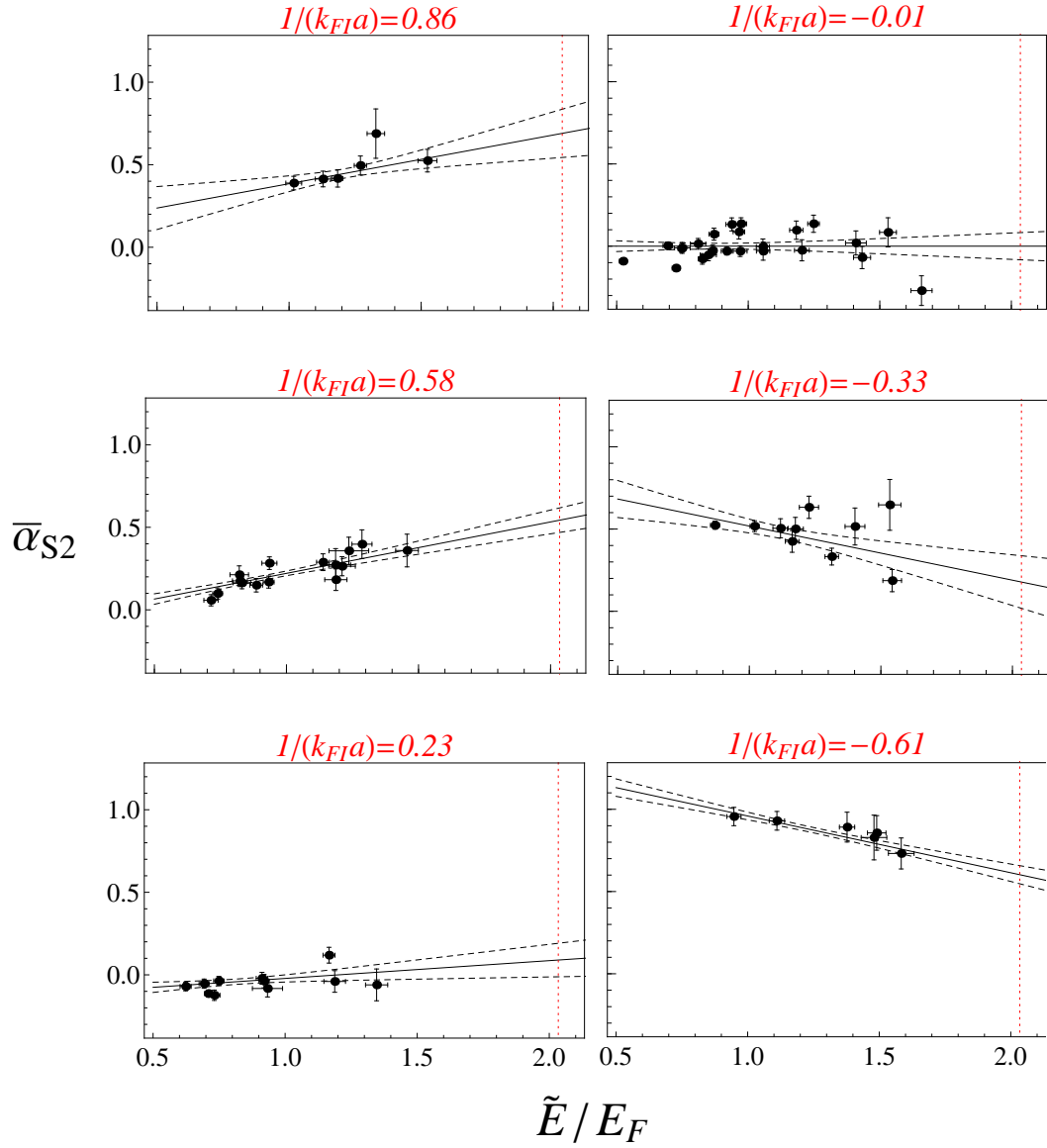
Figure 7.15: Scattering length-dependent shear viscosity coefficient $\bar{\alpha}_{S2}$ as a function of energy $\widetilde{E}$ and interaction strength $1/(k_{FI}a)$. Black lines denote linear fit to $\alpha_{S2}(\widetilde{E})$. Dotted black lines show the range arising from the uncertainty in the straight line fit parameters. Vertical red dotted shows the $\widetilde{E}$ where the minimum of $\bar{\alpha}_{S2}$ occurs at $1/(k_{FI}a) = 0$ in Fig. 7.16.

2 G above the newly established value.

This data displays noteworthy qualitative features. First, there is a clear *decrease* in $\bar{\alpha}_{S2}$ with increasing energy on the BCS side. On the BEC side, $\bar{\alpha}_{S2}$ *increases* with increasing energy, and this rate appears to decrease the closer the scattering length is tuned to its resonant value. Most notable, however, is that for the lowest energies of data sets sharing a $1/(k_{FI}a) = +0.23$ (the value $1/(k_{FI}a)$ on the BEC side that is the closest to resonance), $\bar{\alpha}_{S2}$ takes on consistently *negative* values. Physically, a negative $\bar{\alpha}_{S2}$ does not indicate a negative viscosity, but rather a total $\bar{\alpha}_{S0}$ that is smaller at 800 G than it would be for a cloud of the same initial size at 832 G.

Recall from Chapter 4 that the shear viscosity scales inversely with scattering rate, so an explanation for this decrease in total shear viscosity to the BEC side of resonance should include a mechanism for an enhanced collision rate. A likely possibility is the emergence of a bosonic component [59] of the cloud in the form of either preformed pairs or dimer molecules. In collisions between fermions, the exclusion principle leads to the suppression of elastic scattering events if the final states of scattering process are already occupied. This Pauli blocking effect would be lessened by the presence of additional bosonic degrees of freedom, leading to fewer unallowed final collisional states, and an increased collision rate [60]. Further, although the collisional cross section of two atoms is maximized at resonance, the collisional cross section for molecule-atom scattering is larger than that for atom-atom scattering [46]. A small decrease in the atom-atom cross section could be more than compensated by the finite chance of molecule-atom scattering. This possible explanation is also consistent with the observed increase of $\bar{\alpha}_{S2}$ as a function of energy on the BEC side. Equivalently, the total viscosity
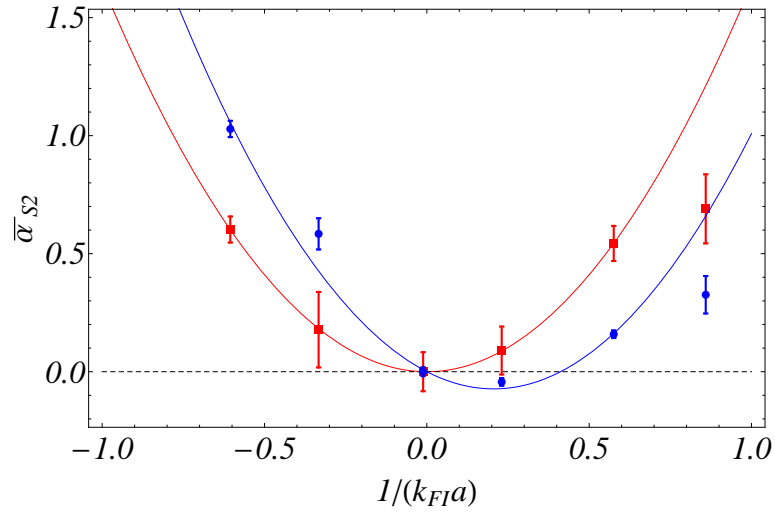
Figure 7.16: Shear viscosity coefficient $\bar{\alpha}_{S2}$ versus interaction strength $1/(k_{FI}a)$ at fixed energies. Blue circles represent α_{S2} obtained from the linear fits in Fig. 7.15 for an energy $\widetilde{E}/E_F = 0.8$. The solid blue curve shows a parabolic fit, which has a minimum, negative value at $1/(k_F a) = 0.21$. The red squares are the result of the linear fits in Fig. 7.15 extrapolated to $\widetilde{E}/E_F = 2.07$, above the measured energy range. The red dashed curve shows the corresponding parabolic fit, which is minimized at resonance. Error bars arise from the uncertainty in the linear fit parameters for the data of Fig. 7.15. As explained in the text, the two right most points are neglected in the parabolic fit.

increases more quickly as function of energy in the BEC regime relative to the unitary value. This behavior could be a result of a decreasing molecular fraction accompanying the energy increase, reducing the collision rate through both the finite atom-atom cross section and the vanishing chance of an atom-molecule collision. On the BCS side of resonance, the observed decrease of the $\bar{\alpha}_{S2}$ (and the total shear viscosity relative to the unitary value) with increasing energy may also arise from reduced Pauli blocking. However, in the BCS regime, this can not be the result of a molecular fraction. Instead, it could come from the gas being less degenerate as the temperature increases, creating less competition for final collision states and increasing the collision rate.

Using the linear fits from Fig. 7.15 for $\bar{\alpha}_{S2}(\widetilde{E})$ at different values of $1/(k_{FI}a)$, the results of plotting $\bar{\alpha}_{S2}$ for the same $\widetilde{E}$ as a function of $1/(k_{FI}a)$ are displayed in Fig. 7.16. The two energies chosen are $\widetilde{E}/E_F = 0.8$, and $\widetilde{E}/E_F = 2.07$, meant to contrast the low energy behavior with trends at higher energies. Note that unlike the energy range around $\widetilde{E}/E_F = 0.8$ in Fig. 7.16 that is surrounded with measured data points, $\widetilde{E}/E_F = 2.07$ is an extrapolation from the linear fits to an energy region where no data was taken. However, the unexpected result of a lower shear viscosity off resonance occurs in the lower energy regime where the data is taken, while the high energy extrapolation demonstrates that the trend in this data still predicts the more anticipated result to occur at higher energies. For the low energy data, the method of displaying $\bar{\alpha}_{S2}$ in Fig. 7.16 makes the shift of the minimum viscosity towards the BEC side more obvious. It also shows $\bar{\alpha}_{S2}$ increasing with energy on the BEC side, and decreasing with energy on the BSC side. The parabolic fits to both the high and low energy data are given by a function of the form

$$\bar{\alpha}_{S2}(\widetilde{E}) = d_1 \frac{1}{k_{FI}a} + d_2 \frac{1}{(k_{FI}a)^2}, \tag{7.51}$$

excluding the $1/(k_{FI}a) = 0.86$ data points, where the value of $\bar{\alpha}_{S2}$ would require an additional odd power of $1/(k_{FI}a)$ in Eq. 7.51. The $1/(k_{FI}a) = 0.86$ data are also quite far into the BEC region, where it is reasonable to attribute their failure to fall on the parabola to either a large molecular fraction, or a divergence in the expansion of $1/(k_{FI}a)$.

A plot of the first and second order fit coefficients d_1 and d_2 from Eq. 7.51 as a function of energy is presented in Figure 7.17. It is notable that the d_2 appears
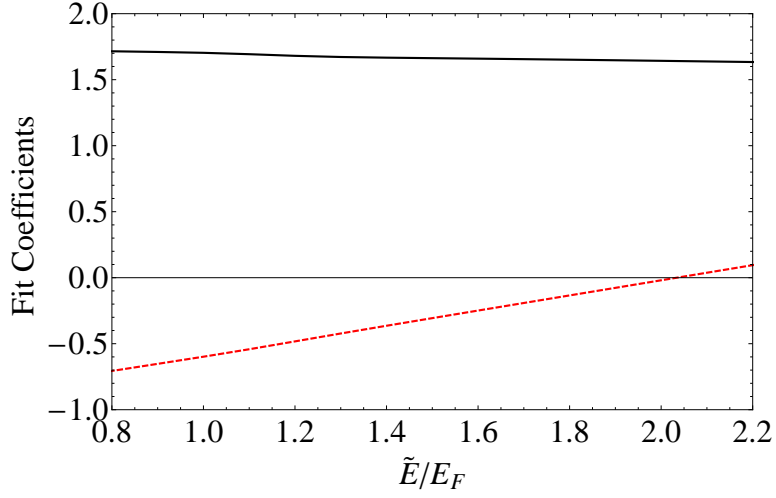
Figure 7.17: Coefficients d_1 of $1/(k_{FI}a)$ (bottom dashed line) and d_2 of $1/(k_{FI}a)^2$ (top solid line) versus energy $\widetilde{E}/E_F$. d_2 shows a negligibly small dependence on $\widetilde{E}$, while d_1 varies linearly.

to be nearly energy independent, while d_1 is an increasing function of energy. This is a more explicit way of indicating that a lower shear viscosity slightly to the BEC will occur only at low energies, and the lowest shear viscosity as a function of scattering length will move back towards the resonant value at higher energies. However, this extrapolation is not to be entirely believed at the *highest* energies, in the regime of $\widetilde{E}/E_F \gg 2$. The extrapolation would indicate that the energy dependent behavior of d_1 would shift the minimum in of the shear viscosity towards the BSC at $\widetilde{E}/E_F \gg 2$. Instead, we expect that d_1 should asymptote at a value of zero, which requires additional data. This would ensure that once the energy increases to a point where the minimum shear viscosity occurs in the unitary regime, that is where the minimum remains. The shift in the minimum η toward the BEC of resonance was not expected, and will provide an impetus for the theoretical study of the shear viscosity of a Fermi gas near a Feshbach resonance.

Bibliography

[1] Gautam Rupak and Thomas Schäfer. Shear viscosity of a superfluid fermi gas in the unitarity limit. *Phys. Rev. A*, 76:053607, 2007.

[2] T.-L. Ho. Universal thermodynamics of degenerate quantum gases in the unitarity limit. *Phys. Rev. Lett.*, 92:090402, 2004.

[3] J. E. Thomas, J. Kinast, and A. Turlapov. Virial theorem and universality in a unitary Fermi gas. *Phys. Rev. Lett.*, 95:120402, 2005.

[4] M.J. Ku, A. T. Sommer, L. W. Cheuk, and M. W. Zwierlein. Revealing the superfluid lambda transition in the universal thermodynamics of a unitary Fermi gas. *Science*, 2012.

[5] C. Cao, E. Elliott, J. Joseph, H. Wu, J. Petricka, T. Schäfer, and J. E. Thomas. Universal quantum viscosity in a unitary Fermi gas. *Science*, 331:58, 2011.

[6] C. Cao, E. Elliott, H. Wu, and J. E. Thomas. Searching for perfect fluids: quantum viscosity in a universal Fermi gas. *New J. Phys.*, 13:075007, 2011.

[7] K. M. O'Hara, S. L. Hemmer, M. E. Gehm, S. R. Granade, and J. E. Thomas. Observation of a strongly interacting degenerate Fermi gas of atoms. *Science*, 298:2179, 2002.

[8] S. Giorgini, L. P. Pitaevskii, and S. Stringari. Theory of ultracold atomic Fermi gases. *Rev. Mod. Phys.*, 80:1215, 2008.

[9] W. Ketterle and M. W. Zwierlein. *Making, probing and understanding ultracold Fermi gases.* IOS Press, Amsterdam, 2008. in Ultracold Fermi Gases, Proceedings of the International School of Physics Enrico Fermi, Course CLXIV, Varenna, 20 - 30 June 2006.

[10] I. Bloch, J. Dalibard, and W. Zwerger. Many-body physics with ultracold gases. *Rev. Mod. Phys.*, 80:885, 2008.

[11] A. Adams, L. D. Carr, T. Schäfer, P. Steinberg, and J. E. Thomas. Strongly correlated quantum fluids: ultracold quantum gases, quantum chromodynamic plasmas and holographic duality. *New J. Phys.*, 14:115009, 2012.

[12] P.F. Kolb and U. Heinz. *Quark Gluon Plasma 3*, page 634. Wold Scientific, 2004.

[13] E. Shuryak. Why does the quark-gluon plasma at RHIC behave as a nearly ideal fluid? *Prog. Part. Nucl. Phys.*, 53:273, 2004.

[14] L.D. Landau and E.M. Lifshitz. *Fluid Mechanics*. Pergamon Press, 1959.

[15] R.B. Leighton R. Feynman and M.L. Sands. *The Feynman Lectures on Physics: Volume II*. Addison-Wesley Publishing Company, 1989.

[16] J. C. Maxwell. On the viscosity or internal friction of air and other gases. *Philosophical Transactions of the Royal Society of London*, 156:249, 1866.

[17] P.W. Atkins. *Atkins' Molecules*. Cambridge University Press, 2003.

[18] P. K. Kovtun, D. T. Son, and A. O. Starinets. Viscosity in strongly interacting quantum field theories from black hole physics. *Phys. Rev. Lett.*, 94:111601, 2005.

[19] M. E. Gehm A. Turlapov J. Kinast, S. L. Hemmer and J. E. Thomas. Evidence for superfluidity in a resonantly interacting fermi gas. *Phys. Rev. Lett.*, 92:150402, 2004.

[20] D.T. Son. Vanishing bulk viscosities and confromal invariance of the unitary gas. *Phys. Rev. Lett*, 98:020604, 2007.

[21] C. Poole H. Goldstein and J. Safko. *Classical Mechanics*, page 84. Addison Wesley, 2002.

[22] Bason Clancy. *Hydrodynamics of a Rotating Strongly Interacting Fermi Gas*. PhD thesis, Duke University, 2008.

[23] Le Luo. *Entropy and Superfluid Critical Parameters of a Strongly Interacting Germi Gas*. PhD thesis, Duke University, 2008.

[24] Kevin Dusling and Thomas Schäfer. Bulk viscosity and conformal symmetry breaking in the dilute Fermi gas near unitarity. *Phys. Rev. Lett.*, 111:120603, 2013.

[25] Michael Gehm. *Preparation of an Optically-Trapped Degenerate Fermi Gas of 6Li: Finding the Route to Degeneracy.* PhD thesis, Duke University, 2003.

[26] Kenneth O'Hara. *Optical Trapping and Evaporative Cooling of Fermionic Atoms.* PhD thesis, Duke University, 2000.

[27] Herman Feshbach. Unified theory of nuclear reactions. *Ann. Phys.*, 5:357, 1958.

[28] L. Pitaevskii and S. Stringari. *Bose-Einstein Condensation*, page 492. Clarendon Press, Oxford, 2003.

[29] M. Bartenstein, A. Altmeyer, S. Riedl, R. Geursen, S. Jochim, C. Chin, J. Hecker Denschlag, R. Grimm, A. Simoni, E. Tiesinga, C. J. Williams, and P. S. Julienne. Precise determination of ^{6}Li cold collision parameters by radio-frequency spectroscopy on weakly bound molecules. *Phys. Rev. Lett.*, 94:103201, 2005.

[30] G. Zürn, T. Lompe, A. N. Wenz, S. Jochim, P. S. Julienne, and J. M. Hutson. Precise characterization of ^{6}Li feshbach resonances using trap-sideband-resolved rf spectroscopy of weakly bound molecules. *Phys. Rev. Lett.*, 110:135301, 2013.

[31] L.N. Copper J. Bardeen and J.R. Schrieffer. Theory of superconductivity. *Phys. Rev.*, 108(5):1175, 1957.

[32] J. L. Bohn C. A. Regal, C. Ticknor and D. S. Jin. Creation of ultracold molecules from a fermi gas of atoms. *Nature*, 424:47, 2003.

[33] K.M. O'Hara S.R. Granade, M.E. Gehm and J.E.Thomas. All-optical production of a degenerate fermi gas. *Phys. Rev. Lett.*, 88:120405, 2002.

[34] Joseph Kinast. *Thermodynamics and SuperFluidity of a Strongly Interacting Fermi Gas.* PhD thesis, Duke University, 2006.

[35] James Joseph. *Precision Measurement of the Sound Velocity in an Ultracold Fermi Gas Through the BEC-BCS Crossover.* PhD thesis, Duke University, 2010.

[36] W. D. Phillips and H. Metcalf. Laser deceleration of an atomic beam. *Phys. Rev. Lett.*, 48:596, 1982.

[37] Christopher J. Foot. *Atomic Physics.* Oxford University Press, 2005.

[38] S. R. Granade. *All-optical Production of a Degenerate Gas of ^6Li: Characterization of Degeneracy*. PhD thesis, Duke University, 2002.

[39] Chenglin Cao. *Universal Quantum Viscosity in a Unitary Fermi Gas*. PhD thesis, Duke University, 2012.

[40] S.R. Granade K.M. O'Hara, M.E. Ghem and J.E. Thomas. Scaling laws for evaporative cooling in time-dependent optical traps. *Phys. Rev. A.*, 64:051403, 2001.

[41] Tin-Lun Ho. Universal thermodynamics of degenerate quantum gases in the unitarity limit. *Phys. Rev. Lett.*, 92:090402, 2004.

[42] Lev P. Pitaevskii Yan-Hua Hou and Sandro Stringari. Scaling solutions of the two-fluid hydrodynamic equations in a harmonically trapped gas at unitarity. *Phys. Rev. A*, 87:033620, 2013.

[43] Rudolf Grimm Yan-Hua Hou Lev Pitaevskii Leonid A. Sidorenkov, Meng Khoon Tey and Sandro Stringari. Second sound and the superfluid fraction in a fermi gas with resonant interactions. *Nature*, 498:78–81, 2013.

[44] Yan-Hua Hou, Lev P. Pitaevskii, and Sandro Stringari. Scaling solutions of the two-fluid hydrodynamic equations in a harmonically trapped gas at unitarity. *Phys. Rev. A*, 87:033620, 2013.

[45] D. S. Petrov, C. Salomon, and G. V. Shlyapnikov. Weakly bound dimers of fermionic atoms. *Phys. Rev. Lett.*, 93:090404, 2004.

[46] D. S. Petrov, C. Salomon, and G. V. Shlyapnikov. Scattering properties of weakly bound dimers of fermionic atoms. *Phys. Rev. A*, 71:012708, 2005.

[47] G. M. Bruun and H. Smith. Viscosity and thermal relaxation for a resonantly interacting fermi gas. *Phys. Rev. A*, 72:043605, 2005.

[48] T.-L. Ho and E. Mueller. High temperature expansion applied to fermions near Feshbach resonance. *Phys. Rev. Lett.*, 92:160404, 2004.

[49] Kerson Huang. *Statistical Mechanics*. John Wiley & Sons, Inc., 1969.

[50] Gavroglu K and Goudaroulis Y. *Through Measurement to Knowledge: The Selected Papers of Kamerlingh Onnes*. Kluwer Academic Press, Dordrecht, 1991.

[51] L.D. Landau and E.M. Lifshitz. *Statistical Physics*. Pergamon Press, 1963.

[52] J.Kinast J.E.Thomas and A.Turpalov. Virial theorem and universality in a unitary fermi gas. *Phys. Rev. Lett.*, 95:120402, 2005.

[53] A. Yariv. *Quantum Electronics.* John Wiley and Sons, New York, 1975.

[54] L. Luo, B. Clancy, J. Joseph, J. Kinast, and J. E. Thomas. Measurement of the entropy and critical temperature of a strongly interacting Fermi gas. *Phys. Rev. Lett.*, 98:080402, 2007.

[55] L. Luo and J. E. Thomas. Thermodynamic measurements in a strongly interacting Fermi gas. *J. Low Temp. Phys.*, 154:1, 2009.

[56] D. T. Son. Vanishing bulk viscosities and conformal invariance of the unitary Fermi gas. *Phys. Rev. Lett.*, 98:020604, 2007.

[57] M. A. Escobedo, M. Mannarelli, and C. Manuel. Bulk viscosities for cold Fermi superfluids close to the unitary limit. *Phys. Rev. A*, 79:063623, 2009.

[58] E. Taylor and M. Randeria. Viscosity of strongly interacting quantum fluids: Spectral functions and sum rules. *Phys. Rev. A*, 81:053610, 2010.

[59] H. Guo, D. Wulin, C.-C. Chien, and K. Levin. Microscopic approach to viscosities in superfluid Fermi gases: From BCS to BEC. http://arxiv.org/abs/1008.0423v3.

[60] G. M. Bruun and H. Smith. Shear viscosity and damping for a Fermi gas in the unitary limit. *Phys. Rev. A*, 75:043612, 2007.

Biography

Ethan Robert Elliott was born December 5th, 1983, in Boston, Massachusetts. After graduating from Lawrence Academy in 2002, he earned his B.A. from St. Mary's College of Maryland in 2006, graduating Summa Cum Laude with induction into Phi Beta Kappa. Following a year of work in a Naval physics laboratory under Frank Narducci, he enrolled in the graduate school at Duke University in 2007. Joining the research group of John Thomas, he contributed to experiments studying the hydrodynamics of strongly interacting Fermi gases as a function of energy and interaction strength, as well as the complete dismantling and successful reassembly of the associated experimental apparatus during a move of laboratory space from Duke to NC State. He was awarded a M.A. and Ph.D. in physics from Duke in May 2014.

Publications

E. Elliott, J. Jospeh, and J. E. Thomas, "Anomalous minimum in the shear viscosity of a Fermi gas," submitted to *Physical Review Letters*.

E. Elliott, J. Jospeh, and J. E. Thomas, "Observation of conformal symmetry breaking and scale invariance in expanding Fermi gases," *Physical Review Letters*, **112**, 040405 (2014).

C. Cao, E. Elliott, J. Jospeh, H. Wu, T. Sh'afer and J. E. Thomas, "Universal quantum viscosity in a unitary Fermi gas," *Science*, **331**, 58 (2011).

C. Cao, E. Elliott, H. Wu, and J. E. Thomas,, "Searching for perfect fluids: quantum viscosity in a universal Fermi gas," *New Journal of Physics*, **13**, 075007 (2011).

T. Abi-salloum, J. P. Davis, C. Lehman, E. Elliott, and F. A. Narducci, "Phase dynamics and interference in EIT," *Journal of Modern Optics*, **54**, 2459 (2007).